

SHIBAURA MACHINE ENGINEERING REVIEW

Mar. 2025

vol.30

Special Feature

Labor Productivity Enhancement



■ Introductory Note	2	Introductory Note
■ Special Article	3	Efforts to Improve Labor Productivity
■ Technical Paper	7	Real-Time Monitoring of Pellet Plastication in a Full-Flight Screw and Kneading Disk Elements of a Co-Rotating Self-Wiping Twin-Screw Extruder by Acoustic Emission (AE) Sensing
	19	Slurry Conditions for Reaction-Induced Slurry-Assisted Grinding of Optical Glass Lens
	26	Subordination Architecture - A New Control Architecture for Autonomous Robots
	38	Development of AI Models to Extract and Evaluate Contact Patterns of Scraping
	43	Development of Interface Control Technology with Medium Vacuum PVD for Achieving All-dry Semiconductor Package Interconnect Formation Process
■ Technical Report	48	Verification of Production Methods Using Environment-Friendly Die-Casting Technology
	54	Research on Causes of Defects in Transparent Resin Molding
	59	Approach to Automating of Sheet/Film Manufacturing System
	63	Tool Edge Position Measurement in 5-axis Indexed Machining
	67	Introduction of Elemental Technologies for Achieving Skill-less Grinding
	71	Construction of Logistics Line with Logi Robo Series
	77	Development of Collaborative Robot Safety System "Dual Safety Core"
	82	Development of a Highly Efficient Production Process for Precision Processing Machine Parts
■ New Product Introduction	87	Total Die-Casting Machine Controller TOSCAST-999
	90	Extra-Large Electric Injection Molding Machine EC3000SXIII
	93	Development of Table-type Horizontal Boring and Milling Machine BTH Stretched Version
	96	Polygon Mirror Generator UFG-150D(PV)
	98	TCmini Series "TC11-02"
	100	SCARA Robot THE800/THE1000
■ Series	102	Manufacturing to Support Society
■ Column	76	Memories of HUM Screw Development for Single Screw Extruder
	81	Rewarding for me
	99	Learning from Challenging the Unknown
■ Patent News	113	Patent Introduction
■ Prepared Critique	117	Prepared Critique



Shigetomo SAKAMOTO

President,
Chief Executive Officer and
Chief Operating Officer,
General Manager of
Machine Tools Company

Technology development and accumulation are a very important asset for us as a manufacturer and is the essence of our business. This Volume 30 of Engineering Review presents the current state and results of our technology development to our stakeholders, and I am very pleased if it awakens their expectations with our company and helps them feel confident about what we do.

This volume's theme is "Labor productivity enhancement." We would like to present several productivity cases that we have developed and commercialized. Please take the time to read this review.

We have been implementing a medium-term management plan called "Management Reform Plan," and this year is the last one in the plan period. We are making all-out efforts to achieve the plan targets, including 135 billion yen in sales, 8.0% in the operating profit rate, and 8.5% in ROE. Managerial measures under way include business structure reforms and investment promotion. The pillars of these measures are product competitiveness and engineering capabilities, which are sources of each company's ability to achieve management goals.

The environment surrounding manufacturers including our company have changed with the times, and what markets and customers want has diversified and we are now required to deliver even higher quality and efficiency. In particular, AI and DX are spreading exponentially, and technological innovation that is under way now can even change the concept of manufacturing equipment. Besides offering standalone products, it is also important to propose solutions based on system engineering, covering upstream and downstream processes as well.

For example, the automobile industry has evolved from internal combustion engines to EVs, shifting from structures with reciprocating engines and transmissions to those with motors and batteries. The parts count has been reduced considerably due to the integral molding of several parts, and we are required to enhance our productivity significantly.

To realize these, just improving our existing

technologies is not sufficient, and it is important to develop technologies in new areas and increase value added by not only hardware but also software.

We will try to acquire and upgrade skills, especially at the R&D center, so that we can always provide cutting-edge technologies. Looking back on our past, we have always provided what was demanded by the times. We have played an important manufacturer role in big markets, including large machine tools during the war, textile machines in the post-war recovery period, and steel machine tools and automobile parts manufacturing equipment in the high economic growth period. Energy, power storage, weight reduction, and recycling are future growth markets, and I think that we need to maintain and develop our technologies so that we can provide equipment that can meet the needs of these markets.

"Labor productivity enhancement" covered in this volume does not only mean cost reduction, but leads directly to SDGs and the sustainability of society, and important considerations are how efficiently we can produce with less energy, whether our products are friendly to people and the nature, and whether the recyclability of produced goods is considered seriously. We will make all-out efforts in these respects as well.

Lastly, because the COVID-19 crisis has cooled down, people are moving more actively in all regions around the globe. In the meantime, many hostilities have occurred, including Russia's invasion into Ukraine and the Israeli-Palestinian conflicts, and geopolitical instability remains unresolved. China and the U.S. have been competing over supply chains.

In these circumstances, we will upgrade our basic technologies continuously, develop new products, and keep ourselves ready to serve our customers at all times by meeting their requests so that our stakeholders will be able to continue their business stably and increase their competitive strengths.

I hope that this Volume 30 presents part of this commitment of ours.

Efforts to Improve Labor Productivity



Masafumi ITO
 Managing Executive Officer,
 General Manager of
 Control Systems Company

1 Introduction

Japan's population peaked at 128.08 million in 2008 and has begun to decline, and is expected to fall below 90 million by 2060, with the aging rate reaching nearly 40%. As the working-age population continues to decline due to the rapid aging of society and falling birthrates, improving labor productivity has become an urgent and ongoing issue. The same trend is seen even in China and other less developed countries that have been leading the world economy so far, and the labor shortage has become a common issue worldwide.

Improving labor productivity is also essential at production sites where machinery, equipment, and systems provided by the Shibaura Machine Group operate, and the degree of contribution to the efficiency improvement at the sites through the added values of products, functions, and services is becoming more and more important.

The Control Systems Company has been in charge of the development of control systems for our products for many years, and has a long history of research and development of various elements related to factory automation, as well as of technology possession. We are proud to have contributed to the improvement of productivity of many of our customers by providing solutions that enable easy automation of production while meeting a wide range of needs in the world, not only through internal sales, but also through external sales of our original products. Solution methods are changing with the times, and various needs are emerging in the aspect of not only hardware but also software represented by DX(digital transformation). In addition, as values have been diversified, the creation of environmentally friendly products is another urgent issue to be addressed. The Control Systems Company is developing its external sales business in three major segments: the Components Division, which develops and sells controllers, servo units, and other products; the Robot Division; and the

System Engineering Division, which handles overall FA equipment. In this paper, we will introduce some examples of products that have been developed and sold for the purpose of improving labor productivity and future efforts of each segment.

2 Examples of Efforts that Contribute to Improving Labor Productivity

2.1.1 Components

In the Japanese market, we started the development and sales of our BS Servo servo system in 1980, ahead of other companies. BS stands for Brushless Synchronous. This product has been adopted by many customers under the trademark Velconic since its initial release. The VLTT series, the initial product, was an analog servo, but in 1991, we developed E series digital servo, which allowed parameter settings from software, rather than hardware, thereby dramatically improving ease of use for the user. Since then, BS Servo has contributed to productivity improvement through further evolution leading to the current series with the downsizing due to the introduction of IGBT devices and with the improvement of CPU performance. The BS servo features a resolver as the motor's sensor, and has been used in many industrial machines such as weaving machines, spring machines, and screw tightening machines that are required to operate in harsh environments, taking advantage of its low failure rate and excellent environmental resistance performance, including vibration resistance. Among such applications, three special case examples are presented below.

(1) Large XY stage for drive simulator manufactured by JRC

This consists of 76 axes with 55 kW servos for a maximum output of 2,100 kW, other remote I/O, and various modules, 98 axes in total.

The large size of this heavy equipment and its required dynamic performance required a very large amount of power, and it was necessary to synchronously control 12 X-axes and 64 Y-axes even with our servo amplifier for 55 kW, which is capable of the highest output. There are as many as 38 control panels alone, 25 of which are lined up on one side of the 45-m-long equipment. Since connecting multiple LAN cables is basically all that is required for input and output signals from the master PLC, labor saving in installation is achieved, and the possibility of irregular malfunctions due to noise is very low. In addition, the time for commissioning has been reduced, and much post-operation monitor information can be provided, which greatly contributes to improved maintainability.

(2) New movable launch pad carrier for H3 launch vehicle (weighing 1,460 tons)

The 12 traveling axes and 28 steering axes, 40 axes in total, make up a single carrier. The transportation of a launch vehicle requires stable traveling with synchronization of each axis. In the past, the final positioning into the hangar was done by manual operation, but with the application of servos, now positioning with $\pm 25\text{mm}$ accuracy can be performed automatically.

Reference: <https://www.rocket.jaxa.jp/rocket/h3/groundEquipment.html>
(Movable launch pad carrier (dolly))

(3) Application to automatic weaving machine

A servo motor is used to control the weaving machine opening frame.

By applying the servo system, the movement pattern of the opening frame can be freely set from the operation panel, significantly reducing the time and labor for fabric setup and changeover by the end-user. In addition, the opening motion curve can be set and changed even during operation, ensuring both quality and productivity.



Fig.1. Automatic weaving machine
(Toyota Industries Corporation JAT910)

2.1.2 Robot

We have been in the business of SCARA robots since their inception in the early 1980's, and are a pioneer company in the field of SCARA robot sales. Our robots were introduced to the fan assembly line at Toshiba Nagoya Plant in 1981 and to the printed circuit board various-shape component mounting line at Toshiba Fukaya Plant in 1982, where they

were first used internally to refine their application technology and create the current product base. Vertically articulated robots also started in the 1980s with the development of the PUMA robot, and after the business transfer to Toshiba Machine (now Shibaura Machine) in 1996, we developed and commercialized a series of semiconductor and LCD handling robots beginning in 2000 to meet demand at production sites. In the latter half of the 2010s, momentum for the creation of environmentally friendly ECPs (eco products) began to build, and we are developing and commercializing new products with the goal of reducing CO₂ emissions by 30% compared to previous products.

SCARA Robot THE1000 "CO₂ reduction" from TH1050A

Manufacturing	0.052 t	Reduction rate 31.8%
Operation	2.46 t	
Disposal	-0.03 t	
Total	2.48 t	

CO₂ reduction comparison

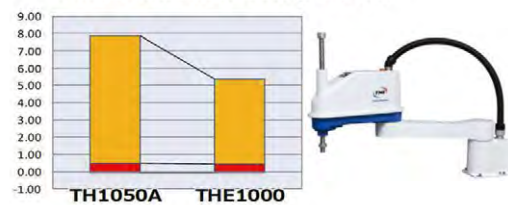


Fig.2. ECP product example, THE1000 (launched in 2022)

2.1.3 System

The Systems Engineering Division has been providing automation systems, mainly utilizing industrial robots, to contribute to the improvement of productivity by saving labor and manpower of our customers. The following are examples of automation systems for injection molding machines and machine tools.

(1) Insert molding automation system

In high-cycle molding, setting inserts into the mold is a simple and hazardous operation. We automated the alignment of inserts with our own high-speed, high-precision SCARA robot and the removal of molded parts with our own highly flexible, vertically articulated robot. This eliminated the need for hazardous work and saved two workers.

(2) Injection molding machine back-end process automation system

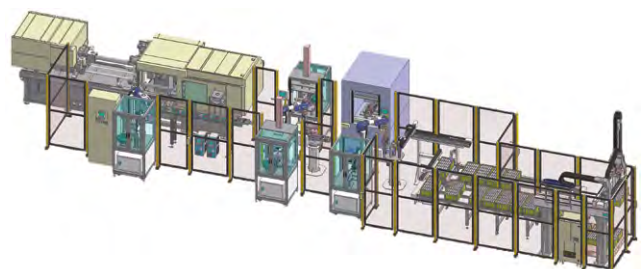


Fig.3. Injection molding machine back-end process automation system

This system fully automated the back-end processes from taking out multiple molded parts, press-fitting inserts, joining molded parts, inspecting, packing into boxes, and stocking boxes. Transportation between each pair of process equipment is performed by three vertically articulated robots, and packing into boxes is performed by a cartesian coordinate robot. This resulted in a manpower saving of more than 3 persons and improved quality stability.

(3) Machine tool loading automation system

This system automates the feeding of materials to machine tools and the taking out of cut workpieces. By placing two machine tools opposite each other and two stockers similarly, with a vertically articulated robot in the center of them, the system saves space and achieves a high utilization rate of the machine tools due to an increase in the number of stocks. As a result, nighttime work could be performed unattended, dramatically improving productivity.

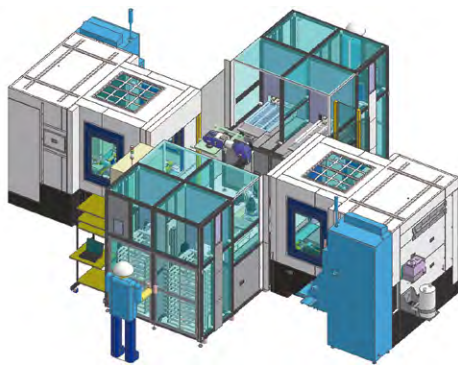


Fig.4. Machine tool automation system

3 Future Efforts and Prospects

3.1.1 Components

We will continue to develop servo amplifiers and servo motors that excel in precision, efficiency, and durability, thereby contributing to improving the productivity of our customers and reducing costs and environmental impact through the energy-saving effects.

Since integration with IoT technology is becoming increasingly important, we will integrate sensors and communication functions into components such as servo amplifiers and controllers, which will enable real-time data collection and remote monitoring. As a result, early detection of malfunctions and more efficient maintenance will be achieved, and the utilization rate of customers' equipment will be improved.

As a means to realize the above, we are currently developing web server functions. In addition, we will utilize artificial intelligence (AI) to enable the automatic setting of optimal control parameters, making it possible to produce high-quality products in a shorter time than before.

In developing products to improve labor productivity,

a wide range of efforts are required, including improvement of control performance, utilization of IoT technology, and introduction of artificial intelligence, etc. Through these efforts, we will contribute to improving the efficiency of our customers' equipment and strengthening their competitiveness.

3.1.2 Robot

Due to the development of MBD and 3D-CAE technologies, it is now possible even to perform precise mechanical simulation in virtual space using robot models, and the speed of robot development has increased to a level that is incomparable to that of the past.

Taking these circumstances into consideration, in addition to further upgrading the functionality of existing robots (SCARA, vertically articulated, orthogonal, etc.), we are accelerating the development of dual-arm cooperative robots that realize the automation in a human workspace, which has been a longstanding issue for us. The increase in fixed costs due to the recent rise in global energy costs has been one of the factors that have reduced the manufacturing industry's willingness to invest in new facilities and equipment. However, the new dual-arm cooperative robot, launched this year, can be installed in the space where human workers used to work for automation with a minimum expansion of the work area. We are continuing to develop this robot as a product that meets recent customers' demand to automate, but not to expand the factory (increase fixed costs).

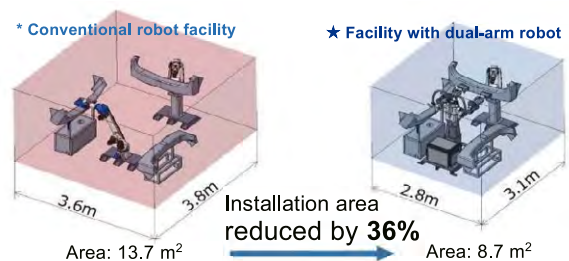


Fig.5. Example of space-saving installation, Human-type dual-armed robot (launched in 2023)

The following describes DX(digital transformation) and cyber security of robots. The performance required for robot products has changed over the years, and it is now indispensable to prepare precise virtual models (i.e., avatars), not just to improve the performance of the arms themselves. Accurate simulations will not only be used for pre-introduction verification, but will also promote technological development, such as placing sensors on virtual robots and using their feedback to virtually verify fault-tolerant functions (i.e., autonomously adjusting operation over time in response to changes over time, such as adjusting acceleration). From an ESG perspective, precision robot avatars will become a

necessity for companies to minimize wasteful resource consumption. At the same time, as it is now commonplace for robots to be connected to general-purpose networks, cyber-attacks have become increasingly stealthy in recent years, and attention is focusing on the development of hardware with built-in cyber security technology to ensure the safety of production programs and data, which are the property of customers. Chips with built-in security functions have already emerged, and applying them will be an essential part of product development in the future.

3.1.3 System

In addition to the declining workforce due to the aging of the population and the declining birthrate, it is predicted that the needs for automation, labor saving, manpower saving, and coexistence of humans and machines to achieve higher productivity, better quality, cost reduction, and safety will further increase. It will be even more necessary for us to integrate our state-of-the-art robot and control technologies, as well as various internal and external hardware and software, to realize production systems that meet the diverse needs of our customers.

The following are the latest case examples in the logistics industry, which is facing the challenge of adapting to a changing labor environment, and the automotive industry, which is undergoing a period of great change.

(1) Depalletizing and cardboard box unpacking system

Work in factory production logistics operations and in distribution warehouses is mainly performed manually by human workers. For example, in food logistics warehouses, a wide variety of cardboard boxes are unpacked using cutters in a labor-intensive manner, making the work site harsh and risky in terms of cutting wounds. Therefore, to reduce the workload, we have proposed a cardboard box unpacking system. The system consists of a process for cutting the sealing tape and a process for cutting the four lids called flaps, making it easier to open the box and remove the contents without damaging them. By combining sensing and robot control technologies, the system can handle a mixed flow of various types of boxes without the need for pre-registration of the types.

Furthermore, by combining with a depalletizing equipment, a series of operations from unloading can be automated.

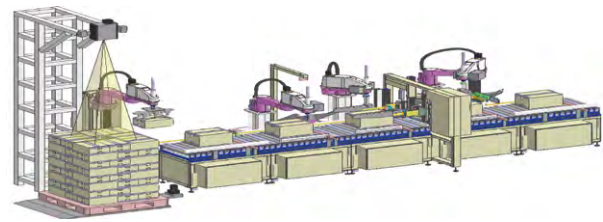


Fig.6. Cardboard box unpacking system

(2) Composite molding system

As shifting to EVs and fuel-efficient vehicles progresses, materials are being replaced with new lightweight, high-rigidity materials. We are working to automate the molding processes of thermoplastic CFRP (carbon fiber reinforced plastics) and other composite materials. In order to use articulated robots to handle stocked materials in the heating and pressing processes, it is necessary to feed heated and irregularly shaped materials into the press molds quickly and accurately, so we use special hands for handling the materials to achieve high quality and high productivity in molding systems.

Even in such a large-scale project, we offer optimal proposals for each customer's requirements, and provide total services from design and fabrication to on-site commissioning.

In addition, our IoT-based centralized management system for condition monitoring, quality data collection, and traceability information for each process contributes to customers' quality control and production efficiency.



Fig.7. Composite molding system

4 Conclusion

This paper presented several case examples resulting in productivity improvements. In all industries and fields, the need for automation and labor saving is expected to increase more and more in the future. We believe it is important to address the various issues and diverse needs of our customers by connecting not only our existing commercial products but also all types of hardware and software with the adjusting skills, control technology, and DX(digital transformation) that integrate them, and by proposing systems. We will continue our research and development to contribute to the improvement of labor productivity and quality, and will continue to take on the challenge of new themes.

Real-Time Monitoring of Pellet Plastication in a Full-Flight Screw and Kneading Disk Elements of a Co-Rotating Self-Wiping Twin-Screw Extruder by Acoustic Emission (AE) Sensing

The plastication of pellets in a co-rotating twin-screw extruder is a significant concern for product homogeneity and stability in the plastic industry. We developed a sensing technology for pellet plastication in a plastication and melting zone in a self-wiping co-rotating twin-screw extruder. The collapse of the solid part of the pellets emits an elastic wave as an acoustic emission (AE) that is measured on the kneading section of the twin-screw extruder using homo polypropylene pellets. The recorded power of the AE signal was used as an indicator of the molten volume fraction (MVF) in the range of zero (fully solid) to unity (fully melted). MVF decreased with increasing feed rate monotonically in the range of 2–9 kg/h at a screw rotation speed of 150 rotations per minute (rpm) because of the reduction in the residence time of pellets in the extruder. However, the increase in feed rate from 9 to 23 kg/h at 150 rpm resulted in an increase in the MVF as the friction and compaction of pellets caused their melting. The AE sensor could elucidate the pellet's plastication phenomena caused by friction, compaction of pellets, and melt removal in the twin-screw extruder.

1 Introduction

Co-rotating self-wiping twin-screw extruder is a continuous polymer processing machine and one of the most widely used screw extruders in the polymer processing industry. It produces pellets, sheets, films, and other plastic products efficiently. The twin-screw extruder transports, plasticates, and melts pellets of plastic resin. When pellets of thermoplastic resin are fed to the twin-screw extruder, the heat transfer from the barrel of the extruder, friction, and adiabatic compression of pellets result in plastication and melting of pellets. [1] If the pellets do not plasticate well in the plastication zone, mixing with additives in the subsequent compounding zone becomes incomplete. Plastication and melting in polymer processing machines are critical elementary steps because they are often the rate-controlling steps that consume 70–80% of the total processing energy input [1]. Additionally, during the melting of polymer blends, a major part of the blend morphology is established [1].



Masatoshi OHARA

Metal & Plastics Industrial
Machine Company
Extrusion Machine
Engineering Department

Keigo INAMORI

Department of Natural System,
Graduate School of Natural Science,
Kanazawa University



Shogo NAGASAWA

Department of Natural System,
Graduate School of Natural Science,
Kanazawa University

Shin-ichi KIHARA

Graduate School of Advanced
Science and Engineering,
Hiroshima University



Kentaro TAKI

School of Frontier Engineering,
Kanazawa University

Keywords : pellet plastication; acoustic emission; melt removal; twin-screw extrusion

The plastication and melting of pellets in a co-rotating twin-screw extruder have been studied mainly by building mathematical models and performing numerical simulations of the plastication zone over the past three decades [2–4]. These models assume that melting occurs primarily by the viscous energy dissipation during the flow of suspensions of solid polymer particulates in melts, with the evolution of melting decreasing the particulate size [1]. Other studies discussed plastic energy deformation via compressive experiments on molded disks of several materials [5–7]. Zhu et al. investigated single pellet deformation using finite element analysis and reported that mechanical energy is converted to heat in this process [8]. The mathematical models and numerical simulations were evaluated by the limited experimental results. Despite the extensive research, studies on real-time monitoring in the plastication zone are limited [9].

Real-time monitoring can raise the alarm and eventually stop the line when the pellet plastication is insufficient. It readily provides the state of pellet

plastication and helps understand the phenomenon. However, the resin temperature and pressure sensors are too fragile to be used in the solid pellets and plastication zones as the solid pellets may collide with the sensors and damage them. Hence, a new type of sensor for resin plastication monitoring is demanded.

In this study, we focused on acoustic emission (AE). AE originates from the transient stress waves that are generated by crack growths and many other kinds of material degradation and deterioration. [10] AE can be applied for monitoring mechanical behaviors of various materials: carbon/epoxy composites [11], glass fiber reinforced polypropylene [12], high-density polyethylene/polypropylene blends [13], natural fiber composites [14], carbon fiber reinforced plastic [15], degraded polypropylene [16], polypropylene/cement [17], etc. Recently, machine learning technology has been applied to the pattern recognition of the AE signal to determine the extent of the damage [18,19].

According to the previous studies on applying AE sensing to various materials, we can expect that collapsing resin pellets in the kneading screw elements emit the AE signal in the extruder.

The AE sensor comprises a piezoelectric transducer and detects ultrasound waves as the AE signal. The ultrasonic wave receiver and transmitter have been applied to the extruders in polymer processing to evaluate the density of polymer melt and the composition of polymer blends [20]. Previous studies have measured the density of molten resin that can be applied to the analysis of plastication in the twin-screw extruder. However, the change in density cannot be directly explained by the change in plastication. The AE signal depends on physical incidents, such as elastic deformation, destruction, and failure of materials, which are directly related to pellet plastication.

Here, a measurement technique to monitor pellet plastication in the extruder using an AE sensor was developed. The effects of screw speed, flow rate, and plastication of polypropylene pellets in the twin-screw extruder were investigated. The experimentally obtained data were discussed with the suggested mechanism previously reported by Gogos et al. [1].

2 Materials and Methods

2.1 Materials

A homo polypropylene (PP, F-704NP) with a melt flow rate (MFR) of 7.0 g/10-min was acquired from Prime Polymer, Minato City, Tokyo, Japan. The resin was used as received. The parameters of the Cross model fitted to the complex viscosity are shown in the Appendix. The melting temperature was measured using a differential scanning calorimeter (DSC-8500, PerkinElmer, Waltham, MA, USA) with a heating rate of 10 °C/min under 20 mL/min flow of

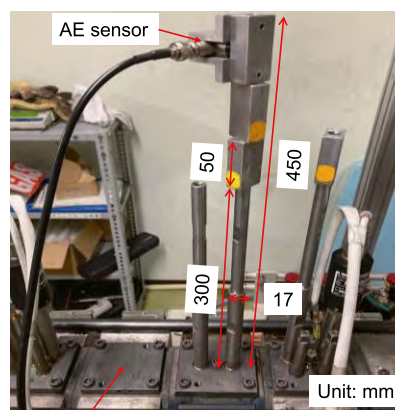
nitrogen. The DSC was calibrated with the Indium standard. The melting temperature was 164 °C.

2.2 AE Sensor

An AE sensor (FAEN-S601, FIRST AE), a built-in amplifier, a 2nd amplifier (EDGE NODE DISCOVERY SEG), and a data acquisition A/D converter (NI DAQ cDAQ-9171 and NI-9775, National Instruments) were connected sequentially. In-house LabVIEW® software was used to collect and record the AE data.

The data acquisition speed was 250 kHz, and the sampling period was 0.2 s.

The AE sensor was attached to a waveguide with a diameter of 17 mm and a length of 300 mm screwed on the barrel of the twin-screw extruder, as shown in Figure 1, to avoid any heat damage to the AE sensor. Three metal blocks, 50 mm in length, were attached to the waveguide. The distance between the barrel surface and the AE sensor was 450 mm. A certain amount of grease (EchoZ+, ECHO ultrasonics) was applied between the AE sensor and the waveguide to reduce the transmission loss. To attach the AE sensor securely to the waveguide without damaging the AE sensor, the same fixing torque (0.35 N·m) should be maintained for every measurement when the AE sensor was fixed on the waveguide. A wind fan was used to continuously cool the sensor.



Barrel of twin-screw extruder

Figure 1. Image of the AE sensor, waveguide, and barrel of the twin-screw extruder.

2.3 Screw Configuration

A co-rotating self-wiping twin-screw extruder (nominal screw diameter 26 mm indicated in Figure 2, screw length to diameter ratio, L/D is 64, TEM-26SX) was used. The screw consists of various screw elements, i.e., a piece of the screw. The order of the screw element can be changed to build a desired screw configuration. We used three different screw configurations (A), (B), and (C) to study the plastication in the twin-screw extruder. The order of screw element's code of screw configurations in the SHIBAURA MACHINE catalog is available in the Appendix.

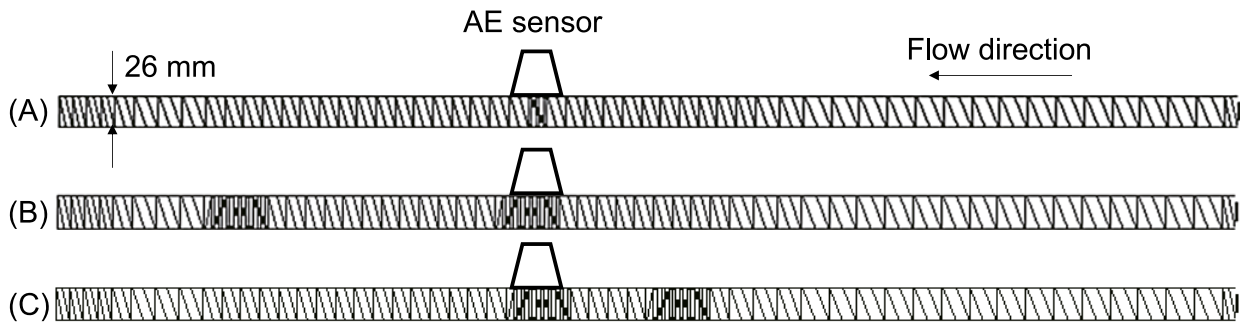


Figure 2. Screw configurations of (A–C) of the co-rotating twin-screw extruder

Configuration (A): It is a simple screw configuration in which one kneading disk element is at 977.5 mm from the feed, and the others are full-flight screw elements, as shown in Figure 2A. The AE sensor was attached above the five-disk forward kneading element. A barrel temperature of 30 °C was used to identify the AE signal of collapsing solid pellets, while that of 195 °C with a short distance of screw heated at 150 °C immediately downstream of the feed port was used to confirm that the molten resin does not emit the AE signal. It should be noted that the barrel temperature of 195 °C was higher than the melting temperature of the sample PP. The examined screw rotation speed and feed rate were 50 screw rotations per minute (rpm) and 2.0 kg/h, respectively.

Configuration (B): The screw configuration (B) was built to understand the effects of feed rate and screw speed on the plastication phenomena in a full-flight screw, as shown in Figure 2B. The five-disk forward, neutral, and backward kneading elements of 27 mm in length located at 965 mm from the feeding port collapse the partially solid pellets that emit the AE signal. The AE signal was used to understand pellet plastication in upstream full-flight screw elements. The barrel temperature was 195 °C at regions away from four full-flight screw elements in front of the feed port. Thus, the melting zone was located at 965 mm from the feeding port. The screw rotation speed increased as follows: 30, 50, 100, 125, 150, 200, and 250 rpm. The feed rate increased as follows: 2.0, 4.0, 6.0, 12, 18, and 23 kg/h. The interval of the measurement was approximately 3 min. Measurements of 12 kg/h at 30 rpm and 18 and 23 kg/h at 30 and 50 rpm were not performed because the pellets were not fed to the feed port continuously.

Two series of experiments were performed. In the 1st series, the screw rotation speed was increased while the feed rate was maintained constant. Subsequently, the process was examined at a higher feed rate from low to high screw rotation speed. In the 2nd series, the feed rate was increased while the screw rotation speed was maintained constant.

In addition, to collect the AE signal of fully solid pellets for the normalization of the AE signal, the

barrel temperature was set equal to the melting temperature at 164 °C.

Configuration (C): The screw configuration (C) was considered to understand the effect of kneading disk elements on the plastication phenomena, as shown in Figure 2C. The five-disk forward, neutral, and backward kneading elements were replaced with full-flight screws. The pellets were plasticized in the replaced kneading disk zone. The AE signal was measured at the downstream kneading zone. The AE signal is possibly generated in the upstream and downstream kneading zones. As the distance between them is set sufficiently long, the AE sensor does not interfere with the AE signal from the upstream kneading zone.

2.4 Residence Time Measurement

The mean residence time of the solid pellets on the full-flight screw was measured as follows. The screw configuration was as same as the upstream configuration from the AE sensor of (B) in Figure 2. The detailed configuration is shown in Table A2 in the Appendix.

The barrel temperature was set to a room temperature of 30 °C. The pellets were fed to the rotating twin screws alone, consisting of full-flight screw elements and no kneading disk elements. The exit of the extruder was open, and no die was attached to it. This operation does not collapse and melt the pellets. The pellets were only transported to the exit of the extruder by the rotation of screws.

In the measurement operation, the rotating screws and the feeder of pellets were abruptly stopped when the mass flow rate reached a steady state of the desired value. The screws were rotated again to transport the remaining pellets in the barrel when the feeder stopped. All the pellets in the barrel were collected, and the mass (m_p) was measured. The mean residence time per meter was calculated as follows:

$$\bar{\tau} = \frac{m_p}{Q_m L_m} \quad (1)$$

Table 1. Residence time per unit meter of solid pellets transported on the full-flight screws at 30 °C.

Residence Time per Meter (s/m)		Screw Rotation Speed (rpm)			
		50	100	150	250
Feed rate (kg/h)	2	43.1	22.9	14.3	10.8
	4	44.8	23.6	15.8	10.8
	6	46.5	23.5	15.7	9.8
	9	53.2	24.4	16.6	10.5
	12	60.1	23.5	16.7	10.5
	18	76.5	26.4	16.6	10.2
	23	- *	31.7	17.6	10.6

* Feed neck occurred. Screw configuration was the “Residence time meas.” in Table A2.

where m_p (kg) is the remained mass of pellets in the barrel when the screws stopped, Q_m (kg/s) is the pellets’ mass flow rate in the feeder, and L_m (m) is the measured barrel distance, which is 0.918 m from feed to head.

The screw rotation speed was changed from 50 to 250 rpm with 50 rpm intervals. The feed rate was increased as follows: 2, 4, 6, 9, 12, 18, and 23 kg/h. The residence time per meter ranges from 9.8–76.5 s/m. The results are summarized in Table 1, and the dependences on the screw rotation speed and the feed rate are plotted.

2.5 Signal Processing

Extrusion of pellets at a barrel temperature of 30 °C produced collapsed pellets in the screw configuration (A) at the screw rotation speed and feed rate of 50 rpm and 2.0 kg/h, respectively. The pellets collapsed between the barrel and screws. The pellets were fully melted, and a clear molten strand was obtained at the exit of the die at the barrel temperature of

195 °C at the same screw rotation speed and feed rates at 30 °C.

A typical time domain and the fast Fourier-transformed AE signals obtained at the barrel temperatures of 30 °C and 195 °C are shown in Figure 3. A strong signal was captured at 0.1 s at 30 °C while no distinct signal was observed at 195 °C in the full range of the time-space. The frequency domain signal indicates that the peaks in the range of 60–80 kHz originated from the AE signals of the collapsing pellets. The signals in the range of 20–60 kHz were superimposed with those of the other phenomena, such as the open-and-close solenoid valves, metal contacting screw and barrel, and other un-clarified noises. Thus, the signals in 60–80 kHz were used in this study as the AE signal of collapsing pellets.

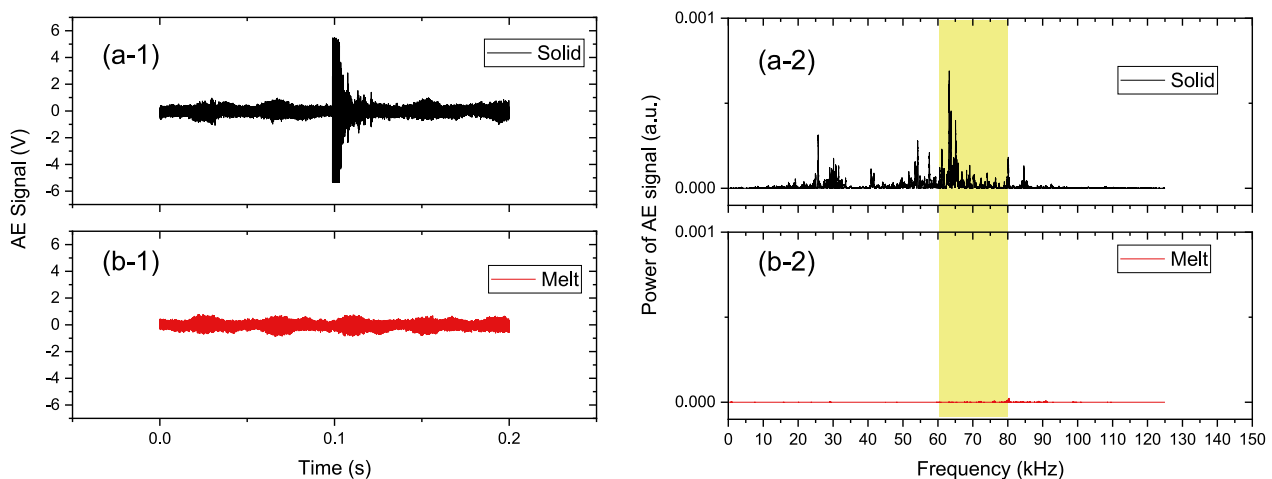


Figure 3. Time domain AE signals at a barrel temperature of (a-1) 30 °C and (b-1) 195 °C. Power of AE signals in frequency domains at (a-2) 30 °C and (b-2) 195 °C. The screw rotation speed and feed rate were 50 rpm and 2.0 kg/h, respectively.

2.6 Molten Volume Fraction (MVF) from AE

A model of AE signal generation, as illustrated in Figure 4, indicates that the AE signal is proportional to the residual solid part of pellets. The recorded time domain signal was processed by the 60–80 kHz bandpass filter. The square of the time domain signal was accumulated during the measurement time of 210 s. Then, the accumulated signal was divided by the number of pellets passed through under the AE sensor for 210 s, which can be calculated by the mass flow rate, measurement time, and average mass of one piece of pellet.

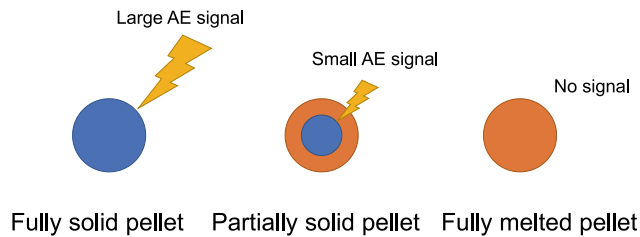


Figure 4. Model of AE signal generation.

Finally, the MVF, χ_p , is calculated as follows:

$$\chi_p = 1 - \frac{S(T_b, Q, N_s)}{S(T_m, 2 \text{ kg/h}, 250 \text{ rpm})} \quad (2)$$

where $S(T_b, Q, N_s)$ is the accumulated signal per pellet. $S(T_m, 2 \text{ kg/h}, 250 \text{ rpm})$ is the reference signal. We could not use the data at room temperature, i.e., at 30 °C, because the pellets could not pass through the three kneading disks, and the motor's torque increased the specification value. The pellets extruded at T_m (164 °C), 2 kg/h, and 250 rpm seemed almost solid and did not stagnate in the kneading disk elements. The further increase in feed rate and/or screw rotation speed caused the torque-over. When the only kneading disk, such as in the case of

screw configuration (A), was used, the torque-over did not occur. However, some solid pellets passed through the one-kneading disk zone without collapsing. Hence, we placed three kneading disks to ensure all the pellets collapsed in the kneading zone.

3 Results and Discussion

3.1 Visual Observation of Partially Molten State Pellets on Rotating Screws

Figure 5a shows the effect of screw rotation speed on pellet plastication. The full-flight screws in an open barrel immediately upstream of the kneading disk under the AE sensor were observed. The characteristic aspects of melting resin varied with the screw rotation speed. The structural aspects of melting pellets in a co-rotating twin-screw extruder were described by Gogos et al. [21-23]. They found seven different states and described their characteristics and definitions. The observed structural state was mentioned following their definition in the parentheses. The clear molten resin on the pushing side of the full-flight screw was observed at 30 and 50 rpm (melt film). The partially melted pellets and clear molten resin were observed at 100 rpm (melt-rich suspension). The partially molten white pellets and their blocks were observed at 150 and 200 rpm (clustered structures). Almost solid pellets rolling on the flight screws were observed at 250 rpm (individual particles).

Figure 5b shows the MVF for each screw rotation speed. The MVF decreases with increasing screw rotation speed. Compared with the images in Figure 5a, the dropping of MVF corresponds to the solid pellet appearance clearly beyond 100 rpm. The MVF can be used to evaluate pellet plastication quantitatively.

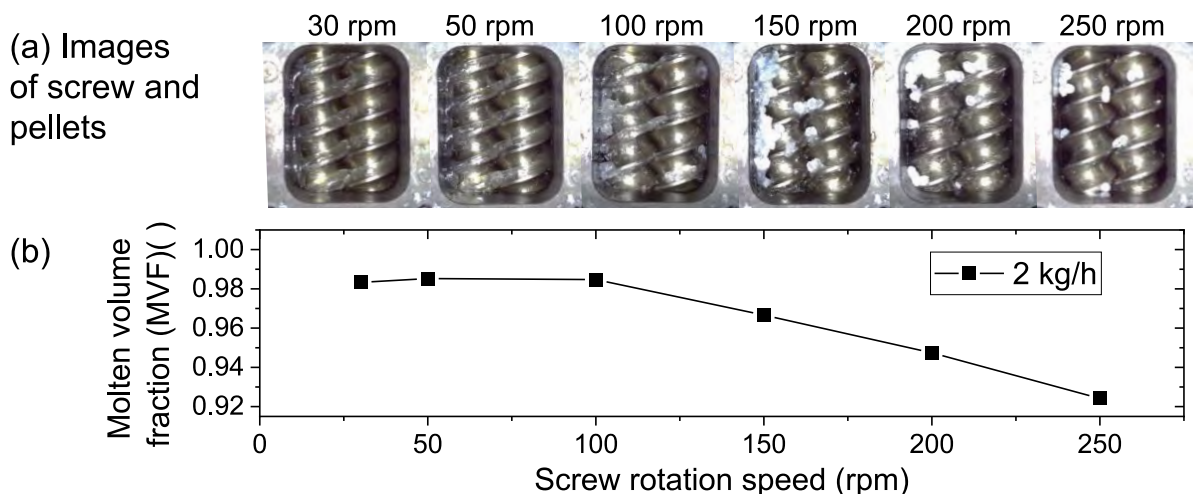


Figure 5. Effect of screw rotation speed on the molten volume fraction (MVF). (a) Visual observation and (b) MVF. The screw configuration was (B). The feed rate was 2 kg/h. The barrel temperature was 195 °C. The videos of the visual observations are available in the Supplementary Materials.

Table 2. Summary of molten volume fraction (MVF) dependence on increasing screw rotation speed at constant feed rates: 1st series*.

MVF ()	Screw rotation speed (rpm)	Feed Rate (kg/h)						
		2	4	6	9	12	18	23
	30	0.98	0.99	0.99	0.99	-	-	-
	50	0.99	0.99	0.99	0.99	1.00	-	-
	100	0.98	0.99	0.97	0.93	0.96	0.99	0.99
	150	0.97	0.96	0.90	0.90	0.92	0.97	0.97
	250	0.95	0.91	0.82	0.85	0.86	0.90	0.93
		0.92	0.87	0.76	0.81	0.82	0.82	0.83

* Screw configuration was (B).

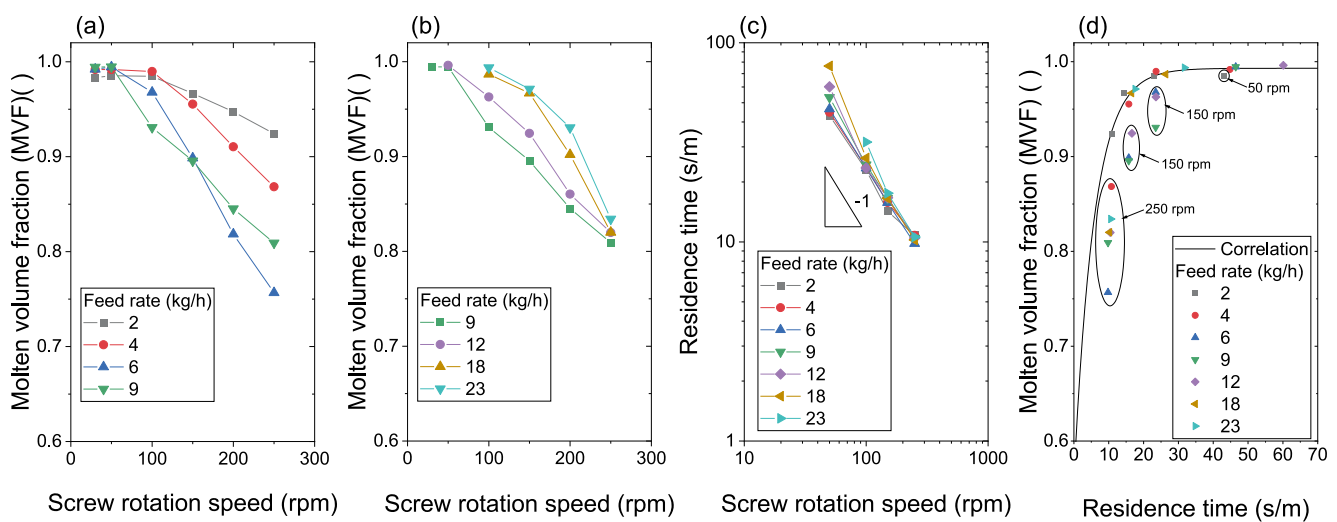


Figure 6. Effect of increase in the screw rotation speed on the molten volume fraction (MVF). The feed rate of (a) 2–9 kg/h, (b) 9–23 kg/h, and (c) residence time per meter of solid pellets in full-flight screws. The residence time was measured for the solid pellets at 30 °C. (d) Relationship between the residence time and molten volume fraction (MVF). The screw configuration was (B)

3.2 Effect of Increase in Screw Rotation Speed on Plastication at a Constant Feed Rate

Table 2 and Figure 6a,b show the effect of screw rotation speed on the MVF at a constant feed rate. The MVF for every feed rate decreased with the screw rotation speed. Figure 6c shows the residence time per meter of solid pellets estimated by Equation (1). The residence time per meter monotonically decreased with increasing screw rotation speed. The slopes of the low feed rate are close to -1 , indicating that the residence time per meter is proportional to the reciprocal of screw rotation speed. The majority of pellets were transported by the drag force of flight screws. The plots of high feed rate, e.g., 12, 18, and 23 kg/h, in slow-screw rotation speed, deviate from the slope of -1 because the holdup of pellets occurred at the high feed rate and slow-screw rotational speed.

Figure 6d shows the relationship between the MVF and residence time per meter. Overall, the long

residence time resulted in high MVF. Therefore, solid pellets must receive heat from the barrel and screws to melt. Hence, the longer the residence time per meter (more than 25–30 s/m in the polymer), the more heat the pellets received, and pellet plastication advanced. However, there are several plots enclosed by circles that deviate from the overall trends. To segregate them, an empirical equation, Equation (3) was fitted to the plots except for the enclosed ones:

$$\alpha = A_1 \exp(-x/t_1) + y_0 \quad (3)$$

where the parameters of Equation (3) were determined by fitting to the experimental data except the data plots enclosed by circles. $A_1 = -0.434$, $t_1 = 5.79239$ (s/m), $y_0 = 0.99309$. The plots on the correlation line and deviated plots indicate that our definition of MVF of Equation (2) is less sensitive to lower MVF and high solid content. Further study is required for the appropriate definition of MVF.

Table 3. Summary of molten volume fraction (MVF) dependence on increasing feed rate at a constant screw rotation speed: 2nd series*.

MVF ()	Feed Rate (kg/h)							
	2	4	6	9	12	18	23	
Screw rotation speed (rpm)	30	0.99	0.99	0.99	1.00	-	-	-
	50	0.96	0.98	0.99	1.00	1.00	-	-
	100	0.98	0.99	0.96	0.91	0.94	0.98	0.99
	150	0.95	0.96	0.92	0.87	0.89	0.94	0.96
	200	0.93	0.91	0.83	0.81	0.80	0.84	0.90
	250	0.88	0.85	0.76	0.76	0.75	0.72	0.78

* Resin is PP-MMFR, and the screw configuration is (B).

3.3 Effect of Increase in Feed Rate on Plastication at Constant Screw Speed

Table 3 and Figure 7a show the effect of feed rate on the MVF at constant screw rotation speed. The MVF decreased at a lower feed rate and turned to increase at higher feed rates for a screw rotation speed higher than 100 rpm. A minimum MVF for each screw rotation speed existed. The feed rate of the minimum MVF shifted to a high feed rate with increasing screw rotation speed. MVF increased monotonically for the cases of 30 and 50 rpm.

Figure 7b shows the effect of feed rate on the residence time per meter. The residence time per meter of each screw rotation speed against the feed rate had no peak. The residence time per meter increased with the feed rate, and its slope depended on the screw rotation speed. A monotonical increase in the residence time per meter above 25–30 s/m anticipates the advance of pellet plastication.

Interestingly, the MVF curves at 50 rpm and those at 100 rpm are different in Figure 7a. The MVF at 100 rpm dropped significantly at 5 and 7 kg/h. The pellets received substantial heat from the barrel at 30 and

50 rpm due to the long residence time. At more than 100 rpm, the residence time was not sufficient to melt the crystalline phase of polypropylene. Thus, the MVF dropped with an increase in the feed rate. Semicrystalline polymer requires heat to reduce the viscosity of the amorphous phase as well as to melt the crystalline phase.

Figure 7c shows the relationship between the MVF and the residence time per meter. The correlation line was drawn by the parameters of Equation (3). The MVF lower than 25 s/m deviated from the correlation line. It indicates that additional shear heating occurred in the starved situation by screw rotation and increased the MVF gradually.

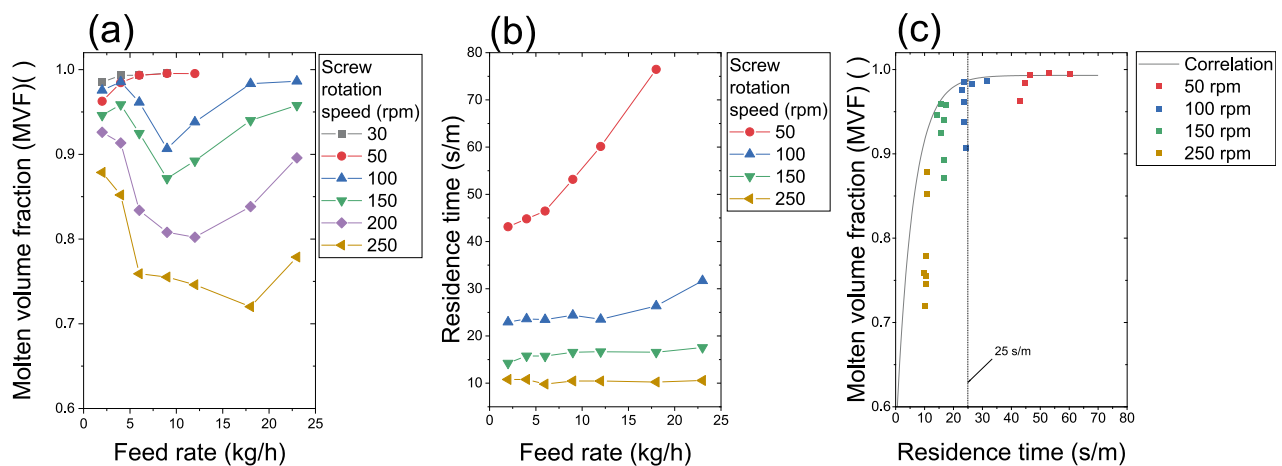


Figure 7. Effect of feed rate on (a) the molten volume fraction (MVF) and (b) the residence time of pellets. The residence time was measured for the solid pellets at 30 °C. The screw configuration was (B). (c) Relationship between the MVF and the residence time per meter. The correlation line was drawn using the parameters and Equation (3).

Figure 8 illustrates the accumulation of pellets in the valley of the full-flight screw zone of twin screws. An increase in the feed rate accumulates the pellets between the barrel and screws. The heat conduction rate of the blue-colored pellets in the side view is lower than that of the orange-colored pellets because the heat conducts through the orange-colored pellets. The amount of received heat per pellet at a high feed rate is lower than that at a low feed rate. Thus, the decrease in MVF was caused by the decrease in the amount of heat per pellet with the increase in feed rate.

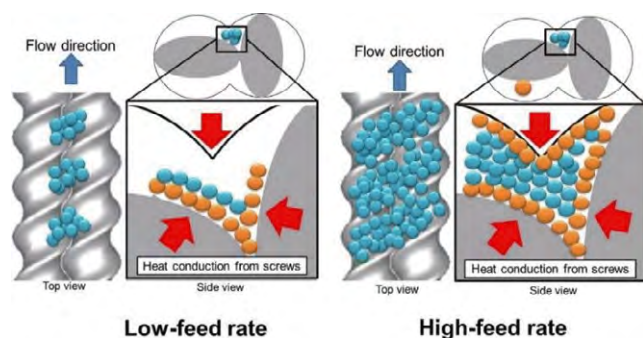


Figure 8. Comparison of the accumulation of pellets in the valley of twin screws in the full-flight screw zone between low feed and high feed rates at a constant screw rotation.

Figure 9 illustrates the holdup of pellets by the kneading disk just below the AE sensor in twin screws. The increase in feed rate causes the holdup of pellets just in the zone before the kneading disk element. The friction and compaction of pellets produce heat, which melts themselves in the zone [23]. Thus, the higher feed rate increased the holdup, friction, and compaction of pellets in the zone. It melts and transforms pellets to increase the MVF at further high feed rates.

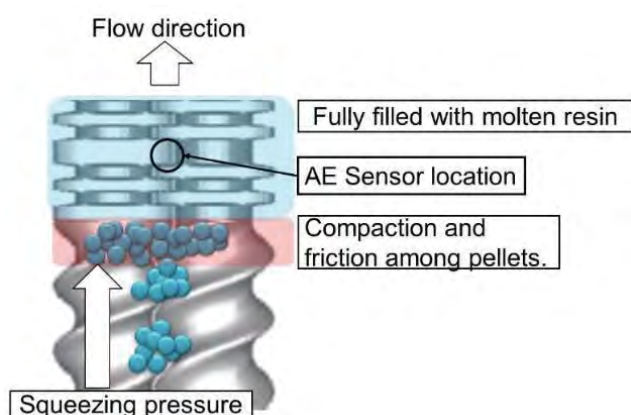


Figure 9. Holdup of pellets by the kneading disk in the twin-screw extruder.

3.4 Effect of Kneading Disk

The effect of the kneading disk was investigated by replacing the full-flight screw with the kneading disk (configuration (C)). Figure 10a shows that the MVF with the kneading disk is 1.0–9.0 kg/h. Further

increase in feed rate slightly decreased the MVF to 0.98. The MVF without the kneading disk (configuration (A)) was lower than that with a kneading disk. The kneading disk facilitated the plastication of pellets efficiently. Figure 10b shows the MVF at a barrel temperature of 175 °C. As expected, the MVF drastically decreases and changes nonlinearly with the feed rate, as observed in Figure 7a. The kneading disk does not always plasticate pellets completely.

4 Conclusions

Plastication of semicrystalline resin pellets in a twin-screw extruder was investigated using the newly developed AE sensing system, which detects the elastic wave and prevents the collapse of the partially melted pellets in the twin extruder. The MVF based on the power of the AE signal per pellet was defined. The feed rate and screw rotation speed affected the MVF nonlinearly. The residence time, accumulation of pellets, friction between pellets, and compaction play significant roles in plastication. Their contribution changes according to the feed rate. Moreover, the kneading disk efficiently enhanced the plastication independent of the feed rate. The compaction of pellets in the kneading disk zone is a significant factor in plastication.

Measurement of plastication using AE sensing has several advantages. The AE sensor does not contact an object directly. The AE sensing can be applied to severe situations in pressure transducers and will detect abnormal plastication via a sudden increase in the AE signal.

The AE sensing and investigation of plastication still have some limitations. Our AE sensing data support the previously proposed plastication mechanism. However, further quantitative analysis with mathematical models, such as finite and discrete element methods, is required. Moreover, plastication is followed by mixing additives, resin, and glass fibers in a typical extrusion process. Therefore, it is necessary to identify and categorize problems arising from mixed signals of glass fiber breakage, inorganic particles, and the blending of different viscoelastic materials.

Supplementary Materials: The following supporting information can be downloaded at: www.mdpi.com/xxx/2kgh100rpm.mp4, [2kgh150rpm.mp4](http://www.mdpi.com/xxx/2kgh150rpm.mp4), [2kgh200rpm.mp4](http://www.mdpi.com/xxx/2kgh200rpm.mp4), [2kgh250rpm.mp4](http://www.mdpi.com/xxx/2kgh250rpm.mp4), [2kgh30rpm.mp4](http://www.mdpi.com/xxx/2kgh30rpm.mp4), [2kgh50rpm.mp4](http://www.mdpi.com/xxx/2kgh50rpm.mp4).

Author Contributions: Conceptualization, K.T. and M.O.; methodology, T.K.; software, T.K.; validation, K.I. and S.N.; formal analysis, K.T.; investigation, T.K.; resources, T.K.; data curation, T.K.; writing—original draft preparation, T.K.; writing—review and editing, K.T.; visualization, T.K.; supervision, S.-i.K.;

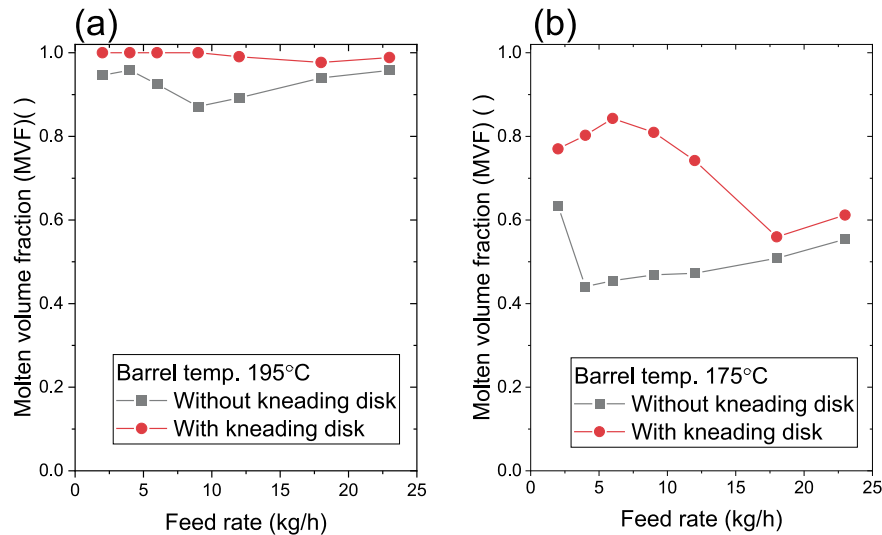


Figure 10. Effect of kneading disk on the molten volume fraction (MVf). The screw rotation speed is 150 rpm. The barrel temperatures were (a) 195 °C and (b) 175 °C, respectively. The screw configuration of “with kneading disk” was (C) and that of “without kneading disk” was (B).

project administration, K.T.; funding acquisition, M.O. All authors have read and agreed to the published version of the manuscript.

Funding: This study was supported by SHIBAURA MACHINE, Japan. Part of the research was supported by a CREST Grant-in Aid (JPMJCR21L3) from the Japan Science and Technology Agency (JST).

Institutional Review Board Statement: Not applicable.

Data Availability Statement: Data are available in a publicly accessible repository.

Acknowledgments: The funders had no role in the design of the study; in the collection, analyses, or interpretation of data; in the writing of the manuscript; or in the decision to publish the results

Conflicts of Interest: The sponsors had no role in the design, execution, interpretation, or writing of the study.

Appendix

The equations of the temperature-dependent Cross model are shown in Equations (A1) and (A2):

$$\eta = \frac{\eta_0}{1 + \left(\frac{\eta_0 \dot{\gamma}}{\tau^*} \right)^{(1-n)}} \quad (\text{A1})$$

$$\eta_0 = B \exp \left(\frac{T_b}{T_r} \right) \quad (\text{A2})$$

Where η is the temperature-dependent viscosity; $\dot{\gamma}$ is the shear strain rate; and n , B , τ^* , and T_b are fitting parameters, which are shown in Table A1. These parameters are determined based on the temperature-dependent experimental data of complex viscosity

following the Cox–Merz rule because the resins are all linear polymers. The shear viscosity can be calculated at an arbitrary temperature of T_r .

Table A1. Cross model parameters of viscosity estimation of the polypropylene used

	n (-)	B (Pa · s)	τ^* (Pa)	T_b (°C)
PP F-704NP	0.4212	8.486×10^{-6}	12,360	9472.1

The order of the screw element's code from the feed to the head of screw configurations in the catalog of SHIBAURA MACHINE [24] is presented in Table A2.

Table A2. The order of screw element's code of screw configurations*.

	A	B	C	Residence Time Meas.
Feeder	-	-	-	-
1	CL-3	CL-3	CL-3	CL-3
2	SC-20/20	SC-20/20	SC-20/20	SC-20/20
3	SC-40/40	SC-40/40	SC-40/40	SC-40/40
4	SC-40/40	SC-40/40	SC-40/40	SC-40/40
5	SC-40/40	SC-40/40	SC-40/40	SC-40/40
6	SC-40/40	SC-40/40	SC-40/40	SC-40/40
7	SC-40/40	SC-40/40	SC-40/40	SC-40/40
8	SC-40/40	SC-40/40	SC-40/40	SC-40/40
9	SC-40/40	SC-40/40	SC-40/40	SC-40/40
10	SC-40/40	SC-40/40	SC-40/40	SC-40/40
11	SC-40/40	SC-40/40	SC-40/40	SC-40/40
12	SC-40/40	SC-40/40	SC-40/40	SC-40/40
13	SC-40/40	SC-40/40	SC-40/40	SC-40/40
14	SC-40/40	SC-40/40	SC-40/40	SC-40/40
15	SC-40/40	SC-40/40	SC-40/40	SC-40/40
16	SC-40/40	SC-40/40	SC-40/40	SC-40/40
17	SC-40/40	SC-40/40	SC-40/40	SC-40/40
18	SC-34/34	SC-34/34	SC-34/34	SC-34/34
19	SC-34/34	SC-34/34	SC-34/34	SC-34/34
20	SC-34/34	SC-34/34	SC-34/34	SC-34/34
21	SC-27/27	SC-27/27	KD-27/5R	SC-27/27
22	SC-27/27	SC-27/27	KD-27/5N	SC-27/27
23	SC-27/27	SC-27/27	KD-27/5L	SC-27/27
24	SC-27/27	SC-27/27	SC-10/20L	SC-27/27
25	SC-27/27	SC-27/27	SC-27/27	SC-27/27
26	SC-27/27	SC-27/27	SC-27/27	SC-27/27
27	SC-27/27	SC-27/27	SC-27/27	SC-27/27
28	SC-27/27	SC-27/27	SC-27/27	SC-27/27
29	SC-27/27	SC-27/27	KD-27/5R	SC-27/27
30	KD-27/5R	KD-27/5R	KD-27/5N	Open head
31	SC-27/27	KD-27/5N	KD-27/5L	←AE sensor here
32	SC-27/27	KD-27/5L	SC-10/20L	-
33	SC-27/27	SC-10/20L	SC-27/27	-
34	SC-27/27	SC-27/27	SC-27/27	-
35	SC-27/27	SC-27/27	SC-27/27	-
36	SC-27/27	SC-27/27	SC-27/27	-

37	SC-27/27	SC-27/27	SC-27/27	-
38	SC-27/27	SC-27/27	SC-27/27	-
39	SC-27/27	SC-27/27	SC-27/27	-
40	SC-27/27	SC-27/27	SC-27/27	-
41	SC-27/27	SC-27/27	SC-27/27	-
42	SC-27/27	SC-27/27	SC-27/27	-
43	SC-27/27	SC-27/27	SC-27/27	-
44	SC-27/27	SC-27/27	SC-27/27	-
45	SC-27/27	SC-27/27	SC-27/27	-
46	SC-27/27	KD-27/5R	SC-27/27	-
47	SC-27/27	KD-27/5N	SC-27/27	-
48	SC-27/27	KD-27/5L	SC-27/27	-
49	SC-27/27	SC-10/20L	SC-27/27	-
50	SC-34/34	SC-34/34	SC-34/34	-
51	SC-34/34	SC-34/34	SC-34/34	-
52	SC-34/34	SC-34/34	SC-34/34	-
53	SC-27/27	SC-27/27	SC-27/27	-
54	SC-20/20	SC-20/20	SC-20/20	-
55	SC-20/20	SC-20/20	SC-20/20	-
56	SC-20/20	SC-20/20	SC-20/20	-
57	SC-20/20	SC-20/20	SC-20/20	-
Head	-	-	-	-

* Screw element names do not reflect the dimensions of the screw element precisely. The exact dimension is a part of confidentiality. CL-3: 3 mm length collar, SC: Full-flight screw, KD: Kneading disk, R: Right-hand, N: Neutral, L: Left-hand configurations. For example, KD-27/5N is a neutral kneading disk of which the length and number of disks are 27 mm and 5, respectively. SC-10/20L is a full-flight reverse screw element of which length and pitch are 10 and 20, respectively.

References

1. Tadmor, Z.T.; Gogos, C.G. Principles of Polymer Processing, 2nd Ed., Wiley-Interscience: Hoboken, NJ, USA, 2006; pp. 984.
2. Bawiskar, S.; White, J.L. Melting model for modular self wiping co-rotating twin screw extruders. *Polym. Eng. Sci.* 1998, 38, 727–740.
3. Potente, H.; Melisch, U. Theoretical and experimental investigations of the melting of pellets in co-rotating twin-screw extruders. *Int. Polym. Process.* 1996, 11, 101–108.
4. Vergnes, B.; Souveton, G.; Delacour, M.L.; Ainser, A. Experimental and theoretical study of polymer melting in a co-rotating twin screw extruder. *Int. Polym. Process.* 2001, 16, 351–362.
5. Kim, M.H. Ph. D thesis, Department of Chemical Engineering, Stevens Institutes of Technology: Hoboken, NJ, USA, 1999.
6. Qian, B.; Gogos, C.G. The importance of plastic energy dissipation (PED) to the heating and melting of polymer particulates in intermeshing co-rotating twin-screw extruders. *Adv. Polym. Technol.* 2000, 19, 287–299.
7. Gogos, C.G.; Qian, B. Plastic energy dissipation during compressive deformation of individual polymer pellets and polymer particulate assemblies. *Adv. Polym. Technol.* 2002, 21, 287–298.
8. Zhu, L.; Narh, K.A. A simplified model for the melting of polymer pellets under compression in a twin-screw extruder. *Simulation* 2006, 82, 543–548.
9. Canevarolo, S.V.; Bertolino, M.K.; Pinheiro, L.A.; Palermo, V.; Piccarolo, S. The use of in-line quantitative analysis to follow polymer processing. *Macromol. Symp.* 2009, 279, 191–200.
10. Vahaviolos, S.J. *Acoustic Emission: Standards and Technology Update*; ASTM: West Conshohocken, PA, USA, 1999.
11. De Groot, P.J.; Wijnen, P.A.; Janssen, R.B. Real-time frequency determination of acoustic emission for different fracture mechanisms in carbon/epoxy composites. *Compos. Sci. Technol.* 1995, 55, 405–412.
12. Barré, S.; Benzeggagh, M.L. On the use of acoustic emission to investigate damage mechanisms in glass-fibre-reinforced polypropylene. *Compos. Sci. Technol.* 1994, 52, 369–376.
13. Niebergall, U.; Bohse, J.; Schürmann, B.L.; Seidler,

- S.; Grellmann, W. Relationship of fracture behavior and morphology in polyolefin blends. *Polym. Eng. Sci.* 1999, 39, 1109–1118.
14. De Rosa, I.M.; Santulli, C.; Sarasini, F. Acoustic emission for monitoring the mechanical behaviour of natural fibre composites: A literature review. *Compos. Part A Appl. Sci. Manuf.* 2009, 40, 1456–1469.
 15. Gutkin, R.; Green, C.J.; Vangrattanachai, S.; Pinho, S.T.; Robinson, P.; Curtis, P.T. On acoustic emission for failure investigation in CFRP: Pattern recognition and peak frequency analyses. *Mech. Syst. Signal Process.* 2011, 25, 1393–1407.
 16. da Silva, J.R.M.; Nunes, L.S.; Rabello, M.S. Use of acoustic emission in the analysis of polypropylene failure caused by photodegradation. *J. Appl. Polym. Sci.* 2019, 136, 46943.
 17. Skalskyi, V.R.; Stankevych, O.M.; Klym, B.P.; Lisnichuk, A.E.; Velykyi, P.P. Identification of the mechanisms of fracture of cement mortar reinforced with basalt and polypropylene fibers. *Mater. Sci.* 2021, 56, 441–453.
 18. Xu, D.; Liu, P.F.; Chen, Z.P.; Leng, J.X.; Jiao, L. Achieving robust damage mode identification of adhesive composite joints for wind turbine blade using acoustic emission and machine learning. *Compos. Struct.* 2020, 236, 111840.
 19. Guo, F.; Li, W.; Jiang, P.; Chen, F.; Liu, Y. Deep learning approach for damage classification based on acoustic emission data in composite materials. *Materials* 2022, 15, 4270.
 20. Coates, P.D.; Barnes, S.E.; Sibley, M.G.; Brown, E.C.; Edwards, H.G.; Scowen, I.J. In-process vibrational spectroscopy and ultrasound measurements in polymer melt extrusion. *Polymer* 2003, 44, 5937–5949.
 21. Tadmor, Z.; Duvdevani, I.J.; Klein, I. Melting in plasticating extruders-theory and experiments. *Polym. Eng. Sci.* 1967, 7, 198–217.
 22. Tadmor, Z.; Klein, I. *Engineering Principles of Plasticating Extrusion*; Van Nostrand Reinhold Company: New York, NY, USA, 1970.
 23. Gogos, C.C.; Tadmor, Z.; Kim, M.H. Melting phenomena and mechanisms in polymer processing equipment. *Adv. Poly. Technol.* 1998, 17, 285–305.
 24. Available online: <https://www.shibaura-machine.co.jp/en/> (accessed on 9 February 2023).

This technical Paper is a reprint of research results published in the MDPI Journal *Polymers*.
Source : *Polymers* 2023,15(5),1140

Slurry Conditions for Reaction-Induced Slurry-Assisted Grinding of Optical Glass Lens

The demand for optical glass lenses is rising owing to the increase in image resolution. Optical glass is a hard and brittle material. Thus, an efficient and precise grinding method is required for optical glass to improve lens quality and productivity. There are a few methods of producing crack-free machined surfaces; however, they provide only limited grinding efficiency. To resolve this issue, the authors' group has proposed the reaction-induced slurry-assisted (RISA) grinding method, which expands the range of ductile-regime grinding by utilizing the chemical-mechanical action of a cerium oxide slurry. In this study, the grinding performance of RISA grinding is experimentally evaluated for different pH levels. The results are compared using Tukey's test, where surface roughness is considered as the characteristic value and the pH value as the analyzed factor. The result shows that RISA grinding efficiently produces a high-quality surface when the slurry is alkaline. The adhesion of cerium oxide abrasives to the wheel in RISA grinding follows the same mechanism as slurry aggregation. In addition, adhesion is more likely to occur when the alkalization of the slurry promotes aggregation. The tank in the slurry supply unit is replaced with a rotating tank to ensure stable RISA grinding with a highly aggregable slurry while preventing aggregation. The performance evaluation shows that a high-quality surface with a surface roughness of less than 10 nm in most parts is obtained. Moreover, the critical depth of cut stably increases by a factor of 5.8.



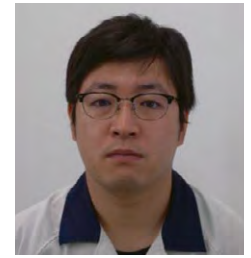
Tappei KAWASATO

Master student/
Department of System Design
Engineering, Faculty of Science
and Technology, Keio University



Hinata TAKAMARU

Master student/
Department of System Design
Engineering, Faculty of Science
and Technology, Keio University



Kazuhisa HAMAZONO

Machine Tools Company
Nano Processing System Division



Masahiko FUKUTA

Expert/
Machine Tools Company
Nano Processing System Division



Katsutoshi TANAKA

Technical adviser/Dr.Eng.
Machine Tools Company
Nano Processing System Division



Yusuke CHIBA

Production Headquarters,
Nikon Corp.



Mikinori NAGANO

Production Headquarters,
Nikon Corp.



Hidebumi KATO

Production Headquarters,
Nikon Corp.



Yasuhiro KAKINUMA

Professor, Department of System
Design Engineering, Faculty of
Science and Technology, Keio
University

Keywords : Ultraprecision grinding, Chemical-mechanical grinding, Optical glass

1 Introduction

The demand for optical glass lenses is rising owing to an increase in image resolution. However, as these lenses are hard and brittle, they are susceptible to cracks even when they are produced via ultraprecision grinding. Ductile-regime grinding has attracted attention because it can produce crack-free machined surfaces. Several methods have been developed for ductile-regime grinding, such as electrolytic in-process dressing [1] and shape-adaptive grinding [2] using a compliant grinding wheel.

In ductile-regime grinding, the maximum cutting depth of abrasive grains must be less than the critical

cutting depth of a material [3], and conventional methods can only achieve a limited grinding efficiency. To resolve this issue, the authors' group has proposed a method of expanding the range of ductile-regime grinding by supplying a cerium oxide (ceria) slurry to the grinding point. This slurry chemically reacts with a glass surface [4, 5, 6]. As this method is assisted by the grinding action of free abrasive grains that produce chemical actions, we refer to this method as reaction-induced slurry-assisted (RISA) grinding. In the present study, we examine the slurry characteristics and analyze the influence of the pH of the cerium oxide slurry and the mechanism through which the ceria

abrasive grains adhere to the grinding wheel. The results are used to improve the slurry supply unit, which can perform RISA grinding in a stable manner.

2 Reaction-Induced Slurry-Assisted (RISA) Grinding

RISA grinding is used to expand the range of ductile-regime grinding by supplying a cerium oxide slurry to the grinding point. We have successfully performed ductile-regime grinding with BK7 at an efficiency five times larger than that of conventional methods [4] and produced a high-quality surface of quartz glass [5].

RISA grinding is a type of chemical–mechanical grinding, where a grinding method for glass using a cerium grinding wheel has been reported [7]. This approach uses fixed abrasives. In RISA grinding, only the coolant is replaced with a slurry, and a conventional resin-bond diamond grinding wheel is used. In other words, it combines free-abrasive and fixed-abrasive grinding. Micron-sized cerium oxide abrasives in the slurry are supplied to the grinding point. They are crushed to a size of several hundred nanometers and adhere to the entire surface of the diamond grinding wheel. The performance of ductile-regime grinding is significantly enhanced when the adhesion of crushed cerium oxide abrasives occurs [4].

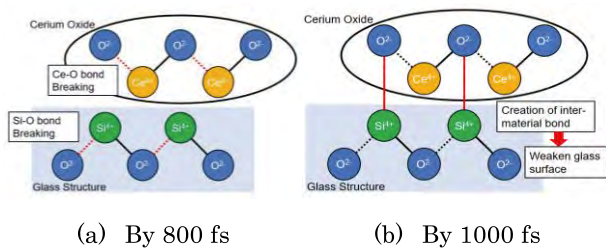


Fig. 1. Chemical reaction between cerium oxide and glass.

The chemical reaction between cerium oxide and the glass surface has been analyzed using molecular dynamics, and it consists of the chain reaction shown in Fig. 1 [8]. The rate of the chemical reaction is of the order of nanoseconds, which is less than the time required for a cerium oxide abrasive to adhere to the wheel surface to abrade the glass surface. Thus, a model has been proposed for the RISA grinding mechanism, in which a cerium oxide abrasive that adheres to the wheel surface comes into contact with the workpiece of glass and chemically softens the surface [4, 5, 6].

However, the mechanism through which cerium oxide abrasives adhere to the diamond grinding wheel in this model has not been clarified. Furthermore, the quality of the machined surface varies depending on the production variations in the slurry [6]. Therefore, it is necessary to analyze suitable slurry characteristics for RISA grinding. With

this background, the effects of the alkalinity of the slurry on RISA grinding are analyzed, and the mechanism by which the abrasives adhere to the wheel surface is discussed.

3 Influence of Alkalinity of Cerium Oxide Slurry on Grinding Performance

3.1 Relationship between Slurry pH and Grinding Surface

Chemical actions are widely employed in the field of polishing; this is referred to as chemical–mechanical polishing. As the polishing rates of various materials vary depending on the pH of the slurry [9, 10], pH is considered to strongly affect RISA grinding, which employs chemical actions.

In this study, sodium hydroxide was prepared to vary the pH of the slurry between four values: 7, 9, 11, and 13. Cross-grinding characteristics were experimentally evaluated using a #2000 resin-bond diamond wheel (diameter: 100 mm) and BK7 optical glass with a radius of curvature of 62 mm. The same grinding conditions were used for all pH levels as shown in Table 1. Two grinding experiments were conducted for each pH level. The RISA grinding process is shown in Fig. 2.

Table 1 Experimental conditions.

Grinding Conditions	
Wheel feed rate [mm/min]	3.0
Work rotation [min ⁻¹]	30
Wheel rotation [min ⁻¹]	7000
Depth of cut [μm]	0.5

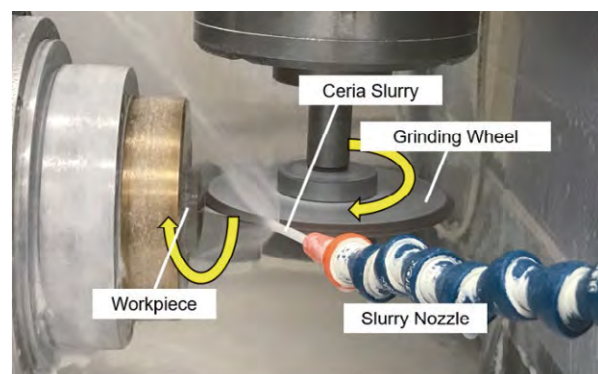


Fig. 2. RISA grinding experiment.

Table 2 Slurry conditions.

Slurry Conditions	
pH	7, 9, 11, 13
Abrasive type	Cerium Oxide
Concentration [wt.%]	5
Abrasive size [μm]	0.6~1.3 (Ave. 1.0)

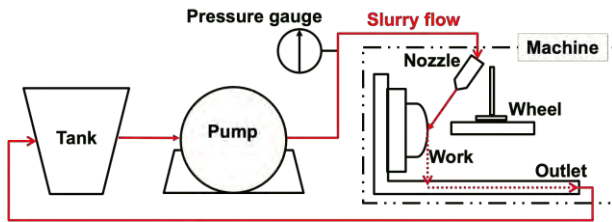


Fig. 3. Slurry supply unit.

The slurry was produced by mixing cerium oxide abrasives with an average grain diameter of $1.0 \mu\text{m}$ at a concentration of 5 wt.% with water, as shown in Table 2. The slurry was supplied to the grinding point by connecting a slurry circulation device to the ultraprecision grinding machine, as shown in Fig. 3. The machined surface produced by RISA grinding was evaluated in terms of surface roughness (S_a) using a white-light interference microscope.

The surface roughness of the ground surface produced using slurries with different pH values is presented in Table 3.

Table 3 Surface roughness (S_a) of machined surface.

Slurry pH	Exp. No. 1	Exp. No. 2	Average
7	27.1 nm	29.5 nm	28.3 nm
9	16.3 nm	11.8 nm	14.0 nm
11	17.1 nm	15.5 nm	16.3 nm
13	16.5 nm	14.7 nm	15.6 nm

The obtained results were utilized to conduct multiple comparisons using Tukey's test, with surface roughness as the characteristic value and the pH value as the analyzed factor.

Tukey's test corrects for the family wise error rate under the partial null hypothesis and employs the honestly significant difference (HSD), which is stricter than the conventional t-test. The HSD is expressed in Eq. (1).

$$HSD_a(\alpha) = \left(\frac{\hat{\sigma}}{\sqrt{n}}\right) \cdot q(a, v_e; \alpha) \quad (1)$$

α is the level of significance, n is the number of experiments repeated under identical conditions (2 in our example) and a is the number of levels of the analyzed factor (4 in our example). v_e is the degree of freedom of the error factor, which is computed as 4

for the present case using Eq. (2).

$$v_e = (n \times a - 1) - (a - 1) = (n - 1)a \quad (2)$$

$\hat{\sigma}$ is the mean square error, which is calculated by subtracting the sum of squares of the effects of the analyzed factors (given by Eq. (3)) from the sum of squares of the overall experiment (given by Eq. (4)) and dividing it by v_e .

$$S = \sum_i^4 (y_i - \bar{x})^2 \times 2 = 258.2 \quad (3)$$

$$T = \sum_i^8 (x_i - \bar{x})^2 = \sum_i^8 (x_i - 18.6)^2 = 273.8 \quad (4)$$

x_i is the surface roughness obtained from a given experiment, \bar{x} is the average surface roughness obtained from all 8 experiments, and y_i is the average surface roughness for a given pH level. $q(a, v_e; \alpha)$ is the upper bound (α) of the studentized range (q distribution) of the a level based on v_e . It shows the range (difference between maximum and minimum values) of observed values that lie within a probability of $(1-\alpha)$ when a observations are made with v_e degrees of freedom.

Assuming a level of significance (α) of 1%, the HSD is computed as given by Eq. (5).

$$HSD(0.01) = \sqrt{\frac{3.9}{2}} \cdot q(4, 4; 0.01) = 1.4 \times 9.2 = 12.8 \quad (5)$$

The effects of the different levels are compared using their averages. The average surface roughness increased as the pH changed from 9 to 13, 11, and 7. pH7 (S_a : 28.3 nm) and pH11 (S_a : 16.3 nm) were the only pairs that showed a difference larger than the HSD, and the difference between pH9 and pH11 did not exceed the HSD. Therefore, only the differences between pH7 and the other pH levels were significant, and there was no significant difference between pH9, pH11, and pH13. This indicated that the quality of the RISA grinding surface was significantly higher when the slurry was alkaline.

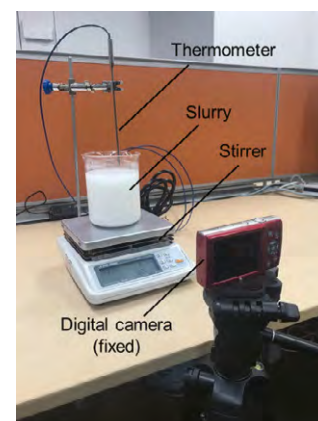


Fig. 4. Observation setup for slurry dispersion.

3.2 Evaluation of Dispersion of Slurry

The dispersion state of the slurry was investigated on the basis of the above experimental evaluation. The slurry was produced again under the conditions listed in Table 2, and its dispersion was observed.

As shown in Fig. 4, the dispersion state of the slurry was captured using a digital camera with fixed lighting and position. Specifically, the slurry was stirred with a stirrer for 10 min, and images were obtained immediately and 20 min after stirring.

The captured images were converted to a 256-gradation gray scale. The differences between the images obtained immediately and 20 min after stirring were displayed in color. The results are shown in Fig. 5. Blue and red indicate the regions that became brighter and darker after 20 min.

As light passes through water, the regions where the slurry concentration is reduced are displayed in blue. In the pH7 solution, the abrasive grains remained dispersed over approximately 3/4 of the beaker after 20 min.

In contrast, the dispersion region became smaller in the pH9, pH11, and pH13 solutions, among which the pH13 solution exhibited pronounced aggregation. The red line at the surface of the slurry was caused by the apparent increase in the water level due to stirring.

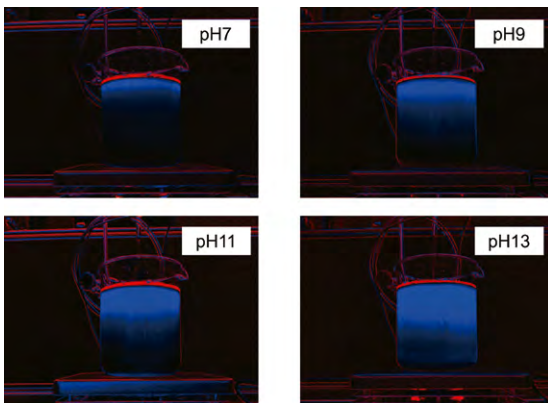
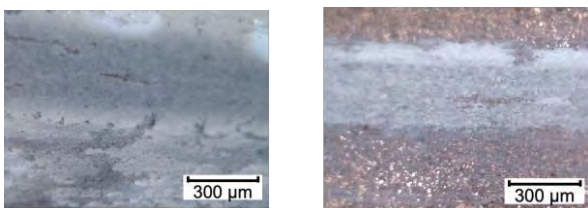


Fig. 5. Result of slurry dispersion after 20 min.



(a) Soon after grinding (b) After wiping

Fig. 6. Wheel surface after grinding.

3.3 Discussion

The wheel surface was observed after RISA grinding, and the results are shown in Fig. 6. The abrasive grains remained on the wheel surface even when it was wiped with a wiper, which indicated strong adhesion. This promoted the chemical alteration caused by cerium oxide. The authors' group showed that RISA grinding increased the grinding load [11]. This was consistent with the concept of adhesion, in which the contact area of the diamond grains on the grinding wheel decreases.

Considering that RISA grinding produces the lowest quality surface when using the pH7 slurry with the highest dispersion, it was likely that the adhesion of cerium oxide to the wheel is caused by slurry aggregation and dispersion state of the slurry affect the quality of that. As the cerium oxide slurry was a colloidal solution, the Derjaguin–Landau–Verwey–Overbeek (DLVO) theory was applied. This theory explains dispersion and aggregation in colloidal solutions. In this theory, the potential (V_t) of the force acting between two particles at distance D is expressed by Eq. (6) [12].

$$V_t(D) = V_a(D) + V_r(D) \quad (6)$$

V_a is the energy due to the van der Waals force and V_r is the energy due to electrostatic attraction. The van der Waals potential between particles with sufficiently large diameters is expressed by Eq. (7).

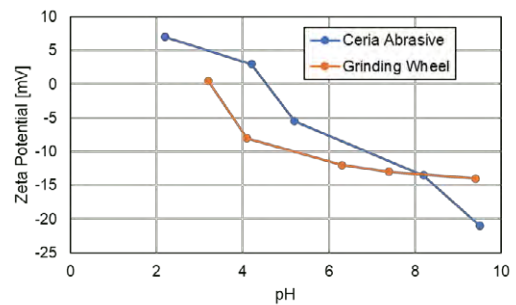


Fig. 7. Zeta potential vs. pH.

$$V_a(D) = -\frac{A}{6D} \left(\frac{R_1 R_2}{R_1 + R_2} \right) \quad (7)$$

R_1 and R_2 are the radius of the particles, and A is the Hamaker constant.

The energy due to electrostatic attraction, V_r , is expressed by the Hogg–Healy–Fuerstenau formula, as given by Eq. (8) [13].

$$V_r(D) = \frac{\epsilon R_1 R_2 (\psi_1^2 + \psi_2^2)}{4(R_1 + R_2)} \left\{ \frac{2\psi_1 \psi_2}{(\psi_1^2 + \psi_2^2)} \ln \left(\frac{1 + \exp(-\kappa D)}{1 - \exp(-\kappa D)} \right) + \ln(1 - \exp(-2\kappa D)) \right\} \quad (8)$$

This formula considers hetero-aggregation and ψ_1 and ψ_2 are the electric potentials of the particles. ϵ is the dielectric constant of the solution and κ is the inverse Debye length.

The zeta potential is typically used as the surface potential of materials. The measured zeta potentials of the grinding wheel and cerium oxide abrasive grains are shown in Fig. 7. The potentials were negative for the pH7 and alkaline solutions. The potential of the cerium oxide abrasive was higher at pH7, the relation was reversed close to pH8; the potential of the grinding wheel was higher in alkaline solutions.

When the zeta potential of the grinding wheel was lower than that of the cerium oxide abrasive, the electrostatic repulsion between the grinding wheel and cerium oxide abrasives was expected to be lower than that between the cerium oxide abrasives, which was advantageous for adhesion. The potential between the particles in the pH9 solution was calculated, and it is shown in Fig. 8. The parameters used for the computation are listed in Table 4. As sodium hydroxide could be used to adjust the pH to 9, the Debye length was calculated assuming a concentration of 10^{-5} mol/L in a 1:1 electrolyte. A Hamaker constant that was suitable for oxides in water was assumed [14, 15]. Furthermore, as the zeta potential is generally lower than the surface potential owing to electrostatic shielding, estimated surface potentials that were slightly higher than the respective zeta potentials were adopted.

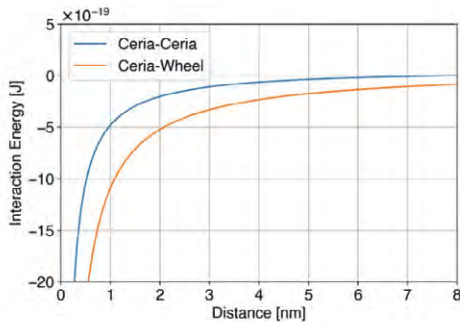


Fig. 8. Interaction energy between ceria-ceria/ceria-wheel.

Table 4 Computation parameters.

Hamaker constant	7×10^{-21}
Ceria surface potential [mV]	-25
Wheel surface potential [mV]	-15
Debye length [nm]	96
Ceria particle size [μm]	1.0

The interaction energy between cerium oxide and the grinding wheel decreased with the distance between them. In addition, it was lower than the interaction between the cerium oxide abrasives. The interaction energy was analogous to the potential

energy, such that a low energy indicated a stable state. This implied that the adhesion of cerium oxide abrasives to the wheel easily occurred in the alkaline solutions.

Therefore, it was assumed that the slurry aggregation and adhesion of cerium oxide abrasives to the wheel were related. Thus, we conjectured that it was necessary to use a slurry with high aggregability to obtain sufficient RISA grinding performance.

4 Proposed Grinding Device

The DLVO theory shows that the adhesion of cerium oxide abrasives to the grinding wheel is promoted by an alkaline slurry in which the aggregation of abrasive grains occurs easily. This should also increase the effect of RISA grinding to improve the surface quality. Therefore, the tank in the slurry supply unit, shown in Fig. 3, was replaced with a rotating tank, as shown in Fig. 9. This made it possible to supply a highly aggregable slurry while preventing aggregation.

RISA grinding tests were performed using the new tank under the conditions listed in Table 1. The measured surface roughness is shown in Fig. 10. A high-quality surface was obtained with a surface roughness of 10 nm or less in most parts. A ductile-regime-machined surface was stably produced up to a distance of at least 13 mm from the center.



Fig. 9. Electrically driven rotating tank.

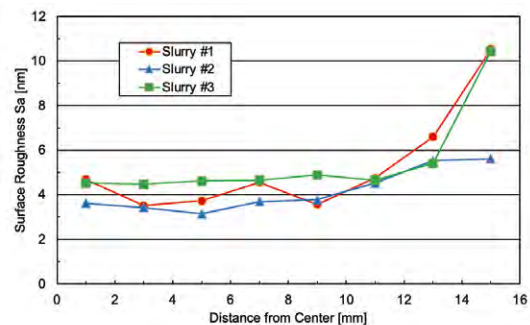


Fig. 10. Machining test results.

Sun et al. [16] proposed Eq. (9) for geometrically calculating the maximum depth of cut (h_m) in cross

grinding.

$$h_m = 2 \sqrt{\frac{R\omega \tan \phi + v}{VCr}} \sqrt{\frac{t}{D}} \quad (9)$$

where R is the distance from the center, ϕ is the angle between the wheel's composite velocity and the center of the machined work, C is the effective abrasive density, r is the average chip width divided by depth, t is the depth of cut, and D is the grinding wheel diameter.

According to Eq. (9), the maximum depth of cut increases with the distance from the center. The maximum depth of cut calculated at a radius of 13 mm, which was the limit for achieving sufficient ductile-regime grinding, was 260 nm, which was 5.8 times larger the typical critical depth of cut of BK7 (45 nm) [3].

The above results indicated that it was possible to stably improve the surface quality of RISA grinding by introducing a slurry supply unit to adequately stir a highly aggregable slurry.

5 Conclusion

We propose RISA grinding to create a high-quality surface with high efficiency. The influence of the cerium oxide slurry characteristics on the grinding performance is investigated. The mechanism by which abrasive grains adhere to the grinding wheel is discussed to elucidate the mechanism of RISA grinding. The results are summarized below.

1. The surface quality of RISA grinding increases when alkaline slurries are used.
2. The adhesion of cerium oxide abrasives to the wheel, which is caused by a mechanism similar to the aggregation of the slurry, is likely to occur when a highly aggregable slurry is employed.
3. A supply unit that can adequately stir a slurry with high aggregability is necessary to fully demonstrate the ability of RISA grinding. The critical depth of cut stably increases by a factor of 5.8 when the supply unit with a rotating tank is implemented.

Note that as the adjustment of the slurry characteristics is accompanied by an increase in the amount of the electrolyte, the alkaline slurry creates a condition in which aggregation occurs more easily. More effective RISA grinding is expected to be realized by adjusting the amount of the electrolyte and pH level.

References:

- [1] Stephenson, D.J., Sun, X. and Zervos, C. "A Study on ELID Ultra Precision Grinding of Optical Glass with Acoustic Emission," *Int. J. Mach. Tools Manuf.*, Vol. 46, pp1053-1063, 2006.
- [2] Zhu, W., Yang, Y., Li, N.H., Axinte, D. and Beaucamp, A., "Theoretical and Experimental Investigation of Material Removal Mechanism in Compliant Shape Adaptive Grinding Process," *Int. J. Mach. Tools Manuf.*, Vol. 142, pp76-97, 2019.
- [3] Gu, W., Yao, Z. and Li, H., "Investigation of Grinding Modes in Horizontal Surface Grinding of Optical Glass BK7," *J. Mater. Process. Technol.*, Vol. 211, pp1629-1636, 2011.
- [4] Kakinuma, Y., Konuma, Y., Fukuta, M. and Tanaka, K., "Ultra-Precision Grinding of Optical Glass Lenses with La-Doped CeO₂ Slurry," *CIRP Ann. Manuf. Technol.*, Vol. 68, pp345-348, 2019.
- [5] Kawasato, T., Hamazono, K., Fukuta, M., Tanaka, K., Nagano, M., Kato, H. and Kakinuma, Y., "Basic Study on Reaction Induced Slurry Assisted Grinding for Quartz Glass," *Proc. 23rd ISSAT*, pp170-174, 2021.
- [6] Kawasato, T., Hamazono, K., Fukuta, M., Tanaka, K., Nagano, M., Kato, H. and Kakinuma, Y., "Experimental Evaluation of Reaction Induced Slurry Assisted Grinding for BK7 Optical glass," *Proc. 10th LEM21*, pp287-290, 2021.
- [7] Zhang, Z., Cui, J., Wang, B., Wang, Z., Kang, R. and Guo, D., "A Novel Approach of Mechanical Chemical Grinding," *J. Alloys Compd.*, Vol. 726, pp514-524, 2017.
- [8] Rajendran, A., Takahashi, Y., Koyama, M., Kubo, M. and Miyamoto, A., "Tight-binding Quantum Chemical Molecular Dynamics Simulation of Mechano-Chemical Reactions During Chemical-Mechanical Polishing Process of SiO₂ Surface by CeO₂ Particle," *Appl. Surf. Sci.*, Vol. 244, pp34-38, 2005.
- [9] Guo, J., Gong, J., Shi, P., Xiao, C., Jiang, L., Chen, L. and Qian, L., "Study on the polishing mechanism of pH-dependent tribochemical removal in CMP of CaF₂ crystal," *Tribol. Int.*, Vol. 150, 106370, 2020.
- [10] Mu, Q., Jin, Z., Han, X., Yan, Y., Zhang, Z. and Zhou, P., "Effects of slurry pH on chemical and mechanical actions during chemical mechanical polishing of YAG," *Appl. Surf. Sci.*, Vol. 563, 150359, 2021.
- [11] Inuma, N., Chen, B., Kawasato, T. and Kakinuma, Y., "Shape error analysis in ultra-precision grinding of optical glass by using motor-current-based grinding force monitoring," *17th MSEC*, 85472, 2022.
- [12] Israelachvili, J.N., Oshima, H., "Intermolecular and surface forces with applications to colloidal and biological systems," Asakura Publishing

,p212, pp275-280, 2013, in Japanese.

- [13] Hogg, R., Healy, T.W. and Fuerstenau, D.W., 1966, Mutual coagulation of colloidal dispersions, Trans. Faraday Soc., Vol. 62, pp1638-1651
- [14] Masuda, H., "Adhesion of Powder Particles", Electrophotography The society journal, Vol. 36 (3), pp169-174, 1997, in Japanese.
- [15] The Society of Powder Technology, Japan, "Terminology of dictionary of powder technology," The Nikkan Kogyo Shimbun, Tokyo, pp 267, 2000., in Japanese
- [16] Sun, X., Stephenson, D.J., Ohnishi, O. and Baldwin, A., "An Investigation into Parallel and Cross Grinding of BK7 Glass," Precis Eng., Vol. 30, pp145-153, 2006.

This technical Paper is a reprint of research results published in the International Journal of Automation Technology.

Source : IJAT Vol.17 No.1 pp. 40-46

Subordination Architecture - A New Control Architecture for Autonomous Robots



Youichiro NAKAMURA

Research & Development
Center
Research & Development
Department



Yuya WADA

Research & Development
Center
Research & Development
Department

Aiming at the practical application of work robots supporting production in factories, we propose the Subordination Architecture, a new control architecture for making robots autonomous based on the concept presented in the previous engineering review. The Subordination Architecture is a control structure that integrates functions such as collision avoidance and force control based on the prioritized multi-objective inverse kinematics solution as its core. While more and more research attempts to provide all robot motions by learning with AI, this proposed architecture enables the robot to instinctively generate appropriate motions linking the arms and traveling part without learning, while avoiding interference with itself and its surroundings, as long as the target poses of the manipulators (arms) are coarsely provided. This paper describes the Subordination Architecture in detail and provides the test results to clarify the properties of the architecture.

1 Introduction

On the production floor, around the value added work such as assembly directly related to production, there are incidental work such as picking, arranging, kitting, and transporting parts, which set up the value added work. Sorting and transportation related to shipping and storage of products are also included in the incidental work. In general, the types of parts and semi-finished products handled and their storage locations vary more in the upstream incidental work that set up the value added work than in the downstream value added work that are set up. The storage configuration and order are also more diverse than after the setup, since this is the stage before the degree of freedom is reduced by the setup. Therefore, the automation of incidental work is more difficult than that of value added work, and most production sites rely on manpower for incidental work. However, the demand for automation of incidental work is increasing due to the shortage of labor, and we are developing a production support robot that can perform incidental work.[1]

Because of the above characteristics of incidental work, robots that perform incidental work must be able to move around in virtually the same facility environment as for humans and work with their vision and hands in the same manner as humans. To achieve this, the robot must be able to properly link its hands and arms with traveling/walking, along with advanced visual recognition functions, to manipulate the recognized objects. However, it is

difficult to teach operations such as naturally stepping up to a position to easily pick up an object by hand or using one's hands while moving in the same way as humans, by using the conventional method of teaching the arm and traveling stop positions. Teaching it by human intuition or trial and error took a lot of time.

We try to solve this problem by increasing the autonomy of robots. In the previous engineering review, we introduced the concept of autonomy and the basic control framework to realize it.[1] In this paper, the Subordination Architecture is proposed as a new overall structure for the autonomous robot control system that incorporates this framework.

The Subordination Architecture is an autonomous robot control structure originating in Japan and completely unique, that integrates functions such as collision avoidance and force control, based on the prioritized multi-objective inverse kinematics solution [2],[3] developed by Tokyo Metropolitan University as the core of the architecture. In recent years, there has been an increase in research worldwide that attempts to use AI, especially deep learning, to provide robots with all of their movements through a huge amount of acquired learning.[4] On the other hand, our proposal, in a departure from such a trend, provides an autonomous mobile robot equipped with arms and traveling functions with a coarse target pose of the object to be manipulated by the fingers/hand. This mechanism allows the robot to autonomously and instinctively generate safe and complex motions that link the traveling and arms without learning,

while avoiding spatial interference and physical contact with itself and its surroundings. This paper describes the Subordination Architecture in detail and provides the test results to clarify the properties of the architecture. In addition, we will look at the application of learning and AI to this architecture.

For the sake of simplicity, this paper compares a robot to a human, so a manipulator attached to a robot is referred to as an arm, and the robot's hand is referred to as a hand.

2 Relationship with Conventional Methods

2.1 Subsumption Architecture

The Subsumption Architecture [5] proposed by Brooks in the late 1980s as a control structure for autonomous robots was an epoch-making achievement, enabling complex behavior in the real world that was not possible before, despite the lack of an environmental model. The control system for an autonomous mobile robot based on the Subsumption Architecture has a layered structure as shown in the example in Fig. 1. The functions of the upper layers utilize the functions of the lower layers in an inclusive or comprehensive manner to achieve the objectives assigned on these layers. In the example in Fig. 1, the collision avoidance function in the bottom layer constantly prevents collisions with its surroundings, while the wandering and exploring functions in the upper layers generate behavior to move around in the environment. The topmost map-building layer then constructs a map of the traveling environment based on the information observed as the robot moves around. Each layer can function independently at any time, and the conflict and coordination of the functions of these layers determines the behavior of the whole robot. The conflict and coordination of the functions of these layers is realized by the upper layer suppressing the input of certain signals flowing through the lower layers, overwriting them with the output signals of the upper layer, or inhibiting the signal output. Therefore, in order to assign a specific task to an autonomous robot, the designer must implement the functions of the layers necessary for the task, and then appropriately design the suppression and prohibition mechanisms and conditions according to the priority of these functions. However, this design was not always easy, resulting in the emergence of many extended forms that incorporated learning functions into the Subsumption Architecture, and composite forms that added work planning functions. [6] These results have been put into practical use in cleaning robots by iRobot, a company founded by Brooks and his colleagues, but such practical applications are limited to mobile robots without manipulators.

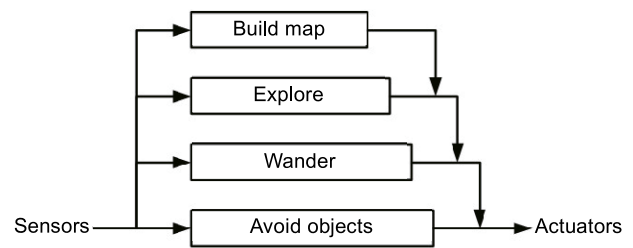


Fig.1. Subsumption Architecture (created based on Reference 6)

2.2 Learning Approach

As discussed in the previous chapter, incidental work in manufacturing require a level of human-like behavior. Not only traveling motion but also interaction between the manipulators and the traveling part are required, and this interaction must be smooth at a level close to that of humans. For such mobile manipulation challenges, many approaches using AI and machine learning have been proposed in recent years. For example, in Reference 7), reinforcement learning is applied to find the position of the traveling part to grab an object on the table without collision. However, the work performed is still limited to grabbing a small object on a table, even though tens of thousands of simulation learning are required after building virtual models of the robot and the environment.

From our point of view as machinists, such a learning approach that relies solely on computer science methods seems wasteful. The reason is that the iterative learning procedure consists of ① searching for a solution, ② applying the solution to simulations or trials on the actual robot, verifying and evaluating whether the realization of the solution causes interference, overload, or arms reaching out of the range of motion, ③ reflecting the evaluation results in learning and re-executing step ① and so on, and in many cases, the direction of overload and force value in each direction obtained in the trial process ②, information that accurately guides the robot's movement in the appropriate direction (e.g., which joint axes are out of the range of motion and how close the body and arms are in which direction), and constraint conditions that are effective in reducing the solution search range are not used in learning. The above reinforcement learning is originally a stoic approach that uses only the results of successful/failed trials for learning. Although it is a powerful learning method, it usually requires a large number of trials for learning due to its characteristics, which makes it not a suitable method for introducing robots in the field in a short period of time.

On the other hand, References 8) and 9) discuss teaching by learning to simulate human demonstrations of specific tasks. However, the tasks executable with this method are limited to the scope of the simulated

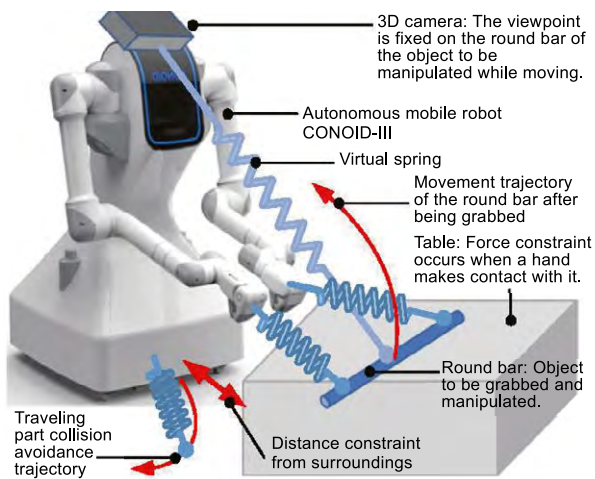


Fig.2. Principle of autonomous behavior generation in the Subordination Architecture

data, and it is not possible to adapt the work behavior to new environments or tasks in an exploratory manner.

Since we are trying to realize a robot for use in the field, we must choose or build a control and learning framework that is suited to the characteristics of the problem to be solved, i.e. field use and rapid deployment in the field, rather than relying on specific computer science methods. The Subordination Architecture differs from existing learning approaches. It allows the control system to have the ability to adapt to or follow various constraints in the real world, so that safe and appropriate behavior is autonomously generated in the process of operating the robot in the real world in real time. In this case, no learning, real-world virtual models or simulation calculations are required. The process of autonomously generating a solution based on advanced control engineering results can be illustrated as a rigid body constrained by a number of virtual springs that starts moving from a certain position and spontaneously stops at a position where its motion is balanced against all constraints (Fig. 2). In this example, the autonomous mobile robot represents a rigid body, and the traveling part, left and right arms, and head camera are each constrained by springs from the target pose. In addition, the rigid body (=robot) is also constrained by the distances from its surroundings. The concept of reducing the amount of solution search by adapting to these constraints is common in numerical computation and is also consistent with claims about human information processing.[10],[11]

The next chapter describes the Subordination Architecture in more detail.

3 Subordination Architecture

3.1 Overall Structure

Fig. 3 shows a functional block diagram of the Subordination Architecture. This block diagram is for CONOID-III (Fig. 8 in Chapter 4), our autonomous production support mobile robot with four axes in the traveling part and six axes in each of the left and right

arms.

Unlike the Subsumption Architecture, the Subordination Architecture does not have a clear layered structure of individual behavior, but rather has a block diagram structure, which is common in control engineering. The function of each block is independent of the other functions, making it easy to update the technology for each function and less dependent on the robot model or form. The core of this control structure is a prioritized multi-objective inverse kinematics calculation function, as described in the previous engineering review. Except for this calculation function and the related motion priority determination function, the work setting section and motion execution control section are no different from those of conventional industrial robots, so this control structure has high affinity with industrial robots. Furthermore, we would like to add that the characteristics of the coordinated linking of each part of this architecture shown in the next chapter are more suitable for humanoid robots.

3.2 Process of Autonomous Generation of Behavior

The process of autonomous generation of behavior described above is explained in more detail based on Fig. 3. As shown in Fig. 3, once the target pose of the hand or manipulated object is determined by object recognition and teaching, the rotation angles of the motors that drive the traveling part and right and left arms are determined by prioritized multi-objective inverse kinematics calculation, and the motors are activated. The resulting travel and manipulation of objects creates an interaction between the robot and the work environment. In this interaction, the robot is subject to four constraints from the work environment and from itself. Adapting to these constraints is the basis of autonomous behavior generation. We will look at these four constraints in turn.

First, when the robot travels, the distance between the robot and its surroundings changes. Accordingly, the robot must avoid collisions with its surroundings (① external distance constraint). Second, when the arm moves, each joint of the arm may try to move out of its range of motion, or a part of the arm may move too close to the body of the robot. The robot must avoid this self-interference (② internal distance constraint). In addition, when a hand operates by holding something, for example, opening a door that can only be rotated, the hand or arm will be overloaded if it does not operate in line with the motion constraint of the object being operated (③ external motion constraint). Furthermore, in this control system based on prioritized multi-objective inverse kinematics, a mutual priority relationship is set for each of the actuators of the left and right arms and the traveling part (④ motion priority constraint).

In this way, the state of the four constraints changes

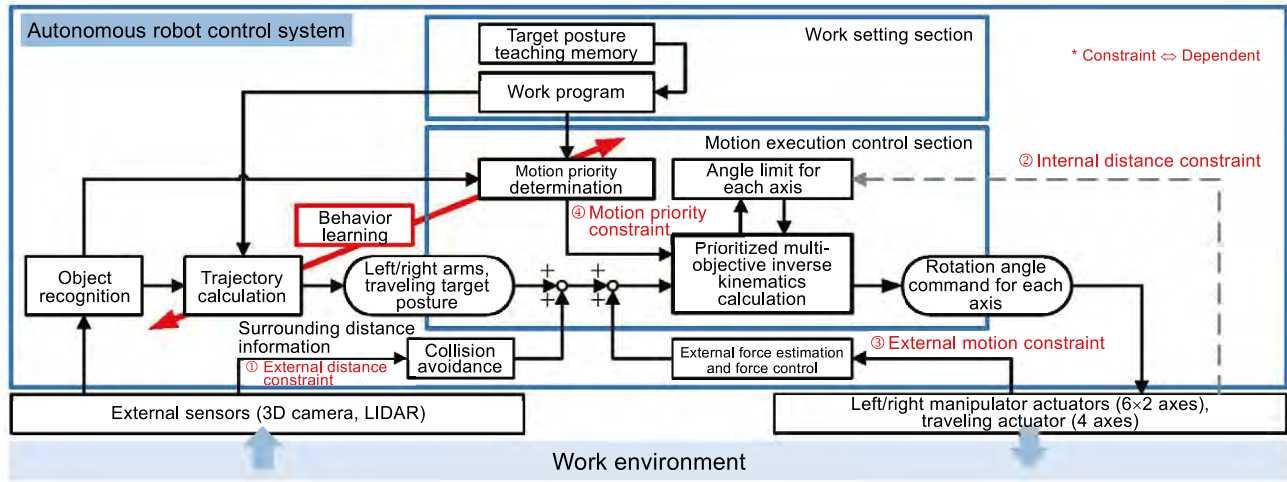


Fig.3. Functional Block Diagram of the Subordination Architecture

during arm movement and traveling, but in the Subordination Architecture, the traveling part adapts to the external distance constraint ① by using the collision avoidance function to prevent stopping due to a collision error. CONOID's collision avoidance function is a unique method suitable for real-time processing that applies the concept of manifold and superquadrics. The arms and traveling part adapt to the internal distance constraint ② in a way that the traveling part compensates for the stopping of the arms. In other words, the angle limit function for each axis prevents the arms from making an out-of-range-of-motion error, and the coordinated control of the prioritized multi-objective inverse kinematics solution (described below) allows the traveling part to compensate for the stopping of the arms. The hands adapt to the external motion constraint ③ by moving the hands in the non-constrained direction using the force control function. This corresponds to the admittance control mechanism, for which the control formulation and evaluation results were presented in the previous engineering review [1]. The mechanism and role of the motion priority constraint ④ are described in sections 3.4 and 3.5.

As described above, the Subordination Architecture generates autonomous behavior by adapting to or following each of the four constraints, whose state changes with the operation of the arms and traveling part. This autonomous behavior allows the robot to continue moving without stopping in response to fewer, coarser teaching errors. In addition, the robot can perform complex movements and behavior by coordinating the arms and traveling. This coordinated linking mechanism will be discussed in section 3.4.

3.3 Behavior Learning

The behavior autonomously generated by adapting to the four constraints through interaction with the work environment will never be the optimal behavior. Although the mechanisms for adapting to the four constraints described in the previous section do not

cause the robot to stop in error, it may still move too close to its surroundings or be subjected to excessive force from the object being manipulated. Furthermore, the trajectory of the traveling part and arms corresponding to the behavior generated as a result of adapting to the constraints cannot be the shortest trajectory that leads from the motion start pose to the target pose.

Therefore, the Subordination Architecture incorporates a function to generate and learn the optimal behavior in the form of a trajectory optimization mechanism that mitigates the occurrence of excessive force and over-approach to the surroundings by learning a small number of trials while shortening the trajectory length. [12],[13],[14]

3.4 Coordinated linkage between the Arms and Traveling

Following the previous engineering review, we will first provide an introduction to the prioritized multi-objective inverse kinematics solution, as it is the basis of the coordinated linking and we will extend the theory of the solution independently in the later sections.

First, the current pose of each of the left and right manipulator hands and the traveling part has an error between the target pose and the current pose, and the pose error vector for the total of 18 DOF is denoted by $e(\mathbf{q}_k)$.

$$e(\mathbf{q}_k) = {}^d\boldsymbol{\chi} - \boldsymbol{\chi}(\mathbf{q}_k) \quad (1)$$

\mathbf{q} is the joint displacement, and k is the iterative step of the iterative calculation of the inverse kinematics solution. In this formulation, 3 DOF for in-plane traveling is treated as 6 DOF. ${}^d\boldsymbol{\chi}$ is the target pose vector of the whole robot that integrates the target poses of the traveling part and the left and right manipulators, and $\boldsymbol{\chi}(\mathbf{q}_k)$ is the current pose vector for the whole robot that aggregates the current poses of the traveling part and the left and right manipulators. This pose error vector is analyzed in more detail in

equation (19) in the Appendix.

Based on the above, this solution considers that each joint receives a virtual torque from the virtual spring between the current pose and the target pose. The virtual spring coefficient matrix $\mathbf{K} \in \mathbb{R}^{18 \times 18}$ is a block diagonal matrix, where each diagonal block is a virtual spring coefficient diagonal matrix of $\mathbb{R}^{6 \times 6}$ for each of the left and right manipulators and the traveling part. The virtual torque that each joint receives from the virtual spring is determined by the following equation.

$$\boldsymbol{\tau}(\mathbf{q}_k) = \mathbf{J}^T(\mathbf{q}_k) \mathbf{K} \mathbf{e}(\mathbf{q}_k) \quad (2)$$

\mathbf{J} is the base Jacobi matrix. Assuming that velocity is generated at each joint by damping from this virtual torque and that the damping coefficient matrix is $\mathbf{D}(\mathbf{q}_k)$, the amount of change in joint displacement in time Δt between iterative steps is determined by the following equation.

$$\Delta \mathbf{q}_k = \mathbf{q}_{k+1} - \mathbf{q}_k = \Delta t \mathbf{D}^{-1}(\mathbf{q}_k) \mathbf{J}^T(\mathbf{q}_k) \mathbf{K} \mathbf{e}(\mathbf{q}_k) \quad (3)$$

Then the joint displacement update rule is expressed by the following equation.

$$\mathbf{q}_{k+1} = \mathbf{q}_k + \Delta \mathbf{q}_k \quad (4)$$

$\mathbf{D}(\mathbf{q}_k)$ is set according to Reference 3)

$$\mathbf{V}_k = \frac{1}{2} \mathbf{e}^T(\mathbf{q}_k) \mathbf{K} \mathbf{e}(\mathbf{q}_k) \quad (5)$$

so that the elastic energy of the virtual spring is appropriately reduced. The traveling part and the left and right manipulators can be assigned a motion priority to reach their target pose. This is done by multiplying the diagonal block matrices of the traveling part and the left and right manipulators, which constitute the virtual spring coefficient matrix \mathbf{K} , by coefficients that determine the motion priorities, which are described in the next section.

Thus, this solution is a mathematical method for solving a kind of optimization problem with equation (5) as the evaluation function. The displacement of each control axis that brings the left and right manipulators and the traveling part to their respective target positions is calculated collectively, according to the motion priorities for reaching the target positions. Then, by changing the angle limit range of each axis and the target poses of the left and right manipulators and the traveling part and their motion priority, various motions can be easily generated where the manipulators and the traveling part coordinate with each other. Equations (2) and (3) in particular play a very important role in this coordinated linking. That is, if the motion priority of one or both of the left and right manipulators is higher than that of the traveling part, the traveling part prioritizes reaching the target pose

of the manipulator over reaching its own target pose, and moves dependently and coordinately to minimize the target pose error of the hands. As a result, the traveling part moves following the manipulators' hand motion, even while it is maintaining its current pose with no motion trajectory given. This means that the motion that is not taught by the human is generated automatically, and yet the motion is coordinated with the higher priority motions of the manipulators. If the motion priority relationship is reversed, the coordination and dependency between the manipulators and the traveling part are also reversed in terms of motion to reach the target pose. The mechanism of this coordinated linking, an important function of the prioritized multi-objective inverse kinematics calculation method, is detailed in the Appendix.

3.5 Setting the Motion Priority

This section describes how to assign motion priorities to the robot's actuators, such as the traveling part, the left and right manipulators. To assign a motion priority to each actuator, construct a virtual spring coefficient matrix \mathbf{K} , multiply each block diagonal matrix corresponding to the traveling part, left and right manipulators by the motion priority coefficients ${}^V\xi_k$, ${}^L\xi_k$, and ${}^R\xi_k$, respectively, and replace them as follows.

$$\mathbf{K} = \begin{bmatrix} \mathbf{K}_V & \mathbf{0} & \mathbf{0} \\ \mathbf{0} & \mathbf{K}_L & \mathbf{0} \\ \mathbf{0} & \mathbf{0} & \mathbf{K}_R \end{bmatrix} = \begin{bmatrix} {}^V\xi_k \mathbf{K}_V & \mathbf{0} & \mathbf{0} \\ \mathbf{0} & {}^L\xi_k \mathbf{K}_L & \mathbf{0} \\ \mathbf{0} & \mathbf{0} & {}^R\xi_k \mathbf{K}_R \end{bmatrix} \quad (6)$$

The motion priority coefficients are damped according to the iteration count k for the inverse kinematics calculation and the degree of reduction of the elastic energy V_k given by equation (5), following the procedure described in Reference 3).

3.6 Loose Gradual Activation of Linking Joint Displacement Limitation

This section and the next section are the scope of our own theoretical extension.

The motion priority settings described in the previous section determine the solution so that the low-priority motion part automatically deviates from the target positional pose and the motion of the high-priority motion part is established. The joint displacement range that initiates motion linking (hereinafter referred to as the "motion linking range") is set within the joint displacement limit that is set as the physical motion range of the joint. When the joint displacement enters this motion linking range, the virtual spring constant \mathbf{K} for low-priority motion is reduced so that priority-based linking is performed.

However, at the start of this linking, a sudden acceleration motion may occur. Therefore, a new control parameter is added to the constitutive equation

of the joint damping coefficient matrix \mathbf{D}_k in equation (3) so that the linking motion starts gently. The joint damping coefficient matrix \mathbf{D}_k is used to calculate the target joint displacement in equation (3), and the change in each joint displacement, $\Delta \mathbf{q}_k$, is obtained by multiplying the virtual torque $\boldsymbol{\tau}_k = \mathbf{J}_k^T \mathbf{F}_k$ occurring at each joint by the inverse matrix of the joint damping coefficient \mathbf{D}_k . Therefore, when the joint damping coefficient \mathbf{D}_k increases, the corresponding joint becomes harder to move.

The constitutive equation of matrix \mathbf{D}_k is given by the following equation.[15]

$$\mathbf{D}_k = \mathbf{J}_k^T \mathbf{K} \mathbf{J}_k + \mathbf{T}_k + \delta_k \mathbf{E}_n + \mathbf{C} \quad (7)$$

In this equation, the joint damper adjustment term \mathbf{C} is newly added as a parameter to adjust the difficulty of joint movement. When the above joint enters the motion linking range, the component of the joint damper adjustment term \mathbf{C} corresponding to that joint is increased to make the motion harder, making it harder for each joint angle to approach the angle limit range.

3.7 Method for Automatically Determining the Travel Target Position

When the user teaches the target pose of the manipulated object or the arm hand and does not need to teach the target positional pose of the traveling part, it is desirable to automatically determine the target positional pose of the traveling part. Although this can be achieved by setting a lower priority for the motion of the traveling part as shown in section 3.5, if the traveling part is always moved with this function enabled, either joint will always be located near the joint angle limit, resulting in poor continuity of motion. Therefore, the target positional pose of the traveling part is usually determined by another method defined below, and the coordinated linking by the prioritized inverse kinematics solution is the final means to continue the motion.

One way to automatically determine the target positional pose of the traveling part is to consider the range of motion of the manipulators. Generally, the range of motion of a manipulator is expressed in the relationship between the base of the manipulator and the center of the wrist joint, called point P. Therefore, the correction amount $\Delta \mathbf{P}$ for the travel target position is calculated such that the length between the base \mathbf{P}_{Base} and point P is kept at a certain appropriate distance R_c .

First, consider a sphere with radius R_c centered at point P (Fig. 4). The radius of the circle cut out of this sphere horizontally at the height of the base \mathbf{P}_{Base} is R_c' . The point \mathbf{P}_{Tar} on the arc between \mathbf{P}_{Base} and the center O of the circle is the appropriate location for \mathbf{P}_{Base} . Then, the difference between \mathbf{P}_{Tar} and \mathbf{P}_{Base} is defined

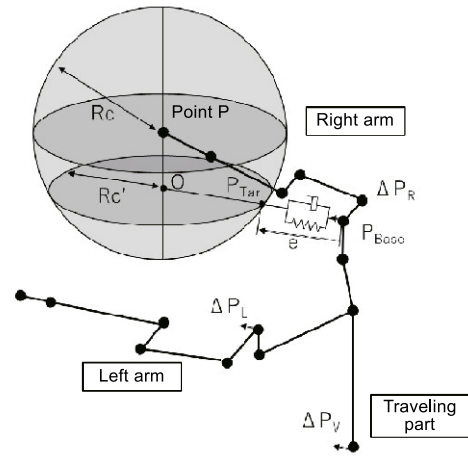


Fig.4. Method for automatically determining the travel target position

as deviation $\mathbf{e} = \mathbf{P}_{\text{Tar}} - \mathbf{P}_{\text{Base}}$, and \mathbf{P}_{Base} is brought closer to \mathbf{P}_{Tar} by virtual spring damper control using this deviation \mathbf{e} as an input. However, since the traveling part does not need to respond in detail to the motion of the arms, this function is activated when the deviation input \mathbf{e} is greater than a certain threshold value.

$$\ddot{\mathbf{e}} = \mathbf{M}^{-1}(\mathbf{K}\mathbf{e} - \mathbf{D}\dot{\mathbf{e}}) \quad (8)$$

\mathbf{M} is the virtual mass. Based on the correction acceleration $\ddot{\mathbf{e}}$ calculated from the above equation, determine the base position correction amounts $\Delta \mathbf{P}$ and $\Delta \mathbf{P}_R$ for the left and right arms, and average them to obtain the position correction amount $\Delta \mathbf{P}_V$ for the traveling part.

4 Validation

This chapter shows the validation results for clarifying the functions described in sections 3.4 to 3.7 in the previous chapter.

4.1 Validating Creation of Various Behaviors by Setting Priorities

First, we examine how the CONOID motion changes with different priority settings using a simulation of the door opening motion. Fig. 5 shows the initial state of the simulation. This simulation simulates CONOID opening a door with its right manipulator hand fixed on the door knob or door handle equivalent. In each figure, CONOID is represented by a skeleton model corresponding to the design dimension values of each part. It is not assumed that CONOID will turn the door handle to unlock the door. The door is assumed to be unlocked from the beginning. Fig. 6 (a) shows the pose of the robot in the initial and final states of the simulation when the traveling part is given a motion priority of 1.0. Fig. 6 (b) shows the change in pose of the left and right manipulators and the traveling part, respectively, from the initial state to the final state. Looking at Fig. 6 (a) and Fig. 6 (b), CONOID is positioned slightly to the right relative to the front of the door opening in the final state. It can be said that

this robot is better positioned to pass through the door opening.

In this simulation, it is assumed that a human teaches the pose of the right hand in each state when the door is opened by 15° relative to the initial state. On the other hand, the pose of the traveling part is automatically calculated by the prioritized multi-objective inverse kinematics solution.

Fig. 6 (c) shows the change in the robot's pose from the initial state to just before the traveling part starts to move. From the initial state to the state shown in this figure where the door is opened 45°, the traveling

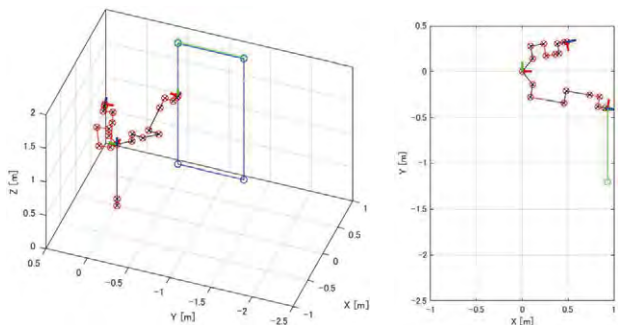


Fig. 5. Initial state of simulation of door opening motion

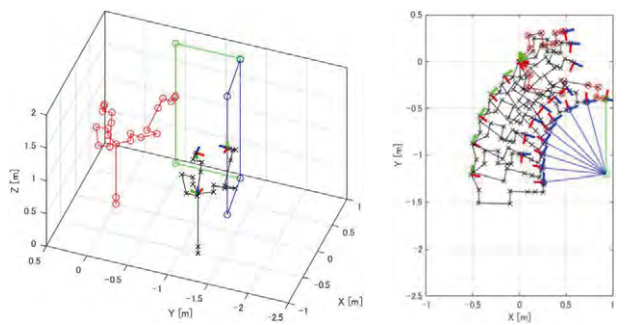


Fig. 6 (a) 3D view Fig. 6 (b) 2D view (plan view)

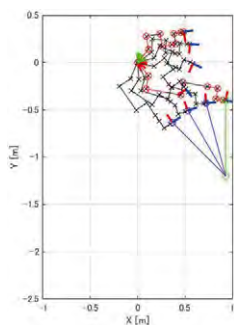


Fig. 6 (c) 2D display (initial motion)

Fig. 6. Simulation result of door opening motion in selfish mode

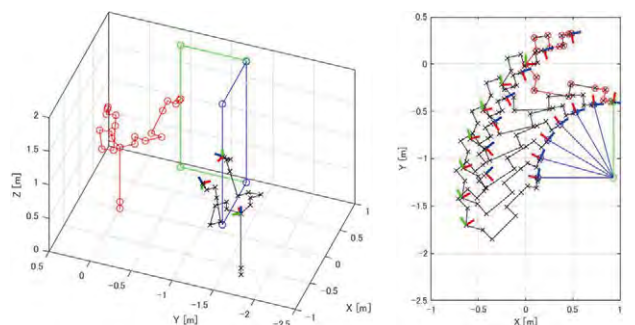


Fig. 7 (a) 3D view Fig. 7 (b) 2D view (plan view)

Fig. 7. Simulation result of door opening motion in altruistic mode

part only turns clockwise while maintaining the same positions in the X and Y directions as in the initial state. Then, in the state shown in this figure, the fourth and fifth links reach a singular pose where they are almost in parallel, and the joint angle of the fourth joint reaches the limit of its range of motion, resulting in the hand of the right arm being unable to move any further. In the subsequent state, the prioritized multi-objective inverse kinematics calculation method works so that the lower-priority traveling part also starts translational motion in the X and Y directions to help the higher-priority right hand reach the target pose. As a result, as shown in Fig. 6 (b), the right hand continues the door-opening motion and the door is opened about 90° relative to the initial state.

Fig. 7 (a) shows the pose of the CONOID in the initial and final states of the simulation when the traveling part is given a motion priority of 0. Fig. 7 (b) shows the change in pose of the left and right arms and the traveling part, respectively, from the initial state to the final state. Looking at Fig. 7 (a) and Fig. 7 (b), the CONOID is positioned to the right of the front of the door opening in the final state. From this position, it is difficult for this robot to pass through the door opening, but it is easy for other people and robots to pass through the door opening.

Thus, only a single change of the motion priority value can give the robot a “hospitable” behavior without learning. On the other hand, the challenge is how to set or design the priority levels according to the situation.

4.2 Coordinated Linking by Teaching the Motion of the Manipulated Object

We tested whether the Subordination Architecture can automatically coordinate the robot's arms and traveling part and generate target commands for each driving part to achieve the above motion by simply assigning the box, the manipulated object, a 135° rotation around a fixed rotation axis and a subsequent rotation of the same angle in the reverse direction for returning (Fig. 8). The box is held on both sides by the end-effectors installed on the hands. This holding position is the positional pose on the object coordinate system taught in advance, which serves as the constraint condition between the two arms and the manipulated object.

Fig. 9 shows the time variation for the target rotation angle assigned to the box by the operator. Fig. 10 shows the CONOID-III skeleton model displaying the target positional pose of each motion part calculated on the actual robot based on the target rotation angle. As shown in this figure, although the box is assigned only rotation around a fixed axis, both arms move in parallel in an arc during the rotation because the hands of both arms are constrained away from the rotation axis of the box. Furthermore, as the distance



Fig.8. Tipping over a cardboard box by an actual CONOID-III robot

between the traveling part and the hands of both arms widens, the traveling part moves forward as if it is pulled by the hands due to the automatic travel position determination function described in section 3.7.

Based on these target positional poses of the

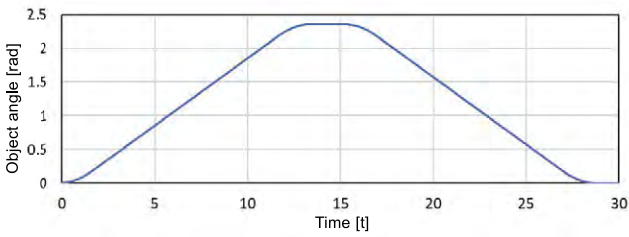


Fig.9. Target rotation angle of the box

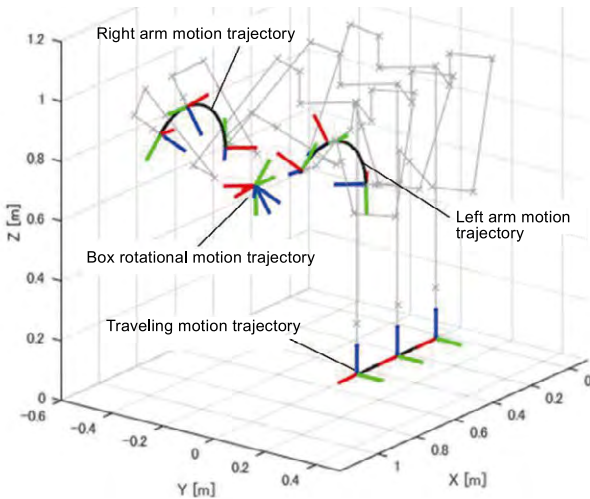


Fig.10. Target positional pose of each part (first half of flipping motion)

traveling part and the hands of both arms, the target angles of each joint of both arms (Fig. 11, Fig. 12) and the target positional pose of the traveling part (Fig. 13) are calculated by the prioritized inverse kinematics solution. It is clear that all the driving parts are intricately linked, even though the operator taught only the simple rotational motion of the box. The target rotation angle assigned to the box is symmetrical between the first half and the second half of the motion, returning to the same 0° at the end of the motion as at the start (Fig. 9), but the target positional pose of the traveling part and the target angles of each joint of both arms for the robot's motion are not symmetrical between the first half and the second half of the motion (Fig. 11 to Fig. 13). In particular, the target positions of axis 1 of both arms and the traveling part in the X direction are significantly different

between the first half and the second half of the motion. In the first half of the motion, the traveling part moves forward as if pulled by the hands, and the traveling part is positioned appropriately for the motion of the arms. Therefore, it is believed that during the return motion in the second half, the traveling part returned about 50 mm less, and the target angles of each joint of both arms were also affected by the result, causing the motion to change.

Fig. 13 compares the target position in the X direction

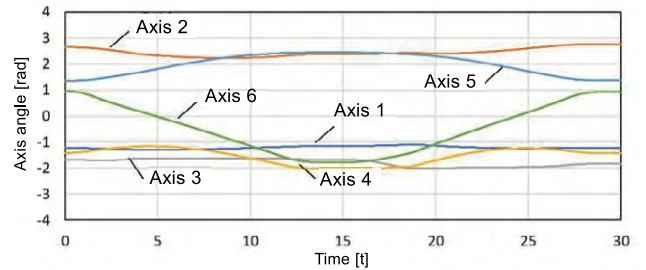


Fig.11. Target angle of each axis of the left arm (flipping motion)

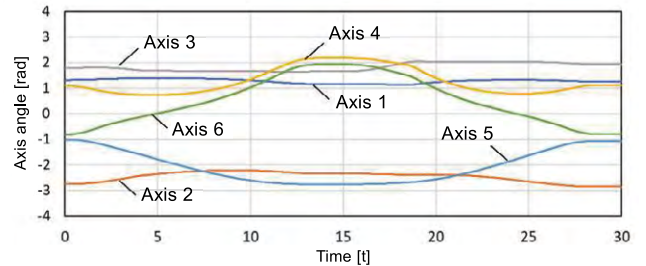


Fig.12. Target angle of each axis of the right arm (flipping motion)

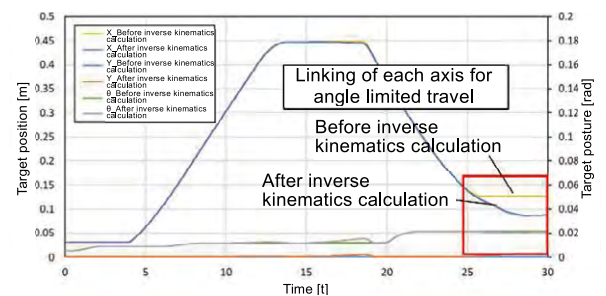


Fig.13. Travel target positional pose before and after prioritized inverse kinematics calculation

of the traveling part (before inverse kinematics calculation: yellow, after inverse kinematics calculation: blue), and shows that after 25 seconds, the value is different before and after the inverse kinematics calculation. This is the result of the coordinated linking mechanism of the prioritized inverse kinematics solution shown in Appendix, whereby the low-priority traveling part deviates from the original target positional pose because the target angles of each

axis of both arms are close to the limit angles, and the target positional pose is updated so that the motion of both arms can be performed. Looking at the target positional poses of each joint of both arms and the traveling part after 25 seconds, there is no sudden acceleration or deceleration and the target displacement changes smoothly, suggesting that the loose activation function of the linking shown in section 3.6 is working appropriately.

5 Insight

5.1 Relationship to Subsumption Architecture

We noted in Chapter 2 that the structure of the Subordination Architecture does not have a clear form of signal connection that determines the layers of behavior and the priority between layers. On the other hand, the motion priority determination function shown in Fig. 3 is a rule-based format that increases the motion priority of traveling when the risk of collision with the surroundings arises as a result of traveling, and prioritizes the motion of traveling to avoid collision over the motion of the hand to pick up an object. At this time, there is a layer structure for the robot's behavior, and the motion priority relationship that creates the layer structure are determined by the motion priority determination function. From the above, it can be said that the Subordination Architecture is an extended form of the Subsumption Architecture.

5.2 Autonomous Behavior and Behavioral Learning

As verified in section 4.2, when flipping the box and then restoring the box's pose, the traveling pose that was derived autonomously according to the box's pose change did not return to the motion start pose. This means that the robot has autonomously found a suitable pose to start flipping the box, relative to the motion start pose coarsely determined by the operator.

Currently, the only learning targets in the autonomously generated behavior of the robot are the mitigation of overload and over-approach to the surroundings, and pose change at the transit points to shorten the travel distance, and there is no function to change the motion start pose or target pose to accommodate the above situations. However, if the motion start pose and target pose can be changed in this way, it will reduce wasted motion, improve the smoothness of motion, and somewhat reduce takt time and battery consumption, so we think it should be added to the behavior learning function in some form.

5.3 Difference from a Learning-Based Approach

When adjusting robot motion in the field, the fact that motion and performance can only be improved by changing the training data is a major limitation. With the method of changing the training data, it is difficult to improve the behavior in a desired direction in a very small portion. In fact, this limitation has been a

problem in practical deep learning pick-and-place robotics systems. In addition, in the traditional learning approach compared in Chapter 2, the motion that a human gives to learning is not always optimal. At least function approximation learning methods, such as deep learning, do not include optimization. Reinforcement learning methods with optimization mechanisms have the problem of requiring a large number of trials, as discussed in Chapter 2.

For the Subordination Architecture, the overall structure of the control system is similar to that of a conventional industrial robot, as described in section 3.1, and the behavior of the robot can be adjusted directly by changing the target pose or changing or adding a transit pose. The behavior learning function can also optimize autonomously generated behavior. The Subordination Architecture is more field-oriented, but also has functionality that goes beyond the research examples using the latest computer science methods.

5.4 Applying AI and Machine Learning to the Subordination Architecture

The Subordination Architecture is a control framework that allows the traveling part and arms of the robot to instinctively and smoothly link with each other without any prior learning or simulation. By making such control intelligent, so that the robot does not need to learn the low-level control side, learning resources can be focused on higher-level areas such as object recognition and work planning. In fact, the behavior learning function of the Subordination Architecture developed by Shizuoka University is capable of generating a trajectory that avoids interference after only a few trials.[12],[13],[14]

In the simulation example in section 4.1, which handles motion priority changes, we mentioned that the challenge is to determine the motion priority according to the situation. The priority determination section shown in Fig. 3 can be implemented using various I/O relationship mapping mechanisms, such as rule-based or neural network mechanisms. Therefore, it would be possible to output the priority for each device by defining the instinctive rules or norms of behavior of the robot in a text format like a legal clause, such as "If you see a person behind an open door, you must give priority to the passage of the person," and having the generative AI interpret them. There may be multiple rules of behavior that apply to each situation, and in such cases, these rules conflict with each other, including contradictory relationships. To determine measures to mediate conflicts, the reinforcement learning criticized in Chapter 2 can also be applied. Conceptual learning that is not directly related to such control can be accomplished through simulation, where there is sufficient room for the use of computer science and DX methods.

Most notably, the Subordination Architecture is

capable of generating complex motion linking for simple commands. During the validation, we observed that the arms and traveling part of the CONOID are autonomously linked with the rotational motion of the box so that the rotational motion is achieved only by the command “Rotate the box 135°”. This suggests that the work can be done with ambiguous linguistic instructions, including voice, and would be easily coordinated with a generative AI.

6 Conclusion

Aiming at the practical application of production assistant robots for incidental work in factories, we proposed the Subordination Architecture, which is the overall structure of the control system for autonomous robots that encompasses the concept of robot autonomy presented in the previous engineering review and the basic framework of control to achieve this concept. We have also shown in validation that the most important feature of this architecture, which can automatically generate coordinated linking of the arms and the traveling part from a small number of teachings.

In response to our customer’s request, we are currently evaluating raw material supply operations using the CONOID with the Subordination Architecture in an area where automation has not been tested. In this validation, the visual pose recognition of the supplied object and the coordinated linking control of the traveling part and arms detailed in this paper are the basis for achieving automation of the work. As mentioned in the previous engineering review, we will commercialize CONOID not as a universal positioning device for multiple fields like conventional industrial robots, but as an autonomous work robot for a specific field with preloaded programs to perform specific tasks. Therefore, we will sequentially add more tasks to be validated and develop the robot to be sold as samples for engineering projects to specific customers as soon as possible.

Acknowledgments: This research was supported by NEDO under the project “Development of Integrated Core Technologies for Next-Generation AI and Robots / Research and Development for Enlarge the Application Fields of Artificial Intelligence Technologies / Research Projects for Reducing setup time and Realizing Multipurpose Capability of Production Assistant Robots based on Machine learning Technologies “. We would like to express our deepest gratitude to Professor Naoyuki Takesue of Tokyo Metropolitan University, Associate Professor Yuichi Kobayashi of Shizuoka University, and Associate Professor Kazuaki Yamada of Toyo University for their collaboration in this project.

References

1. Y. Nakamura, Y. Wada, *Autonomization of Robots in the stage of Transformation from Sustainability to Viability*, *Shibaura Machine Engineering Review*, vol.29 (2022), pp.40-45.
2. M. Sekiguchi and N. Takesue, *Stable Numerical Solution of Inverse Kinematics in Singular Pose and Unsolvable Problem Based on Minimization of Elastic Energy of Virtual Spring*, *Journal of the Robotics Society of Japan*, vol.36, no.9 (2018), pp. 645-653.
3. M. Sekiguchi and N. Takesue, *Fast and Robust Numerical Method for Inverse Kinematics with Prioritized Multiple Targets for Redundant Robots*, *Advanced Robotics.*, vol.34, no.16 (2020), pp.1068-1078.
4. H. Ito, K. Yamamoto, H. Mori, T. Ogata, *Efficient multitask learning with an embodied predictive model for door opening and entry with whole-body control*, *Science Robotics*, 6 April, Vol 7, Issue 65 (2022).
5. *Robust Layered Control System for a Mobile Robot*, R. A. Brooks, *IEEE Journal of Robotics and Automation*, Vol.RA-2, No.1, pp. 14-23, March 1986.
6. G. A. Bekey, *Autonomous Robots -From Biological Inspiration to Implementation and Control* (2017), MIT Press.
7. *Robot Learning of Mobile Manipulation with Reach-ability Behavior Priors*, S. Jauhri, J. Peters and G. Chalvatzaki, *IEEE Robotics and Automation Letters*, Vol.7, Issue 3, pp. 8399 - 8406, July 2022.
8. T. Welschhold, C. Dornhege, and W. Burgard, *Learning mobile manipulation actions from human demonstrations*, in *IROS*, IEEE (2017), pp.3196–3201.
9. T. Welschhold, N. Abdo, C. Dornhege, and W. Burgard, *Combined task and action learning from human demonstrations for mobile manipulation applications*, in *IROS*, IEEE (2019), pp.4317–4324.
10. H. Shimizu, *Seimei To Basho* (1999), NTT Publishing (in Japanese)
11. H. Shimizu, *Seimei-chi To Ba No Ronri* (1996), Chuko-Shinsho (in Japanese)
12. K. Arai, Y. Ishimura, Y. Kobayashi, H. Ibe, *Path generation using haptic information for shortening work teaching time to manipulators and automatic adjustment of the meta parameters*, *Proceedings of the 33rd Autonomous Distributed Systems Symposium* (2021), 1A1-1. (in Japanese)
13. T. Sakakibara, Y. Kobayashi, F. J. Arjonilla Garcia, *Path generation of manipulator based on contact information and automatic tuning of meta-parameter of the path generation*, *Proceedings of the 49th Intelligent Systems Symposium* (2022), ROMBUNNO.C3-3(WEB). (in Japanese)
14. R. Takami, Y. Kobayashi, *Manipulator path generation based on simple motion teaching and contact information*, *Proceedings of ROBOMECH2023*

(2023), 2A1-E14. (in Japanese)

15. M. Sekiguchi and N. Takesue, Formulation Method of Robot Kinematics Considering Versatility and Mobility of Each Joint, Journal of the Robotics Society of Japan, vol.41, No.2 (2023), pp.175-186. (in Japanese)

Appendix

The mechanism of coordinated linking of arms and traveling based on the prioritized multi-objective inverse kinematics solution described in section 3.4 is detailed below. From equation (2), we will expand the formulation in the original literature to cover a robot with a traveling part and manipulators on both the left and right arms. To avoid redundant explanation, we will omit the notation (q_k) from the Jacobi matrix, the error vector, and the current pose vector of the whole robot.

First, expand the virtual spring coefficient matrix K and the base Jacobi matrix J in equation (3) as follows.

$$K = \begin{bmatrix} K_V & \mathbf{0} & \mathbf{0} \\ \mathbf{0} & K_L & \mathbf{0} \\ \mathbf{0} & \mathbf{0} & K_R \end{bmatrix} \quad (9)$$

$$J = \begin{bmatrix} J_s & \mathbf{0} & \mathbf{0} \\ J_{s1} & J_{b1} & \mathbf{0} \\ J_{s2} & \mathbf{0} & J_{b2} \end{bmatrix}, \quad J^T = \begin{bmatrix} J_s^T & J_{s1}^T & J_{s2}^T \\ \mathbf{0} & J_{b1}^T & \mathbf{0} \\ \mathbf{0} & \mathbf{0} & J_{b2}^T \end{bmatrix} \quad (10)$$

The block matrices that constitute K and J are given as follows.

$$K_V = \begin{bmatrix} K_{Vx} & 0 & 0 & 0 & 0 & 0 \\ 0 & K_{Vy} & 0 & 0 & 0 & 0 \\ 0 & 0 & K_{Vz} & 0 & 0 & 0 \\ 0 & 0 & 0 & K_{VRx} & 0 & 0 \\ 0 & 0 & 0 & 0 & K_{VRy} & 0 \\ 0 & 0 & 0 & 0 & 0 & K_{VRz} \end{bmatrix} \quad (11)$$

$$K_L = \begin{bmatrix} K_{Lx} & 0 & 0 & 0 & 0 & 0 \\ 0 & K_{Ly} & 0 & 0 & 0 & 0 \\ 0 & 0 & K_{Lz} & 0 & 0 & 0 \\ 0 & 0 & 0 & K_{LRx} & 0 & 0 \\ 0 & 0 & 0 & 0 & K_{LRy} & 0 \\ 0 & 0 & 0 & 0 & 0 & K_{LRz} \end{bmatrix} \quad (12)$$

$$K_R = \begin{bmatrix} K_{Rx} & 0 & 0 & 0 & 0 & 0 \\ 0 & K_{Ry} & 0 & 0 & 0 & 0 \\ 0 & 0 & K_{Rz} & 0 & 0 & 0 \\ 0 & 0 & 0 & K_{RRx} & 0 & 0 \\ 0 & 0 & 0 & 0 & K_{RRy} & 0 \\ 0 & 0 & 0 & 0 & 0 & K_{RRz} \end{bmatrix} \quad (13)$$

$$J_s = \begin{bmatrix} n_{v0} & n_{v1} & \mathbf{0} & \mathbf{0} & \mathbf{0} & \mathbf{0} \\ \mathbf{0} & \mathbf{0} & \mathbf{0} & \mathbf{0} & \mathbf{0} & n_{v2} \end{bmatrix} \quad (14)$$

$$J_{s1} = \begin{bmatrix} n_{v0} & n_{v1} & \mathbf{0} & \mathbf{0} & \mathbf{0} & n_{v2} \times (p_L - p_V) \\ \mathbf{0} & \mathbf{0} & \mathbf{0} & \mathbf{0} & \mathbf{0} & n_{v2} \end{bmatrix} \quad (15)$$

$$J_{s2} = \begin{bmatrix} n_{v0} & n_{v1} & \mathbf{0} & \mathbf{0} & \mathbf{0} & n_{v2} \times (p_R - p_V) \\ \mathbf{0} & \mathbf{0} & \mathbf{0} & \mathbf{0} & \mathbf{0} & n_{v2} \end{bmatrix} \quad (16)$$

Here, n represents the rotational axis vector (unit angular axis vector) of the joint. n_{v0} (translation in the X direction), n_{v1} (translation in the Y direction), and n_{v2} (each rotational axis vector around the turning Z-axis) of the traveling part are given as follows.

$$n_{v0} = \begin{bmatrix} 1 \\ 0 \\ 0 \end{bmatrix}, \quad n_{v1} = \begin{bmatrix} 0 \\ 1 \\ 0 \end{bmatrix}, \quad n_{v2} = \begin{bmatrix} 0 \\ 0 \\ 1 \end{bmatrix} \quad (17)$$

p_V (the reference position of the traveling part), p_L (the hand position of the left manipulator), and p_R (the hand position of the right manipulator) are given by the following equations.

$$p_V = \begin{bmatrix} p_{Vx} \\ p_{Vy} \\ p_{Vz} \end{bmatrix}, \quad p_L = \begin{bmatrix} p_{Lx} \\ p_{Ly} \\ p_{Lz} \end{bmatrix}, \quad p_R = \begin{bmatrix} p_{Rx} \\ p_{Ry} \\ p_{Rz} \end{bmatrix} \quad (18)$$

The pose error vector e in equation (1) is also broken down one level further into three vectors: e_V (pose error of the traveling part), e_L (pose error of the left manipulator hand position), and e_R (pose error of the right manipulator hand position).

$$e = {}^d\chi - \chi = \begin{bmatrix} e_V \\ e_L \\ e_R \end{bmatrix} \quad (19)$$

From the above, equation (2) can be expanded as follows.

$$\tau = \begin{bmatrix} \tau_V \\ \tau_L \\ \tau_R \end{bmatrix} = J^T K e = \begin{bmatrix} J_s^T & J_{s1}^T & J_{s2}^T \\ \mathbf{0} & J_{b1}^T & \mathbf{0} \\ \mathbf{0} & \mathbf{0} & J_{b2}^T \end{bmatrix} \begin{bmatrix} K_V & \mathbf{0} & \mathbf{0} \\ \mathbf{0} & K_L & \mathbf{0} \\ \mathbf{0} & \mathbf{0} & K_R \end{bmatrix} \begin{bmatrix} e_V \\ e_L \\ e_R \end{bmatrix} \quad (2')$$

For this equation (2'), first look at the virtual spring coefficient matrix K . As shown in equations (9) and (11), K , which is a block diagonal matrix multiplied by the motion priority, is actually a diagonal matrix. Therefore, there is no correlation of different actuators or correlation of each control degree of freedom of different actuators between the three actuators of the traveling part, left and right manipulators.

Looking at the transpose matrix J^T of the base Jacobi matrix, which is also a block diagonal matrix, in equation (2'), the three transpose block matrices in the first row, from left to right, represent the amount that the translational velocity and rotational angular velocity in three-dimensional space of the traveling part, left manipulator hand, and right manipulator hand, respectively, contribute to the joint angular velocity of the traveling part. From this, the joint angular velocity of the traveling part is correlated with the motion speed of the left and right manipulator hands. Therefore, according to equation (2') or equation (2), the pose errors of the left and right

manipulators affect the driving torque of the traveling part via the correlated term of \mathbf{J}^T , and also affect the calculation of the displacement increment of the traveling part in equation (3). This can be confirmed by further breaking down the driving torque $\boldsymbol{\tau}_v$ of the traveling part in equation (2').

First, using equations (17) and (18), equations (14) to (16) can be broken down into equations (20) to (22) respectively.

$$\mathbf{J}_s = \begin{bmatrix} 1 & 0 & 0 & 0 & 0 & 0 \\ 0 & 1 & 0 & 0 & 0 & 0 \\ 0 & 0 & 0 & 0 & 0 & 0 \\ 0 & 0 & 0 & 0 & 0 & 0 \\ 0 & 0 & 0 & 0 & 0 & 0 \\ 0 & 0 & 0 & 0 & 0 & 1 \end{bmatrix}, \quad \mathbf{J}_s^T = \begin{bmatrix} 1 & 0 & 0 & 0 & 0 & 0 \\ 0 & 1 & 0 & 0 & 0 & 0 \\ 0 & 0 & 0 & 0 & 0 & 0 \\ 0 & 0 & 0 & 0 & 0 & 0 \\ 0 & 0 & 0 & 0 & 0 & 0 \\ 0 & 0 & 0 & 0 & 0 & 1 \end{bmatrix} \quad (20)$$

$$\mathbf{J}_s^T = \begin{bmatrix} 1 & 0 & 0 & 0 & 0 & 0 \\ 0 & 1 & 0 & 0 & 0 & 0 \\ 0 & 0 & 0 & 0 & 0 & 0 \\ 0 & 0 & 0 & 0 & 0 & 0 \\ 0 & 0 & 0 & 0 & 0 & 0 \\ 0 & 0 & 0 & 0 & 0 & 1 \end{bmatrix}$$

$$\mathbf{J}_{s1}^T = \begin{bmatrix} 1 & 0 & 0 & 0 & 0 & 0 \\ 0 & 1 & 0 & 0 & 0 & 0 \\ 0 & 0 & 0 & 0 & 0 & 0 \\ 0 & 0 & 0 & 0 & 0 & 0 \\ 0 & 0 & 0 & 0 & 0 & 0 \\ -(p_{Ly} - p_{Vy}) & p_{Lx} - p_{Vx} & 0 & 0 & 0 & 1 \end{bmatrix} \quad (21)$$

$$\mathbf{J}_{s2} = \begin{bmatrix} 1 & 0 & 0 & 0 & 0 & -(p_{Ry} - p_{Vy}) \\ 0 & 1 & 0 & 0 & 0 & p_{Rx} - p_{Vx} \\ 0 & 0 & 0 & 0 & 0 & 0 \\ 0 & 0 & 0 & 0 & 0 & 0 \\ 0 & 0 & 0 & 0 & 0 & 0 \\ 0 & 0 & 0 & 0 & 0 & 1 \end{bmatrix},$$

$$\mathbf{J}_{s2}^T = \begin{bmatrix} 1 & 0 & 0 & 0 & 0 & 0 \\ 0 & 1 & 0 & 0 & 0 & 0 \\ 0 & 0 & 0 & 0 & 0 & 0 \\ 0 & 0 & 0 & 0 & 0 & 0 \\ 0 & 0 & 0 & 0 & 0 & 0 \\ -(p_{Ry} - p_{Vy}) & p_{Rx} - p_{Vx} & 0 & 0 & 0 & 1 \end{bmatrix} \quad (22)$$

The pose error vector that was broken down one level further in formula (19), can be broken down one level further.

$$\mathbf{e}_v = \begin{bmatrix} e_{Vx} \\ e_{Vy} \\ 0 \\ 0 \\ 0 \\ e_{VRz} \end{bmatrix}, \quad \mathbf{e}_L = \begin{bmatrix} e_{Lx} \\ e_{Ly} \\ e_{Lz} \\ e_{LRx} \\ e_{Lry} \\ e_{LRz} \end{bmatrix}, \quad \mathbf{e}_R = \begin{bmatrix} e_{Rx} \\ e_{Ry} \\ e_{Rz} \\ e_{RRx} \\ e_{RRy} \\ e_{RRz} \end{bmatrix} \quad (23)$$

The first to third elements of the error vectors \mathbf{e}_v , \mathbf{e}_L , and \mathbf{e}_R are errors in the translation components in the X, Y and Z directions, respectively, between the current pose and the target pose. In addition, the fourth and fifth elements are the angular axis vector components in the X, Y and Z directions that represent the angular error between the current pose and the target pose.

From the above, the driving torque $\boldsymbol{\tau}_v$ of the traveling part in equation (2') can be expanded as follows.

$$\boldsymbol{\tau}_v = \begin{bmatrix} \tau_{Vx} \\ \tau_{Vy} \\ 0 \\ 0 \\ 0 \\ \tau_{V\theta} \end{bmatrix} = [\mathbf{J}_s^T \quad \mathbf{J}_{s1}^T \quad \mathbf{J}_{s2}^T] \begin{bmatrix} \mathbf{K}_V & \mathbf{0} & \mathbf{0} \\ \mathbf{0} & \mathbf{K}_L & \mathbf{0} \\ \mathbf{0} & \mathbf{0} & \mathbf{K}_R \end{bmatrix} \begin{bmatrix} \mathbf{e}_v \\ \mathbf{e}_L \\ \mathbf{e}_R \end{bmatrix}$$

$$= \begin{bmatrix} K_{Vx}e_{vx} + K_{Lx}e_{Lx} + K_{Rx}e_{Rx} \\ K_{Vy}e_{vy} + K_{Ly}e_{Ly} + K_{Ry}e_{Ry} \\ 0 \\ 0 \\ 0 \\ \mathbf{A} \end{bmatrix}$$

$$\mathbf{A} = -K_{Lx}e_{Lx}(p_{Ly} - p_{Vy}) + K_{Ly}e_{Ly}(p_{Lx} - p_{Vx}) - K_{Rx}e_{Rx}(p_{Ry} - p_{Vy}) + K_{Ry}e_{Ry}(p_{Rx} - p_{Vx})Rz + K_{VRz}e_{VRz} + K_{LRz}e_{LRz} + K_{RRz}e_{RRz} \quad (24)$$

Equation (24) shows that the errors between the current pose and target pose of the left and right manipulator hands affect the driving torque of the traveling part. Therefore, the prioritized multi-objective inverse kinematics solution described above is implemented in the prioritized multi-objective inverse kinematics calculation method, and a controller incorporating this prioritized multi-objective inverse kinematics calculation method is installed in the robot. This allows the robot to move its manipulator hands closer to the target position, even if the target position cannot be reached with the manipulators alone, by using the traveling part for complementary movement.

Development of AI Models to Extract and Evaluate Contact Patterns of Scraping

**Taku HOSHIYA**

Research & Development
Center
Research & Development
Department

**Masato TOMINAGA**

Research & Development
Center
Research & Development
Department

In developed countries, the working-age population is decreasing due to population decline and aging, and the shortage of manpower at production sites is becoming an issue. In particular, scraping work involves a lot of qualitative evaluation, and there is a concern that it will be difficult to hand down the techniques to the next generation. In this study, we proposed an approach to replace qualitative evaluation with quantitative evaluation by utilizing AI, and created two models, contact pattern extraction AI and contact pattern evaluation AI, which resulted in a high-performance model. However, it was found that there was an issue in improving the precision of the contact pattern evaluation AI. This may be due to incomplete label information in the training data. In the future, we will incorporate clustering methods to improve the label information in order to improve the precision, which will be reported in the future.

1 Background of Study

Recently, many developed countries are experiencing population decline and aging, which is accelerating the decline of the working-age population. This situation, especially the retirement of skilled workers and the lack of manpower, has caused problems with the lack of proper handing down of techniques. At domestic production sites, the lack of manpower has already led to the individualization of work, which could create a vicious cycle toward the decline of technological capabilities.

At production sites, there are still many qualitative evaluations based on the five senses in processing and inspection processes. Such evaluations are still needed in today's increasingly digitalized society, but qualitative evaluations may cause differences in evaluation criteria among workers, which may lead to variations in quality. Therefore, replacing qualitative evaluation with quantitative evaluation will clarify the evaluation criteria and thus ensure uniform quality.

Especially in developed countries, there is a need for labor savings at production sites as the working-age population is expected to decline. In order to realize labor saving, automation is considered essential, and digitalization is important as its preliminary step. However, in the current situation,

where many qualitative evaluations remain and human judgment is required, complete digitization cannot be achieved, and effective automation may not be possible.

This paper presents the need to replace qualitative evaluation with quantitative evaluation in order to address these issues using an example. Specifically, the introduction of a quantitative evaluation method by digitizing the qualitative evaluation performed in scraping work using AI will be made. Scraping is a cutting work to improve sliding properties by creating small grooves or indentations on a surface. By digitizing qualitative evaluation, we expect to establish a foundation for promoting digitalization and automation, reduce variation due to qualitative evaluation, and establish an efficient production process, thereby improving quality and productivity at production sites.

2 Purpose

The purpose of this study is to create an AI that extracts the contact pattern from the scraped surface imaging data and an AI that evaluates the contact pattern, thereby replacing the qualitative evaluation with a quantitative evaluation.

3 Methods

The evaluation of scraping work uses a qualitative visual evaluation method. Fig. 1 shows contact patterns generated on actual scraped parts.



Fig.1. Example patterns for qualitative evaluation

Fig. 1 shows the 1-inch square images of contact patterns extracted from the actual scraped surface. Workers evaluate the quality of the scraping work based on the information obtained from the contact pattern. Therefore, for quantitative evaluation, it is necessary to quantify the goodness of contact patterns as shown in Fig. 1.

In this study, two AIs were used to evaluate contact patterns.

3.1 Contact Pattern Extraction AI

The first of the two is a contact pattern extraction AI. It is not unusual for AIs that handle images to be greatly affected by the environment in which the images were taken. In order to address this issue, it is necessary to prepare a large amount of data under various environmental conditions, but it is not a realistic task. Therefore, in order to improve versatility, we created an AI that extracts contact patterns and generates binary images. To generate binary images, we built a contact pattern extraction model based on U-net [1], one of the deep learning methods effective for image domain classification. Fig. 2 shows the simplified structure of U-net.

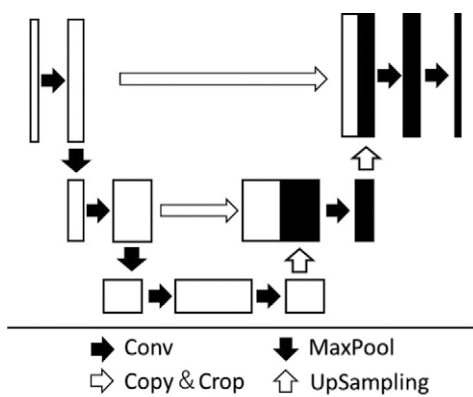


Fig.2. U-net model structure

As shown in Fig. 2, U-net is an auto-encoder [3] with a convolution layer [2]. The difference between U-net and conventional auto-encoders is that U-net uses the convolution information from the encoder section as input to the decoder section, which enables finer

domain classification than before. U-net generally performs supervised training. Fig. 3 shows an example of the training data used in this study.

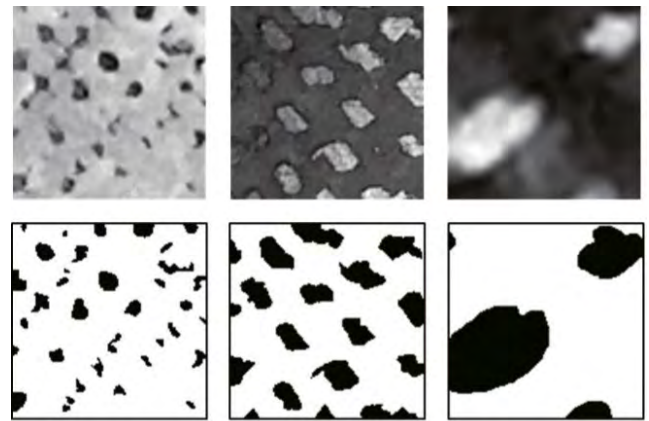


Fig.3. Training data for pattern extraction AI

The upper row of Fig. 3 shows the input images converted to grayscale from the contact pattern images shown in Fig. 1, and the lower row shows the training images annotated from the input images with the contact pattern areas in black and other areas in white. The reason for the grayscale conversion is to reduce the influence of the aforementioned photographing environment, and is that the RGB information was judged to be unnecessary for contact pattern extraction. The input images were captured using a camera attached to an ordinary tablet computer, rather than using a special imaging system. This was because of the cost advantage and to reduce the burden on the workers.

Table 1 shows the training conditions for the contact pattern extraction AI model.

Table 1. Training conditions of pattern extraction AI

Input data shape	(128,128,1)
Output data shape	(128,128,2)
Activation function (intermediate layer)	LeakyReLU [4] [alpha:0.01]
Activation function (output layer)	Softmax
Loss function	Categorical Crossentropy
Optimization method	Adam [5] [learning rate: 0.001]

The output data shape in Table 1 is (128,128,2) because training is performed using data converted from the training images in Fig. 3 to the One-Hot representation.

3.2 Contact Pattern Evaluation AI

The second AI is an AI that evaluates the contact patterns extracted in the previous section. Extracted

and binarized contact pattern images were used as input data for the evaluation AI. The evaluation AI has a structure that combines a convolution layer and a fully-connected layer. Fig. 4 shows a simplified diagram of the model structure used in this study.

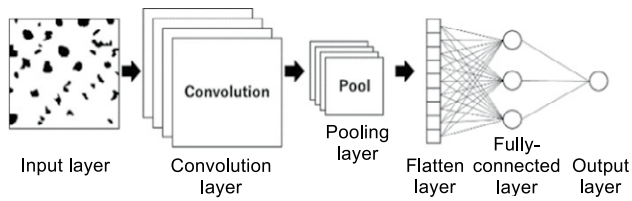


Fig.4. CNN model structure

In the output layer shown in Fig. 4, the result of the goodness judgment of the input contact pattern is output as a numerical value. This makes it possible to quantitatively evaluate whether the input contact pattern is good or bad.

Table 2 shows the training conditions for the evaluation AI.

Table 2. Training conditions for pattern evaluation AI

Input data shape	(128,128,1)
Output data shape	(1)
Activation function (convolution layer)	LeakyReLU [alpha: 0.01]
Activation function (fully-connected layer)	ReLU
Activation function (output layer)	Sigmoid
Loss function	Binary Crossentropy
Optimization method	Adam [learning rate: 0.001]

4 Result

4.1 Contact Pattern Extraction AI

Table 3 shows the accuracy of the trained model and Fig. 5 shows the output results. All evaluation data used in this paper are ones not used in the training process.

Table 3. Accuracy rate of training data and validation data

Training data	0.9975
Validation data	0.9911

Fig. 5 shows, from left to right, the input images, the training images, and the output images. The contact pattern extraction AI is trained to produce an output

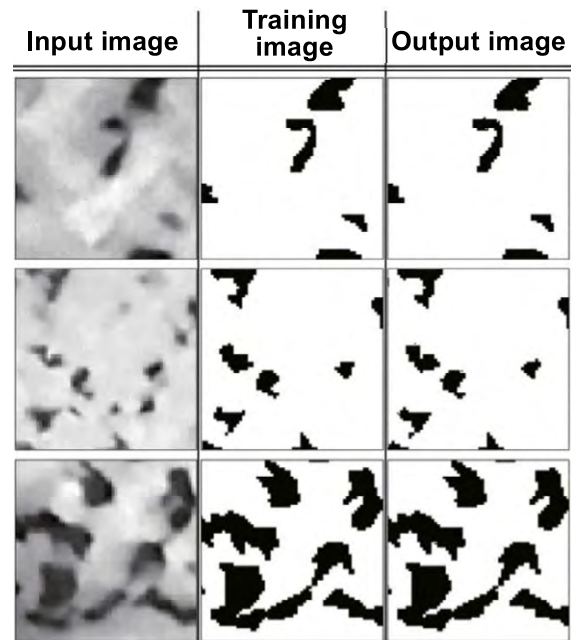


Fig.5. Result of pattern extraction by AI

image equivalent to the training image from the input image. As shown in Fig. 5, there is no significant difference between the training images and the output images. Table 3 shows that the accuracy of the validation data is also high, indicating that the created model is quite accurate for contact pattern extraction. Since the accuracy alone is not enough to evaluate the pixel-by-pixel discrepancy, the average IoU, which is one of the evaluation indices for the segmentation task, was used as an index for evaluating the model. IoU is a value indicating the degree of overlap between the correct and predicted regions, and the average IoU is the value obtained by calculating IoU for multiple classes and averaging them. The formula for calculating the average IoU is shown in Equation (1), where n is the number of classes to be classified.

$$\text{Average IoU} = \frac{1}{n} \sum_{i=1}^n \frac{|A_i \cap B_i|}{|A_i \cup B_i|} \quad (1)$$

From equation (1), the average IoU for the validation data was found to be 0.9888. Generally, the closer the IoU is to 1, the more accurate the model, and a model with the IoU of 0.5 or higher is said to be accurate. Consequently, based on the accuracy and average IoU value, the created model is useful with little contact pattern discrepancy.

4.2 Contact Pattern Evaluation AI

The contact pattern evaluation AI handles binary classification of images. Table 4 shows the accuracy of the trained model.

Table 4. Accuracy of training data and validation data

Training data	0.9243
Validation data	0.8733

Table 4 indicates that the accuracy performance is more than 80% for both training and validation data. Next, Table 5 shows the confusion matrix, which is often used to evaluate the performance of binary and multi-level classification models. The confusion matrix shows the number of matches and mismatches between the model's predictions and the true target (correct label), and can be used to evaluate how accurately the model was able to predict which classes, misclassification trends, etc.

Table 5. Confusion matrix

	Goodness of prediction	Badness of prediction
Goodness of true	TP 114	FN 8
Badness of true	FP 20	TN 79

Based on Table 5, the precision and recall are calculated to further evaluate the performance of the model. Equations (2) and (3) show the formula for calculating precision and recall, respectively. Table 6 summarizes the calculated precision and recall.

Precision:

$$\frac{TP}{TP + FP} \quad (2)$$

Recall:

$$\frac{TP}{TP + FN} \quad (3)$$

Table 6. Precision and recall

Precision	0.8507
Recall	0.9344

Table 6 shows that among the contact patterns predicted as good, about 85% were actually good contact patterns, and among the data that were actually good, about 93% of the contact patterns were correctly predicted. This indicates that about 15% of the data that the AI predicted as good contact patterns actually contained bad contact patterns, and that

about 7% of the good contact patterns would be predicted as bad contact patterns.

Next, the ROC curve and AUC [6] were used to perform evaluation. The ROC curve and AUC are used as indicators to evaluate the performance of the classification model using precision and recall. The contact pattern evaluation AI ROC curve and AUC are shown in Fig. 6.

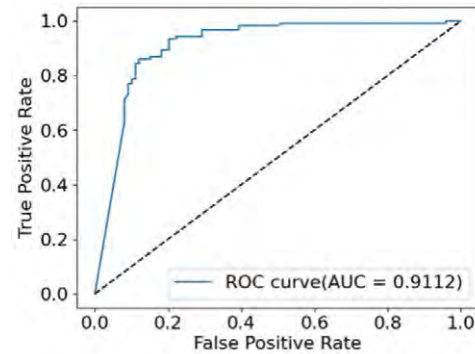


Fig.6. ROC curve and AUC

Fig. 6 shows that the AUC value is 0.9112. In general, the closer the AUC is to 1, the higher the performance of the model, and thus, it can be said that a useful model of the contact pattern evaluation AI could also be created.

4.3 Challenges for Improvement of Precision

In this study, the contact pattern extraction AI and contact pattern evaluation AI were created. Each AI model has a high performance in terms of the evaluation index. However, as a contact pattern evaluation AI, the precision of about 85% is not a high figure when quality assurance is taken into consideration. As mentioned above, about 15% of the products judged to be good by the AI may be defective, so precision should be maintained at a level close to 100%.

Possible reasons why the precision was not able to achieve a high level of performance this time could be that the label information of the training data was not optimal, or that the training data was insufficient. However, in this study, the contact pattern extraction AI was created to create a highly versatile AI model from a small amount of data for the purpose of reducing the amount of data acquisition. Therefore, this study focuses on the possibility that the label information was not optimal.

In this study, the contact pattern evaluation AI was trained by linking the output results of the contact pattern extraction AI with the labels of good and bad. Since labels are created manually by humans according to the judgment based on qualitative evaluation, the AI model may not be more accurate if the label information is incomplete. Since labels are created with binary values of good and bad, it is possible that the model may not be good at judging

good or bad. Qualitative evaluations by humans are sometimes based on vague senses such as 0.8 vs. 0.2 rather than 0.0 vs. 1.0. Since the labels used in this study did not include information on this ambiguity, it is thought that the relationship between the contact pattern features and the labels could not be fully captured accurately. As can be seen from the accuracy in Table 4, the difference in accuracy between the training data and the validation data suggests that the validation data included data that were difficult to classify with binary values. Fig. 7 shows the training curve of the contact pattern evaluation AI.

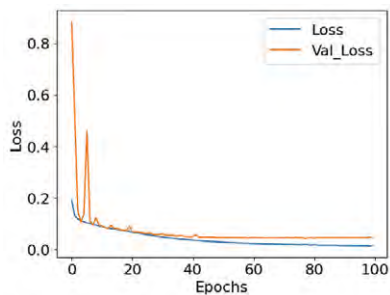


Fig.7. Learning curve of pattern evaluation AI

The validation of the contact pattern evaluation AI used the learning model at 38 epochs in Fig. 7, which indicates that there are no signs of overlearning in the model itself. Therefore, it is quite possible that incomplete label data is a factor.

We believe that the incompleteness of label information can be solved by grouping contact patterns using a clustering method and adjusting the label values for each cluster. For example, by penalizing the label information according to the distance in the feature space between the contact pattern that can be said to be 100% good and the contact pattern that can be said to be 100% bad, AI may be able to perform a quantitative evaluation of ambiguous data, so we will continue our study.

5 Conclusion

In this study, we were able to create high-performance AI models for scraping, one for contact pattern extraction based on the photographed data of scraped surfaces and the other for contact pattern evaluation. However, utilizing AIs to enhance quality requires further accurate models, so we will continue to improve them. It is expected that quality and productivity will be improved at production sites by utilizing AIs. We intend to utilize evolving digital technologies and explore further innovative approaches in the future to provide new value to the industrial world.

References

1. O. Ronneberger, P. Fischer, and T. Brox, "U-Net: Convolutional Networks for Biomedical Image Segmentation," arXiv:1505.04597 [cs.CV], 18 May 2015.
2. Yann LeCun, Bernard Boser, John S. Denker, Donnie Henderson, Richard E. Howard, Wayne Hubbard, Lawrence D. Jackel, Handwritten Digit Recognition with a Back-Propagation Network, Proceedings of the IEEE, Vol. 86, No. 11 (November 1998), pp.2278-2324.
3. Vincent, Pascal, et al., Extracting and Composing Robust Features with Denoising Autoencoders, Proceedings of the 25th International Conference on Machine Learning (ICML-2008), 2008.
4. Maas, Andrew L., Awni Y. Hannun, and Andrew Y. Ng, Rectifier Nonlinearities Improve Neural Network Acoustic Models, Proceedings of the 30th International Conference on Machine Learning (ICML-13), 2013., pp.3-11.
5. Diederik p. Kingma & Jimmy Lei Ba, ADAM: A METHOD FOR STOCHASTIC OPTIMIZATION, 3rd International Conference for Learning Representations, San Diego, 2015
6. James A. Hanley, Barbara J. McNeil, The meaning and use of the area under a receiver operating characteristic (ROC) curve, Radiology, Vol. 143, No. 1 (April 1982), pp. 29-36.

Development of Interface Control Technology with Medium Vacuum PVD for Achieving All-dry Semiconductor Package Interconnect Formation Process



Kazuhiro FUKADA

Research & Development
Center
Research & Development
Department

The recent changes in the world situation have been accompanied by a rapid increase in information, which is forcing semiconductors, especially cutting-edge logic ICs, to become even more highly integrated and faster. It is imperative for semiconductor back-end-of-line processes to deploy front-end-of-line process technologies, and there is an urgent need to develop process technologies and manufacturing equipment optimized for back-end-of-line processes. Among back-end-of-line processes, electrolytic plating seed layer deposition is a process that is attracting particular attention, and the current electroless plating method is reaching its limits for next-generation fine interconnect formation processes. Therefore, we propose a process to form a seed layer using a medium-vacuum PVD system.

This paper describes the next-generation semiconductor package substrate formation process centered on a medium vacuum PVD system that we propose.

1 Introduction

In order to achieve higher integration of semiconductor package substrates, not only ultra-finer LSIs mounted on CPUs and GPUs, but also formation of fine circuits of several μm width on organic package substrates on which LSIs are mounted is required. For the miniaturization of organic substrate circuits, it is essential to form a conductor layer with high adhesion on the smooth surface of the insulating material. However, the conventional wet process cannot ensure adhesion to the smooth surface, making it difficult to form fine circuits. Our deposition equipment employs a vacuum integrated process [1],[2] system, which enables surface modification using plasma and formation of a highly adherent conductor layer by sputtering in a medium vacuum (100 Pa to 0.1 Pa) environment to achieve high-speed tact time [2].

A printed interconnect board on which logic ICs are mounted has a multilayer structure consisting of 10 or more layers of interlayer insulating film called build-up film. The interconnect in each layer is formed by electrolytic plating. Currently, the seed layer formation necessary for electrolytic plating uses electroless plating [3], and it is known that the adhesion of electroless plating to the insulating material is obtained by physical anchoring to the rough surface of the insulating material. However, miniaturization requires smoothness of the surface of insulating

materials, and electroless plating cannot obtain sufficient adhesion to such smooth substrates. A seed layer formation method using sputtering is being developed as a new process for next-generation package substrates that will replace electroless plating [2],[4],[5]. Since the seed layer formed by sputtering has a different adhesion method from electroless plating, it can achieve high adhesion to smooth surfaces. In addition, the number of processes can be reduced compared to electroless plating, and thus yield improvement in the back-end-of-line processes can be expected. Generally, in the case of a process that forms a conductor layer by sputtering, a structure in which copper is deposited on an adhesion layer such as Ti or Cr is considered. However, this structure requires not only the etching of Cu but also the removal of adhesion layers such as Ti or Cr during the seed layer removal process in circuit formation, and there are also many problems such as the environmental impact and safety issues of the chemicals used. To solve these problems, we have developed a conductor layer formation process using a vacuum integrated process [1], and have realized a highly adhesive direct copper conductor layer formation process that does not require metal adhesion layers such as Ti and Cr by promoting chemical bonding between the resin and copper through surface modification using O₂ plasma. Since

this process is performed under medium vacuum conditions, the tact time is short, and the interconnect formation process does not require catalyst removal or metal adhesion layer removal, making it suitable for miniaturization and advantageous for high-speed transmission characteristics. Next-generation printed interconnect board formation processes tend to convert conventional wet processes to dry processes as much as possible, and thus not only seed layer formation but also the preceding process needs to be made dry.

This report presents a method to make the preceding process of a seed layer formation dry in order to realize a next-generation printed interconnect board formation process with the above-mentioned high adhesion direct copper conductor layer formation process.

2 Printed Interconnect Board Formation Process

This chapter describes the process flow used to manufacture semiconductor package substrates. Fig. 1 shows the process flow of circuit formation using a semi-additive process (SAP method) on an ABF build-up substrate. First, an ABF substrate (GXT31) with FR-4 core material is desmeared for surface sparsification and dehydrated by oven heating. Subsequently, plasma surface modification is performed and a conductor layer (300 nm) is formed by copper sputtering in medium-vacuum sputtering equipment LPP-450. In patterning, a dry resist film is attached using a vacuum laminator and exposure is performed, followed by development. Then, the interconnect layer is increased by electrolytic plating, followed by annealing to strengthen the adhesion between the substrate and the seed layer. Finally, seed layer etching is performed to complete the circuit formation.

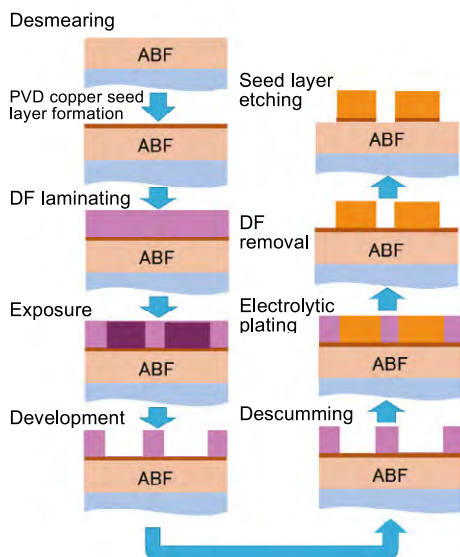


Fig.1. Process flow of semiconductor package circuit formation

In the previous report [2], wet desmear with permanganate was used in the desmear process, which is the process before seed layer formation. In this report, in order to approach the next generation semiconductor packaging process that satisfies customer requirements, a dry method of surface sparsification was tried instead of the wet method, and the adhesion to the ABF substrate was checked.

3 Overview of Experimental Apparatus

3.1 Outline of Equipment

We fabricated medium-vacuum sputtering equipment LPP-450 for direct copper conductor layer formation. Fig. 2 shows an external view of the equipment, and Table 1 shows its specifications. Fig. 3 shows a top view of the equipment. In the case of the equipment described in the previous report, the double-sided electrodes of the HCD and sputter were arranged diagonally [2], but the equipment fabricated this time has the HCD and sputter electrodes facing each other as shown in Fig. 3. This arrangement made it possible to shorten the time required for metal deposition.



Fig.2. Medium-vacuum PVD equipment

Table 1. Specifications of equipment

Outer dimensions	4,200×2,800×2,100 mm
Chamber volume	450 L
Substrate size	Max 630×540 mm
Sputtering method	DC magnetron method
Plasma method	RF remote Type
Deposition Rate (Cu)	~35 nm/sec
Film thickness uniformity	<10% (max-min)/(2XAvg)
Tact time	240 sec (standard process)

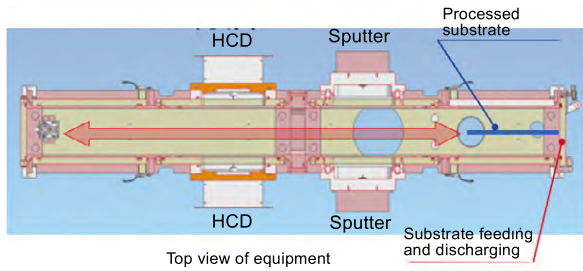


Fig.3. Outline of equipment

The LPP-450 medium-vacuum sputtering equipment has two plasma electrodes and two sputtering electrodes, and is characterized by its ability to modify and deposit films on both sides of a substrate in a single vacuum process.

The following is the substrate processing procedure of LPP-450, where the lower side of Fig. 3 is the surface A, which is processed first, and the upper side is the surface B, which is processed second.

- After loading a substrate, evacuate to a processable pressure of 0.1Pa.
- Plasma-treat on the surface A to modify it.
- Plasma-treat on the surface B to modify it.
- Similarly, Cu-sputter on the surfaces A and B.
- Open to the atmosphere and remove the substrate.

Normally, vacuum deposition equipment evacuates to a high vacuum range (0.1 Pa to 10⁻⁵ Pa), and in the case of resin base materials, vacuum evacuation requires a long time to achieve such a high vacuum range due to gas generation from the material. However, the process developed this time allows processing in a medium-vacuum range, which significantly reduces the exhaust time and can be completed in 240 seconds per process at a minimum. The maximum substrate size that can be processed by the equipment is 640 mm×530 mm, which is the industry standard maximum size for printed interconnect boards.

3.2 Study of Dry Desmear Method

This section describes a study of the dry desmear process. Three types of methods were investigated: UV light irradiation, heat-assisted plasma, and microwave plasma. As a result, the microwave plasma method with less thermal history showed better adhesion. Therefore, we decided to target the microwave plasma method.

Fig. 4 shows an electron microscope image of the surface of an ABF substrate after desmearing by the microwave plasma method. From this figure, it can be seen that numerous fillers were generated on the surface. These fillers are SiO₂ fillers contained in ABF, and sputtering in this state inhibits adhesion with the resin surface. Normally, the filler is removed by ultrasonic cleaning with deionized water. However, after cleaning with deionized water, a drying process

is required before proceeding to the next process, resulting in a long process tact time.

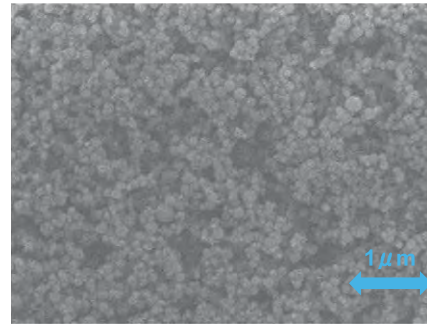


Fig.4. ABF surface after plasma-desmearing

We focused on dry ice blasting as a dry filler removal process. An overview of dry ice blasting is shown in Fig. 5. Dry ice blasting uses compressed air to impact dry ice several μm in diameter onto the substrate to clean the surface, which uses physical energy, making it suitable for removing minute objects such as those in this case.

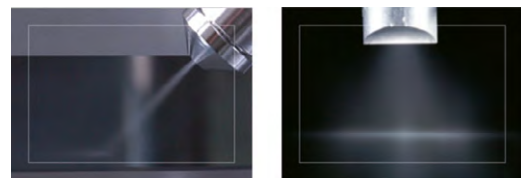
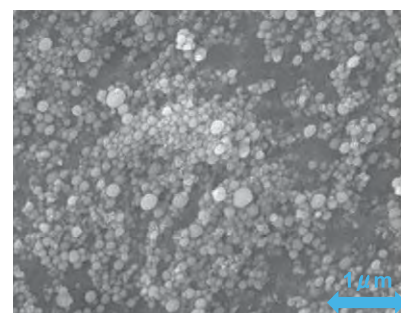
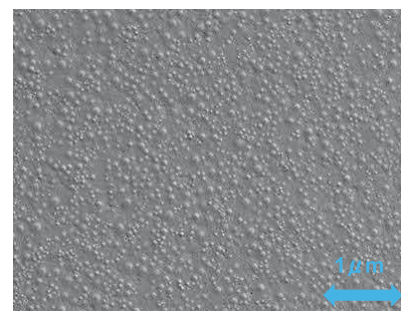


Fig.5. Overview of dry ice blasting

Fig. 6 shows the result of dry ice blasting after plasma desmear.



(a) Weak conditions



(b) Strong conditions

Fig.6. Surface SEM image after dry ice blasting

Fig. 6 shows that dry ice blasting reduces the amount of filler remaining on the surface, and that the filler can be completely removed from the surface by strengthening the blasting conditions.

3.3 Evaluation Result of Adhesion to Dry Ice Blasted Substrate

It was found that dry ice blasting can remove filler from the surface, and thus adhesion evaluation was conducted by plating and peeling test. Fig. 7 shows an example of evaluating a sample fabricated by the following process: Plasma-treat a 50 mm square surface with LLP-450, form a seed layer by sputtering, and then form a 25 μm thick Cu film by electrolytic plating, followed by annealing and then measuring the peel strength using a peel strength tester. The measurement conditions were a 90° pull angle, a pull speed of 50 mm/min, and a test width of 1 cm.

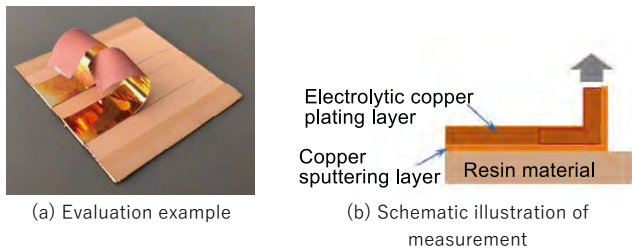


Fig.7. Peel test evaluation example and schematic illustration of measurement

In order to understand the trend of dry ice blasting, two displacement parameters were used: the nozzle pressure of blasting and the stage movement speed. Fig. 8 shows the peel strength dependency of the stage movement speed, and Fig. 9 shows the peel strength dependency of the nozzle pressure of blasting.

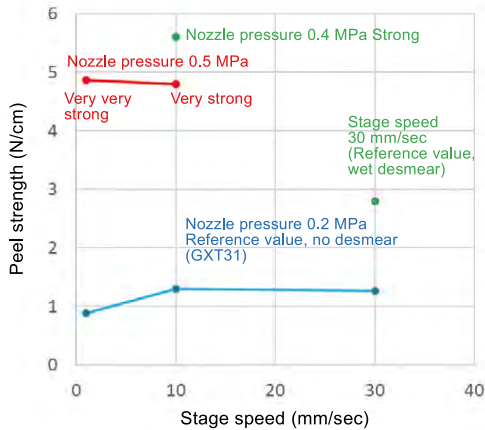


Fig.8. Peel strength dependency of stage movement speed

Fig. 8 shows no relationship between stage movement speed and peel strength.

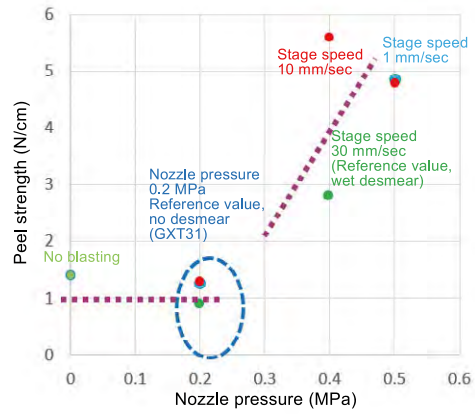


Fig.9. Peel strength dependency of nozzle pressure

Fig. 9 shows the relationship between the nozzle pressure of blasting and the peel strength: the peel strength increases with nozzle pressure when nozzle pressure exceeds 0.2 MPa. Since the adhesion force required for patterning is 4 N/cm or higher, the combination of plasma desmear and dry ice blasting can be considered practical for the next-generation semiconductor packaging method as long as the dry ice blasting conditions are 0.4 MPa or higher.

3.4 Loose Filler Removal Model

Fig. 10 and Fig. 11 show models with improved adhesion due to filler removal by dry ice blasting.

Ordinary filler removal methods such as ultrasonic cleaning with pure water or other methods can remove filler generated on the surface after plasma treatment as shown in Fig. 10, but they cannot remove filler entangled with resin. Therefore, sufficient adhesion between the resin and the Cu seed layer cannot be obtained.

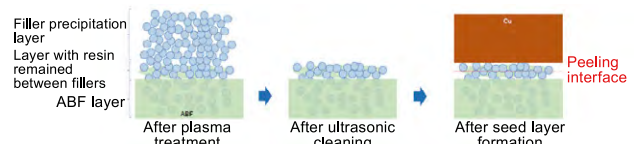


Fig.10. Adhesion improvement mechanism by conventional filler removal method



Fig.11. Adhesion improvement mechanism by dry ice blasting filler removal

On the other hand, dry ice blasting can remove filler entangled with resin together with the resin by blasting pressure as shown in Fig. 11. As a result, a bare resin interface can be created, leading to sufficient adhesion at the resin-Cu interface.

4 Conclusion

In this paper, we proposed a next-generation printed interconnect board formation process using a conductor layer using medium-vacuum PVD and conducted an adhesion strength test, which is an important evaluation item. Dry ice blasting after plasma desmear greatly improved adhesion. For the next step, we plan to form interconnect and evaluate electrical characteristics using the all-dry printed interconnect board formation process presented in this paper.

References

1. Fukada, Fukuyama, Namba, Kurihara, Sueki, Development of vacuum integrated PVD+CVD deposition equipment - Application to moisture-resistant multilayer Al-SiO-NbO reflective film for combiner-type HUD - Shibaura Machine Engineering Review Vol. 28 13-16, 2021
2. Fukada, Ueyama, Application of high-speed plasma surface modification equipment to next-generation printed interconnect board circuit formation process - Shibaura Machine Engineering Review Vol. 29 35-39, 2021
3. SUN, Jiang-Yan, et al. Adhesion study between electroless seed layers and build-up dielectric film substrates. *Journal of The Electrochemical Society*, 160.3: D107, 2013.
4. OH, Yoong, et al. Adhesion of sputter-deposited Cu/Ti film on plasma-treated polymer substrate. *Thin Solid Films*, 600: 90-97, 2016
5. T. Goto, et al, "Adhesion Characteristics of Magnetron-Sputter-Deposited Copper on Smooth Cycloolefin for Realizing Wiring with High-Frequency Signal Propagation", *Transaction of The Japan Institute of Electronics Packaging*, Vol. 1, No. 12, pp.12-19

Verification of Production Methods Using Environment-Friendly Die-Casting Technology



Satoshi TOMIOKA
 Metal & Plastics Industrial Machine Company
 Metal & Plastics Industrial Machine Technology Department

Currently, in addition to the need to reduce the weight of vehicles that employ many die-castings, efforts to reduce environmental impact, including manufacturing processes and price competitiveness, are required even more than before. Although the die-casting cycle time is determined by the casting conditions of the entire line, such as the dies and peripherals, it is also very important to shorten the working time of the die-casting machine.

Therefore, we realized a high cycle by changing the die-clamping part of the die-casting machine from a hydraulic system to an electric system. In addition, we compared the quality by the production method incorporating the related technology to reduce the environmental load and that by the conventional method [1] to confirm its effectiveness. The results are as follows.

1 Concept of Energy-Saving

The three main basic output elements of a die-casting machine are (1) clamping force, (2) injecting force, and (3) extruding force. These three require high power output and high responsiveness, so hydraulic drive is the mainstream for die-casting machines. Hydraulic driven machines feature compact size, high output, and high responsiveness, but they have problems due to insufficient management of operating oil and oil leaks. On the other hand, electric driven machines excel in the stability of repeated production and energy efficiency, but an attempt to achieve output and responsiveness comparable to hydraulic driven machines leads to a larger size and higher cost. In addition, there are regions that are difficult to reach with the current underlying technologies. Of efforts considering these advantages and efforts to address these challenges, this report focuses on electric clamping.

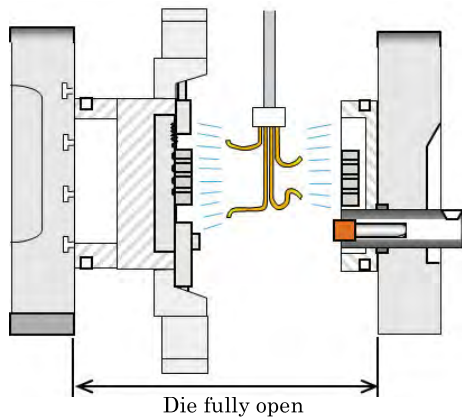
2 Concept of Energy-Saving

Table 1 shows the characteristics of electric driven die-casting machines. Converting the clamping action from hydraulic to electric driven type is expected to improve energy efficiency and repeatability and shorten cycle time during die opening and closing. In addition, by utilizing the stopping accuracy, which is one of the advantages, it becomes possible to use the intermediate stop operation of die opening and closing.

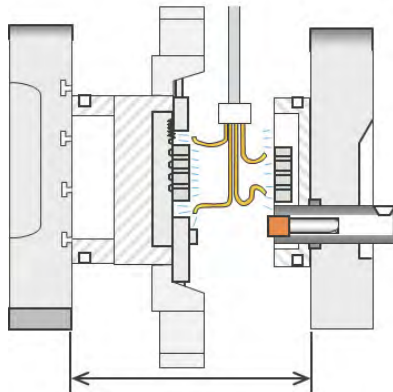
Table 1 Characteristics of electric driven die-casting machines

Advantages	<ul style="list-style-type: none"> • Energy saving • Good repeatability • Fast die opening and closing • Intermediate stop of die opening/closing possible
Current challenges	<ul style="list-style-type: none"> • Requires inventory of spare parts (addressing long lead time of electrical parts) • Requires a control panel for amplifier (addressing to layout of panel installation)

Fig. 1 (a) shows a schematic diagram of a typical application of a release agent by a spray to a die when the die is fully open. As shown in the drawing, the release agent is applied while keeping a certain distance or more between the tip of the spray cassette nozzle and the surface of the die. On the other hand, Fig. 1 (b) shows spray application to an intermediately closed die using electric die clamping. When the agent is sprayed after bringing the movable die (movable die plate) close to the spray nozzle, the amount of release agent can be reduced, and its scattering can be prevented.



(a) General application by spray



(b) Application by spray to intermediately closed die using electric die clamping

Fig.1 Release agent application during spraying

3 Verification Method Using Die-Casting Machine

Fig. 2 shows the die-casting machine used for comparative verification (7 years since the beginning of operation). Its maximum clamping force is 3500 kN, and the clamping mechanism can be selected from an electric drive (Fig. 3.a) or hydraulic drive (Fig. 3.b). This die-casting machine employs a hydraulic driven system for injection and extrusion operations.

**Fig.2** Die-casting machine with a clamping force of 3500 kN (servo oil as pressure source, with intensification accumulator)

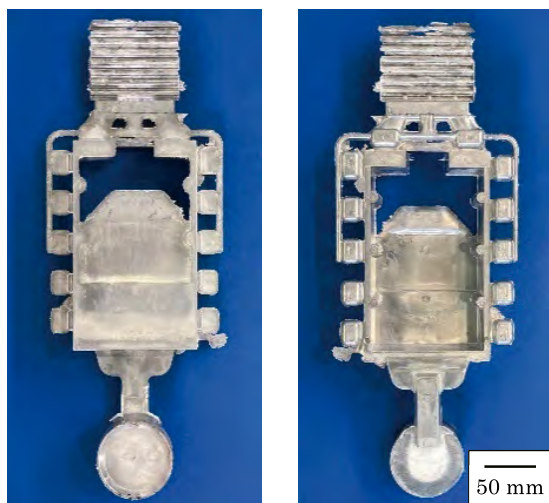
(a) Electric clamping type



(b) Hydraulic clamping type

Fig.3 Selection of clamping driving unit

The spraying device is air-driven, direct-acting type, and we applied the Aldice OE-SF release agent made by Nippon Graphite Industries, Co., Ltd. to cavities every shot using a 30-nozzle spray cassette. We measured the amount of release agent applied using a clamp-type flowmeter attached to the periphery of the fixed pipe through which the release agent passed. The product was taken out using a take-out device and die-casting was performed in a fully automatic cycle. Before the experiment, we removed the operating oil from the hydraulic tank of the die-casting machine, cleaned the tank, and then used a new oil. The operating oil used was HYDOL HAW-K (water-glycol operating oil) manufactured by MORESCO Corporation. The cover shapes shown in Fig. 4 were used for the product. Die conditions are shown in Table 2 and die-casting conditions are shown in Table 3. The die-casting material used was clean AD.12 molten metal treated with Ar bubbling in a holding furnace. The molten metal temperature in the holding furnace was set at 670°C and the casting temperature in the sleeve spout was set at 660°C. To evaluate the quality of the die-cast products, a portion of the products was used to obtain the porosity volume ratio inside the castings from CT analysis. The environmental impact of die-cast production was examined by measuring the amount of power consumed during one cycle in the fully automatic mode of the hydraulic clamping type and the electric clamping type, respectively. In addition, in order to investigate the product release resistance during extrusion, a pressure sensor was attached to both the head side and the rod side of the extrusion cylinder to simultaneously measure the operating pressure.



Fixed die side

Movable die side

Fig.4 Product shape

Table 2 Die conditions

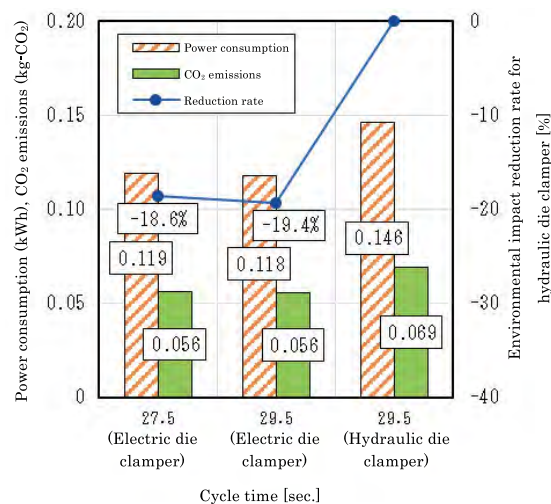
Die thickness	411 mm
Average wall thickness	2.0 mm
Cast weight	1.1 kg
Fill weight	0.9 kg
Product weight	0.7 kg
Gate's cross-sectional area	2.34 cm ²
Tip diameter	φ70 mm

Table 3 Cast conditions

Low injection speed	0.2 m/s
Injection acceleration speed	3.0 m/s
Injection deceleration speed	1.0 m/s
Casting pressure	85.5 MPa
Pressure rising time	18 ms
Increased pressure holding time	3.0 sec.
Injection tracking limit position	345 mm
Clamping force	100%
Die opening and closing speed	100%
Die timer (Curing)	6.0 sec.
Extrusion stroke	20 mm
Forward and backward extrusion speed	100%

4 Power Consumption and CO₂ Emissions

Fig. 5 shows the power consumption and CO₂ emissions per fully automatic cycle in actual casting. CO₂ emissions were calculated assuming that 1 kWh of electricity consumption generated 0.472 kg of CO₂. The operating time of each automatic machine attached to the die-casting machine was adjusted to 2.1 sec. hot water supply time, 9.5 sec. spray time (including release agent application and air blow) and 4.8 sec. product take-out time. Calculation of the environmental impact per cycle confirmed that the impact for hydraulic clammer was about 19% lower than that for electric clammer. Furthermore, since the cycle time can be reduced by 2 sec. by electric die clamping, further mitigation of environmental impact can be expected by reviewing the operating timing of the entire peripheral equipment.

Fig.5 Power consumption and CO₂ emissions per fully automatic cycle in actual casting

(*Calculated on the assumption that 1 kWh of power consumption generates 0.472 kg of CO₂.)

5 Influence of Drive System of Die Clammers on Product Quality

The product quality was evaluated by CT analysis of the porosity rate (percentage of cast volume and product volume) inside half of the product on the final fill side shown in Fig. 6. Fig. 7 shows the porosity rate obtained from CT analysis in die-casting using electric and hydraulic clammers. In addition, CT images are also shown, and the porosities observed in the product CT images are distinguished by color mapping for each size. In this die-casting condition, porosities were observed relatively frequently in the final fill portion and in the thick-walled area in the center of the boss. In addition, since the molten metal state, die, and injection conditions were almost the same, no differences in the formation of porosities due to differences in the die clamping drive system were observed.

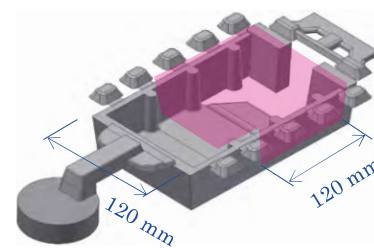


Fig.6 Sites of product CT analysis

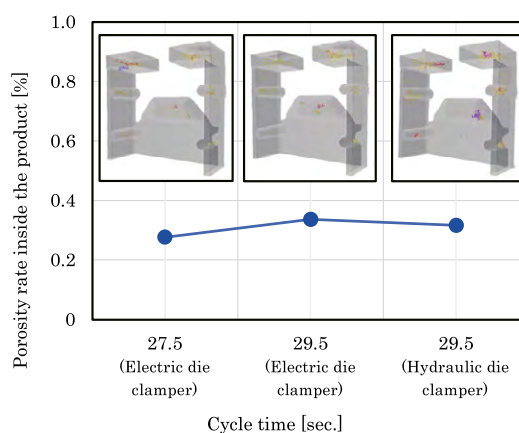


Fig.7 In-product porosities obtained from CT analysis

6 Influence of Amount of Release Agent Applied on Release Force

Fig. 8 shows an example of waveforms of the measured extrusion pressure and release force with release agent spray time set to 0.5 sec., spray pressure (release agent pressure) set to 0.5 MPa, and air pressure set to 0.4 MPa (amount of applied release agent: 72 mL). The pressure on the head and rod sides of the extrusion cylinders was measured, and the net extrusion force was calculated based on the pressure-receiving area of the extrusion cylinder. Furthermore, the peak value of the extrusion sliding resistance in a dry cycle (blank operation) (about 3 kN at a die temperature of 250°C this time) was subtracted from the calculated extrusion force to obtain the release force using the following equation.

$$\text{Release force} = \text{Extrusion force during actual casting} - \text{Extrusion force during drying}$$

After the product is extruded from the die, the pressure on the rod side of the extrusion cylinder increases, and the peak release force value appears. The peak value near this initial operation is called the release force.[2]

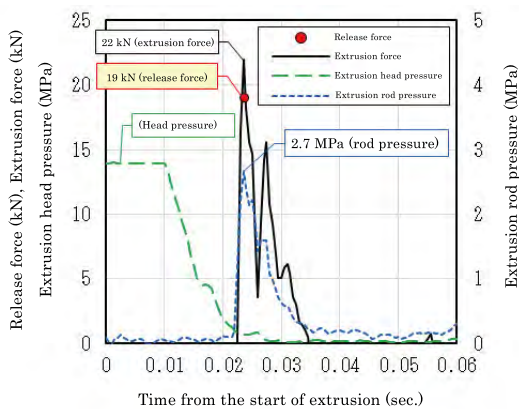


Fig.8 Waveforms of measured extrusion pressure and release force

Fig. 9 shows the effect of the amount of release agent applied on the release force in general spraying (release agent applied to a fully open die). The distance from the tip of the spray nozzle to the movable cavity surface (spray distance) is 150 mm and the spray pressure is 0.5 MPa. As the amount of release agent applied decreases, the release force tends to increase, indicating that the amount of release agent adhered to the cavity surface generates the product release force.

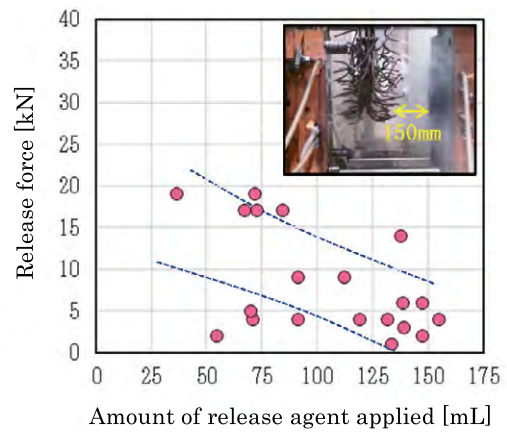


Fig.9 Effect of amount of release agent applied on release force at 150 mm spray distance

Fig. 10 shows the effect of the amount of release agent applied on the release force during spraying to a die intermediately closed by electric die clamping. The distance from the tip of the spray nozzle to the movable cavity surface is 30 mm and the spray pressure is 0.25 MPa. As the amount of release agent applied decreased, the release force also tended to decrease, which contradicted the results obtained from general spraying of Fig. 9. Therefore, we performed reproduction tests using other methods, and the results are described later.

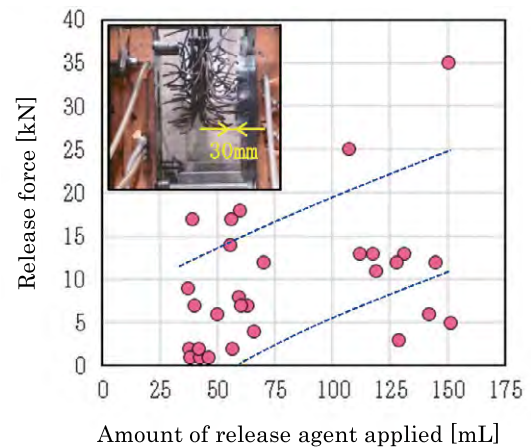


Fig.10 Effect of amount of release agent applied on release force at 30 mm spray distance

Fig. 11 shows the effect of spray pressure (release agent application pressure) on the release force. Based on the results of verification of general spraying (spray distance: 150 mm) and spraying to intermediately closed dies (spray distance: 30 mm), we applied the amount of release agent that showed a relative reduction in release force. Regardless of the spray distance, increasing the spray pressure tended to decrease the release force. In this spraying method including the shape of release agent discharge nozzle, control of spray pressure is considered to be important in addition to control of application amount in production activities.

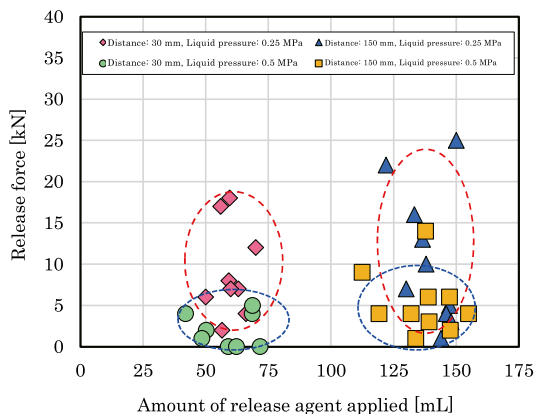


Fig.11 Effect of spray pressure on release force

Fig. 12 shows the relationship between the amount of release agent applied and die surface temperature and porosity rate inside products. In order to measure the mold surface temperature, the cavity surface of a movable die just before the beginning of die closing operation was measured with a thermocamera. It was confirmed that with the amount of release agent applied in this measurement, the amount of release agent applied does not affect the die surface temperature or the porosity rate in products, although there is variation.

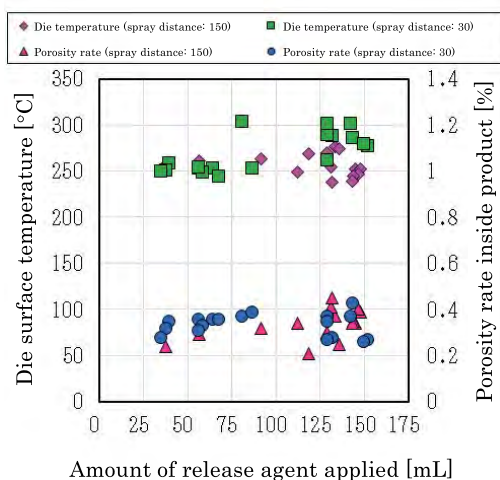


Fig.12 Relationship between the amount of release agent applied and die surface temperature and porosity rate inside products

7 Measuring Release Force with a Test Device

As a test to reproduce the results presented in Fig. 10, we investigated the relationship between the amount of release agent applied and the release force using Lub Tester U (a testing device for evaluating release agent performance) manufactured by MEC International Co., Ltd. In this method, a cylindrical ring die is placed on a steel plate coated with release agent, molten metal is poured into the cylindrical die, and the tensile load is measured with a load cell after solidification to calculate the release resistance. Table 4 shows the conditions for the release agent application. Using 12 ADC materials held at 650°C as molten metal, the iron plate temperature was

measured before and after the release agent was applied.

Fig. 13 shows the effect of the amount of release agent applied on the release resistance. As the amount of release agent applied decreased, the temperature of the steel plate before pouring tended to increase, but the release agent tended to decrease. Therefore, it was confirmed that the measurement result of release force using this device and the verification results of die-casting shown in Fig. 10 show a similar tendency.

Table 4. Conditions for app of release agent Lub Tester U

Steel plate size	200 × 200 × 30 mm
Steel plate temperature	150°C (before release agent is applied)
Release agent pressure	0.12 MPa
Air pressure	0.2 MPa
Application time	0.5 sec., 1.0 sec., 3.0 sec.
Application distance	100 mm, 200 mm
Application angle	90° (perpendicular to the surface)
Spray gun	YCD-35 by Yamaguchi Giken Co.,Ltd.
Release agent	San value Z made by Sanwayuka Industry Corporation

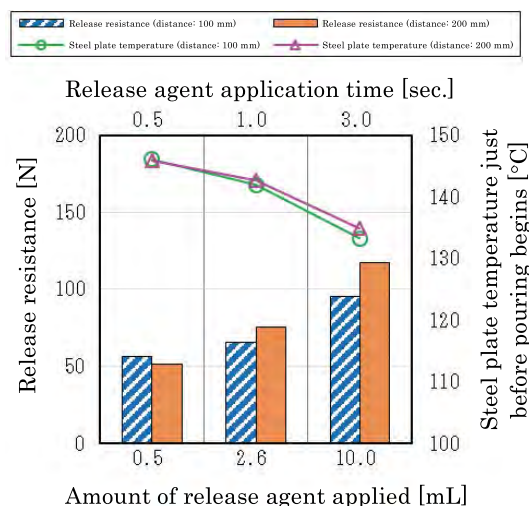


Fig.13 Effect of the amount of release agent applied on the release resistance

Fig. 14 shows the release agent pattern on an iron plate after application. (a) At a coating amount of 0.5 ml, the release agent pattern remains in the center where the ring is set, but (b) at a coating amount of 10 ml, the release agent is shifted in the peripheral direction. This indicates that even if much release agents were applied, not much of release agent actually adhered to the steel plate [3], [4] as film layers.

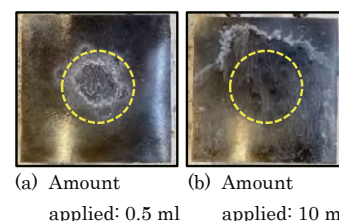


Fig.14 Release agent pattern on steel plate

8 Summary

Comparative studies were conducted on both the environmental impact and quality of the production method incorporating environmental impact-reducing elements and the conventional production method.

It was confirmed that by converting the clamping mechanism of the die-casting machine with a clamping force of 3,500 kN from the hydraulic driven type to the electric driven type, the environmental impact was reduced by about 19%. Besides, the cycle time reduced by approximately 6% (2 sec.).

The generation of porosities inside products is not affected by the drive system for opening or closing a die.

The product release force varies depending on the spray application conditions, and application after moving the die close to the spray by electric clamping reduces the amount of release agent used and cycle time (Fig. 15), making it an environmentally friendly manufacturing method.

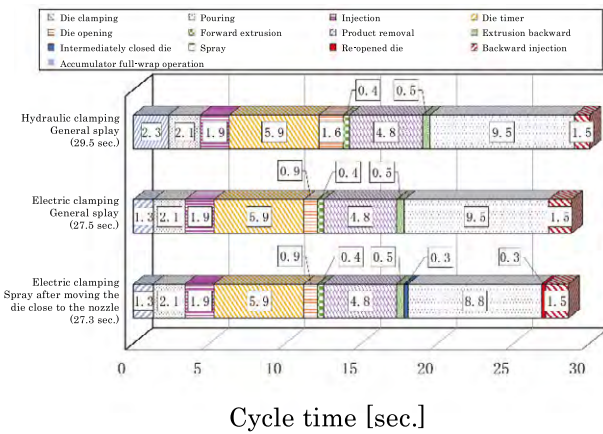


Fig.15 Comparison of each process in one cycle time

Reference

- 1 Satoshi Tomioka, Satoru Aida, and Toshiaki Toshima: Proceedings of the Japan Die Casting Congress, JD22-21 (2022) 127
- 2 Norio Shiga: Study on Die Cast Releasing, 531 (1999) 55
- 3 Naomi Nishi: Thinking about die-casting, The Die Casting News (2010) 171
- 4 Ryusuke Izawa, Koji Togawa, Hirobumi Ohira, Masanao Kobayashi, Isami Yamaguchi: Proceedings of the Japan Die Casting Congress, JD04-15, (2004) 77

Research on Causes of Defects in Transparent Resin Molding



Daisuke YOKOŌ

Metal & Plastics Industrial
Machine Company
Metal & Plastics Industrial
Machine Technology
Department

In the molding of transparent resins, defects that occur within the molded pieces but are not visible in the molding of opaque resin are treated as problematic, resulting in defective products. For the growth in productivity, it is essential to develop injection molding machines that are less prone to generating defects even in transparent resin molding. This report, being intended to determine the cause of defects generated in the molding of PMMA, a type of transparent resin molding, describes the findings regarding the conditions under which defects were observed and the phenomenon occurred within a barrel in that instance. This research was conducted as a part of the initiative by Future-Oriented Injection Molding Technologies, Social Cooperation Program of Institute of Industrial Science, the University of Tokyo.

Keywords: Injection Molding; PMMA ; visualizing barrel

1 Preface

In recent years, the automobile industry has undergone a period of significant transformation and innovation. It is expected that utilization of transparent resin will increase in the future, such as weight reduction of automobiles, higher interior design, increased use of on-vehicle sensors because of improved automatic drive technology, or enlarged on-vehicle displays. This will consequently result in rise of demand for transparent resin molding.

In the molding of transparent resins, defects that occur within the molded pieces but are not visible in the molding of opaque resin are treated as problematic, resulting in defective products. Particularly in the case of resin molding used in optical products, even minor inclusion of foreign substances or color change inside causes functional damage to the products. The quality standard in transparent resin molding is high. Hence, various efforts have been made at production sites to lower failure rate even a little and increase productivity, including strict material management and optimization of molding conditions.

This suggests that it will become more important in the future to develop injection molding machines meeting high quality for transparent resin.

This report is intended to determine the cause of defects generated in the molding of PMMA, a type of

transparent resin molding. This describes the results of our research on the conditions and factors that caused the defects by visualization analysis inside the barrel and other means, focusing on the molding defects that are believed to have occurred during the plasticization of resin.

2 Defects and problems in molding of PMMA resin

The defects that occur in PMMA molding include occurrence of black streaks (Fig. 1) and mixing of foreign substances, which are also common in normal molding processes. In addition to these, white streaks (Fig. 2) have been identified as an inherent defect to transparent resin molding, which are visible only when exposed to strong light in a dark place. Other than these defects generated in mold products, the following has been observed in the molding process of transparent resin PMMA especially. A phenomenon that extreme declines in screw rotation torque and retract speed occur during charging, and consequently destabilize charge time therefore cycle time.



Fig.1. Black streaks



Fig.2. White streaks

An investigation determined that these molding defects occur more frequently under a condition where charging becomes unstable. The condition for this was that both cycle time and charge stroke are long, which is typically set for the molding of so-called thick lenses. Therefore, we focused on cycle time and charge stroke to establish the molding conditions for the experiment in this research.

3 Experiment method

With the cooperation of Institute of Industrial Science, the University of Tokyo, the experiment was conducted by using the visualizing barrel owned by the institute. Table 1 and Fig. 3 show the specifications of the experimental device. Several parts of this visualizing barrel are of glass insert structure which enables observation of internal melting process of resin that are not visible with ordinary barrels. We installed high-speed cameras at the positions where each range of observation windows (A to F) can be observed to record resin melting processes from the start to end of charging. In addition, low-speed purging was adopted without using a mold because there was a risk that the observation window glass would not withstand injection pressure. Table 2 shows experimental conditions.

Table 1. Experimental Device

Screw diameter	36 mm
Flight pitch	36 mm
Screw groove depth	Supply zone: 2 mm Charge zone: 5.5 mm

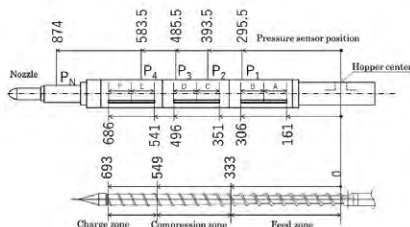


Fig.3. Positional relation between observation windows, pressure sensors, and screw

Table 2. Experimental Conditions

Resin	PMMA
Screw speed	50 min ⁻¹
Back pressure	15 MPa
Barrel temperature	Supply zone: 230°C Compression zone: 240°C Charge zone: 240°C
Cycle time	60 sec, 240 sec
Charge stroke	36 mm, 90 mm, 144mm

In light of the fact that charge/plasticization process is an unsteady phenomenon, it is necessary to employ an analysis method that facilitates comprehending the temporal change of the phenomenon. Hence, we created extended lamination images from a video recorded in the experiment. The extended lamination images were created by clipping the slit part boxed in red in the right-hand photo of Fig. 4 at optionally selected time intervals, and by laminating the clipped images as shown in the left-hand image of Fig. 4. With this method, it is possible to comprehend the temporal change inside the barrel at a glance.

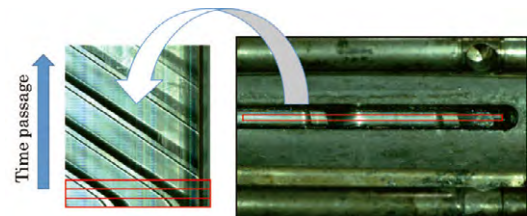


Fig.3. Extended lamination images

Furthermore, we installed pressure sensors at P2, P3, P4, and PN positions of Fig. 3 to measure the pressure change inside the barrel. We decided not to install a pressure sensor at P1 position although it was technically possible, owing to a fear of breakage caused by friction with unmelted resin.

4 Experimental results and review

Fig. 5 shows the extended lamination images of observation windows A through D from the start to end of charging under the conditions of 240 sec cycle and 90 mm charge stroke. Note that each of images from A through D in Fig. 5 shows a different shot, with not necessarily the continuity between phenomena observed from adjacent images. Fig. 6 shows pressure distribution in axial direction at each screw position during charging, Fig. 7 the relationship between screw position and charge torque during charging, and Fig. 8 the relationship between screw position and screw retract speed during charging.

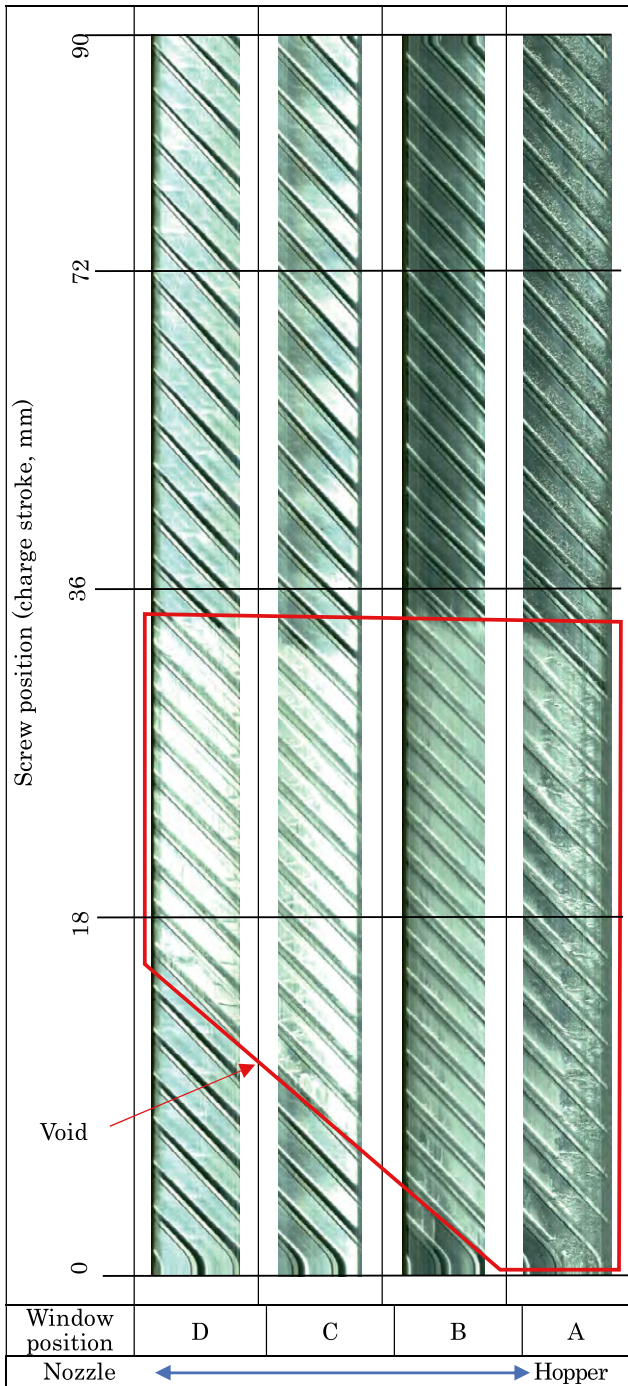


Fig.5. Visualized image inside barrel

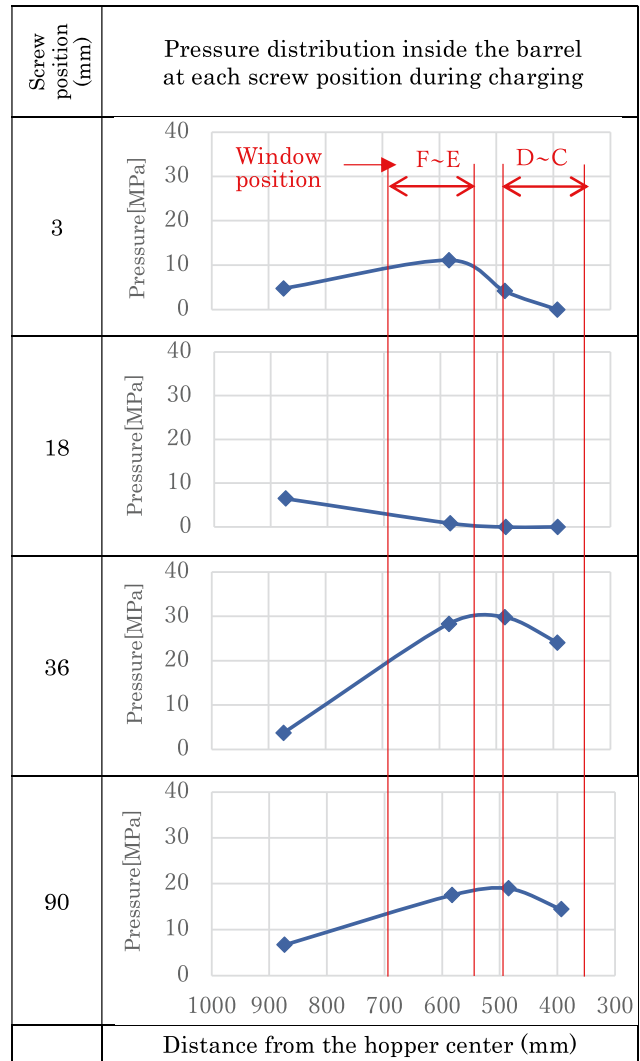


Fig.6. Pressure distribution inside barrel at each screw position during charging

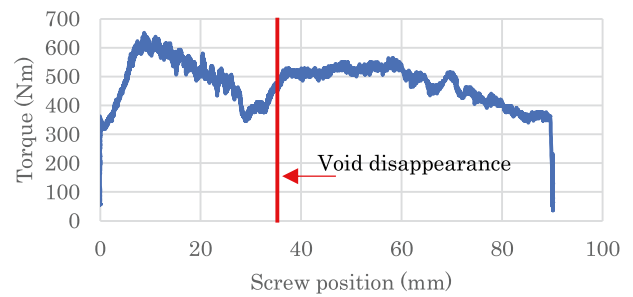


Fig.7. Screw rotation torque during charging

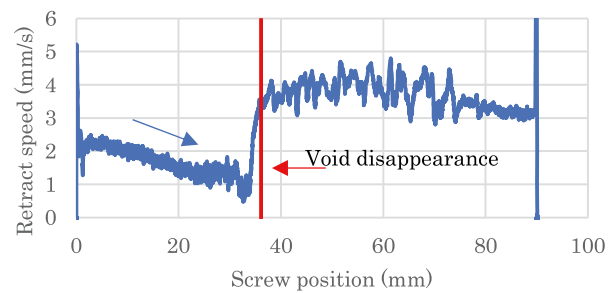


Fig.8. Screw retract speed during charging

From the visualized image of barrel inside of Fig. 5, it can be observed that the white area started to spread immediately after charging toward the nozzle from the resin melting start point in the observation window. This eventually extended to a very wide range from window A to D, and then disappeared when charging was done up to the screw position of 36 mm. Moreover, graphs in Fig. 6 corresponding to the timing at white area generation (screw positions: 3 mm and 18 mm) indicate that the pressure inside the barrel did not rise in the vicinity of hopper and rose at approximately the same time the white area disappeared (screw position: 36 mm). Based on the above, the white area is considered to be voids (or a state that is almost devoid of density). It is possible to consider that voids generated inside the barrel unfilled with resin occurred diffused-reflection of light and were observed as whitening phenomenon in the image.

Furthermore, Fig. 7 and 8 demonstrate that the screw rotation torque and retract speed declined at the time voids arose or expanded, and that they rose at the time voids disappeared. This fluctuation is considered to have occurred as a result of screw racing caused by voids generated inside the barrel, temporarily making it nearly empty.

Although voids confirmed in the study of Mr. Tatsuno [1] are not as extensive as voids observed in this research, these are viewed as the same phenomena and the cause of which is considered to be melt plugging phenomena (Fig. 9) inside the barrel. The mechanism of melt plugging phenomenon is as follows: During waiting process after charging, only the surfaces of some pellets in contact with barrel inner surfaces are melted by heat conducted from the inner face. This will form melt films which function as lubricant. Thus pellets and the barrel slip making the screw and pellets corotate, preventing pellets from being conveyed.

Although there were some differences in the extent, this type of phenomena was observed in all experimental conditions that used PMMA. Table 3 shows the generation time and the range of voids under each condition.

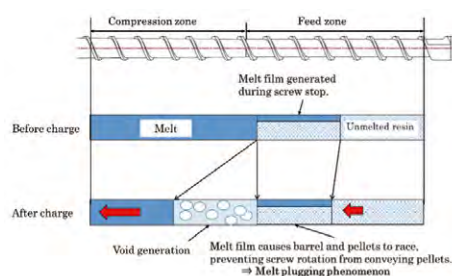


Fig.9. Void generation due to melt plugging phenomenon

Table 3. Void Generation Status on Each Condition

Conditions	Generation time (sec)	Observed from
Cycle time: 240 sec Charge stroke: 90 mm	17	A~D
Cycle time: 60 sec Charge stroke: 90 mm	2	A~B
Cycle time: 240 sec Charge stroke: 144 mm	16	A~D
Cycle time: 240 sec Charge stroke: 36 mm	11.5	A~B

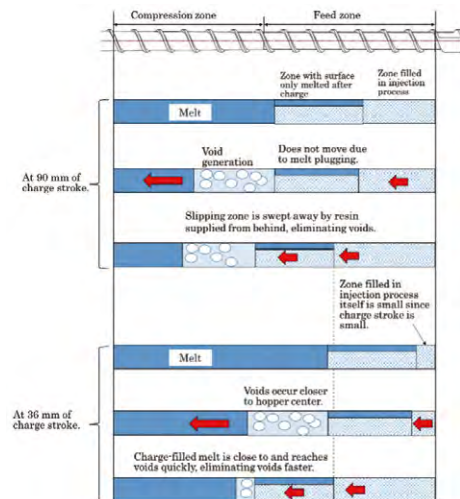


Fig.10. Difference in speed to eliminate voids due to charge stroke variation

The result of Table 3 shows that the occurrence of voids was inhibited by a large amount although it was not completely eliminated in the condition of 60 sec cycle time. This demonstrates that the cycle time (waiting process) has a great influence on the generation time and range of voids. This is considered to be by the prolonged waiting time enlarging the range of resin at the surface layer to be melted being in contact with barrel inner face.

On the other hand, while void statuses in charge stroke conditions of 90 mm and 144 mm were approximately equal, generation time in the condition of 36 mm was comparatively short. Regarding the void range, it was impossible to simply compare them since the point where resin began to melt was outside the observation windows and the entire voids could not be observed in the 36 mm condition. It is possible to consider that this phenomenon is linked to the fact that the melting start position becomes more proximate to the hopper side as charge stroke decreases. It is inferred that shortening the charge stroke relatively reduces the distance from the hopper center position to voids. This hastens sweeping the slipping zone of the resin newly supplied from the hopper and conveyed by screw rotation, resulting in the earlier elimination of voids.(Fig.10)

Based on these experimental results and the fact

that the condition consisting of long cycle time and long charge stroke is prone to defects in the molding of PMMA as discussed in Chapter 2, it is possible to judge that voids cause defective molding of PMMA. The mechanism of the cause is considered as follows.

- (1) Voids occur inside the barrel due to melt plugging.
↓
- (2) Pressure inside the barrel lowers temporarily, and flammable MMA (methyl methacrylate) gas is generated from resin.
↓
- (3) Temperature rises instantaneously by the adiabatic compression of gas at the moment of void disappearance.
↓
- (4) Black streaks occur when internal gas ignites due to temperature rise. White streaks occur when it does not ignite but remains in the molten resin.

5 Conclusion

In this research, we conducted visualization analysis by using a visualizing barrel to investigate the cause of defects in PMMA molding, a type of transparent resin molding, and finally obtained the following knowledge.

- (1) Under certain conditions in PMMA molding, voids occur over a wide range inside the barrel during charging.
- (2) Voids spread toward the nozzle from the resin melting start point.
- (3) Voids are considered to be caused by a melt plugging phenomenon, and is particularly likely to occur under molding conditions for long cycle time and long charge stroke.
- (4) The cause of the black or white streaks generated in PMMA molding is considered to be voids that occur inside the barrel.

Although not introduced in this report, we have obtained an experimental result which demonstrates that optimizing the screw shape enables suppressing the voids as a result of incorporating the findings from this research. From this, we are currently engaged in commercialization of the best plasticization unit for PMMA resin molding, and preparing to propose the best machine specifications for the molding of transparent resin.

Acknowledgments

This research is a part of the initiative by Future-Oriented Injection Molding Technologies, Social Cooperation Program of Institute of Industrial Science, the University of Tokyo. We would like to express our sincerest gratitude to Mr. Tatsuno at Institute of Industrial Science, the University of Tokyo, and Mr. Yokoi, the laboratory director of YOKOI Labo, for their great support in the usage of the experimental device as well as the review and consideration of the experimental results.

References

1. Tatsuno, Michihiro, Visualization Analysis of Reciprocating Plastication Process by Glass-Inserted Heating Cylinder. Part II : Plastication Process of Various Resins (2001), Vol. 13, No. 2, 126.

Approach to Automating of Sheet/Film Manufacturing System



Takuro KATO

Metal & Plastics Industrial
Machine Company
Extrusion Machine
Engineering Department

Abstract The sheet/film manufacturing system is composed of multiple units including extruder, T-die, polishing unit, stretching machine and winder which require different skills to operate respectively. Startup and operating condition setting of each unit in particular, are left to operator's capability and experience and tend to become personalized. Hence demands are growing to enable any operator to start production operation in a short period of time, or to realize automating and labor saving intended for mishandling prevention, skill transfer, or safety enhancement. This paper introduces the automating technology of startup and features of automating and labor saving of condition adjusting for production operation.

1 Introduction

Human resource shortage and skill transfer inability due to the retirement of experts have become serious problem in the manufacturing field. On the other hand, high quality and high productivity are demanded from the market. It is, however, difficult for inexperienced operators to achieve production operation level the same as experts. Moreover, enhanced safety is demanded for the sheet/film manufacturing system because it has many hot or rotating parts. Realization of automating and labor saving is demanded as measures for these situations.

It is expected to address human resource shortage and skill transfer, to standardize forming process for stabilization of product quality and reduction of troubles due to operation mistakes, and to secure operator's safety, by means of automating and labor saving of the sheet/film manufacturing system.

We are working on developing the technology corresponding to the automating and labor saving of the sheet/film manufacturing system to meet such demands.

2 Outline of sheet/film manufacturing system

In the sheet/film manufacturing system using extrusion (Fig. 1), the extruder melts resin, T-die spreads the melt width to discharge it in sheet shape, and rolls in the polishing and cast roll units cool and solidify the sheet.

For usage where formed sheet is stretched further, the system passes the sheet through the draw unit (stretching in sheet flow direction) and the stenter (stretching in cross direction of sheet) or the simultaneous biaxially-stretching machine (stretching in both longitudinal and cross directions simultaneously), before the winder to obtain the final product.

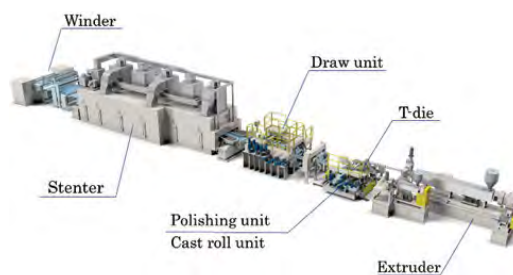


Fig.1. Sheet/film manufacturing system

3 Issues and solutions in the passing process of sheet/film forming

Sheet/film forming by extrusion has the advantage of high productivity because of continuous production. When starting up production operation, however, the system has sheet/film passing process through respective units, which requires a lot of manpower and time. This section introduces technologies recently developed, which are automatic sheet/film passing between the T-die and polishing unit and into the stenter, and automating and labor saving of the winder.

3.1 Between T-die and polishing unit

At the beginning of passing process, the operator passes the melted resin discharged from the T-die into rolls of the polishing unit. In this working, the operator handles melted resin at high temperature exceeding 200°C and works close to rotating hot rolls. Hence improving the safety is strongly expected. Usually the melted resin discharged from the T-die is passed through rolls by hand or rod, or by using a rope or guide film. When using a guide film or rope to pass the melted resin through rolls, however, fouling or scratches on rolls may be transferred to the product film.

As a measure for this, there was a need for automatic passing, but it was difficult to achieve it because of the following two reasons.

One is the difficulty in cutting melted resin. Scissors and cutters can easily cut solidified sheet/film, however, cutting the melted resin is difficult. Hence it is necessary to establish a cutting method suitable for melted resin. The second is handling the melted resin. It is necessary to establish a method for gripping melted resin of unsteady shape to carry it between rolls while cooling.

We have developed a technology to automatically cut the resin discharged from the T-die, attach the melted resin onto the carrier, and pass it between rolls with the carrier. (Fig.2) (Patent pending.)

Development is underway at our small test facility, but we plan to gradually expand the range of target resins since they are limited. For handling melted resin, the automatic gap adjusting function of the hydraulic servo system described below can be used to automate roll gap adjusting right after melt. This enables sheet condition to be stabilized quickly.

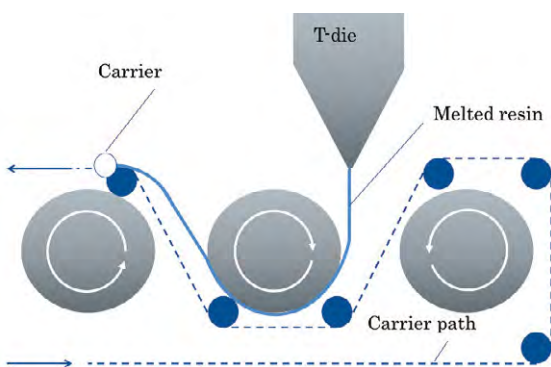


Fig.2. Polishing/cast roll unit melt passing model

3.2 Stenter

The stenter has sheet/film guide rolls at the inlet and the position of sheet/film grip to stenter clips is located at the end of the inside. Since the sheet/film is gripped with clips running from the front of the guide roll side at high speed, it is necessary to secure the safety to prevent the operator from contacting the clips.

We made it possible to pass sheet/film into the

stenter without making operator's hands close to dangerous areas, by installing the suction belt feeder shown in Fig. 3 at the inlet of the stenter.

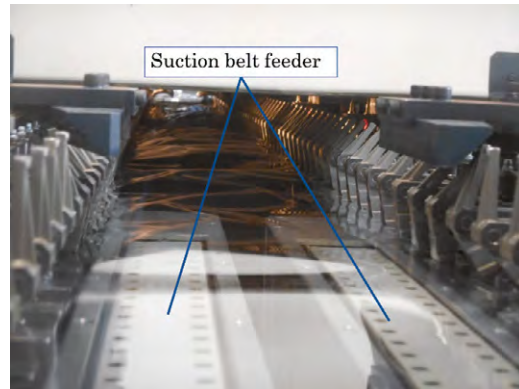


Fig.3. Belt feeder of our test stenter

As shown in Fig. 4, the suction belt feeder has a structure consisting of suction chambers connected via relief valves. The chambers change the suction range depending on the carry position of film tip, enabling stable suction and carrying the sheet/film over their entire length. (Patent No. 6212512)

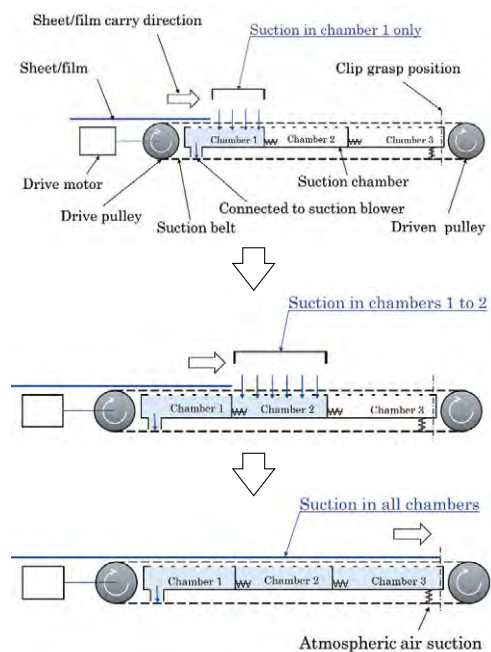


Fig.4. Suction belt feeder structure

3.3 Winder

Conventional winders automatically change winding only, while often relying on manual labor for the subsequent process.

Recently, automating and labor saving of the entire sheet/film manufacturing system has been progressing, including attaching the air shaft and paper tube and carrying wound bobbin with carry cart into an automatic warehouse.

The above sheet/film passing technology is expected to minimize the number of operators at startup. In addition even if the sheet/film manufacturing system stops temporarily because of a sudden trouble, the

system can be safely restarted by a limited number of workers, minimizing the impact of the trouble on the production plan.

4 Issues and solutions in adjusting production conditions

After sheet/film passing, the system increases forming speed and adjusts production conditions to start product take-up. Since the system is composed of a number of units to be adjusted, the time required to complete adjusting and the loss of raw material tend to vary greatly depending on operator's skill.

The following describes our automatic adjusting and operator assistance functions.

4.1 Automatic extruder startup

In some cases, the extruder is accompanied by multiple feeders, injection pumps, and gear pumps. Conventionally, operating conditions of each unit were checked in real time to change parameters when starting the extruder. Hence startup time and raw material loss depended on operator's skill level, which varied greatly.

The automatic startup system of our latest process controller, EXTVISOR-VI, pre-registers the parameters of each unit and creates recipes to enable setting changes on production conditions at the touch of a button, reducing startup time, standardizing startup operation, and reducing troubles due to operation mistakes. (Fig.5)

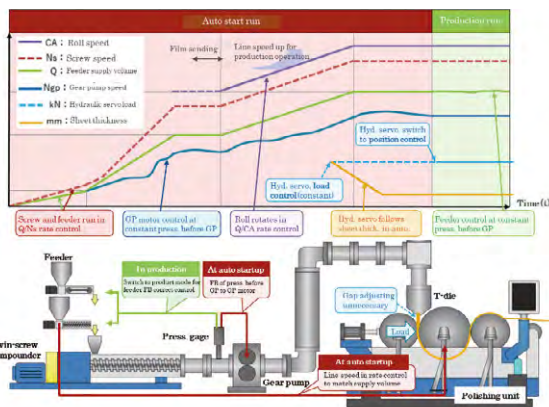


Fig.5. Automatic startup

4.2 Automatic die

Automatic die is an automating and labor-saving technology that we have been proposing for quite a while.

To make the film thickness uniform, the lip gap is adjusted by turning the T-die adjust bolts. In the case of wide T-die with a number of adjust bolts, adjust time varies greatly depending on operator's skill and experience in adjusting the thickness.

After manual rough adjusting, our automatic T-die adjusts the film thickness by feeding back the reading of in-line thickness gauge to the automatic

die and by adjusting the T-die lip gap by means of thermal expansion of heat bolts. Manual coarse adjusting can be made easily and quickly by referring to the operation guide.

4.3 Hydraulic servo

Hydraulic servo is an automating and labor-saving technology that we have proposed as well as automatic die.

Conventionally, roll gaps were adjusted by moving wedges installed between the bearings on both sides of rolls. This gap requires fine adjusting in increments of 0.01 mm, which is difficult even for skilled operators because of screw backlash moving wedges and stick-slip caused by the friction of wedges. It was necessary to fine-tune the difficult roll gaps every time the sheet/film thickness was changed. In the wedge method, pressing load by the hydraulic cylinder is applied to both the sheet and wedge. Hence the load applied directly to resin could not be measured, and thus no concept to control the load onto sheet/film existed.

We have developed and adopted a hydraulic servo type roll gap adjusting system as a roll gap adjusting mechanism. (Fig. 6)

This system is equipped with a high-precision position sensor for the hydraulic cylinder. Then a servo motor drives the bidirectional pump to enable high-precision control of roll gap. Adopting no wedge, the system eliminates occurrence of stick slip caused by friction assures excellent reproducibility. While sensitive adjusting was done in the wedge method, the servo hydraulic system sets the roll gap numerically using a touch panel and thus enables quantitative control. (Fig. 7)

Furthermore load applied to the sheet has become possible to be measured accurately with a pressure sensor equipped on the head side of hydraulic cylinder since wedges are no longer needed. It becomes possible to shift to load control which controls the load constant in changing gaps. The roll pressing load is maintained constant while enabling the roll gap follow sheet thickness change automatically.

This function automates fine adjusting the roll gap, which used to be done at every change of sheet/film thickness conditions. (Patent No. 4698334, et al.) Load is set numerically using a touch panel as with the roll gap, enabling quantitative control.

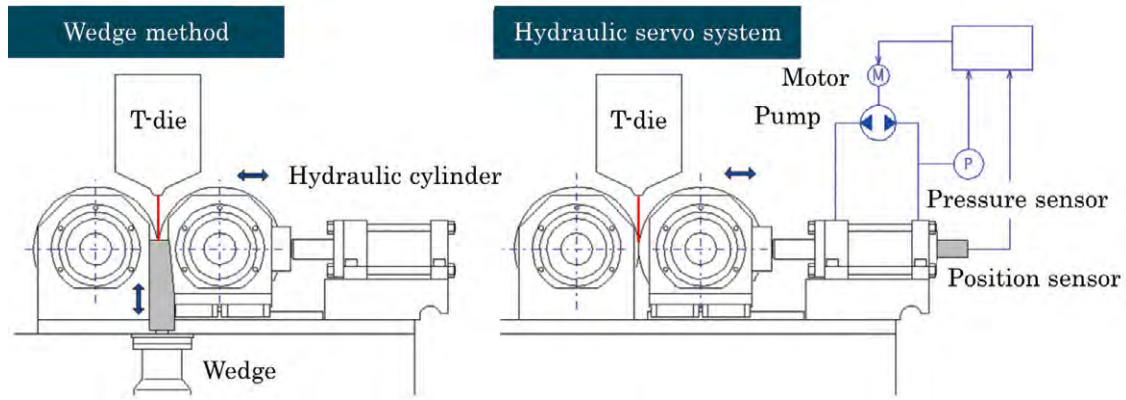


Fig.6. Comparison between wedge method and hydraulic servo system



Fig.7. Operation screen of hydraulic servo system

5 Conclusion

This paper has introduced automating and labor saving in sheet/film manufacturing system. We are convinced that the automating and labor-saving technologies we propose are effective in reducing time or material loss, preventing mishandling trouble, and improving human resource shortages, skill transfer, and safety.

We will advance the development related to the sheet/film manufacturing system to contribute to the society.

References

1. Yamaguchi, Operator Support Functions and Automating in Extrusion Manufacturing, Vol. 27 (2019) pp.12-15.
2. Ministry of Economy, Trade and Industry; Ministry of Health, Labor and Welfare; Ministry of Education, Culture, Sports, Science and Technology, White Paper on Manufacturing Industries in 2023 (Promotion of Manufacturing Infrastructure Technology in FY2022), June 2023, pp. 29

Tool Edge Position Measurement in 5-axis Indexed Machining



Yosuke HIGUCHI

Research & Development
Center
Research & Development
Department

When machining while changing the tool posture, such as in 5-axis indexed machining, the position of the tool edge (machining point) after the posture change is generally determined by geometric calculations. However, the parameters used for calculation may become incorrect due to long-time machining or changes over time. On the other hand, if the tool edge position can be directly measured with a non-contact measuring device or other means, various error amounts included at the moment of measurement can be compensated together. This report describes the process of measuring the tool edge position at any angular position and the error factors that may occur.

1 Introduction

5-axis indexed machining is a method of machining by positioning two rotating axes at any angle and controlling the remaining three orthogonal axes. Because this method is similar to the operation of conventional 3-axis machines, it is easier to use than simultaneous 5-axis machining (in which all 5 axes are controlled during machining) and has many advantages such as reduced setup work and shorter tool lengths compared to 3-axis machines.

However, indexing the machined surface by rotating axes necessarily involves coordinate transformations and offsets. In such cases, it is common to use the coordinate rotation function of the CNC or to calculate the offset amount by a program and apply it to the coordinate system. However, these calculations include calculation terms that refer to positional errors of the machine's rotation axes that have been measured in advance. These error amounts are known to change with machine aging and temperature changes during machining, and users take countermeasures by adjusting the error amounts through automatic measurement before machining.

On the other hand, some machine tools have a function to change the tool axis to a specific angle by replacing the attachment, which is the part where the tool is mounted. Depending on the workpiece to be machined, different types of attachments are used for different machining operations. However, if the dimensional difference between attachments cannot be accurately controlled, unintended steps

may be resulted on the machined surface.

In order to solve such problems, we propose a method of identifying and correcting the 3D position of the tip of a tool that needs to be offset by applying a non-contact tool measuring device. By directly detecting the tool center point position, it is possible to determine the amount of error, including the displacement that occurs in the spindle, attachment, and machine structure in which the tool is mounted. This report describes the process of measuring the tool edge position and the error factors that need to be addressed.

2 Features, Configuration, and Measurement Method of Measuring Equipment

2.1 Features of Measuring Equipment

This report uses a non-contact tool measuring device, Dyna Line manufactured by Big Daishowa. The main feature is the T-shape arranged two linear CMOS image sensors (Fig. 1). Following the instruction manual, hereinafter the horizontal line element is referred to as the X-axis sensor, the vertical line element as the Z-axis sensor, and these line-shaped image sensors as the line sensors. The line sensors detect the shadow cast by a tool by using the light projected from the LED light source to determine the presence or absence of the tool. The line sensors have the following three measurement functions. Each measurement function operates separately on the X-axis and Z-axis sensors.

- ① SKIP signal output
- ② Scan measurement (precise measurement with the image sensors)
- ③ Focal value measurement (focusing of the tool)

The SKIP signal is output to the machine tool at the moment when the tool interrupts the line sensor, and the NC machine tool is equipped with a function to record the coordinates and stop the machine at the time this signal is received.

2.2 Configuration

Among our lineup of machine tools, we have a double-column machining center equipped with a 5-axis head as a model that can perform 5-axis indexed machining. In this report, we configured measuring equipment for the MPC-H, a double-column machining center that can be equipped with a 5-axis head attachment, and verified the measurement.

The 5-axis head of MPC-H is a spindlehead swivel type attachment with two rotating axes (B/C-axes). In order to follow the tool posture changed by the B/C-axes, a swivel axis (hereinafter referred to as CT-axis) is also provided on the measuring device side (Fig. 2). The CT-axis controls the approach direction of the tool center point viewed from the measuring equipment. By applying coordinate rotation, measurement can always be performed with a movement command in the same direction as viewed from the measuring equipment.

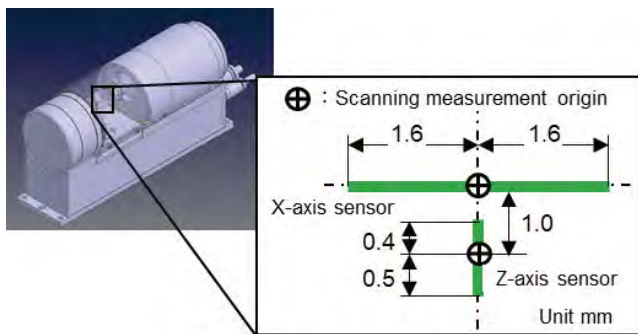


Fig.1. Measurement scope

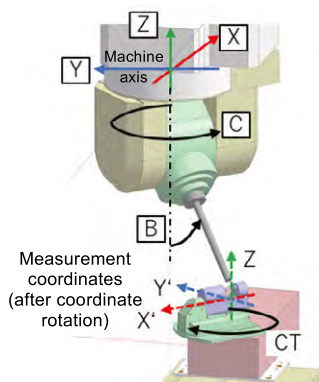


Fig.2. 5-axis head and measuring device swivel axis

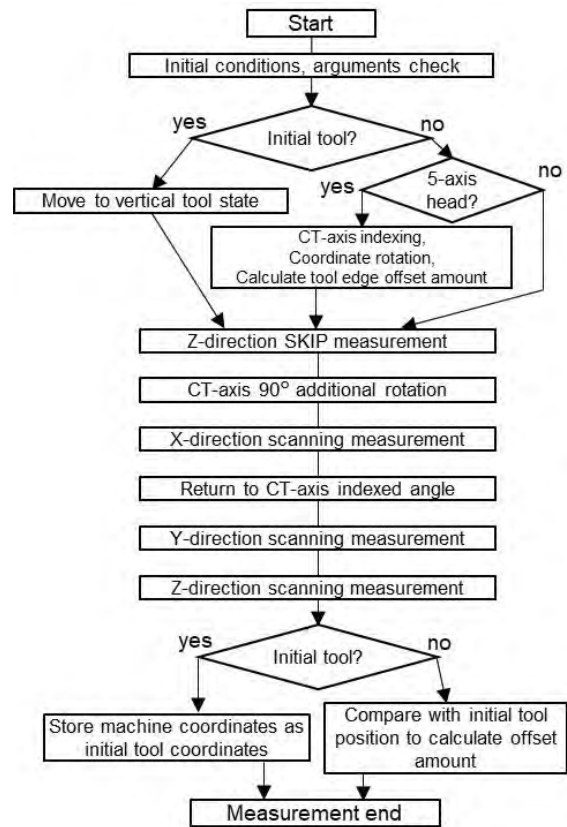


Fig.3. Measurement flow

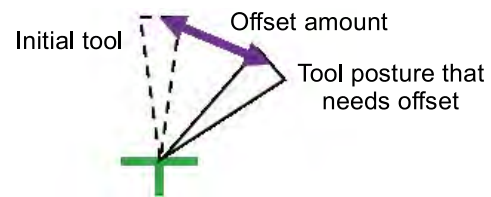


Fig.4. Offset amount

2.3 Measurement Method

To execute measurement operation, a measurement program was created using the G-code functions, which give various commands to the machine tool, and the custom macro functions, which command calculations and conditional branching, and then executed. The main measurement flow is shown in Fig. 3.

The initial tool, which is used as a reference for the offset amount, is assumed to be the vertical tool state. For example, using the vertical tool state (B0. C0.) of a 5-axis head as the initial tool, first store the machine coordinates when the line sensor and the tool center point are aligned. Next, after moving the B/C-axes to any tool angle, similarly obtain the machine coordinates when the line sensor and the tool center point are aligned in the same way. In this way, you can calculate the amount of offset of the tool center point due to the B/C-axes movement (Fig. 4).

3 Verification and Consideration

3.1 Method and Result of Verification

To verify the offset amount obtained from the measurement, machining was actually performed and evaluated. The following verification machining was performed assuming that the method of evaluating the relative positions of the surfaces machined with the B/C-axes of the 5-axis head changed and the step between them was appropriate. The target verification result was set that the step between the surfaces machined facing the same direction was within $\pm 5 \mu\text{m}$ relative to the reference surface (total step within $10 \mu\text{m}$).

Processing Procedure

- ① Change the tool to Tool 1.
- ② Machine the reference plane (red parts in Fig. 5) in the posture of B0C0.
- ③ Measure the tool center point position with the B/C-axes angles changed.
- ④ Flatten the specified area.
- ⑤ Repeat the steps ③ to ④.
- ⑥ Change the tool to Tool 2, and repeat the steps ③ to ④.

Machining Conditions

Tool 1: $\phi 12$ ball end mill

Tool 2: $\phi 8$ ball end mill+

S8000, F1500, cutting depth 0.1 mm, AICC2 during machining

Machining angle: B0,5,10,15 C0,90,180,-90

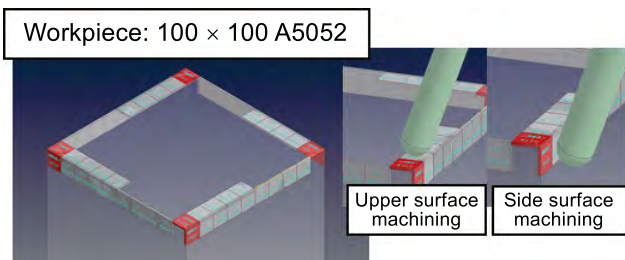


Fig. 5. Verification machining workpiece

The step between the machined surfaces was measured with a touch pointer attached to the spindle. The following table summarizes an example of the verification machining results.

Table 1. Verification machining result 1 (without CT-axis rotation error correction)

		Unit μm				
	Target	Upper surface	+X side surface	+Y side surface	-X side surface	-Y side surface
max.	$5 \geq$	10	3	0	9	5
min.	≥ -5	-4	-11	-6	0	-2
Δ	$10 \geq$	14	14	6	9	7

The maximum value of $10 \mu\text{m}$ for the upper surface direction is considered to be caused by chips adhering to the tool prior to the measurement of the tool center point, since there is no reproducibility in the location where this occurs and it always appears as a positive value through several verification machining operations. Since a certain pattern was observed in the results of the side surfaces, we decided to proceed with the verification with the assumption that this was caused by the error described below.

3.2 Causes of CT-axis Rotation Error and Its Countermeasures

Detailed examination of the machining results brought an expectation of a relationship between the CT-axis angle at the time of tool center point position measurement and the step between the machined surfaces. Therefore, we investigated the positional relationship between the CT-axis rotation and the line sensor (Fig. 6). Because it is difficult to mechanically adjust the center of rotation of the CT-axis and the center of the line sensor to align them, the error amount from the center of rotation of the CT-axis to the line sensor was recorded, and the line sensor position at any CT angle was calculated by performing 2D coordinate rotation calculation.

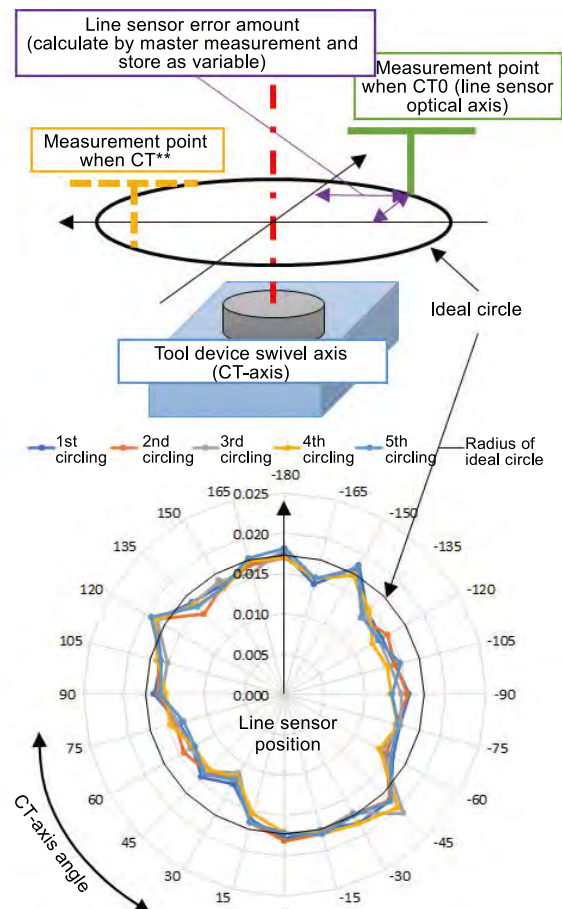


Fig. 6. Line sensor ideal turning trajectory and actual turning trajectory

However, when the position of the line sensor was actually measured, it was found that the trajectory was not ideal as expected from the correction calculation, and an error of several μm was found to occur depending on the rotation angle. This error was considered to be a CT-axis rotation error, and the following verification was conducted to investigate the cause.

- ① Readjust the components to investigate whether the cause is an assembly error or not.
- ② Investigate the runout of the upper surface of the rotary table and its effect on the measuring section (line sensor).

With regard to ①, the components of the measuring device were reground to adjust the parallelism, etc., and then the CT-axis rotation error was measured again. However, the same error trend was still observed after the adjustment, suggesting that the effect of the assembly error was small.

With regard to ②, a high-precision rotary table unit was incorporated in the device as the mechanism that swivels the measuring equipment. The runout of the upper surface of the rotary table due to swiveling was measured to be $\pm 1 \mu\text{m}$, which is sufficiently accurate as a purchased part from a practical standpoint. However, when the calculation was made taking into account the height from the upper surface of the rotary table to the line sensor, which performs the measurement, it was found that the runout increased to several μm there.

From the results of ① and ②, the cause of the CT-axis rotation error is considered to be the expanded effect of the rotary table upper surface runout due to the height of the line sensor from the upper surface.

It was found that the error was caused by the rotation mechanism, but it is not practical from a cost standpoint to purchase or fabricate a rotation mechanism that can reduce the error to near zero. On the other hand, measuring the CT-axis error several times showed that the magnitude of the error and the angle at which the error occurred had a reproducibility. Based on these results, a measure against CT-axis rotation error was developed by storing a data table of CT-axis angles and error amounts in the machine and adding a program to apply the data table to offset calculations.

3.3 Result of CT-Axis Rotation Error Correction

A data table was set up to provide a correction for CT-axis rotation error, and the effect of the correction was evaluated by verification machining similar to that in 3.1. Table 2 shows an example of the results obtained by applying the CT-axis rotation error correction.

Table 2. Verification machining result 2 (with CT axis rotation error correction)

		Unit μm				
	Target	Upper surface	+X side surface	+Y side surface	-X side surface	-Y side surface
max.	$5 \geq$	3	3	4	4	3
min.	≥ -5	-4	0	0	0	-1
Δ	$10 \geq$	7	3	4	4	4

By applying the data table to correct the CT-axis rotation error, the verification goal was achieved in all aspects.

4 Conclusion

The achievement of the verification target in 3.3 proves that correction by tool edge position measurement using a non-contact tool measuring device can be performed with sufficient accuracy for practical use. In addition, we were able to demonstrate the effectiveness of the correction data table as a measure against errors that occur in the measuring device swivel axis, the CT-axis.

References

1. BIG DAISHOWA Japan CO., LTD., Dyne Line optical line sensor type tool measuring equipment website, https://www.big-daishowa.co.jp/products/product_detail.cgi?_rid=101

Introduction of Elemental Technologies for Achieving Skill-less Grinding



Shintaro KODAMA

Machine Tools Company
Machine Tools Engineering
Department



Masahiko FUKUTA

Machine Tools Company
Machine Tools Engineering
Department

Focusing on setup works, the quality of which tends to vary depending on the worker's skill, among ultra-precision mold machining processes, we studied automated technologies for workpiece centering and grinding wheel contact checking. We have realized a workpiece centering system that enables independent of the worker's skill by controlling the CNC, measuring probe, and hammering piezo actuator, and a grinding wheel contact checking system that prevents excessive cutting and reduces air cutting without relying on the sense of a skilled worker by high-speed, high-precision analysis of spindle behavior at the time the grinding wheel makes contact with the workpiece to calculate the contact position. Furthermore, both of these systems are designed to perform measurement and analysis in-process, which allows them to be applicable to expanded usages, such as centering of rough-surface or imperfect-circle workpieces and checking of contact with free-form surfaces.

1 Introduction

Ultra-precision machines have been developed and commercialized from the 1980s. Since 2000, linear motor drive technology and other technologies have enabled them to achieve positioning accuracy of 1 nanometer, and sub-nanometer roughness and shape accuracy of several tens of nanometers have become possible. These technologies are now being applied to the processing of optical component molds, including molds for lenses mounted on smartphones etc., but the life cycles of such products are short and there is a constant demand for more functional components. For this reason, such processing requires advanced processing technology and skilled machine operation, and therefore, issues such as skill training and a shortage of human resources have been pointed out.

In the case of grinding automotive lens molds, high precision machining of a small quantity of various shapes is required, and therefore, the setup skill is one of the important factors. First, since commercially available chuck systems do not provide sufficient workpiece mounting accuracy, manual centering is often required. Highly skilled workers can perform the centering in a short time, but some workers require a lot of time and even cannot adjust the workpiece to the required position. The next process is to check the contact of the grinding wheel. The grinding process using a fine-grained grinding wheel

is sub-micrometer cutting, so the contact detection is difficult with AE sensors or the like, and checking of the contact visually increases the checking time or causes risk of damage to the grinding wheel due to contact load, depending on the skill level of the worker.

In this paper, we focus on the workpiece centering and contact checking, which may become an issue, and report the results of our study on skill-less technologies to support workers.

2 Automatic Workpiece Centering

2.1 Conventional Workpiece Centering and Its Issue

Molds for lenses, which are rotationally symmetrical in shape, are cut by turning. Therefore, before cutting, centering of the workpiece to align with the center of rotation of the work spindle based on the workpiece edge is necessary. The workpiece centering by a worker consists of the following steps: hold the workpiece on the vacuum chuck located on the spindle end face with vacuum pressure, check the edge runout of the workpiece using a dial gauge or the like while rotating the workpiece, and hammer an appropriate position of the workpiece to adjust it so that the runout becomes within the allowable error range. The allowable runout error is approximately 2 to 3 μm for general molds, and 0.1 to 0.2 μm for optical component molds, which require high

accuracy. Compared to the demand for cutting, there is a great shortage of skilled workers who can finish the centering work in a short time. Therefore, a skill-less system that enables even inexperienced workers to perform stable workpiece centering is required.

2.2 System Configuration

To solve this issue, we developed an automatic workpiece centering system. Fig. 1 shows the system configuration, and Fig. 2 shows the external appearance of the system during the operation test.

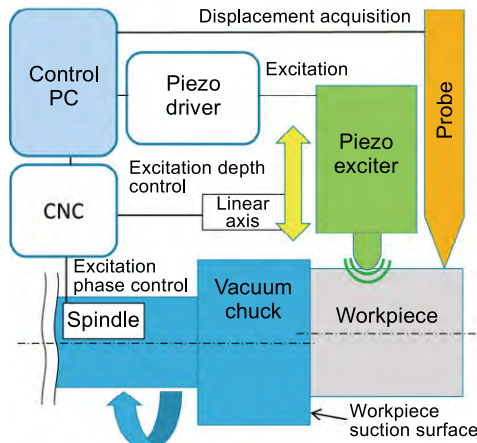


Fig.1. Configuration of automatic centering system

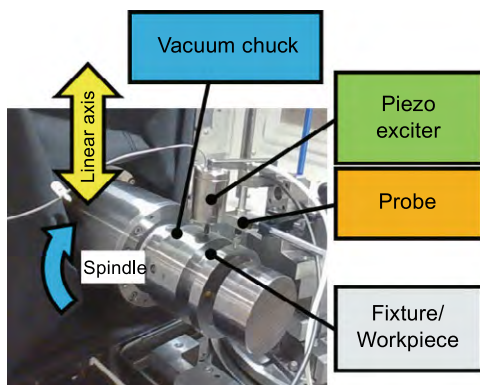


Fig.2. System appearance

This system is a CNC lathe having the work spindle equipped with a rotary positioning function consisting of a piezo actuator that strikes the workpiece and a probe that measures the workpiece runout. The workpiece centering process is controlled by a PC that communicates with the CNC and provides necessary axis movement instructions. In an operation test using a workpiece weighing approximately 5 kg, this system achieved a residual runout of 1.4 μm (excluding roughness) in 4 minutes and 20 seconds of operation time from the initial state with a runout of 130 μm . With the conventional centering method, which presses the machine linear-motion axis directly against the workpiece on the vacuum chuck and moves the workpiece in the direction to correct the error, the amount of movement of the linear-motion axis cannot be equal to the amount of

movement of the workpiece for the following reasons, making accurate positioning difficult.

- ① Until the workpiece begins to slide, a large load is placed on the servo amplifier due to static friction.
- ② Once the workpiece starts sliding, transition to the dynamic friction region where the friction force is smaller occurs and the workpiece slides a large distance at a time.
- ③ The force from the linear-motion axis is lost and returning to the static friction region occurs.

The steps ① to ③ occur repeatedly.

The developed system can, despite having a short stroke of about 30 μm , efficiently transfer impact force to the workpiece by excitation using a piezoelectric actuator according to the procedure shown in Fig. 3. The workpiece movement is minimized in the static friction region and can be made with a small load in the dynamic friction region. However, since the discrepancy between the amount of linear-motion axis movement and the amount of workpiece movement still remains, the correction is made in installments while measuring the correction results, rather than correcting all of the residual amount of workpiece runout at once.

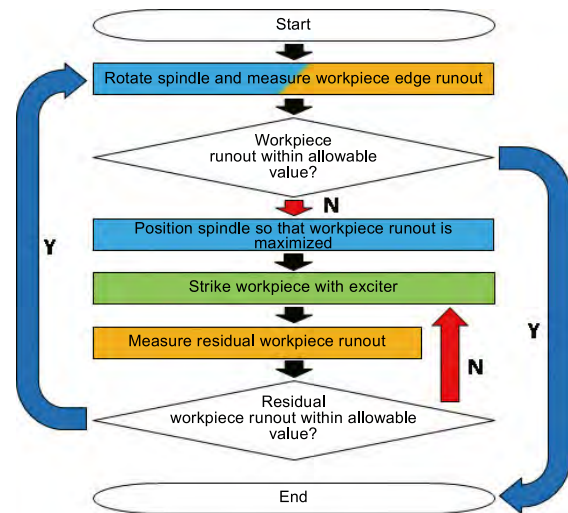


Fig.3. System operation flow

2.3 Efforts to Improve Centering Accuracy

To improve the centering accuracy of this system, the following efforts were made.

- ① Calibration of measurement position and striking position

Due to the fact that the workpiece runout correction is performed while measuring the residual amount of workpiece runout, and due to the overall machine configuration and stroke limitations, the probe and exciter of this system are in phase in the spindle angle direction, but they are offset in the spindle axial direction. With this arrangement, the cross section of the workpiece to be measured by the probe and the cross section of the workpiece to be struck by the exciter are not the same. Therefore,

there is an effect of the coaxiality and cylindricity of the workpiece, so the distance between the exciter and the striking position fluctuates depending on the spindle angle. To address this, the system stores the value pairs of the spindle angle (excitation phase) and linear axis position (excitation depth) when the exciter strikes the workpiece. In trials where three or more value pairs are stored, as shown in Fig. 4, the cross section of the workpiece at the strike position can be calculated using the contact history between the workpiece and the shaker, and the depth of excitation at which the exciter and workpiece come into contact can be predicted. As a resulting effect, even when the residual workpiece runout is less than a few μm , the possibility of the runout correction amount exceeding it is reduced.

② Removal of workpiece surface shape component

The runout measurement of an ideal workpiece with a perfect circle in the cross section of the measuring section results in a sine curve with the spindle angle on the horizontal axis and the amount of runout on the vertical axis, and the equation (1) holds in this case.

$$\rho_{ideal} = \alpha \cos(\theta - \beta) \quad (1)$$

ρ represents the measured amount of workpiece runout with respect to the spindle angle, θ the spindle angle ($0 \leq \theta \leq 2\pi, [\text{rad}]$), α the maximum amount of workpiece runout, and β the spindle angle at which the workpiece runout is maximum ($0 \leq \beta \leq 2\pi, [\text{rad}]$).

In reality, the workpiece has a unique surface shape (waviness, roughness), which appears as an error component. When this is represented by a function $f_{(\theta)}$ with respect to θ , the equation (2) holds.

$$\rho_{real} = \alpha \cos(\theta - \beta) + f_{(\theta)} \quad (2)$$

Therefore, when the population of ρ_{real} is defined with a sufficient number of θ sampling points, the function fitting with parameters α and β can be calculated so that the sum of the squares of the residual $f_{(\theta)}$ is minimized. This method can be applied even when some θ cannot be measured with a probe, as in the case where there is a D-cut, which is partially notched to avoid interference with the lens barrel during the assembly process, in the measurement cross section.

This system uses this method to detect the "ideal cross-sectional shape that can be regarded as a perfect circle with the surface component of the workpiece removed" as shown in Fig. 5.

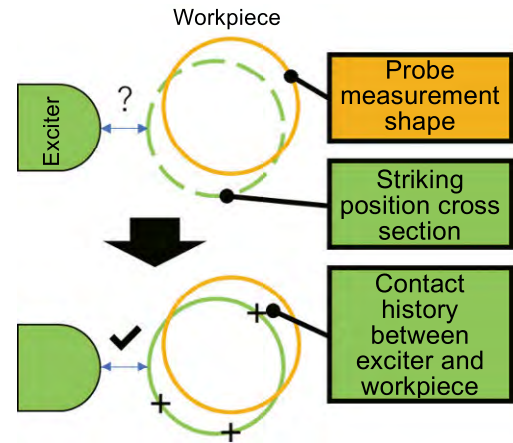


Fig.4. Detection of ideal cross section shape

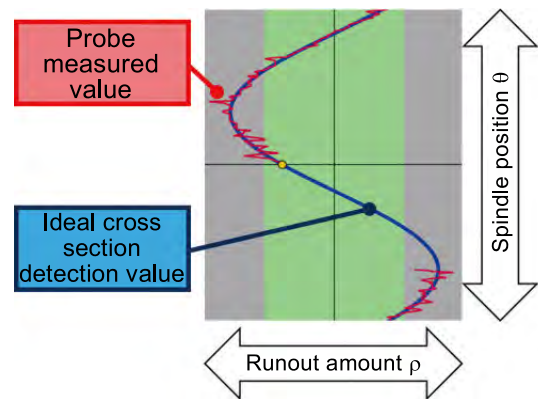


Fig.5. Difference between probe measurement cross section and strike cross section

3 Automatic workpiece contact checking

3.1 Conventional Contact Checking and Its Issue

The machining of optical lens molds often uses small and fine-grained grinding wheels with a diameter of 10 mm or less and a granularity of #3000 or finer. In addition, since the machined shape is a curved surface, properly setting the machining start point where the grinding wheel first makes contact is an important setup work to achieve efficient machining and good machining quality. In the case of sub-micrometer cutting, generally known wheel contact detection methods such as AE sensors do not provide sufficient contact signals, so the contact is judged by visually capturing slight changes in spindle behavior while manually rotating the grinding wheel. Therefore, workers may not be able to identify the contact sufficiently depending on their skill level, resulting in increased checking time and the risk of damage to the grinding wheel due to contact load.

3.2 System Configuration

In order to obtain a high-quality machined surface, tool spindles mounted on ultra-precision machines employ aerostatic bearings and use motors and drivers capable of high-precision rotation speed control. The developed system, shown in Fig. 6, enables high-speed detection at the time of contact by detecting the pulse signal used to control the

rotation speed with the spindle maintained at a lower speed than usual. In addition, by incorporating this signal into the high-speed skipping operation, a fixed cycle of the approach of the grinding wheel, contact detection, and avoidance operation is established, enabling automation of contact checking at any position.

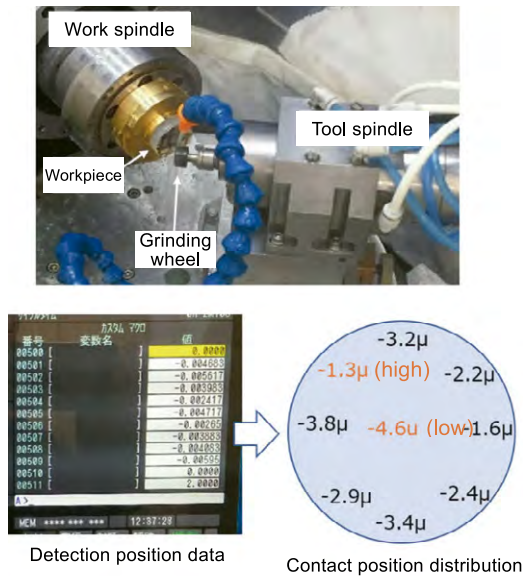


Fig.6. Automatic contact checking system

3.3 Extended Application to Free-form Surfaces

Tool scanning paths in machining are generated using our proprietary software. Since information such as tool trajectory and contact position with the workpiece can also be obtained, it is possible to calculate the contact position of the grinding wheel on the free-form surface. This means that by registering theoretical positions on a free-form surface in advance, it is possible to automatically check contact at multiple locations. Figure 7 shows an example of contact position detection. The highest and lowest positions can be determined, and the machining start point that minimizes air cut and the total depth of cut required for machining the entire surface can be recognized automatically.

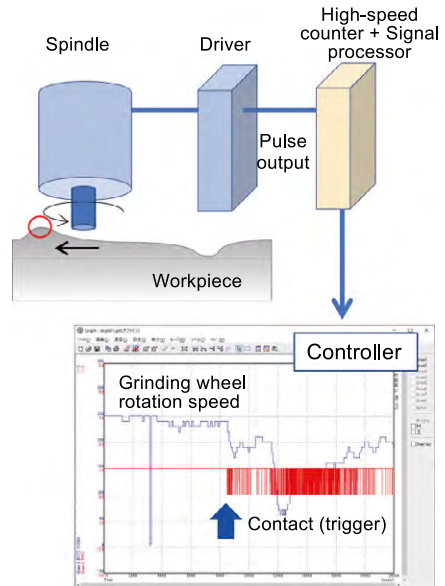


Fig.7. Example of free-form surface contact position detection

4 Conclusion

This paper introduced a skill-less technology that focuses on setup works in grinding processes. While processing quality will continue to become more sophisticated in the future, the shortage of human resources and the transfer of technical skills will continue to be issues that must be addressed. To deal with these issues, we would like to contribute to our customers by proposing skill-less technologies that take advantage of the characteristics of our processing machines.

Construction of Logistics Line with Logi Robo Series



Yasuharu SASAKI

Control Systems Company
System Engineering
Department

At work site of in-factory distribution in manufacturing industry, manual operations constitute the majority. The manual operations include loading and unloading operations, an unpacking operation, and the like. The loading and unloading operations are hard work of carrying a heavy load, and the unpacking operation has a risk of injury such as cutting fingers with a cutter. To automate these operations, our company has commercialized a robot system “Logi Robo series” for logistics sites. The Logi Robo series is classified into two types: a palletizing system “Logi Robo SP” for loading and unloading; and an unpacking system “Logi Robo TC/FC” for unpacking operation. Both the systems have high reliability by adopting a new model SCARA robot THE1000/TS5000 and are designed by taking operation environments into consideration to achieve space saving, handling of multiple types, and high usability. In this paper, these two types will be introduced.

1 Introduction

While automation (FA) of a factory production line in manufacturing industry has been advancing, operations at production/logistics sites, such as a receiving operation of raw materials and parts, a feed operation to a production line, and a shipping operation of finished products, are mainly manually carried out due to restriction in space and necessity of handling wide variety of loads. For example, loading and unloading operations are hard work of carrying a heavy load, and an unpacking operation has a risk of injury such as cutting fingers with a cutter due to lacking in concentration in repetitive opening operations. Further, due to recent labor shortage and a growing need of shifting to a non-contact/non-interactive operation manner as a countermeasure against infectious disease, such burdensome operations at production/logistics sites are strongly required to be automated and/or robotized [1]. Under such circumstances, our company has commercialized our own robot system “Logi Robo series” for logistics sites. The Logi Robo series is classified into two types: a palletized system “Logi Robo SP” for loading and unloading; and an unpacking system “Logi Robo TC/FC” for unpacking operation. The following describes basic structures, features, and introduction effects of the Logi Robo SP and Logi Robo TC/FC.

2 Palletizing Robot “Logi Robo SP”

2.1 Basic Structure and Palletizing Operation

Fig. 1 illustrates the outer appearance of Logi Robo SP (SCARA robot type Palletizing system). Logi Robo SP is constituted of a vertically movable SCARA robot having a SCARA robot mounted to an elevating orthogonal robot and a thin-type electric turntable mounting a pallet thereon. SCARA robot and turntable are disposed such that a pallet held by the robot reaches at least a part of the turntable.

COMPO ARM BE60G is adopted for the orthogonal robot, and THE1000 is for the SCARA ROBOT. Our COMPO ARM BE60G and THE1000 are the latest ones and have high reliability, whereby a maximum load capacity of 20 kg (except the hand part) is achieved. The Low back pain prevention guidelines in the workplace by the Ministry of Health, Labor and Welfare specify that the weight of a load that can be carried by a woman is 24% or less of her weight and less than 20 kg. That is, our Logi Robo SP can sufficiently handle the weight of a load treated in the site.

As a stacking/placing range, a standard pallet size (1,100 mm × one pallet) is assumed, but two pallets and special pallets can be dealt with as options.

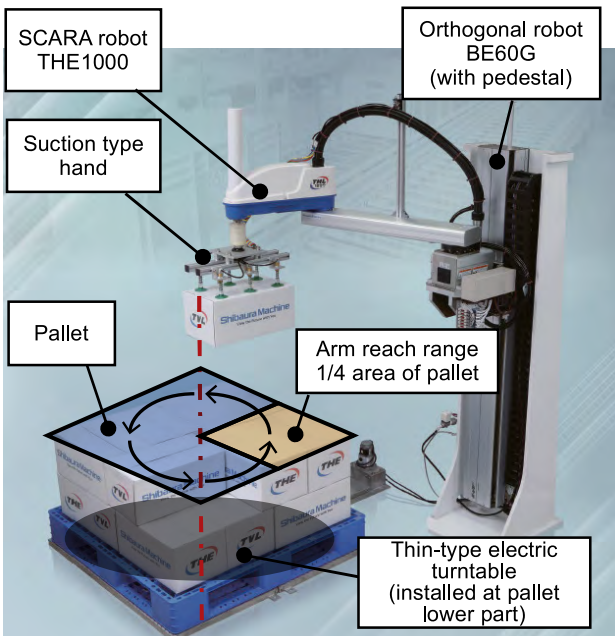


Fig.1. Outer appearance of Logi Robo SP

A suction type as illustrated in Fig. 2 is employed as the hand. The top surface of a load is held at six suction cups with plungers, whereby stable conveyance can be achieved even for a slightly deformed load and for a case where a space between stacked loads is narrow.

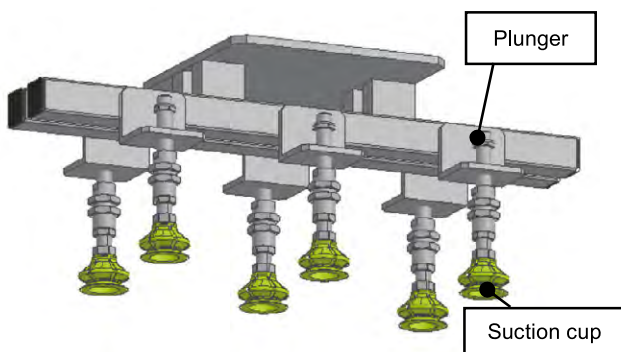


Fig.2. Hand structure of Logi Robo SP

The stacking operation will be described using Fig. 3. First, loads are stacked on an empty pallet in a reachable range of the robot arm. Then, after stacking in 1/4 area is completed, the pallet is rotated 90 degrees by the rotation of the turntable. Then, after stacking in 1/4 area is completed again, the pallet is rotated 90 degrees again. That is, after stacking of a certain number of boxes is completed, the pallet is rotated 90 degrees. The boxes are stacked on the pallet while this operation is repeated. In depalletization, the boxes are unloaded from the pallet in the reverse procedure.

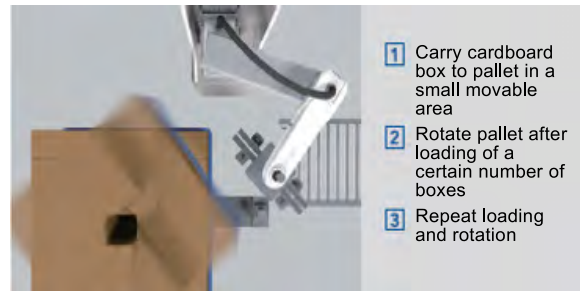


Fig.3. Stacking operation

2.2 Features and Introduction Effects

The above-described unique structure is adopted for Logi Robo SP to achieve excellent features, and various introduction effects are expected when it is introduced to a production/logistics site.

① Space saving

With the above-described structure combining the vertically movable SCARA robot and electric turntable, Logi Robo SP can cope with a standard pallet size of 1,100 mm with a reach of 1,000 mm. Thus, the installation space is about 2,200 mm × 2,500 mm. On the other hand, a conventional vertically articulated four- to six-axis palletizing robot has a reach of 2,000 mm or more, so that an installation space of about 2,500 mm × 5,000 mm is assumed to be required. Fig. 4 illustrates a comparison of the installation space between Logi Robo SP and the conventional palletizing robot. Logi Robo SP only requires an installation space not more than half of that the conventional palletizing robot requires, thus significantly reducing the installation space.

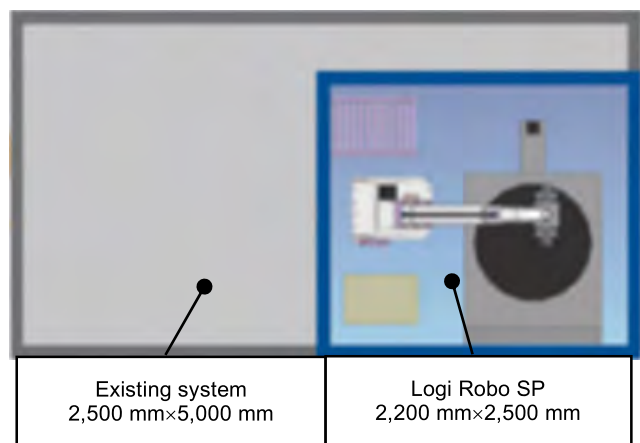


Fig.4. Comparison of installation space

② High throughput

The Logi Robo SP uses SCARA robot to perform high-speed turning operation and completes one conveying cycle (operation from holding of one load to holding of subsequent one load) in about 10 sec at the shortest. Further, interlock control is established by making use of an external interface to check presence/absence of a load to be fed to a feed conveyer or the holding state of a robot hand, thereby achieving flexible synchronization with an existing

line.

③ Handling of multiple types

Logi Robo SP can previously store therein the type of loads of different sizes or weights and how to arrange loads to be stacked on a pallet, called "loading pattern". Fig. 5 illustrates typical loading patterns. At operation time, when only the load type and loading pattern are selected on a touch panel, palletizing operation is automatically started. The suction type hand has a variable pitch structure, and adequately designing the pitch of the suction cups can eliminate the need of type-based hand exchange or adjustment.

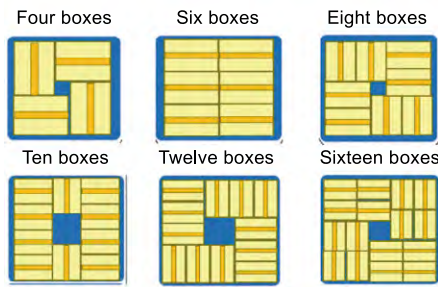


Fig.5. Typical loading patterns

④ Usability

Logi Robo SP is designed by taking into consideration simple operability on the touch panel, as well as facilitation of pallet exchange.

Fig. 6 illustrates our own thin-type electric turntable. As a result of compactly designing a transmission mechanism to the turntable and a load support structure, a maximum load capacity of 800 kg has been achieved, and the thickness of the turntable has been reduced to 35 mm. In addition, a slope is installed as an option to allow even a powerless worker to easily exchange a pallet by using a hand lift.

Further, since no obstacle is present around the electric turntable, the access direction to the pallet to be exchanged can be freely selected. This can achieve an optimum workflow line according to the installation layout at the work site.

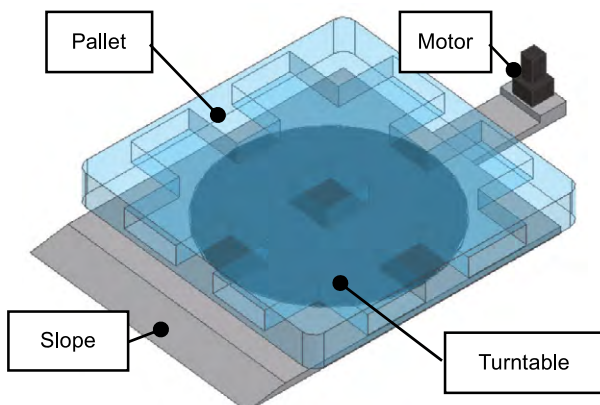


Fig.6. Electric thin-type turntable

3 Unpacking Robot "Logi Robo TC/FC"

3.1 Basic Structure and Unpacking Operation

Fig. 7 illustrates the outer appearance of Logi Robo TC/FC (Tape cutting system/Flap cutting system). Logi Robo TC/FC has three blade-equipped SCARA robots THE1000 arranged in the conveyor traveling direction. The unpacking operation for a cardboard box conveyed on the conveyor includes in the order mentioned below: cutting a top surface tape, opening/cutting outer flaps (outer lids), and opening/cutting inner flaps (inner lids).

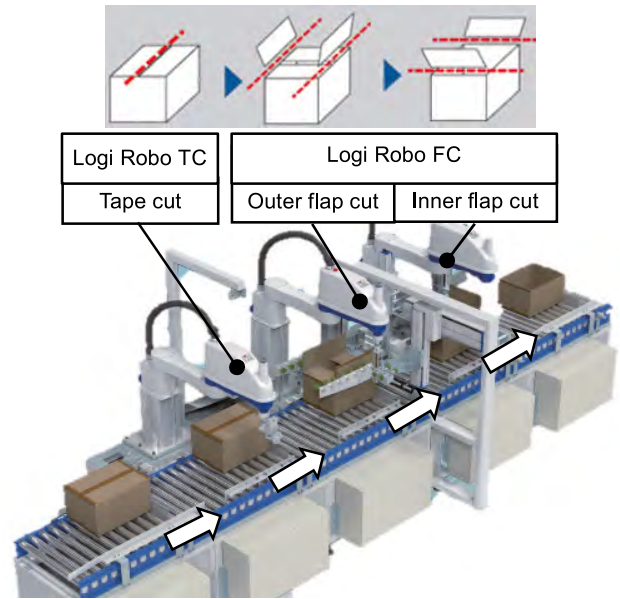


Fig.7. Outer appearance of Logi Robo TC/FC

① Logi Robo TC

As illustrated in Fig. 8, Logi Robo TC is a unit in which one SCARA robot with a vertically suspended cutter cuts the tape stuck, in an H-shape or I-shape, to the top surface of the cardboard box.



Fig.8. Tape cut

② Logi Robo FC

Logi Robo FC is a unit in which two SCARA robots respectively cut the outer and inner flaps (lids) of the cardboard box after Logi Robo TC cuts the top surface tape. As illustrated in Fig. 9, the cutting operation of the outer flaps includes: 1) the suction type hand holds the flaps; 2) the hand rotates in the

flap opening direction to open the flaps; 3) the SCARA robot with a horizontally extending cutter cuts the outer flaps while reciprocating thereinside; and 4) the SCARA robot sucks the cut flaps and discards them into a chute. The same operation applies to cutting of the inner flaps.

In the case of a small box (minimum size: L250 mm × D230 mm × H100 mm), a space around the flaps in a lid-opened state is very narrow. The compact structures of the SCARA robot and cutter allow cutting operation to be performed in a narrow space between flaps of slightly more than 200 mm.

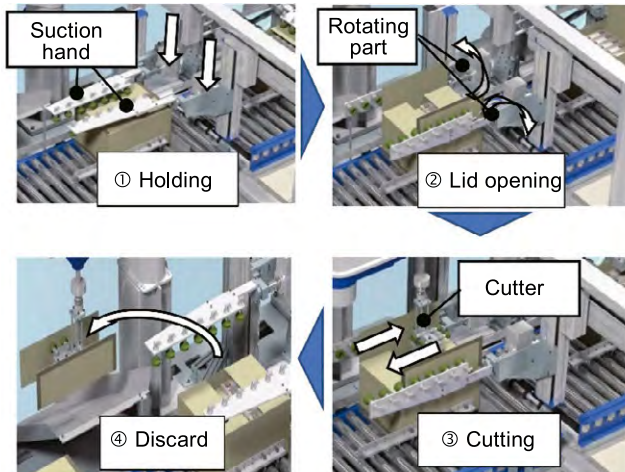


Fig.9. Outer flap cutting operation

3.2 Features and Introduction Effects

The Logi Robo TC/FC has the following features, and various introduction effects are expected.

① Caring about contents

Logi Robo is configured to cut the tape without putting the blade into the box, so that the cutting depth can be set small. The basic structure of a cutter for tape cut is illustrated in Fig. 10.

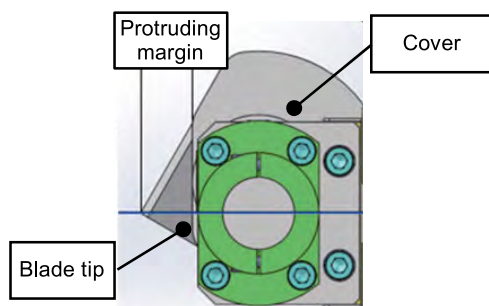


Fig.10. Cutter basic structure

The thickness of the box is 3 mm (B-flute which is a comparatively thin type), while the thickness of the tape is as small as 0.3 mm (thick gummed tape). The protruding margin of the cutter blade can be set sufficiently small with respect to the box thickness even in consideration of followability to the uneven surface of the box, which may prevent the blade tip from entering inside the box.

On the other hand, Logi Robo FC cuts the folded

part from the inner side of the erected flaps (Fig. 9 ③) in a lid-opened state (Fig. 9 ②). Thus, the blade tip does not enter inside the box.

As described above, there is no fear that Logi Robo TC/FC damages the contents of the cardboard box, that is, it is designed considering the quality of a final product to the maximum.

② Manpower-saving and labor-saving for subsequent process

Logi Robo FC performs flap cut (Fig. 9 ③), discards the cut flaps (Fig. 9 ④) and sends the resultant box (having no lids) to the subsequent process.

This allows the cardboard boxes to be directly arranged on a storage rack in a warehouse or a factory, leading to manpower saving and labor saving for the subsequent picking process.

③ Space saving

As illustrated in Fig. 7, Logi Robo TC/FC is configured such that the conveyor and SCARA robot are disposed parallel to each other to have a reduced width. Further, having a structure capable of being directly connected to an existing conveyor line, Logi Robo TC/FC need not have an additional connection unit in the longitudinal direction.

Reduction in the apparatus size leads to space saving.

④ Handleability to multiple types and mixed flow

Logi Robo TC/FC measures the size of all cardboard boxes to be supplied. Specifically, Logi Robo TC/FC measures the box size using a laser displacement gauge before tape cut, sends measurement data to a controller of each SCARA robot, and calculates a cutting path to follow.

Each time the cardboard box is supplied, the Logi Robo TC/FC performs size measurement, data sharing, and correction to thereby cope with various box sizes and random flow thereof.

⑤ Usability

Logi Robo TC/FC exhibits simple operability on the touch panel and the above-described handleability to multiple types and mixed flow to eliminate the need of troublesome initial setting and setting change.

3.3 Approach to Elongation of Blade Service Lifetime

If the blade service lifetime is short, a worker needs to exchange the blade with high frequency, thus limiting the effect of automation using Logi Robo TC/FC. Also from the viewpoint of cost effectiveness, a blade with high durability is required to be designed.

As an approach to elongation of blade service lifetime, comparison in durability was made (specifically, continuous cutting of cardboard boxes under the same conditions) between a blade made of tool steel and a blade made of a special alloy. Fig. 11 illustrates cuttability, and Fig. 12 illustrates a blade wear state.

In the tool steel blade, defective cutting occurred due to insufficient cutting performance at a stage when cutting distance had reached about 0.5 km, and progress of wear of the blade was confirmed. On the other hand, in the special alloy blade, defective cutting did not occur even at a stage when cutting distance had reached 7 km or more, and the blade experienced substantially no wear.

From these results, the special alloy blade is adopted for Logi Robo TC/FC. The service lifetime of this blade is 7 km (nominal value).

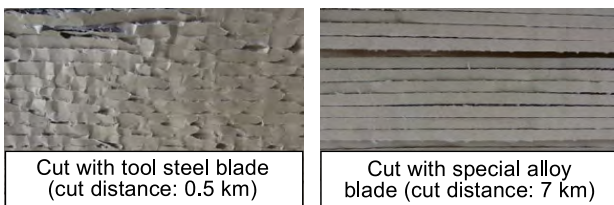


Fig.11. Comparison in cuttability

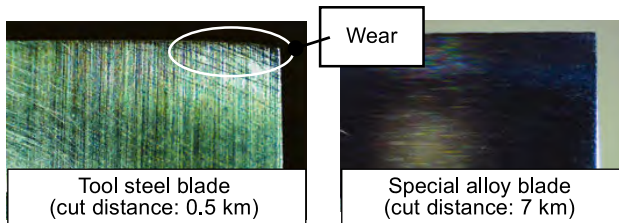


Fig.12. Comparison in blade wear (enlarged view)

4 Combination Examples of Logi Robo Series

Mounting a vision system to Logi Robo SP to allow automatic recognition of the position and size of boxes on a pallet enables depalletization. In the subsequent process, Logi Robo TC/FC is combined for interlocking with the above Logi Robo SP, enabling automation of a wider range of applications.

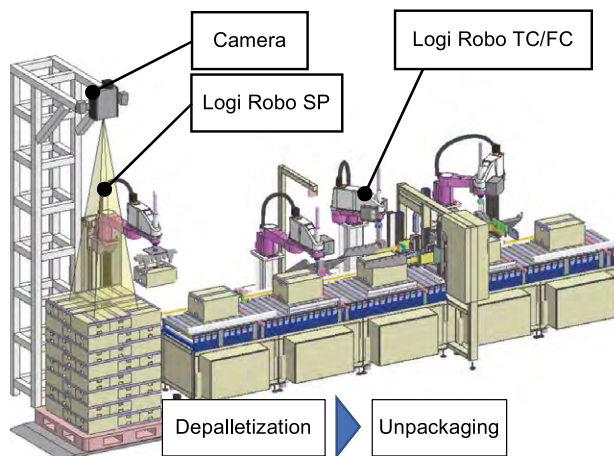


Fig.13. Combination example of Logi Robo series

Fig. 13 illustrates a combination example of Logi Robo SP (depalletization-enabled) and Logi Robo TC/FC.

4 Summary

The basic structures, features, and introduction effects of Logi Robo SP and Logi Robo TC/FC equipped with our own SCARA robot THE1000 have been described. By introducing Logi Robo series to production/logistics sites, automation and manpower saving are achieved, which can lead to improvement in labor productivity.

References

1. Ministry of Land, Infrastructure and Transport, I. Significance of Developing Comprehensive Physical Distribution Policy, Developing Comprehensive Physical Distribution Policy (fiscal 2021 to 2025), pp.1-3.

Memories of HUM Screw Development for Single Screw Extruder



Teiji SHIMIZU

Retired Engineer from
SHIBAURA MACHINE CO., LTD.

HUM screw is an abbreviation for high UNIMELT screw, which is a screw having UNIMELT with improved performance. During development, we recorded the cylinder internal pressure when the screw is in the compression using an electro-magnetic oscillograph to compare pressure profiles. As a result, we could stabilize cylinder internal pressure with the HUM screw and achieved significant increase in extrusion volume. We obtained an unexpected result to have achieved the effect that the galling resistance between the

cylinder and screw, which had been a source of concern, was greatly improved. We publicized these features to users. One of the users we delivered such product gave thanks to us for the increase in productivity and invited us over for a special dinner. This is also an unforgettable memory.

Thanks to the accumulation of technical data from our predecessors, we have learned that the scale-up theory is valid for the screw, which is the lifeblood of the extruder. I hope that the engineers on active duty will continue to improve the simulation technology using the latest technology such as AI. Continuity is the father of success.

Development of Collaborative Robot Safety System “Dual Safety Core”

Introductory Note

Special Article

Technical Paper

Technical Report

New Product

Series

Patent News

Prepared Critique



Kazuhiro KATSUMATA
Control Machine Company
Robot Engineering Department



Kentaro ISHIBASHI
Control Machine Company
Robot Engineering Department



Wataru MATSUNAGA
Control Machine Company
Robot Engineering Department

This article reports the “Dual Safety Core” which is a safety system for collaborative robot according to ISO 10218-1. Dual Safety Core consists of a safety board, sensors, and safety-related components. Especially, reliability of the safety board is according to ISO 13849-1 and IEC 61508-1 to IEC 61508-7. In order to realize requirements according to these standards, a safety board having two CPUs was developed.

In this safety system, all failures including system, hardware and software were analyzed from the design phase, and safety board was designed that these failures are detected. By these results, “Dual Safety Core” which is safety system having high reliability safety board for collaborative robot was realized.

1 Introduction

1.1 Collaborative Robot and Safety System

In introducing industrial robots, a safety fence is required to be installed so as not to allow workers to enter a work area [1]. The robot installation area can be several times larger than movable range of robot motion, because the safety fence shall be properly placed.

On the other hand, a collaborative robot is defined to be a type of robot designed to work alongside humans, allowing the robot and humans to work in the same area. The installation area of collaborative robot is expected to be smaller than that of the industrial robot, because placement of the safety fence is eliminated.

The collaborative robot operates in the same area as humans and is thus strongly required to have a mechanism for not doing harm to humans. This request is achieved by a safety system. Fig. 1 shows the typical safety system. This safety system consists of safety part (Safety Board), input devices, sensors, and a related switch. The safety related part is connected in series to a control. If a failure of a motor is detected by the sensor, the safety system directly cuts off power supply without through the control. Further, if stop request is issued from the input device using safety related equipment, the safety system cuts off power supply to stop the motor.

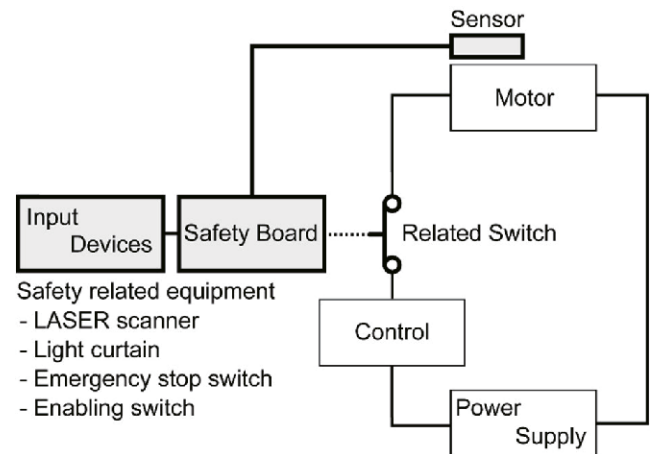


Fig.1. Conventional safety system

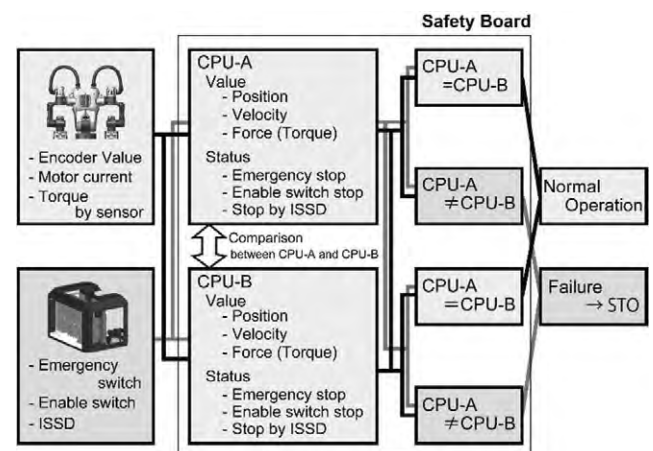


Fig.2. Dual Safety Core

Therefore, the safety system is required to have the following functions of:

- Monitoring motor operation using sensor
- Monitoring stop signal input using safety related equipment
- Stopping motor

Table 1. Requirement of safety board

PFH *Note 1	6.5×10^{-7} [H ⁻¹]
DC: Diagnostic Coverage	90% or more
SFF: Safe Failure Fraction	90% or more

[Note 1] Average frequency of dangerous per hour

Table 2. Safety function

1	STO	Safe Torque OFF
2	SOS	Safe Operating Stop
3	SS1-r	Safe Stop 1 ramp monitored
4	SS2-r	Safe Stop 2 ramp monitored
5	Stop function by ISSD *Note 2	

[Note 2] Input signal switching device

1.2 Operations Required for Collaborative Robot

It is easy to realize a safety system that stops a robot by cut off the power supply after pressing an emergency stop switch as shown in Fig.1

In collaborative robot, force and pressure limitation is required in the case of quasi static and transient contact between persons and the robot [2]. And, the collaborative robot shall be performed with in limitation which accord to standard [2]. With the system as shown in Fig. 1, it is very difficult to realize a safety system that operates the robot within the limitation according to standard.

The status without failure or with failure of robot operations is determined based on monitoring of the position velocity and force (torque). If the position, velocity and force is monitored within threshold value, operation without failure is determined. While, there is monitored outside threshold, operation with failure determined.

If the operation with failure is determined by safety system, the system cuts off the power supply so as to prevent the robot from doing harm to humans.

On the other hand, if operation without failure is performed, the safety system appropriately decelerated and stops the operation depending on such situations following. For example; persons enter the area where a robot works; persons and a robot work in the same area; robot operates unmanned.

The threshold value in operation without failure or with failure is not fixed value except for some exceptional cases. Accordingly, threshold values for position, velocity, and force are calculated each time required. By adding "calculation of position, velocity, and force (torque)" to the functions mentioned in

1.1, there is achieved a functional safety system that performs the following operations:

- Stop robot operation without servo-off and resume
- Switch from non-collaborative motion to collaborative motion (or from collaborative motion to non-collaborative motion)
- Stop upon due to detection of force over limitation

1.3 Dual Safety Core

Safety Board constituting the safety system illustrated in Fig. 1 is implemented in a robot controller in the form of a single substrate. This substrate is constituted by independent hardware separated from a main substrate for controlling robot operations and an amplifier for calculating robot operations and supplying power to a motor.

Safety Board is required to have the highest reliability among the components constituting the collaborative robot. To achieve this request, we have developed Safety Board having a redundant structure using two CPUs (CPU-A and CPU-B) and a safety system "Dual Safety Core®" using this hardware.

Fig. 2 shows the configuration of Dual Safety Core. Dual Safety Core calculates the position (angle), velocity (angular velocity), and force (torque) of each axis (joint) from an encoder value, a motor current value, and a sensor value. Specifically, a humanoid-type double-arm collaborative robot now under development calculates the position, velocity, and force of each axis from the encoder and motor current values of 16 axes, and a plurality of force sensor values. The CPUs (CPU-A and CPU-B) perform calculation using the same encoder, motor current, and sensor values and the same expression. When the results calculated by the CPU-A and CPU-B coincide with each other, normal operation is determined: on the other hand, when they do not coincide with each other, occurrence of a failure is determined. When normal operation is determined, operation is continued. When occurrence of a failure is determined, the robot is stopped. Dual Safety Core repeatedly performs the calculation and normality/abnormality determination per several milliseconds.

Table 1 shows safety-related specifications of Dual Safety Core. These are specified in ISO 13849-1:2016, IEC 61508-2:2010, and IEC 61508-1 to IEC 61508-7. PFH is a failure probability. The failure probability of single CPU and memory is typically about 1.0×10^{-5} . When Safety Board is designed using the one CPU with memory, the PFH shown in Table 1 is very difficult to achieve.

However, in the case of the structure shown in Fig. 2, the PHF is calculated as a probability (theoretical value: 1.0×10^{-10}) in which a failure occurs simultaneously in two CPUs with components, so that even when a component having a failure probability of about 1.0×10^{-5} is used, the PFH shown in Table 1 can be achieved.

1.4 Safety Function

Dual Safety Core has 16 safety functions. Table 2 shows five main functions selected from among the 16 safety functions. STO (Servo Torque Off) and SOS (Safe Operating Stop) are stop functions. STO is a stop function of performing stop operation in a servo-off state. STO requires servo-on for operation resumption. SOS is a stop function of performing stop operation while maintaining servo-on state. Operation resumption in SOS is executed without servo-on. SS1-r is a function of performing deceleration for STO stop. SS2-r is a function of performing deceleration for SOS stop. Stop function by ISSD is a signal input function of an external input device such as a safety laser scanner or a light curtain.

In normal emergency stop operation, power is directly cut-off after button depression. On the other hand, by combining functions shown in Table 2, it is possible to achieve such a robot operation as to perform deceleration involving threshold monitoring after depression of the emergency stop button to perform SOS stop and promptly switch to power cut-off operation when determining that the deceleration falls outside the threshold value.

2 Design of Dual Safety Core

2.1 Safety Design of System

It can be seen from Table 1 that DC (safe-side failure rate) and SEF (dangerous-side failure detection rate) are 90% or more, which means that the dangerous-side failure rate that cannot be detected in the entire system is 1% or less.

In designing the system of Dual Safety Core, FMEA for the entire system was carried out first. Specifically, 70 types of components that constitute the system were selected, and then causes (overvoltage, overcurrent, short-circuit, disconnection, fixation, etc.) by which the main components went in failure were investigated for each component. Then, phenomena of the failures caused by these causes were assumed, and failure detection methods were classified. Diagnosis numbers (error numbers) for detecting all the assumable failures were defined. There was designed a system free from failures that cannot be detected by performing failure analysis at the design stage. The number of types of selected main components was 70, and one type of component had a plurality of failure causes, so that the number of failures to be analyzed was 398.

2.2 Hardware Safety Design

Dual Safety Core has Safety Board as its hardware. In the safety design of Safety Board, PFH and DC were calculated after determination of components so as to prove high reliability.

In designing Dual Safety Core, 12 reliability block diagrams were created. Fig. 3 is a reliability block diagram of STO shown in Table 2. This block diagram includes 12 blocks.

PFH and DC are calculated for each reliability block diagram. Dual Safety Core has two CPUs on Safety Board, so after Selector Switch, the connection of blocks branches into two systems.

In calculation of PFH, the failure probabilities of all components constituting Safety Board are investigated and accumulated. After accumulation of the failure probabilities for each block (CPU-A, etc. of Fig. 3), the failure probabilities of all blocks are calculated to determine failure probabilities for respective reliability block diagrams. The failure probabilities are compared among 12 reliability block diagrams, and a failure probability of the worst case is set as PFH of the safety system.

In calculation of DC, the safe-side failure detection rates of all components are investigated and averaged. After average calculation for each reliability block diagram, the safe-side failure detection rates are compared among 12 reliability block diagrams, and a safe-side failure detection rate of the worst case is set as DC of the safety system.

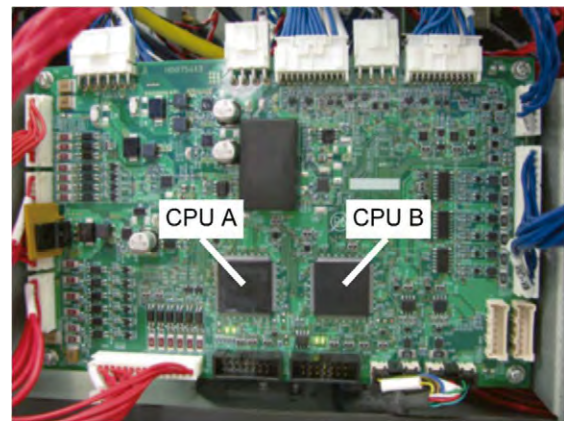


Fig.4. Safety board of Dual Safety Core

The number of blocks in the reliability block diagram is 12, and each block is constituted of a plurality of components, so that the total number of components in Fig. 3 is about 500. The total number of components

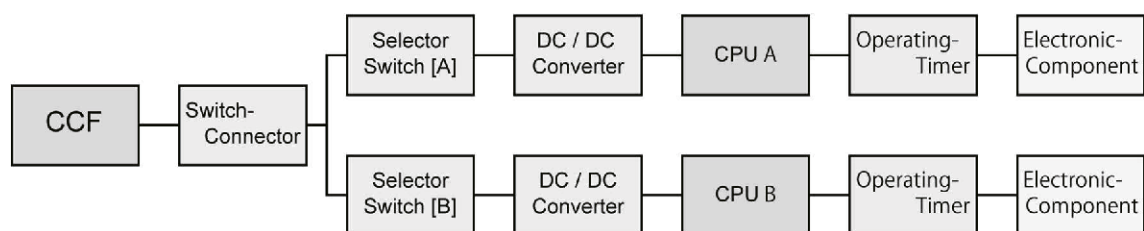


Fig.3. Reliability block diagram of STO

in the entire Dual Safety Core is about 8,000.

Fig. 4 is a photograph of Safety Board. The two CPUs (CPU-A and CPU-B) are mounted on a single substrate. Based on the results of calculation of PFH and Fig. 4, there has been designed Safety Board achieving high reliability conforming to Table 1.

2.3 Safety Design of Software

To achieve 1% or less of the dangerous-side detection rate, software of Dual Safety Core was designed such that a failure is detected in units of block. Then, detection evaluation of all assumable failures was made. In this evaluation, whether it is possible or not to detect a failure by the diagnosis number (error number) described in chapter 2.1 was determined. This failure detection evaluation was carried out before software coding.

After software coding, a failure of “execute two times” “omit” “input wrong value”, or the like was made to occur on software for each function constituting the software, and evaluation was made such that the diagnosis number corresponding to the failure would be detected.

The total number of blocks in Dual Safety Core is 76, and a plurality of types of failures were to be made to occur for each block, so 200 or more failure detection evaluations were carried out. From the evaluation results, it was confirmed that failures occurring in all the functions constituting software operating on Dual Safety Core would be detected by the diagnosis numbers described in chapter 2.1. Thus, there has been achieved software that satisfied the specifications illustrated in Table 1.

3 Operation of Collaborative Robot

Fig. 5 shows the operation of a collaborative robot achieved by Dual Safety Core. Table 3 shows the relation between safety monitoring and robot operation. In Fig. 5, two sensors (safety laser scanner or light curtain) are used to set a safety distance. When a human is outside the set safety distance area, a robot performs a non-collaborative motion. During the non-collaborative motion, the

position of the robot is monitored. On the other hand, during a collaborative motion, the position, velocity, and force (torque) are monitored.

Fig. 5 (a) is a view illustrating a state where a human enters the safety distance area. In this state, a robot shifts from the non-collaborative motion to collaborative motion. In the state illustrated in Fig. 5 (a), both SS1-r and SS2-r are possible. Switching between SS1-r and SS2-r is made under a parameter setting.

Fig. 5 (b) is a view illustrating a state where a human enters a collaborative area where a human and a robot work together. In the state illustrated in Fig. 5 (b) through SS1-r, the robot continues the collaborative motion.

In this case, when the human contacts the robot to apply thereto a force of a predetermined threshold or more, the robot stops according to STO. In the state illustrated in Fig. 5 (b) through SS2-r, the robot stops according to SOS. In this case, when the human contacts the robot to change the robot position by an amount equal to or more than a predetermined threshold, the robot stops according to STO.

Fig. 5 (c) is a view illustration of a state where a human goes out of the safety distance area. When the robot performs the collaborative motion in the state illustrated in Fig. 5 (b), he or she shifts from the collaborative motion to non-collaborative motion. When the robot stops according to SOS in the state illustrated in Fig. 5 (b), he or she is self-restored from stop to active and shifts from the collaborative motion to non-collaborative motion.

Achievement of operations shown in Fig. 5 and Table 3 actualizes a collaborative robot. The collaborative robot automatically shifts from the non-collaborative motion to collaborative motion or vice-versa depending on the position relative to (distance from) a human. In the collaborative motion, the robot operates with a force equal to or less than a value specified in [2], so that he or she is guaranteed not to do serious harm to humans.

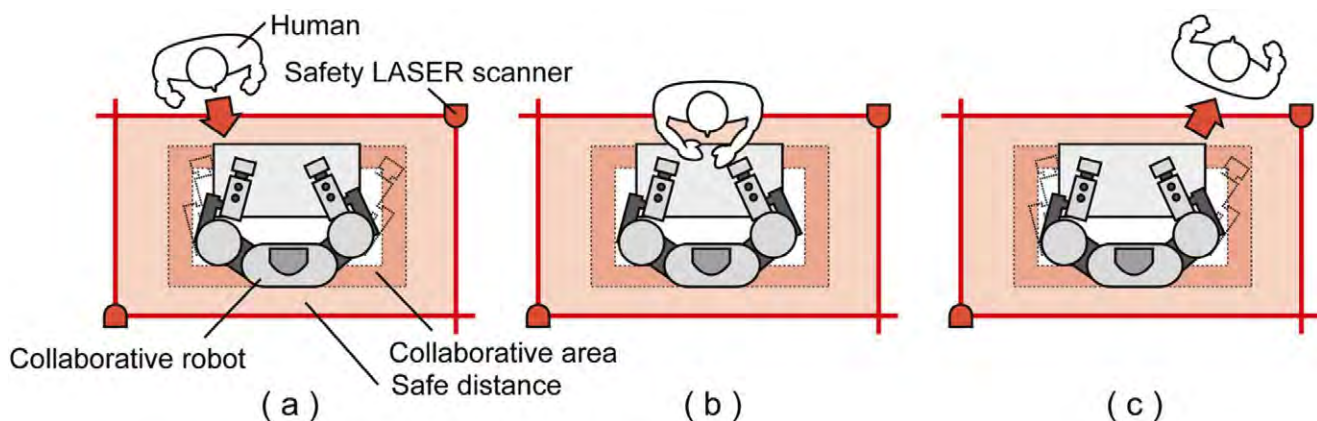


Fig.5. Safety motion of collaborative robot using Dual Safety Core

Table 3. Relationship between safety monitoring and robot motion

	(a)	(b)	(c)
SS1-r	Motion with non-collaborative to collaborative condition by SS1-r	Motion within collaborative condition speed	Motion with collaborative to non-collaborative condition according to SS1-r
SS2-r	Motion with non-collaborative to collaborative condition by SS2-r	SOS	Motion with Self-recovery. Motion with collaborative to non-collaborative

4 Conclusion

“Dual Safety Core” of collaborative robot safety system has been developed.

Safety Board implemented in Dual Safety Core achieves high reliability having PFH conforming to ISO 13849-1: 2023 and DC and SFF conforming to IEC 61508-2:2010 and IEC 61508-3:2010. The safety system conforms to functional safety standard IEC 62061:2021, and machinery standard can be used without change when a system integrator integrates a double-arm collaborative robot to a system. A robot having Dual Safety Core is provided with safety functions for allowing collaborative work with a human in the same area and achieves motions as illustrated in Fig. 5.

This eliminates the need of providing a safety fence in the area using the collaborative robot. The installation area of the collaborative robot is significantly reduced as compared with the installation area of an industrial robot requiring a safety fence, which may contribute to improvement in production efficiency.

References

1. ISO 10218-1, Robot and robotic devices – Safety requirements for industrial robots – Part1: Robots (2011), pp.15-16
2. ISO/TS 15066, Robot and robotic devices – Collaborative robots (2016), pp.21-24

COLUMN

Rewarding for me



Naoto TOGASHI

Metal & Plastics Industrial
Machine Company
Extrusion Machine
Engineering Department

After more than a decade with the company, I feel that the strength of extrusion business is “Try anything”.

Extrusion projects are made-to-order for each customer in terms of product application (separators or food containers), product width, production speed, or and ancillary equipment.

Having no concept of the standard, I have to admit that I haven’t got used to my job from the beginning of my employment until now.

In recent years, requests for automating have been increasing due to safety and labor-saving considerations. We recently spent three months for overseas products to launch equipment with

automated film passing function.

It took a lot of hard work to establish the new technology, which involved modifying the equipment, reviewing the sequence, and checking the load operation all in one shot. With the cooperation of many customers and relatives involved, we managed to get to the acceptance inspection. I feel that it is a rewarding environment for engineers to have many opportunities to be involved in new technologies.

I have heard that the BSF manufacturing system, our major product currently, began with a consultation from a customer having no experience in such field. I feel that our small “Try anything” attitude has led to the large business we have today.

We will continue to broaden our vision and improve our skills to meet the demands of our customers.

Development of a Highly Efficient Production Process for Precision Processing Machine Parts



Naoki SUGIYAMA

Production Center
Machinery & Production
Engineering Department



Asao SASAKI

Production Center
Machinery & Production
Engineering Department



Masahiko NAGATA

Production Center
Machinery & Production
Engineering Department



Ryosuke FUJIMOTO

Production Center
Machinery & Production
Engineering Department

Grinding, cutting, and precision machining of lenses, precision molds, and reflective mirrors requires high motion accuracy, positioning accuracy, and temperature control in processing machines. Our precision processing machines use V-V roller guide ways, which have a simple structure and high rigidity. To minimize minute undulation, we have been pursuing improvements in needle accuracy, the guide way surface finishing method, the introduction of the needle to the moving body, the shape of the discharge portion, and so on. The main parts of these precision processing machines are manufactured in our own factory. This paper reports on a new process that improves productivity by automating the grinding process from casting material development to the finishing of the V-V roller guide way surface on our ULG series of precision processing machines.

1 Introduction

In recent years, the need for larger capacity and higher resolution in imaging information devices has been increasing. In line with this, high precision in the nanometer range is required in the precision machining of lenses for optical parts and molds for lenses. In our precision processing machines, we realize high motion accuracy, positioning accuracy, and temperature control to ensure high processing accuracy, and we aim to further improve accuracy.

These precision processing machines use V-V roller guide ways, which have a simple structure and high rigidity. To minimize minute undulation, we pursue improvements in needle accuracy, the guide way surface finishing method, the introduction of the needle to the moving body, the shape of the discharge portion, and so on.¹⁾

The Production Center allocates production of cast parts for our products to internal and external suppliers, with the aim of supplying parts with the best balance of quality, cost, and delivery (QCD) according to the situation. The bed used to process the V-V roller guide way is a casting made in-house, and is the part that becomes the base of a precision processing machine. The finished surface of this guide way has high specification requirements for hardness, machining accuracy, and surface roughness, and increasing productivity while meeting these requirements is an issue. However, it is difficult to increase production from the current level with

conventional materials and processing methods.

The bottleneck in production is the stage of precision surface finishing with hand scraping. Hand scraping work is a process in which the machined surface profile of surfaces for which high flatness accuracy is required, such as sliding surfaces of machine tools, is ascertained by matching comparison of the machined surface profile, and high portions of the surface are finished with a chisel-like blade called a hand scraper to obtain the desired finished surface.²⁾ In hand scraping work, the surface of a reference master and the machined surface are matched and compared, and contact portions, which are convex portions that are touching the master, are scraped off.²⁾ Uneven hardness of the casting and the machining accuracy of the pre-processing greatly affect the working time. Here, we will report on our efforts to improve production efficiency from casting to machining by modifying the casting material, changing the casting design to achieve uniform hardness, and changing the machining method in the process before hand scraping work to improve machining accuracy and automation.

2 Evaluation Method

The beds of our ULG precision processing machines are manufactured with castings made in-house, and consist of two V-V roller guide ways. They are manufactured through the processes of casting, machining (machining processing and planar

processing), and hand finishing (hand scraping work and precision surface finishing). Uniformity of the hardness of the V-shaped sliding surfaces has been achieved by modifying the material, and efficiency improvements have been carried out by changing the machining method.

2.1 Improvement of casting materials

Conventionally, FC350 (JIS G 5501, ISO 185) has been adopted for ULG beds for its hardness and vibration-damping performance. Other than C, Si, Mn, P, and S, to stabilize hardness, Cr, Cu, and Sn are added. Modification of the material was carried out as follows. In general, hardness increases with a faster cooling rate during solidification, but the addition of Cr and Sn increases the effect of the cooling rate on hardness. Therefore, the minimum amount was added to obtain the required hardness while suppressing an increase in the local hardness. Since Cu concentrates Mn in the eutectoid cementite³⁾ and assists in its function of stabilizing pearlite, the amount of Mn was increased to ensure hardness, and an appropriate amount of Cu was added. To obtain more uniform hardness, late inoculation with Fe-Si-based inoculant was performed with inoculant placed in the ladle in addition to the pouring method in the pouring basin to refine the crystal grains.

Variations in hardness are influenced by the cooling rate and are caused by external and internal positioning of the product and differences in wall thickness. To improve uneven hardness, a casting design was studied using a casting simulation (ADSTEFAN, Hitachi Industry & Control Solutions, Ltd.) to minimize the temperature difference at the completion of molten metal filling, including the installation of a chiller, the shape and arrangement of sprue runners and basins (flow paths of molten metal), and so on. Fig. 1 shows the temperature distribution 5,000 seconds after the completion of pouring for the conventional casting design and the casting design with cooling temperature control.

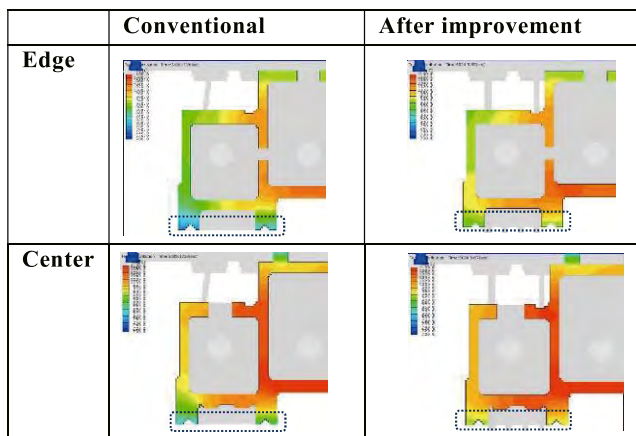


Fig.1. Temperature distribution with cooling control (after 5,000 seconds)

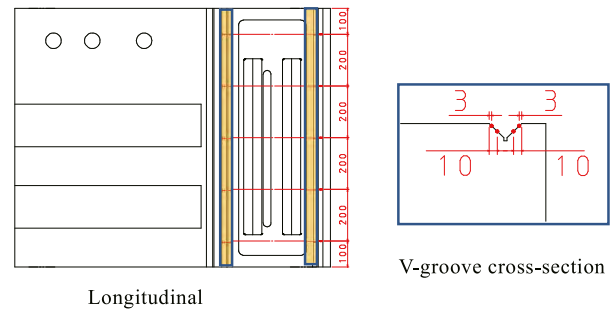


Fig.2. Hardness measurement positions

Comparing the temperature distribution of the V-shaped sliding surfaces (within the dotted-line areas in the figure) where uniformity of hardness is required, the conventional casting design resulted in a temperature distribution of 800 to 1,000 °C at the edge and center, with a large difference of approximately 200 °C. On the other hand, the casting design with cooling temperature control resulted in a temperature distribution of 940 to 990 °C at the edge and center, with the difference reduced to about 50 °C. The hardness (HB) of the V-shaped sliding surfaces of the bed produced with each casting design was measured at 40 points (Fig. 2) in the longitudinal and depth directions, and uniformity was evaluated by standard deviation.

2.2 Processing method improvement

Since the V-shaped sliding surfaces are elements directly linked to the accuracy of the machine, the final accuracy is dependent on the precision surface finishing work by hand scraping. This process requires long hours of ultra-precise manual work by skilled workers, which is a factor in lengthening the manufacturing lead time. Therefore, we attempted to reduce the manual finishing time by improving the machining accuracy of the previous process. The machining was changed from conventional planar processing to grinding processing to improve accuracy, and the grinding processing was also made more efficient. Grinding processing experiments were carried out and evaluated in two stages: confirmation of grinding processing accuracy and conversion of grinding processing to mass production.

2.2.1 Confirmation of grinding processing accuracy

Grinding processing accuracy was evaluated by manufacturing a test piece. The evaluation positions (pitch, angle, and tilt) of the test piece and V-shaped sliding surfaces are shown in Fig. 3. The test piece is a partial model with a V-shaped sliding surface shape of an actual ULG bed, but the casting design was adjusted using the simulation to produce a temperature distribution equivalent to that of the full model with cooling temperature control for the cooling rate. The chemical composition of the molten metal and inoculation treatment were also the same conditions

as the full model.

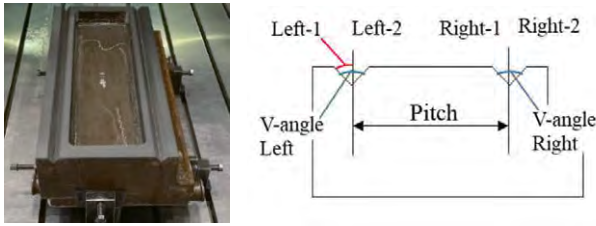


Fig.3. Test piece reproducing the V-shaped sliding surfaces

The test piece grinding processing was carried out one face at a time using a grinding processing machine with a swivel grinding head (Curvic 5° indexing) turned 45° for each face. After the processing, numerical evaluation was performed with a 3D measuring machine (MMZ-M 163012, Carl Zeiss).

2.2.2 Conversion of grinding processing to mass production

After confirming the feasibility of reducing the time for the precision surface finishing work by hand scraping by confirmation of grinding processing accuracy, we planned to ensure stable accuracy and support conversion to mass production. The target parts were expanded to a total of four parts, including tables with V-shaped sliding surfaces like the bed, and a specialized jig capable of grinding processing of parts with V-shaped sliding surfaces equivalent to one ULG unit at a time was considered (Fig. 4).

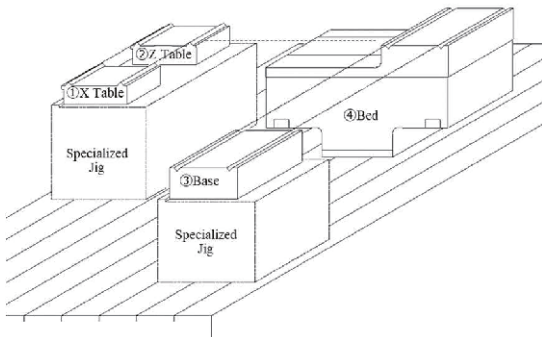


Fig.4. Exterior appearance of specialized jig

3 Results and Discussion

3.1 Effects and considerations of casting material improvement

Regarding hardness, in the case of the conventional chemical composition and casting design, some portions included hard metal structures that hindered the hand scraping work, and the standard deviation of hardness was 3.2. As a result of the casting design in which the chemical composition was optimized and the molten metal flow path and chiller were changed, the standard deviation was 0.5, and stable uniformity with hardness that satisfied the mechanical specifications was achieved. Note that a separate casting test specimen (JIS G 5501) that guarantees the mechanical properties of the ULG casting material has a tensile strength of 350

to 400 MPa and a hardness of 240 to 260 HB.

Here, inferring the metallurgical structure from the simulated temperature distribution of the ULG bed in Fig. 2, the bed edge with the conventional casting design is generally solid at less than 1,000 °C. We can infer that the solid and liquid phases are mixed at around 1,150 °C in the interior of the central portion. Thus, the central portion of the ULG bed cools slower than the edge portion if proper cooling temperature control is not performed according to the size of the product, and temperature differences are likely to occur even within the same product. This distribution of temperature is reflected in the distribution of hardness, which affects the product as a difference in hardness (unevenness).

Fig. 5 shows the temperature distribution 1,000 seconds after the completion of pouring for the conventional casting design and the casting design with cooling temperature control. The temperature of the V-shaped sliding surfaces was compared for each casting design in the initial cooling state after filling with the molten metal (dotted-line areas in the figure). In the conventional casting design, the topmost surface of the sliding surfaces is quenched to below 800 °C. We can infer that the V-shaped sliding surfaces after 1,000 seconds have a hard metallographic structure (ledeburite) with partially crystallized pro-eutectoid cementite due to quenching. Although the topmost surface portion is quenched, the quenched structure is not distributed at a constant depth due to the effect of the temperature of internal portions where cooling is slow, and in addition to the structure variation during eutectic solidification, the structure variation is more complicated due to the effect of the lamellar spacing of the pearlite structure during eutectoid solidification. As a result, we can infer that variations in hardness occurred on the sliding surfaces. The temperature of the V-shaped sliding surfaces of the temperature-controlled casting design is higher than that of the conventional casting design, and is near 1,000 °C. Because this slowed the cooling rate, we can infer that the formation of pro-eutectoid cementite was suppressed, and the local hardness increase was eliminated.

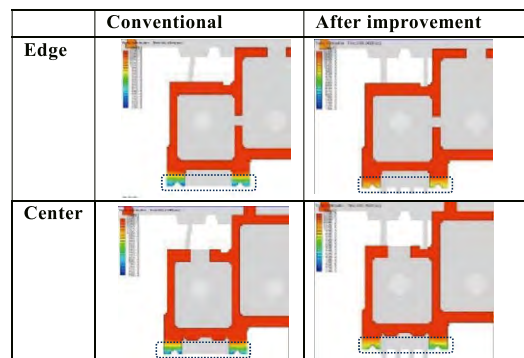


Fig.5. Temperature distribution with cooling control (after 1,000 seconds)

3.2 Results of processing method improvement

The results of the processing method improvement are described below.

3.2.1 Effects and considerations of grinding accuracy improvement

The evaluation results are shown in Table 1. For Left-1 and Left-2, tilt occurs, and V-angle right is significantly negative. In general, it can be evaluated that the angle variation is large. Due to this angle error, a gap of about $\pm 5.0 \mu\text{m}$ occurs on the V-shaped sliding surfaces, which makes it impossible to obtain a good result in estimation. The angle error is thought to have been caused by the pitching behavior of the swivel grinding head when it was stroked.

Table 1. Evaluation Results

Item	Part	Expected Value	Result
One-side angle	Left-1	45°	44.9930°
One-side angle	Left-2	45°	45.0098°
V-angle left	V left	90°	90.0028°
One-side angle	Right-1	45°	44.9880°
One-side angle	Right-2	45°	44.9889°
V-angle right	V right	90°	89.9776°
Pitch	—	350 ± 3 μm	± 1.5 μm

As a result of measuring the straightness in the vertical plane of the processing machine, M-shaped behavior was observed between strokes of about 3,500 mm, and a maximum difference in elevation of 52 μm was confirmed. When converted to the tilt of the swivel grinding head, this results in the occurrence of a maximum tilt of $\pm 150 \mu\text{m}/\text{m}$. This straightness accuracy is an accuracy provided as an inverse curve tending to offset deflection and torsion caused by the weight of the grinding head itself when it is stroked,⁴⁾ but it became clear that it is the main cause of angle error in this grinding process.

Therefore, machine accuracy correction was carried out to suppress this tilt. The results before and after correction are shown in Fig. 6. The results of carrying out test grinding after accuracy correction show that it became possible to improve the gap on the V-shaped sliding surfaces due to angle error to $\pm 1.8 \mu\text{m}$.

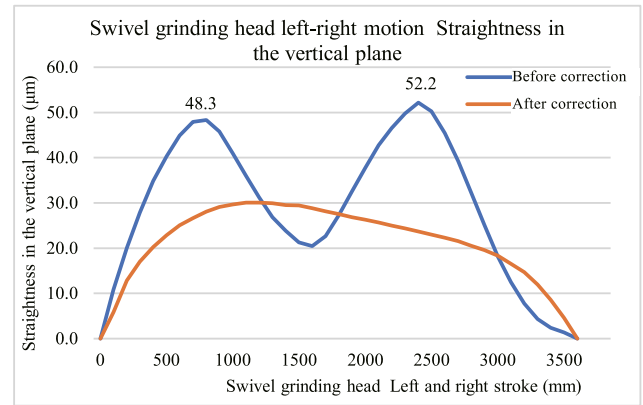


Fig.6. Swivel grinding head accuracy

After the improvement, estimation of the pitch and angle accuracy were made by placing the test piece in contact with the master. The results showed that a good estimate could be obtained on all surfaces, and it was evaluated that it was possible to reduce the time of the hand scraping work.

3.2.2 Effects and considerations of mass-production conversion of the grinding process

Conversion to the use of a specialized jig is expected to make the grinding position fixed in place, to suppress decreased accuracy due to variation in the setup method, and to improve efficiency by automatic grinding of four parts. Fig. 7 shows a photograph of the appearance of workpieces set on a specialized jig.



Fig.7. Photograph of the appearance of the specialized jig

In normal plane grinding work, grinding of one part per work pallet is typical, but conversion to the use of a specialized jig has enabled simultaneous processing of four parts. In addition, by utilizing a touch sensor function and automatic wheel change (AWC) function and by developing an NC program linkage function, work that used to take about 20 hours before introduction has been reduced to about 10 hours. Furthermore, by realizing conversion from attended to continuously automated operation, nighttime unattended operation has become possible.

Also, with regard to pitch accuracy, processing at the same position each time (constant value) and stabilization of the setup clamping force become possible, and stable production with the required accuracy of $\pm 3 \mu\text{m}$ became possible.

Introductory Note | Special Article | Technical Paper | Technical Report | New Product | Series | Patent News | Prepared Critique

3.3 Verification of improvement effects

As improvement effects due to improving the casting material and raising the precision of the grinding process as well as mass-production conversion of the grinding process, the productivity of the precision surface finishing work by hand scraping improved, and the production efficiency increased by 20% compared to the conventional method. Moreover, the equipment operation rate of the relevant grinding processing machine has also increased by 15% compared to the conventional method, and a significant improvement has been achieved.

4 Conclusion

- 1) By adjusting the casting chemical composition and the casting design of the ULG bed, hardness uniformity of the V-shaped sliding surfaces was achieved, and due to material improvements, delays in the hand scraping work could be suppressed.
- 2) The specialized jig, touch sensor function, automatic wheel change function, and NC program linkage enable simultaneous grinding of four parts. The required accuracy of $\pm 3 \mu\text{m}$ is met, while the machining time is halved from 20 hours to 10 hours in unattended operation.
- 3) Improved integrated production technology from casting to machining has reduced the hand scraping work time, which had been a production bottleneck, and increased production efficiency by 20% compared to the conventional method.

References

- 1) Katsutoshi TANAKA: Transactions of the Japan Society of Mechanical Engineers (C) 75 (2009) 757
- 2) Masahiko ONOSATO: Journal of The Society of Instrument and Control Engineers 37 (1998) 7
- 3) Sadato HIRATSUKA, Setsuo ASO, Toru MARUYAMA: Journal of Japan Foundry Engineering Society 89 (2017) 10
- 4) Makoto SAGARA: Journal of the Japan Society of Mechanical Engineers 107 (2004) 1024

Total Die-Casting Machine Controller TOSCAST-999

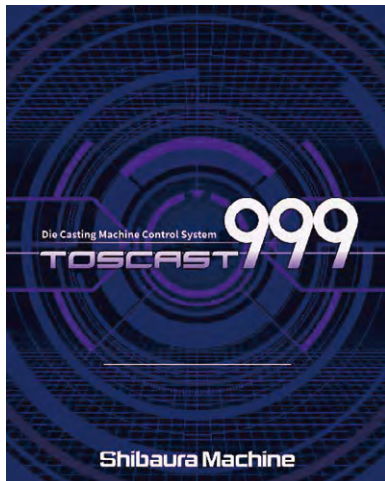


Fig.1. Illustrative image of a die-casting machine and TOSCAST-999

1 Overview

In addition to the conventional demand for improved quality, the current die-casting industry faces various challenges such as CO₂ reduction and the trend of human resources leaving the industry, both in Japan and abroad.

Therefore, die-casting machines are required not only to improve performance but also to reduce the defect rate, reduce CO₂ emissions by more efficient productivity and the like, and reduce dependence on operators' skills.

To meet these needs, we have developed a new controller, TOSCAST-999 (Fig. 1).

2 Features

2.1 GUI That Leverages a Large Screen

We configured a GUI that allows users to customize the display with two screens above and below, improving usability with more information on the display and fewer screen changes (operations), as well as combining a full display. (Fig. 2)

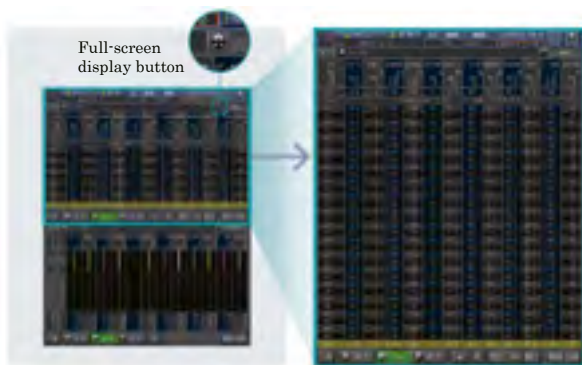


Fig.2. Screen configuration and overall view

2.2 Reviewed Screen Structure

We inherit the functions of the first generation of TOSCAST, continuing development up to the latest model, TOSCAST-999. Technological developments have achieved complex control, which has made condition settings more complex. Additionally, because the specifications have been inherited, they coexist with conventional functions. These make the current GUI difficult for users to understand.

We reviewed these issues for TOSCAST-999 from the user's point of view and improved the screen configuration by rearranging the display items for each device, allowing users to operate the model intuitively and smoothly. (Fig. 3)



Fig.3. Review of screen configuration

2.3 Condition Setting Screen

As mentioned in the previous section, the operation can be customized in detail, but the condition setting is complex to make. This in itself is important in terms of reflecting users' desires in operations, but users who do not require that much may only feel complicated.

Additionally, users need to become "familiar" with such settings, as well as the terminology in the die-casting industry and names used in our company, which are not commonly known. To solve this, we improved the design of the setting screens. The names of input items alone may be difficult for users to understand, so we expressed the correspondence between addressed items with operations in design so that users can imagine the operation. We believe that this will improve the accuracy of condition settings and break away from the dependence on engineers' "getting too accustomed." (Fig. 4)

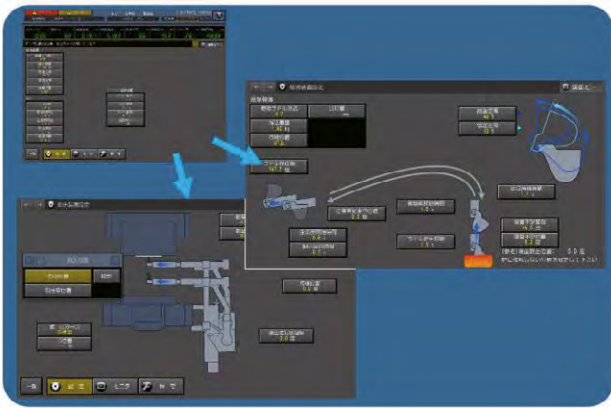


Fig.4. Redesign of the condition setting screen

2.4 Document Viewing Functions

To further improve usability, we added document viewing functions for documents such as the user manual. In conjunction with this, the user manual has been increased in volume to include devices that enable users to operate the machine smoothly.

In addition, the function allowing for quick access to a target page of the document from the Help button as a 'help function' shortened the process to solve problems. (Fig. 5)

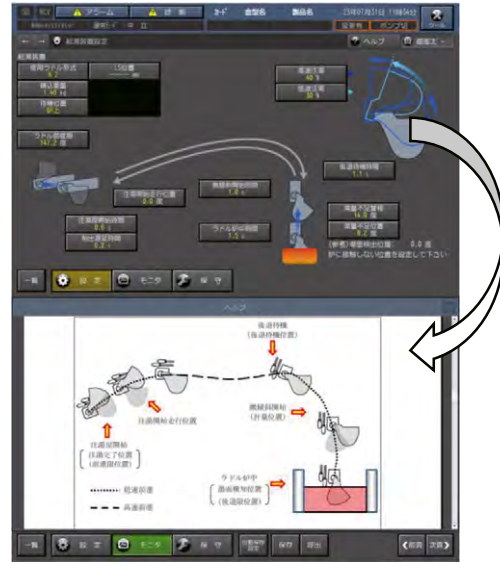


Fig.5. Help functions

2.5 Enhanced Injection Waveforms (Quality Data)

With the advancement of casting technology, user companies have taken various measures for "quality improvement" and "better management and visualization." Changes in the temperature of materials and dies, which are not easily observed, are important factors. These user companies seem to be proceeding in the direction of "more strict control." Typical examples include a device that improves quality by vacuuming the inside of a die to treat the degree of vacuum as quality data. Such function is getting more common these days, and users are demanding further functions to, for example, measure the degree of vacuum in multiple locations.

Conventional models support the three basic waveforms and up to two optional waveforms, but due to increasing user demands, this number was sometimes insufficient. For this reason, we have increased the number of waveforms of TOSCAST-999 to 20, including optional 6 systems to meet user requirements.

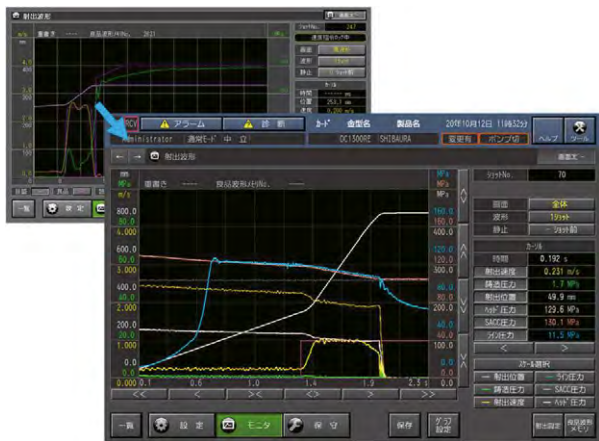


Fig.6. Enhancement of waveform functions

3 Conclusion

Because not many products have been shipped so far, only a few companies have received feedback from users with good reputations.

As a future perspective, we plan to add features that directly benefit users' production sites, such as a casting condition support function and a thermography function that can be easily linked to TOSCAST-999.

From the perspective of creating functions not only for major manufacturers but also for many other small and medium-sized enterprises, we will continue to further improve functions and appeal to the die-casting industry.

Extra-Large Electric Injection Molding Machine EC3000SXIII



1 Outline

An extra-large class of 3000 tons has joined the EC-SXIII series, a line-up of electric injection molding machines. With this release, we have lined up the products from the small 50-ton to the extra-large 3000-ton class.

In light of the recent acceleration of the switch to electric vehicles, EC3000SXIII will meet the increased demand for large resin parts due to the growing weight reduction of auto body. With its high cycle molding and energy saving performance, as environmental-conscious equipment, EC3000SXIII will contribute to improving client's LCA* ratings.

*LCA: Life Cycle Assessment

2 Features

The development concept of EC3000SXIII was to provide "The highest productivity of electric toggle type machines". Table 1 shows major specification values. The following lists the six features of this machine.

2.1 The fastest dry-cycle in the industry

EC3000SXIII inherits the linear guide support structure for movable platens which has been employed since EC-SX series released in 2009. "Low slide resistance" and "Long-life rectilinear accuracy", the features of linear guide, are of great benefit to extra-large machines whose movable platens and molds weigh tens of tons. By combining the guide with servo motors driven by our dynamic acceleration/deceleration control, we successfully improved both speed and accuracy. Shortening the mold open-close time (dry-cycle time) is directly connected to a growth in productivity (reducing cycle time). The dry-cycle of EC3000SXIII is 7.2 sec, the fastest in the industry. (Fig. 1) Being faster than competing electric toggle type machines by 1.2 sec (14%), the machine has a great advantage over high cycle molding.

Table 1. Major Specification Values.

Clamp unit		EC3000SXIII	
Clamping force	kN	29400	
Distance between tie rods	mm	2110×1810	
Platen dimensions (H×V)	mm	3000×2350	
Opening stroke	mm	1800	
Open daylight (max.)	mm	3700	
Closed daylight (min. - max. mold)	mm	1000~1900	
Injection unit		i215AM	i240AM
Screw diameter	mm	140	150
Injection volume calculated	cm ³	11840	13600
Injection pressure	MPa	180	175
Holding pressure	MPa	150	150
Injection speed	mm/s	130	130
Maximum screw speed	min ⁻¹	114	106
Screw torque	N·m	12700	17300
Plasticizing capacity (PP + talc)	kg/h	940	1050

2.2 High plasticizing capacity

Typically, the high cycle molding of the large resin parts for automobiles takes 30 to 40 sec, and shortening the charge time in the cycle is an issue. Excess time for the charging process (plasticizing) that is not completed during the mold open-close and resin cool down processes increases the cycle time. To address this issue, we have developed a special ESB screw aiming for further improvement of plasticizing olefin resin. (Fig. 2) Along with speeding up screw rotation, plasticizing capacity for 1050 kg/h ($\phi 150$) was achieved, resulting in a 46% improvement over the existing screw (SDB). This improvement has the effect of reducing the time required to charge 3 kg of resin by 4.7 sec.

For molding automotive interior parts, mixtures made by mixing colorless resin pellets and coloring materials (masterbatch) are used. To improve the color dispersion in that case, mixing nozzles with an internal mechanism that mixes a masterbatch and resin are available. The nozzle is superior in terms of color dispersion, however, it has disadvantages, such as increased filling pressure due to pressure loss in resin flow path and difficulty in replacing old resin inside. To resolve the drawbacks while ensuring the color dispersion performance, we have developed a Cross ring (optional) with improved filling

pressure and color change performance. Fig. 3 shows pictures comparing the color dispersion. By using the ring in conjunction with a back pressure rise in charging, we confirmed the color dispersion performance equivalent to mixing nozzles. The Cross ring reduces filling pressure loss by 57% compared with mixing nozzles. This reduction leads to lower power consumption, and the improvement in color change performance is expected to reduce the amount of disposal resin at changing.

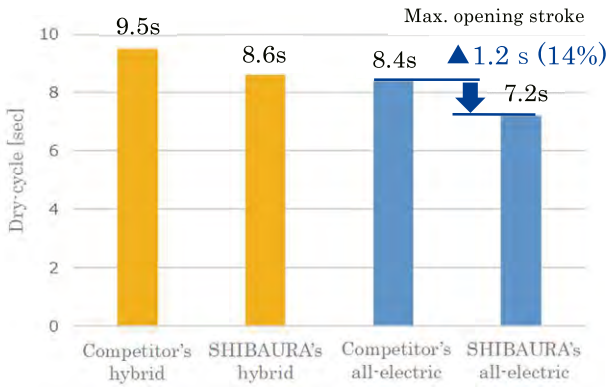


Fig.1. Comparison of dry-cycles

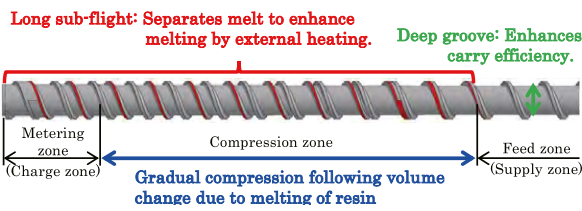


Fig.2. High plasticizing ESB screw

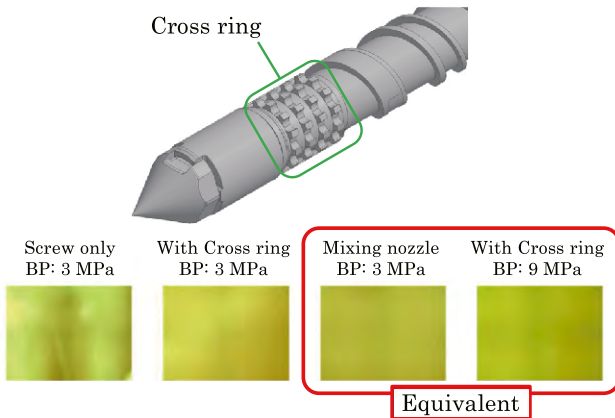


Fig.3. Comparison of color dispersion

2.3 Shortened mold change time

In various small-lot production, it is necessary to change molds frequently. When changing to a mold of different thickness, the toggle type mold clamp unit had a time-consuming drawback in mold thickness setting because of its structure. To overcome this weak point, we employed the linear guide support of link housing and servo motor drive to increase the travel speed in mold thickness setting by 5 times. The larger the thickness difference, the greater the improvement effect. In the case of 700 mm difference, it shortens 4 min and 34 sec (274 sec). (Fig. 4)

Moreover, “INDUSTROL” equipped on our controller INJECTVISOR V70 functions to automate a sequence of processes, such as material supply stop after production, nozzle retraction, automatic purge (color change), mold change, molding condition change, mold warming-up and production start. (Fig. 5) In the past, it was necessary to add a special operation circuit to the machine, which was a costly and time-consuming process. However, users can set up consecutive operation by simply arranging operation icons in order on the “INDUSTROL” screen, which makes it easy for you to streamline the preparation work.

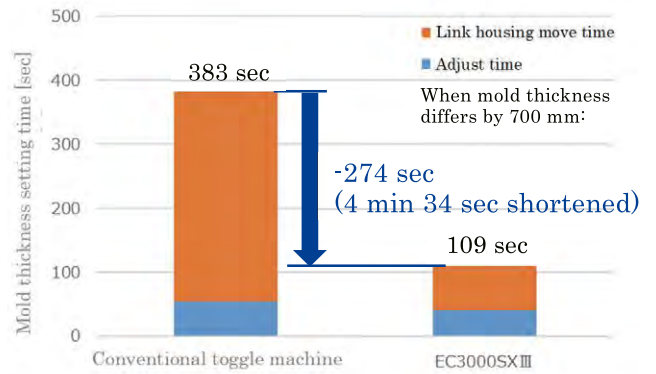


Fig.4. Comparison of mold thickness setting time



Production plan



Preparation function

Fig.5. INDUSTROL screen

2.4 Shortened downtime

Since EC3000SXIII is driven by multiple high-capacity servo motors, it is necessary to increase the capacity of servo amplifiers, the power source of the motors. For the power source, EC3000SXIII uses a synchronous drive system combining multiple small amplifiers instead of a single large amplifier. (Fig. 6) Small type amplifiers are readily available since they are used in small type injection molding machines, and adopting them relatively shortens the downtime due to a sudden amplifier malfunction. Moreover, it becomes easy to prepare maintenance parts by unifying amplifiers with small types whose price is relatively affordable.

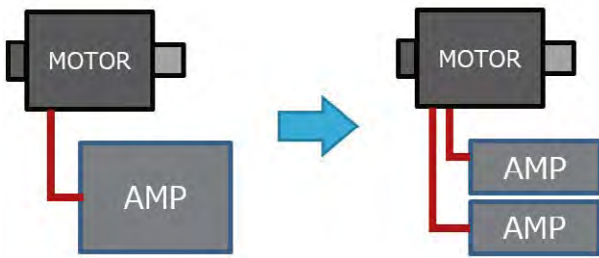


Fig.6. Configurations of servo motors and amplifiers

2.5 Space-saving

The total length and width of EC3000SXIII are the shortest of the competing electric toggle type machines (length: 16.8 m; ϕ 150 screw, width: 4.6 m). This space-saving design improves the flexibility of plant inside layout. Even compared with hybrid type machine ED3000 having composite clamp unit of a superior structure in total machine length, EC3000SXIII is compact with 1 m difference in total length.

2.6 Clean environment and maintainability improvement

By supporting the movable platen with linear guides, tie rod bushings were no longer needed. (Fig. 7) By eliminating the adhesion of grease to tie rods, the grease does not adhere to the mold or molded products, resulting in the improvement of the cleanliness in production sites where operators frequently get inside the machine for some purposes, including mold inspection. Moreover with the conventional slide plate support, aging deterioration due to abrasion on slideways leads to poor parallelism of the mold platens. The linear guide support encounters no aging deterioration, resulting in a significant improvement in machine maintainability.

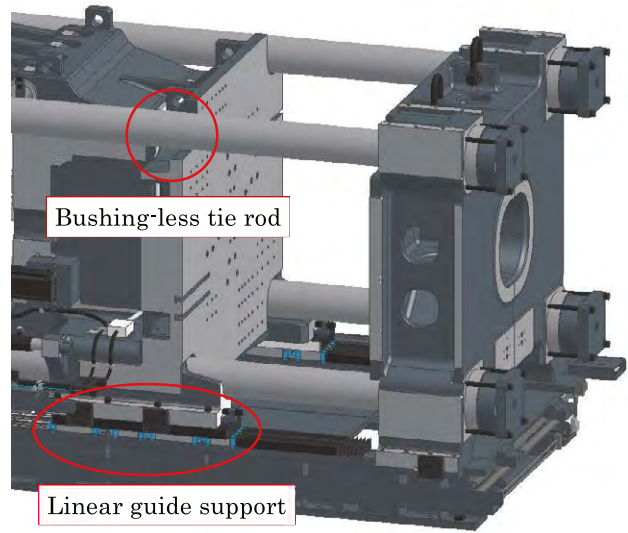


Fig.7. Bushing-less (without bushing) tie rod structure

3 Conclusion

In alignment with the SDG's vision of realizing a low carbon society, we have developed EC3000SXIII, which contributes to users through its higher productivity of injection molding and energy saving performance. We will continue to develop injection molding machines to meet the demands from society for our products.

Development of Table-type Horizontal Boring and Milling Machine BTH Stretched Version

1 Overview (Background/Aim of Development)

Wind power generator manufacturers have begun to bring large offshore wind power generation equipment to market in order to increase power generation efficiency and reduce CO₂ emissions. Mass production of 12-15 MW (megawatts) wind power generation equipment is scheduled to begin in 2024, and 16-20 MW in 2026 or later. As a result, 30,000 new wind power generation units are expected to be installed worldwide by 2035. The component sizes for 16 MW and above will be larger, and the stroke of each axis and table loading capacity of the existing BTD/BTH machines are insufficient for the manufacture of such components. Therefore, in order to be able to handle larger workpieces ahead of competitors and to compete with double-column machine tools, we have developed a stretched version of the BTH early on and propose the superiority of horizontal boring machines.

Fig. 1 shows the appearance of the current BTH machine.

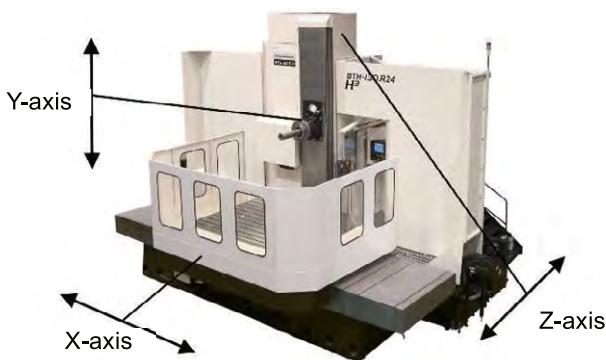


Fig.1. BTH-130.R24

1.1 Market Trend

Fig. 2 shows the market for power generation equipment. As can be seen from the graph, solar power generation equipment and wind power generation equipment account for about 70% with the increase in the total installed capacity.

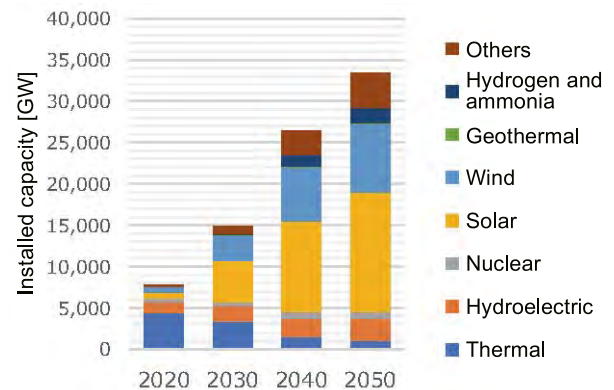


Fig.2. Forecast of installed capacity by power generation source (global, based on our research)

Furthermore, according to the market size of wind power generation until 2030 (Fig. 3), offshore wind power generation is expected to grow significantly: the increase rate of power generation equipment between 2020 and 2030 is expected to be about 2.6 for onshore wind power generation equipment and 8.6 times for offshore wind power generation equipment.

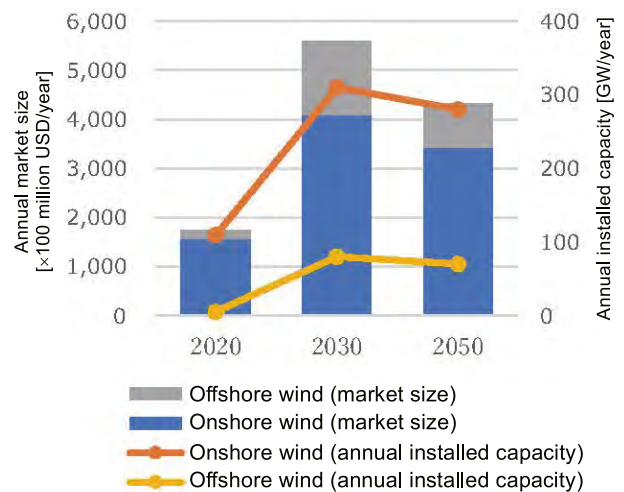


Fig.3. Forecast of market size of wind power generation equipment (global, based on our research)

1.2 Market Analysis

As mentioned at the beginning of this report, in response to the new installation of larger wind power generation equipment of 12 MW or more scheduled to begin in 2024, we have decided to work on the early development of a stretched version of BTH, targeting the manufacturing sector of wind turbines, which account for about 25% of the components used in the equipment.

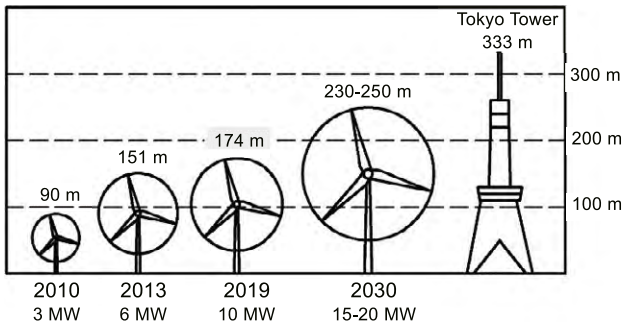


Fig.4. Increase in size of offshore wind turbines (Based on our research)

2 Target Workpiece

As the equipment becomes larger, the size of the speed increaser shown in Fig. 4 also increases. The dimension ϕD , which affects the necessary X and Y strokes of the machine tool, is 1,000 mm to 1,200 mm for 10 MW equipment, but exceeds $\phi 3,000$ mm for 15 MW or more. The strokes of current machines, including competitors' products, are inadequate.

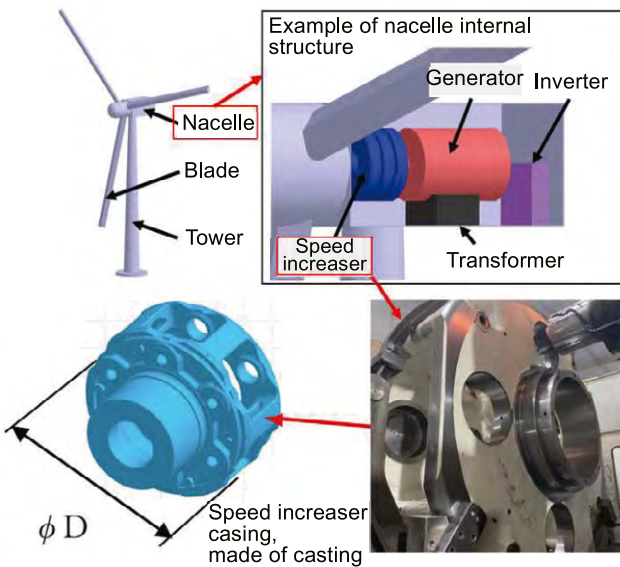


Fig.5. Target workpieces (Based on our research)

3 Stretched Version

3.1 Necessary Machine Specifications for Target Workpiece and Comparison of Competitors' Products

As shown in Table 1, the machine tools, including competitors' ones, can have the X-axis stroke of 4,000, but the available maximum Y-axis stroke is 3,000 mm, which is insufficient for machining workpieces larger than $\phi 3,000$ mm.

Table 1. Necessary machine specifications for target workpiece and comparison of competitors' products

Specification value	Company K (Japanese)	Company P (overseas)	Necessary machine specifications for target workpiece
X-axis stroke	mm 4,000	4,000	4,000
Y-axis stroke	mm 3,000	2,000 3,000	3,500
Z-axis stroke	mm 2,000	2,300 2,700	2,200 (500-2,700)
Table size	mm 2,000x2,200	2,000x2,500 2,500x3,000	2,000x2,400
Loading capacity	ton 30	30	30

3.2 Comparison between Current Machine and Stretched Version

The stretched version has all the axis strokes extended compared to the current machine, and especially the Y-axis stroke is extended by 1,000 mm compared to the existing machine, so machining capability at high elevations is required. In order to achieve the required machining capability, it is important to ensure machine rigidity to improve machining accuracy in high-elevation cutting. Note that machining capability here refers to the performance for achieving the required dimensional accuracy of the finished workpiece, not related to the cutting amount.

In order to ensure machine rigidity, it is necessary to design a machine that takes into account machining with the spindle fed, which is a characteristic of horizontal boring machines. Therefore, we fabricated a test piece assuming the target workpiece and verified machining at high elevations with a similar machine.

Table 2. Comparison of specifications between existing machine and stretched version

Specification value	Current BTH-150.R24	BTH-150.R24 Stretched version
X-axis stroke	mm 3,500	4,000
Y-axis stroke	mm 2,540	3,500
Z-axis stroke	mm 1,500	2,200
Table size	mm 2,000x2,400	2,000x2,400
Loading capacity	ton 25	30

4 Machining Verification with Similar Machine

4.1 Summary of Machining Test

As shown in Fig. 6, high-elevation large-diameter boring was performed with the spindle fed to measure the roundness, cylindricity, hole pitch, and surface roughness of the machined hole, as well as machine vibration (chatter) during machining, to verify whether the expected required accuracy was met.



Fig.6. Test machining

Machining locations:

3 locations: 1,500 mm, 2,200 mm, and 3,060 mm from table top

Machining conditions:

V120 m/min, feed 0.06-0.1 mm/rev

Workpiece material:

FC300 (Size: 700×2,100×160 mm)

4.2 Machining Test Result

The high-elevation large-diameter medium-finish and finish boring tests demonstrated good results, and it was confirmed that there was no chattering even when machining at a high elevation of $Y=3,060$ mm. Furthermore, accuracy and surface roughness measurements also showed good results.

Based on these results, it was determined that the required accuracy could be met with the same level of machine rigidity as that of the similar machine, and we started designing the machine.

5 NC Specifications

For the control of the machine, the latest CNC system “FANUC Series 31i-B Plus” is installed and a high-speed CPU is employed to improve the capabilities of block processing and macro operations, which contribute to high-speed, high-precision machining. The number of look-ahead blocks can be optionally expanded up to 200% of the previous model.

In addition, Shibaura Machinery’s unique program support function enables high-precision machining of workpieces for wind power generation equipment, which is becoming larger and larger.

6 Development and Production Schedule

We proposed this development in March 2023 and started the design in April 2023. The first unit is targeted to be shipped in March 2024. Sales activities of the developed version have already begun, and as of August 2023, we have received an order for one unit and inquiries from several companies. This development is not a model change or a new model,

but rather an optional version of the current machine.

7 Conclusion

We will be the first to introduce a machine tool that can handle workpieces for offshore wind power generation equipment, which is becoming larger and larger in order to further increase power generation from renewable energy sources, thereby also contributing to the SDGs.

Polygon Mirror Generator UFG-150D(PV)

1 Introduction

Polygon mirrors are components used for laser beam scanning and have been used in digital multi-function printers, medical devices, measuring instruments, analyzers, etc. A polygon mirror generator is a machine that generates the mirror surface by cutting each surface of the mirror with a diamond tool.

In recent years, there have been increasing demands to specify the direction of cutting marks on the surface depending on applications, to create smooth concave shapes in addition to simply flat shapes, and to mass-produce relatively large polygon mirrors, such as for ranging sensors for automated vehicles (LiDAR). However, our UFG-80C(P) horizontal polygon mirror generator alone has problems such as limited direction of cutting marks and difficulty in handling large workpieces. Therefore, we have newly developed a vertical polygon mirror generator UFG-150D(PV), which has a rotary axis tilted by 90 degrees compared to the conventional polygon mirror generator UFG-80C(P). Fig. 1 shows the appearance of the developed polygon mirror generator and Fig. 2 shows a polygon mirror photograph.



Fig.1. Appearance of developed polygon mirror generator

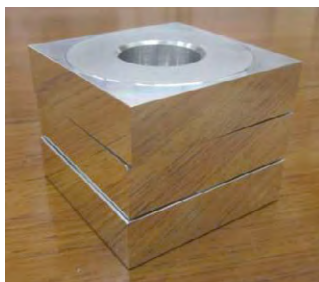


Fig.2. Polygon mirror

2 Feature

2.1 Increase in Travels and Tool Holder Size

To handle both large and small workpieces, the X-axis and Z-axis travels were changed from 70 mm to 200 mm and from 85 mm to 100 mm, respectively. In addition, in order to improve the productivity, the tool holder diameter was increased from 125 mm to 175 mm, and the maximum number of tools was increased from 2 to 4.

2.2 Change of NC

To meet a demand to create a smooth concave shape on the mirror surface, the NC was changed from FUNUC Series 0i MF-Plus to FUNUC Series 32i-MODEL B Plus, which allows finer commands, and the minimum setting increment for the linear X- and Z-axes was reduced from 0.1 μm to 0.01 μm .

2.3 Employment of Air Bearing for B-axis Indexing Table

The conventional bearing and worm gear on the B-axis indexing table was replaced with an air bearing and built-in motor, resulting in improved indexing accuracy, longer service life, and easier maintenance due to the reduced number of parts.

2.4 Automated Workpiece Exchange

By adding an automatic workpiece exchanger as optionally available equipment, workpiece transfer to and from the machining chamber and chip cleaning there can be automated, enabling mass production and manpower saving (Fig. 3).

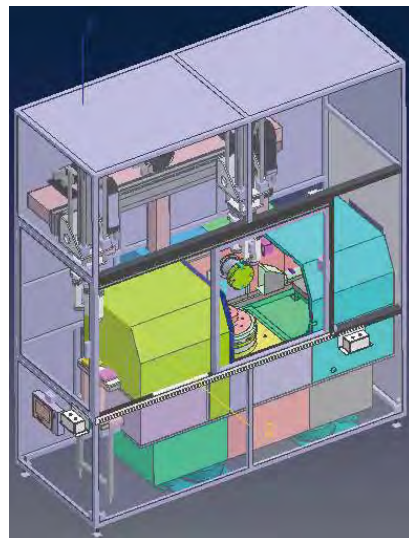


Fig.3. Automatic workpiece exchanger

3 Specifications

Table 1 shows the main specifications of the developed polygon mirror generator. The items in blue are changes from the previous model.

Table 1. Main specifications

	UFG-150D(PV)	UFG-80C(P)
X-axis travel mm	200	70
Z-axis travel mm	100	85
B-axis travel deg	Unlimited	Unlimited
Tool holder diameter mm	175	125
X-axis feed rate mm/min	10 to 1250	10 to 1250
Z-axis feed rate mm/min	10 to 1250	10 to 1250
B(C)-axis feed rate deg/min	10 to 1250	10 to 1250
X-axis minimum setting increment μm	0.01	0.1
Z-axis minimum setting increment μm	0.01	0.1
B(C)-axis minimum setting increment deg	0.0001	0.0001

4 Effects and Examples

4.1 Capability of Handling Large Workpieces and Improvement of Machining Efficiency

With a larger tool holder and extended travel of the linear axes, four-sided polygon mirrors with a maximum face size of 100 mm \times 100 mm can now be generated. In the case of thin polygon mirrors, the productivity of which is improved by stacking multiple pieces and machining them at once, now it is possible to generate approximately 1.5 times as many pieces as with the conventional machine. In addition, the vertical type has the advantage that the direction of workpiece stacking and the cutting feed direction (X-axis) are orthogonal, so the X-axis travel distance does not change even when the number of stacked workpieces is increased, resulting in no increase in machining time. Fig. 4 shows the inside of the machining chamber.

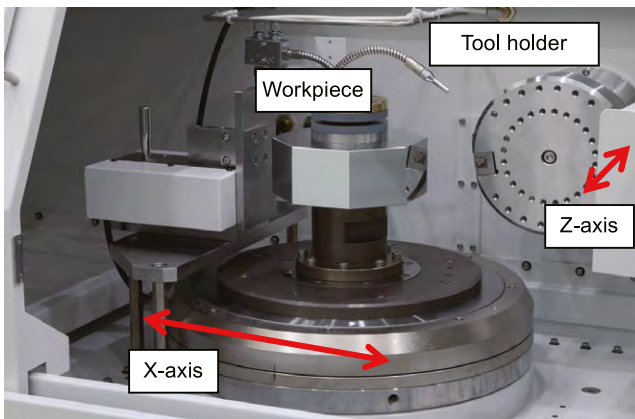


Fig.4. Inside of machining chamber

4.2 Concave Shape Cutting

By reducing the minimum setting increment of the linear axes to 0.01 μm (10 nm), smooth curved surfaces with a concave center of about 200 nm in depth can now be generated in addition to flat surfaces (Fig. 5)

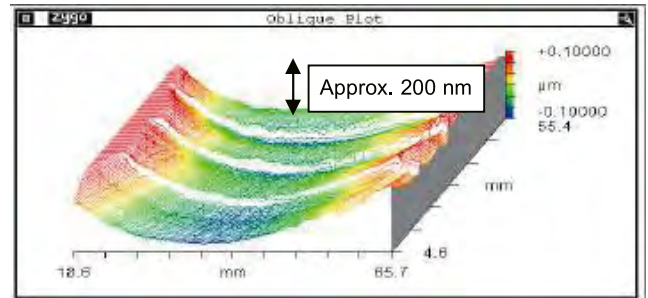


Fig.5. Example of generating curved surface

4.3 Higher B-axis Positioning Accuracy

The positioning accuracy of the B-axis indexing table, when comparing uncorrected values, has improved from ± 4 seconds with the conventional polygon mirror generator to ± 2.8 seconds.

5 Conclusion

As the demand for polygon mirrors is expected to increase further in the future, their productivity needs to be improved. For this purpose, we will contribute to the productivity improvement by increasing the spindle speed, increasing the size of tool holder, performing machining verification to realize 1-pass machining instead of 2-pass machining, and further improving the efficiency of automatic exchangers.

TCmini Series “TC11-02”

1 Overview

TCmini, a microcomputer board that can be programmed by ladder language (PLC language), is a controller capable of achieving optimum functions, size, and cost in accordance with customer needs.

While our current model TC5-02 has been employed in wide fields such as industrial and commercial equipment, we have developed TC11-02 with reinforced network function to meet further market needs.

TCmini employs a new MCU¹⁾ and achieves significant improvement in control performance, reinforcement of network function, and the like while maintaining compatibility with TC5-02 in terms of mounting interface and function.

1):MCU (Micro Controller Unit): a built-in microprocessor equipped with many peripheral functions, such as memories (ROM, RAM, etc.) and I/O-related functions in one integrated circuit.

2 Features

2.1 Improved Controllability

Ladder arithmetic processing time is 1/2 longer than that taken by our current model.

2.2 Increase in Capacity of Ladder Program and Data Register

Ladder program capacity:1.3 times larger than our current model
Data register capacity: two times larger than our current model

2.3 Reinforcement of Network Function

Ethernet communication:Modbus/TCP master/slave control,
Web server function²⁾
CUnet communication³⁾: master/slave control

2):Web server function:

Function of reading/writing internal data from a standard browser of a tablet, a smartphone, a PC or the like.

With the web server function, a low-cost remote monitoring system not requiring an external server can be achieved.

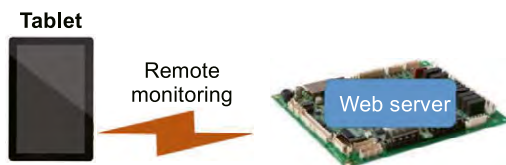


Fig.1. Web server function

3):CUnet communication: Multi-master type remote I/O network

Featured in high noise resistance and long- distance communication
Up to 64 controllers can be connected to one network.

2.4 Additional Functions

Two analog inputs (4-20 mA/0-5 V)
Two analog outputs (4-20 mA/0-5 V)
One serial communication (RS485)
Calendar function as standard item

2.5 Specification Comparison

Table 1. Compared with current model

Item	TC11-02	TC5-02 (current model)
Power supply voltage	5 VDC	5 VDC
External dimension	135(H)×220(W)	135(H)×220(W)
Using ambient temperature	-10°C to 60°C	0 to 60°C
USB communication (for development)	1	-
Ethernet communication	1	-
CUnet communication	1	-
Calendar function	1	-
Serial communication	4	3
Analog input/output	4/2	2/-
Thermistor input	4	4
General input/output	16/16	16/16
Panel I/F	1	1
Extended substrate I/F	1	1
Processing time	5 ms or shorter at 4 kW	10 ms or shorter at 4 kW
Ladder program capacity	32 k words	24 k words
Data register capacity	4096 words	2048 words



Fig.2. TC11-02 Outer appearance

2.6 Effects/Examples

TC11-02 achieves acceleration of ladder arithmetic and reinforces network functions (Ethernet, CUNet, etc.) which are highly demanded by users and has thus become a product supporting achievement of Smart Factory.

[Application Example]

Industrial equipment: Water heater, Chilled tower

Commercial equipment: Business laundry machine,
Coin-operated laundry

3 Conclusion

TC11-02 developed this time reinforces network functions such as Ethernet to thereby widen its application field, and we are going to expand sales thereof.

COLUMN

Learning from Challenging the Unknown



Takuya SHINDO

Research & Development
Center
Research & Development
Department

Engaging in research and development using emerging technologies is like sailing into uncharted waters. XR (Extended Reality) technology, for example, has the potential to change our lives in the future, but is still in an early stage at this point.

After joining this company, I was put in charge of XR technology development. At the time, there was very little knowledge about XR technology within the company, and I remember feeling anxious about it. At the same time, I felt that it was a great opportunity to acquire new knowledge and develop myself by facing unknown problems and difficulties associated with the use of an emerging technology.

My first XR project was the development of an XR application to be used in our product technology briefings for employees.

Failure was not an option, but at the same time, it was necessary to provide a completely new experience. The development itself went smoothly, but on the day of the actual launch, the device overheated more than we expected, and also a sensor calibration error caused the application to crash. Although this was an unexpected situation, with the support of those involved in the project, we were able to resolve the problems and achieve success. It was not a perfect success, but I learned the value of venturing into uncharted territory and the value of understanding what I can obtain from that achievement.

I believe it is important to have the courage to venture into unknown territory. To do this, we need to have confidence in our own knowledge and skills, and change our way of thinking to not be afraid of failure and see each experience as an opportunity to learn. By continuing to challenge ourselves and having our own vision and perspective, we can create a new chart that will guide us in shaping the future.

SCARA Robot THE800/THE1000

1 Overview

Assembling/conveying robot market expands its demand particularly in the field of automobile-related industries, EMS, and smartphone-related industries. Assembly and conveyance processes rely heavily on manpower and have thus a strong demand for automation. Smartphone-related industries and on-vehicle battery-related industries expand their market mainly in Asia. To respond to an increase in demand of an on-vehicle battery due to vehicle electrification, there is a need to develop a robot for conveying on-vehicle battery. Since the load capacity of our existing THL series may become insufficient for heavy weight of the on-vehicle battery. This is the background for development of our functionally-expanded machine, SCARA robot “THE800/THE1000” having a maximum load capacity of 20 kg and achieving wide operating range.

2 Features

2.1 Features of THE800/THE1000

The outer appearance of THE800/THE1000 is illustrated in Fig. 1. As compared with our conventional model THL800/THL1000, the first arm has higher stiffness despite almost the same weight. The third axis (Z-stroke) achieves a wider operating range of 420 mm by default (conventional model: 300mm). TS5000-MS that has significantly been improved from TS3000/TSL3000 in terms of communication function and program language is adopted for a controller. When being combined with TS5000-EMS, THE800/THE1000 becomes compatible with CE. At present, THE800/THE1000 can also cope with a cap specification, (Fig. 2), a bellows specification (Fig. 3), a suspension specification (Fig. 4), and a specification of cable length 15 m (maximum) between robot and controller and plans to support various options (clean specification, dust and drip proof specification [IP65] etc.). Besides, THE800/THE1000 is compatible with logistics automation unit Logi Robo series combining SCARA robot “THE1000”, orthogonal robot “BE60J”, controller “TS5000-MS-AD” for five-axis control.



Fig.1. Outer appearance of THE800/THE1000

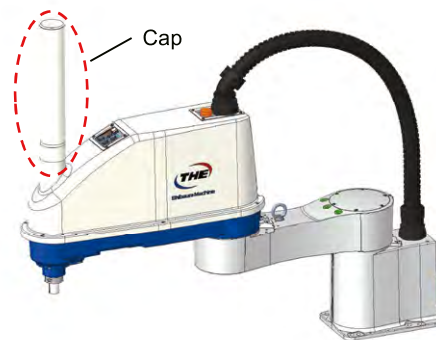


Fig.2. Outer appearance of THE800 (cap specification)



Fig.3. Outer appearance of THE800 (bellows specification)

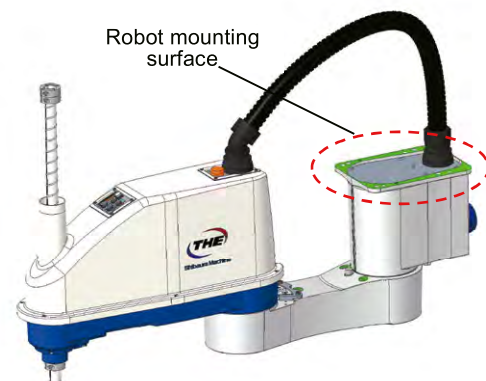


Fig.4. Outer appearance of THE800 (suspension specification)

2.2 Specification

The specification of THE800/THE1000 is as shown in Table 1.

Table 1. Specification of THE800/THE1000

Type		THE800	THE1000	Unit
Structure		Horizontally-articulated		-
Axis configuration		4	4	-
Arm length	Entire length	800	1,000	mm
	First arm	350	550	mm
	Second arm	450	450	mm
Motor capacity	First axis	1,000		W
	Second axis	750		W
	Third axis	750		W
	Fourth axis	200		W
Operating range	First axis	±132		°
	Second axis	±152		°
	Third axis	0 to 420		mm
	Fourth axis	±360		°
Maximum speed*1	First axis	300		%/s
	Second axis	540		%/s
	Third axis	2,200		mm/s
	Fourth axis	1,100		%/s
	Synthesized	8,400	9,500	mm/s
Rated load		5		kg
Maximum load		20		kg
Allowable inertia moment		0.6		kgm ²
Positioning repeatability*2	X,Y	±0.025		mm
	Z	±0.01		mm
	C	±0.01		°
Mass		46	49	kg
Cable length between robot and controller		3.5		m
Connectable controller		TS5000-MS TS5000-EMS (CE specification)		

*1: Maximum speed and acceleration/deceleration rates and may be limited according to the motion pattern, load mass and amount of offset.

*2: Positioning repeatable accuracy in one-direction movement, when the environmental temperature and robot temperature are constant. It is not the absolute positioning accuracy.

2.3 Effects/Examples

As compared with our conventional machine THL800/THL1000, the maximum synthesized speed is improved by about 1.9 times (THE800: about 1.95 times, THE1000: 1.9 times). The maximum load is also improved by two times (10kg → 20kg). THE800/THE1000 is adopted for a palletizing/depalletizing unit and a cardboard box unpacking apparatus in logistics automation unit Logi Robo series.



Fig.5. Logi Robo SP applied with THE1000

3 Conclusion

By the development of THE800/THE1000, line-up (arm length 400mm to 1,000mm) of high-speed, high stiffness, and high trajectory accuracy THE series is completed.

In the future, we would like to enrich available options so as to meet various user requirements and to sequentially market them. In some manufacturing processes for on-vehicle battery, there may be required IP65 and/or banning of using copper-based materials, so enrichment of available options is essential. We promise to do our best for maximizing customer satisfaction.



Masato INATSU

Executive Officer,
Senior Manager of Machine
Tools Sales Department,
Machine Tools Company

Machine tools are indispensable for manufacturing parts, which make up various tangible objects in the world. Parts vary in shape, and suited machine tools vary depending on their shape. Examples include a lathe, which rotates a workpiece, and a machining center, which rotates a tool. It is no exaggeration to say that parts are often made using machine tools, hence the term "mother machine," and that their machining accuracy determines the quality level of finished products. So, how has this machine tool evolved? This report describes the evolution of social needs and the evolution of machine tools as much as possible, using the history of our product development as an example.

1 Introduction

1.1 The Origin of Machine Tools

There are various theories about the origin of machine tools. Of these, the Rokuro wheel, which is still used to make tea bowls and pottery, can be said to be the prototype of machine tools. A wheel operator places clay on a rotating disk (table) and hand-rotates the disk while forming the clay into a round shape like a bowl or pot. The first use of this wheel is said to date back to the Stone Age (6000 to 2400 BC), and the lathe, a machine tool, was created using the principle.

Furthermore, in the Egyptian period (around 1480 BC), the use of a technique called Yumigiri (bow drill) began, in which the bowstring was wrapped around a stick and the bow was pushed down to rotate the stick, making a hole. The "drilling machine" was created using this principle.

The "bow lathe" was created in the Egyptian period by combining the "wheel" and "bow drill" principles, wrapping a string around a workpiece, attaching a tread board to the end of the string, and rotating the workpiece by stepping on the board to machine the rotating workpiece using the blade.

For a while afterward, machine tools using elasticity, water power, and other power sources continued being used until the modern Industrial Revolution.

James Watt invented the steam engine in 1769, but we had to wait for the invention of the "boring machine" (1775) by John Wilkinson (England) for the steam engine to be put into practical use. The invention was designed to machine the inner surface of a cylinder, the heart of a steam engine, and made it

possible to machine the inner surface, which had been done manually. The hand-machining error was at least 1 cm in roundness, but his invention reduced it to about 1.5 mm, contributing greatly to improving the performance of steam engines.

As mentioned, machining uses rotational and linear motions. Furthermore, the emphasis on structure and rigidity improved the accuracy and performance of linear and rotational motions, creating machine tools with better accuracy. Constant technological development of those elements has led to the current machine tools. We offer various products to the world based on such development efforts.

1.2 History of Shibaura Machine

Explaining Shibaura Machinery's manufacturing needs tracing our history.

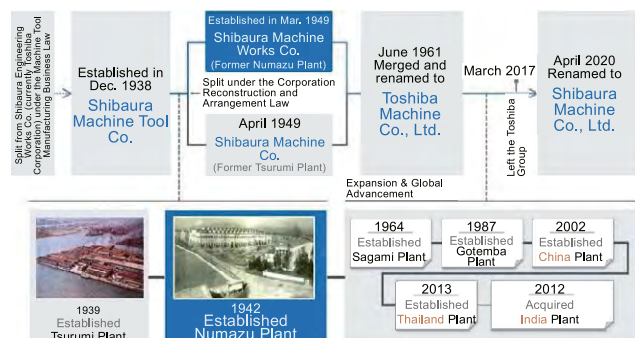


Fig.1. Business transition of Shibaura Machinery

In 1938, in accordance with the Machine Tool Manufacturing Business Law, a special national law enforced to strengthen military capabilities, we

started to enhance our support for manufacturing machine tools, which were cornerstones of military-related production and were subject to relevant regulations. Shibaura Machine Tool Co., Ltd. was established as a new company to allow the Machine Tool Department of Shibaura Manufacturing Co., Ltd. (now Toshiba Corporation) to operate independently (Fig.1).

Machine tools are indispensable equipment for manufacturing weapons, and the higher the technology, the better weapons can be manufactured, which led to the split and independence as a national policy. In that sense, we were manufacturing machine tools for manufacturing weapons following national policies rather than the needs of society. The first machine produced by Shibaura Machine Tool was a 12 m rifle lathe that was ordered in 1940 (Fig.2).

Since then, we continued to expand its business to meet social needs, establishing and abolishing businesses in textiles, injection molding, die casting, extrusion molding, precision machining, control systems, and so on.

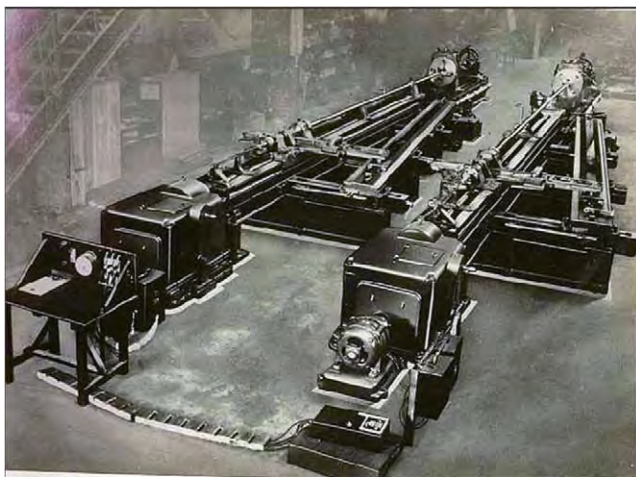


Fig.2. Rifle lathe for 12 m rifles ordered in 1940

This report summarizes how products in the machine tool business, which I am responsible for, have changed in response to changing social needs and satisfied the needs of society.

2 Reconstruction of Japan and Machine Tools

2.1 Starting Point

In 1913, a Japanese steam turbine ship, the Anyo Maru, got stuck at sea. The cause was that the gears in the turbine reduction gears were not aligned, so the load was concentrated on one tooth, damaging it. In the wake of the accident, Kametaro Fujishima (later president of Shibaura Machine Tool), an engineer at the time, believed that Japan, surrounded on all sides by the sea, needed to trade with other countries, and thus the development of shipbuilding technology was necessary for Japan. He believed that he had to manufacture high-precision turbine reduction gears

in Japan, committing himself to the development of the master gear hobbing machine.

His insight accurately matched the social needs of the time and has been passed down as a part of our DNA.

As mentioned in Chapter 1, during World War II, we mainly manufactured machine tools for weapons according to orders by the Japanese military and sold them, but after the war, the manufacture of machine tools was banned.

Even in such a situation, we captured the needs of society and maintained itself by manufacturing electric refrigerators (Fig.3) and tobacco rollers (Fig.4). Later, in January 1949, the then-Ministry of Commerce and Industry designated the Numazu Plant as one of the four most important machine tool plants in Japan. In March 1949, Shibaura Machine Works Co. was established based on the Numazu Plant under the Corporation Reconstruction and Arrangement Law, where machine tool manufacturing resumed.

As the country recovered after the war, society encountered a major turning point. Promoting the development of infrastructure and vitalization of trade, which are necessary for the development of the nation's economy, required the development of infrastructure, such as constructing more power generation facilities, building railway networks, building ships, and improving roads. This needed iron, also known as "rice in industries."



Fig.3. Electric refrigerator (1946)

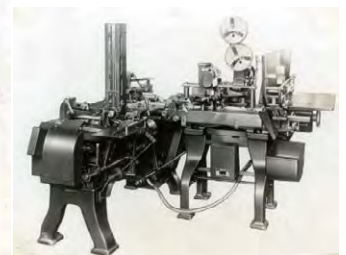


Fig.4. Tobacco roller (1947)

2.2 Along Japan's Fresh Start

Following the maxim that "Iron is the nation," the Japanese government concentrated funds and resources on increasing steel and coal production in 1947.

2.2.1 Machine Tools Manufactured during the War

Going back briefly to our history in wartime, during the war, we continued to produce machine tools to address the needs of society (the nation). After the production of the rifle lathe mentioned earlier, we completed the 3 m vertical lathe T-30/35 in August 1940 and the large

vertical lathe with a maximum swing of 11m the following year (Fig.5).

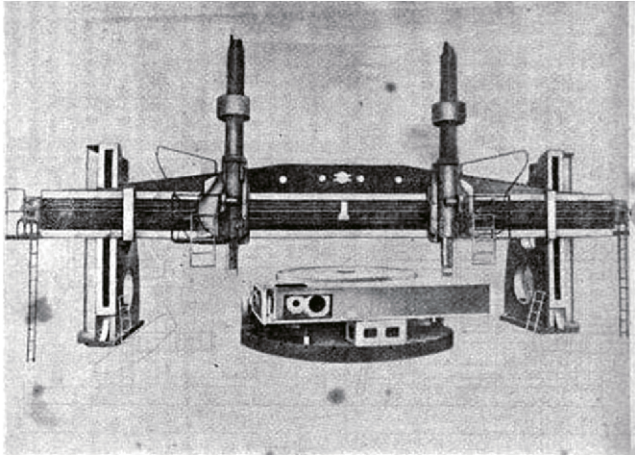


Fig.5. 11 m vertical lathe

Both machines are manually operated except for the table spindle, but surprisingly, both machines have two turrets. In December 1940, we also completed the table-type horizontal boring machine with face plates, laying the foundation for the horizontal boring machine. In 1942, we also completed the surface grinder KPL, the vertical-axis rotary table surface grinder KB-8 (Fig.6), and the large horizontal lathe DK with a swing of 2 m and a center distance of 15 m, which may have been utilized for machining artillery battery parts at that time.

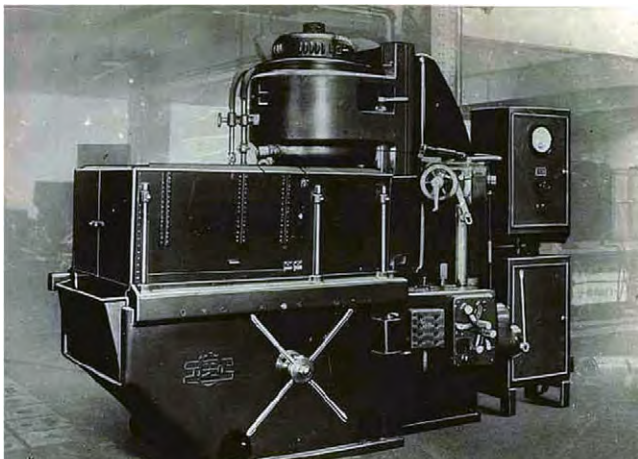


Fig.6. Surface grinder KB-8

Furthermore, in 1943, a double-column flat machining machine, which is the basic structure of the current double-column machining center, was completed (Fig.7).

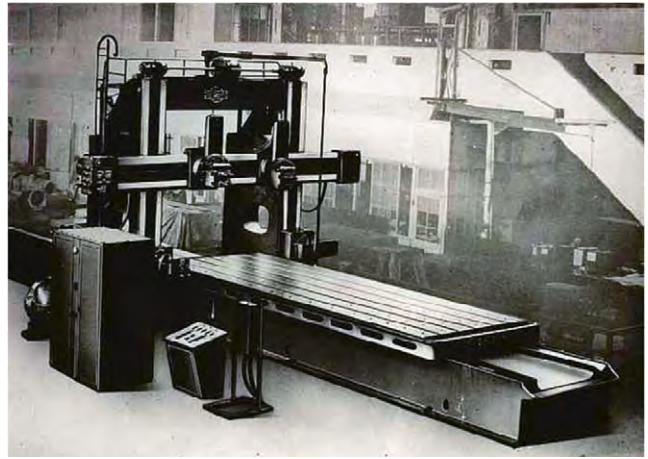


Fig.7. Double-column planing machine

The production of machine tools necessary to machine large parts used in the military can be regarded as the basis of our current large machine tools.

2.2.2 Postwar Reconstruction Period

As mentioned earlier, postwar reconstruction needed iron production. At the same time, publishing started to boom, boosting the demand for paper. The demand for machines to grind rolls for paper production increased, and we received orders and started development of the Roll grinder KRP-955 for paper production, our first large machine tool (Fig.8). We developed it based on a sketch of a roll grinder from Farrell in the United States during the war, incorporating a mirror finish, which was originally developed as a feature not found in Farrell, and we completed it in 1951. In the following year, we also completed the mill roll grinder for steelmaking KRP-1350. We conducted extensive internal and external research on these two machines. Based on the results, we completely changed the design and completed the 3rd machine, demonstrating the world's highest accuracy, which received extensive media coverage.

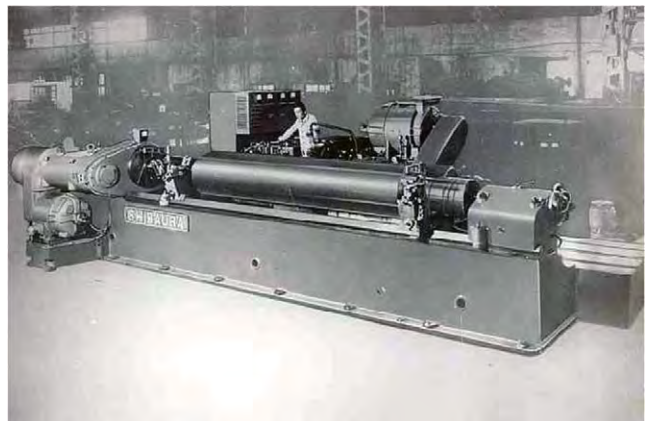


Fig.8. The first roll grinder, KRP-955

In the shipbuilding business as well, we advanced the development of the master gear hobbing machine that we had conceptualized since before the war. We

completed the first domestically produced 5 m master gear hobbing machine in 1953. The indexing accuracy was 8 seconds for CW and 6 seconds for CCW, which was very high for the time (Fig.9).



Fig.9. Master gear hobbing machine HRS-500

In addition, the national railways, which were playing active roles as a means of land transportation, suffered severe damage in the war. With the urgent need to revive and improve land transportation, it was decided to quickly produce machine tools for vehicles, and in the spring of 1946, five machine tool companies, including us, were selected to carry out this policy. In October 1947, we applied for a machine tool manufacturing license and received an order for driving wheel lathes at the end of the year.

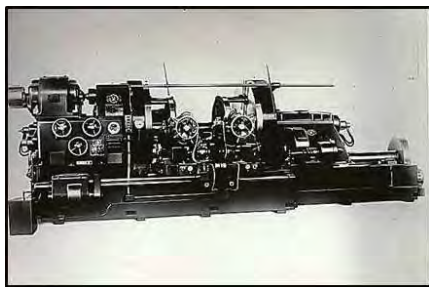


Fig.10. The first postwar machine tool, driving wheel lathe

In 1948, four factories, including ours, were designated as "Important Plant in Japan" by the Ministry of International Trade and Industry on the recommendation of Japan National Railway. In the same year, we completed the first postwar machine tool, a driving wheel lathe. The project continued for about 2 years and helped revive domestic transport.

3 Social Needs and Machine Tools

3.1 High Economic Growth Period

After the postwar reconstruction, Japan experienced rapid economic growth from 1955 to 1973. Overseas trade was regarded as important for economic development, which increased the demand for ships, leading to increased demand for steel manufacturing.

Large vessels require machining large parts such as reduction gears and gearboxes to turn screws. To address this, we completed the first floor-mounted horizontal boring machine, BSF-26, in 1954 and produced the second one, BSF-15Q (Fig.11), and the vertical broaching machine the following year, which were exhibited at the 2nd Tokyo International Trade Fair. A broaching machine is a machine tool that machines (Fig.12) keyways on gears and other components. Keyway machining was also required for gears for ships machined by our master gear hobbing machines, and we produced large vertical broaching machines to meet this need. In addition, we improved the accuracy of the gear of the machine so that master gear hobbing machines can address high-accuracy machining.



Fig.11. Large horizontal boring machine

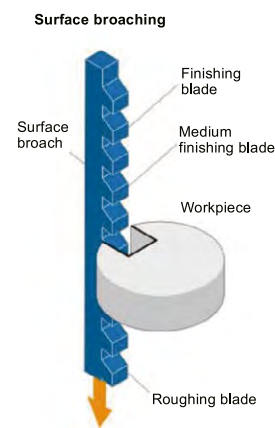


Fig.12. Broaching

In August 1955, we entered into a technical partnership with a French company, Berthiez, for single-post vertical turret lathes and four large vertical lathes (table diameters: 800, 900, 1,000, and 1,400 mm). In 1956, we imported Berthier's original vertical lathe with tracking control TB-10 and exhibited it at the 3rd Japan International Fair.

3.1.1 Beginning of Needs for Automobile Mass Production

Reconstruction started to progress, and accordingly, mass production of automobiles also began. Together with Nissan Motor Co., Ltd. and Hitachi Seiki Co., Ltd., we worked on "research and implementation of transfer machines" and completed and delivered transfer machines for cylinder block machining to Nissan Motor Co., Ltd. in July 1956. This project won the Okochi Production Award in April 1957. With the advent of this transfer machine, mass production of automobile engines began.

3.1.2 The Beginning of NC

Before and after World War II, all machine tools were manually operated using gears, cams, feed screws and

clutch mechanisms. Machine tools are said to be "machines that make machines" and thus called "mother machines." They feature the adjustment of the relative positions and speeds between tools and workpieces for machining. It means that because operators made the adjustment, they were familiar with the "quirks of individual machines" to secure machining accuracy. In 1949, at the request of the U.S. Air Force, John T. Parsons collaborated with the Massachusetts Institute of Technology on an NC device for the purpose of numerically controlling machine positions and speed information and programming motions for machining, and developed the world's first NC device in 1951 and the first NC milling machine in the following year. This was the beginning of NC machine tools. Using the development as an opportunity, machine tool manufacturers began developing NC-equipped machine tools. In 1958, with the support of Toshiba Corporation, we began developing the Numerically Controlled Automatic Turret Lathe, and the following year exhibited the VTN-10 Numerically Controlled Turret Lathe at the 6th Tokyo International Trade Fair. In 1959, we completed the table-type horizontal boring machines, BFT-11A and 13A, which are still our main machines, and the following year, we completed the BFT-9(S)NC equipped with an NC device, giving birth to the original table-type horizontal milling boring machine (Fig.13).



Fig.13. Table-type horizontal boring milling machine BFT-9(S)NC

3.1.3 Meeting the Needs of Large Parts Machining
 After the development of NC machines, Shibaura Machine Works Co. acquired and merged with Shibaura Machine Co. in June 1961 and changed its trade name to Toshiba Machine Co., Ltd. It was when the need for machining large parts increased, and a large plant was constructed (completed) at Numazu Plant in December of the same year. In April 1962, Japan's largest horizontal floor-mounted boring machine (ram type), BSF-32/19, was awarded the Japan Society of Mechanical Engineers Award as a machine tool that

could contribute to large-scale machining. With the completion of this large-scale factory, we focused on the production of large machine tools to address large parts machining and developed large vertical lathes for heavy electric machines. In July 1963, we completed one of the largest vertical lathes (two turrets), TWI-80/120 (maximum machining diameter: 12 m) in Japan, for the Japan Steel Works M&E, Inc. Muroran Plant. (current Japan Steel Works M&E, Inc.) The machine employed the first full-scale hydraulic static pressure guide, and this technology is the basis of the current static pressure guide (Fig.14). By improving the production capacity of large machine tools, we contributed to the improvement of Japan's infrastructure and trading capability and supported the high economic growth.



Fig.14. Large vertical lathe TWI-80/120

Propellers for ships also needed large parts machining. In 1965, a propeller boss processing machine, PB-32, was completed as a machine dedicated to machining large-diameter tapered holes, end faces, and keyways in propeller bosses for incorporating drive shafts into propellers for large ships. The following year saw the completion of PBD-80A for Kobe Steel, dedicated to machining propeller blade surfaces (Fig.15).

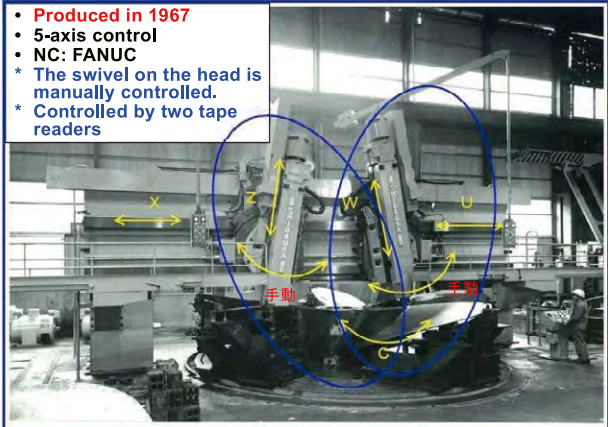


Fig.15. PBD-80A dedicated to matching propeller blades

This blade-surface processing machine was equipped with 2 spindle heads and featured simultaneous 5-axis control of 4 straight axes and 1 table-turning axis using the NC device. Until then, the shape of the blade had been machined manually by checking the shape with a pattern board, but the new machine realized some automation of shape machining by 5-axis control with the 2 tape readers. In recognition of its achievements, the machine was awarded the Nikkan Kogyo Shimbun's Top 10 New Products Award in 1968.

The completion of large factories and the installation of NC devices made it possible to manufacture a variety of large machine tools, which realized shapes that were difficult to machine manually. This led to the development of large machines dedicated to components such as hydroelectric waterwheel blades and propellers for large ships. We developed large dedicated machines, such as waterwheel blade processing machines (5-axis NC machines) and large 5-axis numerically controlled milling machines for curved surfaces of waterwheel runners. In addition, we received increased demand for floor-mounted horizontal boring machines and large vertical lathes equipped with NC devices from heavy electrical machine companies, increasing their production of these large machines.

The market demand shifted to NC installation, and we applied the NC technology we had accumulated in producing large machines to roll lathes, roll grinders, table-shaped horizontal boring machines (horizontal general-purpose machines), and general-purpose vertical lathes, which marked the beginning of NC machines. In October 1968, the era of machining centers arrived with the completion of their first self-branded NC machining center with an automatic tool changer, MC-6A.

3.1.4 Further Complex and Efficient Large Machines

With the age of heavy-and-long continuing, the demand for large and dedicated machines necessary for heavy electric machines, steelmaking, etc. continued, but large machines, which must not cause machining defects, needed to reduce the risk of failure caused by changeover. Changeover was needed for changing processes, such as turning, milling, and drilling, which posed a risk of failure each time. The market began to demand decreases in changeover as a major challenge for larger machines.

To meet this need, we started to conceptualize a large double-column multitasking machine tool in February 1968, beginning the design work in November. A large double-column multitasking machine tool turn miller, TM-53/90A, was completed in April 1970 (Fig.16). The machine is a multitasking machine that can perform turning and milling with a milling head and turning head, and is equipped with two FANUC NC machines, F260B, to support automation.



Fig.16. Turn miller TM-53/90A

It is a gantry-type machine tool with a double-column head and turret that moves forward and backward, looking like it crosses over a large turning table. Currently, various manufacturers are making machine tools more multitasking, but we have been developing multitasking machines to satisfy social demands for multitasking since more than 50 years ago.

We continued to meet the demands for automation and greater efficiency in large machines, and in August 1970, completed the gantry-type NC plano miller MG-24/14A (Fig.17). This machine is an ultra-large NC machine tool with a gantry width of 11 m and a length of 23 m (in the direction of the forward and backward direction of the gantry) with an NC device F220 equipped.



Fig.17. Gantry type NC Plano Miller MG-24/14A

This machine made it possible to program the machining of casings and others of large turbines, leading to greater efficiency.

3.1.5 Efforts to Improve the Accuracy of Large Machines

I would like to briefly describe our efforts on large machine tools as mother machines. We produce large machine tools, which are used to machine large parts for the main unit of machine tools. Therefore, the machining accuracy of parts of the machine tools

greatly affects the accuracy of the finished machine tools. This is called the "copying principle of machine tools." The "copying principle of machine tools" refers to the characteristic that "the accuracy of the parts to be machined depends on the accuracy of the machine tools that machine them." Then, a question arises: Can the machine tool not achieve higher accuracy than the machine tool that machined them? Finishing parts with accuracy beyond the copying principle was realized by adding craftsman's skills to adjust "scraping" and others in machined parts. The "craftsmanship" of professionals is and always has been important to improve machine accuracy.



Fig.18. The machine dedicated to worm & rack and nut processing MWR-3510

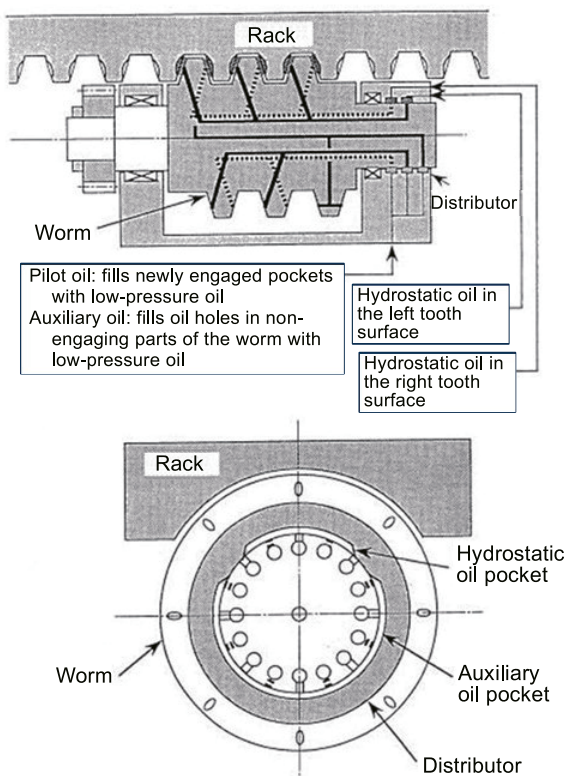


Fig.19. Overview of static pressure worm and rack mechanism

In addition to "craftsman's skills," the development of new structures and mechanisms is an essential means

of improving machine accuracy. We have refined our static pressure technology for manufacturing ultra-large machine tools. Static pressure technology makes it possible to bear high masses reaching tens of tons or more and is an essential technology for manufacturing very large machine tools. However, the rack-and-pinion mechanism was often employed to linearly move objects of such a high mass, but it had various problems such as backlash, aging deterioration, service life, and vibration. Solving these problems improves the accuracy of ultra-large machine tools. We have developed a "static pressure worm and rack" mechanism to solve them. Even with a theoretical design, we faced another problem: there were no processing machines to actually construct the mechanism. We also developed a processing machine to construct the new mechanism (Fig.18). The development improved the accuracy of ultra-large machine tools and the accuracy of parts for large machine tools, which enabled us to meet the need for higher precision. The "static pressure worm and rack mechanism" is a combination of a semicircular rack and a worm. Supplying hydrostatic oil to each blade of the worm causes a static pressure effect between the rack and worm, achieving stable linear motion even with heavy loads (Fig.19). This technology was also used for manufacturing large parts for machines other than machine tools, contributing to higher accuracy in the machining of large parts in the industries of heavy electrical machine manufacturing and shipbuilding.

4 Diversification of Social Needs

More machine tools were equipped with NC devices, which advanced program-controlled machining. The "National Income Doubling Plan" was approved by the Ikeda Cabinet in 1960, and the 1964 Tokyo Olympics were to be held. Triggered by those, Japan began to improve delayed infrastructure, advanced industrialization, promoted free trade, improved human capacities as well as science and technology, and transformed industrial structures, which rapidly grew Japan's economy and led to a period of high economic growth.

4.1 Mass Production and Machine Tools

In the high economic growth period, exports of industrial products increased, and more general households could afford to purchase home appliances and automobiles. To meet these demands, manufacturers needed to mass-produce products. This needed mass production of parts to be machined with machine tools, which increased mass production of workpieces, and continuous automatic operation of machine tools became the need of the time.

The trend can be seen in the development history of our machine tools. The first was the automation of vertical lathes. Conventionally, when workpiece machining was

completed, the worker picked up the completed workpiece from the table, cleaned the table, and set up and centered the new workpiece for processing. The setup and cleaning were bottleneck processes. This led to the development of an automatic change function for short workpieces of a diameter of about 1 m requiring a relatively short time for machining. A function to automatically change the pallet (table) on which the workpiece is to be set (APC: Automatic Pallet Changer) was developed and an NC vertical lathe equipped with this device was completed, realizing continuous automatic machining of same-shaped workpieces and contributing to the mass production using turning (Fig.20).



Fig.20. NC vertical lathe TMC-13A (with automatic pallet replacement function)

The need for automation increased further. In 1968, an Automatic Tool Changer (ATC) was installed on an NC horizontal machining center to automate machining with many tool changes, meeting the need for more efficient machining. The need for automation extended to highly versatile table-type horizontal boring machines, and in the early 1970s, we completed the table-type horizontal boring machine equipped with ATC and APC installed, BTN-10B, to meet the needs of automatizing horizontal boring machines. These automation technologies have become the basic technology of today's machine tools.

In addition, the transfer machines mentioned in Section 3.1.1 were needed more to mass-produce engine parts in the automotive industry, and the machines were also introduced by various automobile manufacturers.

4.2 The Oil Crisis

Japan continued to grow at a rapid pace, but it was at geopolitical risk just as today.

That was tight crude oil supplies and soaring oil prices that occurred twice in the 1970s. In 1973, the Yom Kippur War broke out, which triggered the first oil crisis (continued until March 1977), and in 1978, the second oil crisis (continued until March 1983) occurred,

triggered by the Iranian Revolution.

The surge in crude oil prices caused significant damage to various industries, initiating energy-saving efforts. In addition, pollution-related regulations were tightened, and efforts have been made to conserve resources, save energy, and improve work environments. Emissions controls were also a pressing issue in the automotive industry because it needed to comply with the U.S. Muskie Act in early 1970. This made the automobile industry work on "low fuel consumption" and "emissions regulations," reducing energy loss by improving the accuracy of engine parts, decreasing NOx, and improving energy efficiency by making cars lighter. This trend was followed by similar efforts in the shipbuilding and construction machinery industries, resulting in demand for better accuracy and higher speed of machine tools.

4.3 Improvement of Energy Efficiency and Machine Tools

Then, what were required of the machine tools? A very few of them are explained below, taking shipbuilding as an example.

4.3.1 Machining Screws for Large Ships

Some screws for large ships are as large as 10 meters in diameter. A rotational power produced by the engine is transmitted to the screw, which rotates the screw, cruising the ship due to the resistance against the water. Poor shape or surface condition of the screw causes vibration or noise, and cavitation due to pressure difference results in energy loss, losing the energy required to propel the ship. Therefore, it is necessary to machine screw shapes as close to the theoretical value as possible. The propeller blade processing machine shown in Fig.15 had two spindle heads. A total of four straight axes and one table turning axis were NC-controlled simultaneously, but the spindle heads were turned manually. Because the turning position of the spindle head was determined manually before machining with the program, level differences were created on the machined surface, which was finished by hand. We added a turning axis to the spindle tip in the same axis configuration and produced 9-axis machines in 1976. By installing a FANUC NC device, we realized simultaneous 9-axis-controlled machining, which minimized manual intervention in machining, achieving highly accurate propeller machining. The result was reduced vibration and noise, improving the energy efficiency of ships (Fig.21).

Introductory Note
Special Article
Technical Paper
Technical Report
New Product
Series
Patent News
Prepared Critique

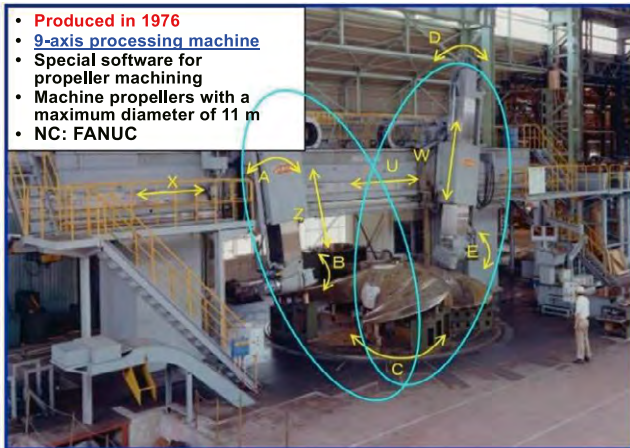


Fig.21. Simultaneous 9-axis-controlled propeller blade processing machine MBP-110

4.4 Transition of Machining Dies and Molds for Automobiles

With the advancement of NC machine tools, higher speed and better accuracy were demanded for machine tools. This section describes how machine tools have evolved to meet the demand, although partially, using as an example the changing needs of machining automobile dies and molds.

4.4.1 NC Installation in Processing Machines for Automobile Dies and Molds

Roughly speaking, there are three dies and molds for making parts for car body and interior. One is the body, which is pressed out of thin steel sheets using a die, another is plastic parts for interiors and so on made by injection molding machines, and the other is engine parts of aluminum castings made using die-casting machines. Each of these parts is produced using a die and mold, which are machined and made by a machine tool. Steel sheet bodies, plastic products, and aluminum die-cast products account for a high proportion of the overall mass of a vehicle, and the shape accuracy of dies and molds plays an important role in reducing the weight of the vehicle. There are two types of dies and molds, female and male, which are mass-produced by molding the material in a die.

In the 1960s and 70s, machining of dies and molds was performed with devices equipped, following machine tools with horizontal or vertical spindles. Then, in the late 1970s, NC-controlled horizontal machines were used to perform roughing, with finishing performed by double-column machining centers. When the machining is complete, the male and female dies and molds are fitted together to check the engagement and then adjusted by hand to complete them. Poor shape accuracy of dies and molds leads to time-consuming hand finishing, and variants in wall thickness of products formed with the adjusted die leads to uneven strength and increased mass of the molded product. Therefore, reducing the weight of automobiles requires finishing the shape of dies and

molds with high accuracy. Around this time, every household demanded one automobile, increasing the demand for dies and molds, so the demand for shorter die production lead time (LT) increased, resulting in the demand for shorter machining time of dies and molds.

4.4.2 Meeting the High-speed and High-accuracy Demands of Processing Machines for Dies and Molds

As more machine tools were installed with NC devices, servo motors were used in machine tools. The result was improved positioning accuracy of machine tools, and even non-skilled workers were able to machine with high accuracy. Onward, NC devices continued evolving. To learn more about the evolution of our NC devices, please read our Engineering Report No. 29.

Years passed, and personal computers (PCs) became commercially available in the 1980s, and general households began to own a PC.

Since then, the NC devices installed in machine tools also improved in processing performance, speed, and memory capacity, allowing for machining using large-scale programs.

When people started to use CAM to create machining programs, die and mold machining programs were also created using CAM, making it possible to produce even more complex and highly functional dies and molds. Around this time, NC devices, CAM software, and cutting tools began to evolve rapidly. Of course, it was necessary to develop machine tools that followed this evolution. Ball screws, linear guides, BRGs, and servo motors, which were indispensable for their feed mechanisms, were required to evolve for higher speeds, making them evolve rapidly as well.

In line with the demands for high-speed and high-accuracy die and mold machining and the evolution of NC devices, we also developed the MPF series of double-column machining centers with built-in motor spindles with a spindle speed of 6,000 min⁻¹ for die and mold machining in 1992 (Fig.22).

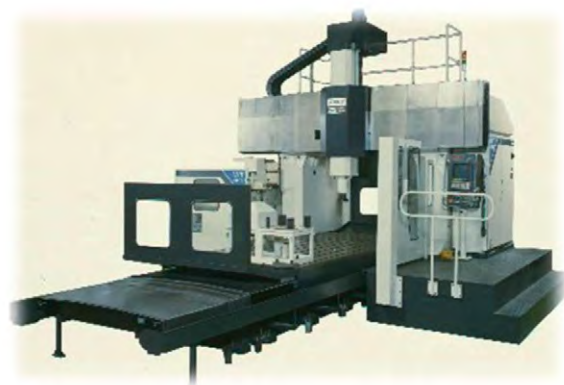


Fig.22. Double-column machining center MPF-2140A

As the die and mold machining accuracy improved,

dies and molds also became larger to improve production efficiency, so processing machines meeting their size and mass were required. Many of Japan's die and mold processing plants had limited space, making it difficult to introduce large-die (mold) processing machines. Therefore, we believed that we needed a machine tool that could machine large dies and molds in a small space, and in 1994 we developed the MPF-C series of double-column machining center with a spindle speed of $8,000 \text{ min}^{-1}$, which could machine large dies and molds in a small space at high speed (Fig.23).



Fig.23. MPF-C series double-column machining center

Equipped with a table with a maximum loading mass of 10 tons (size: $1.8 \text{ m} \times 1.4 \text{ m}$), the machine can be fitted in a space of 6 tsubo (19.8 m^2). It was well received by many customers as a machine capable of machining large dies and molds in a small space with high speed and high accuracy.

4.3.3 Dealing with Complex Die and Mold Shapes

As automobiles continued to be made lighter around the latter half of 1990, bumpers and other parts that had previously been made of metal were changed to resin (plastic) products. This increased streamlined parts, and the dies and molds for bumpers and instrument panels became deeper and more complex. Besides, other dies and molds for automotive interiors also became more complex-shaped, which increased the amount of data in a machining program. Furthermore, LAN equipment in plants became more common, making it necessary to address high-speed, high-capacity communication for LAN, PC, and NC, and each of them continued to evolve rapidly. The spindle speed of machine tools was also improved to address higher speeds, leading to a rapid evolution of tools.

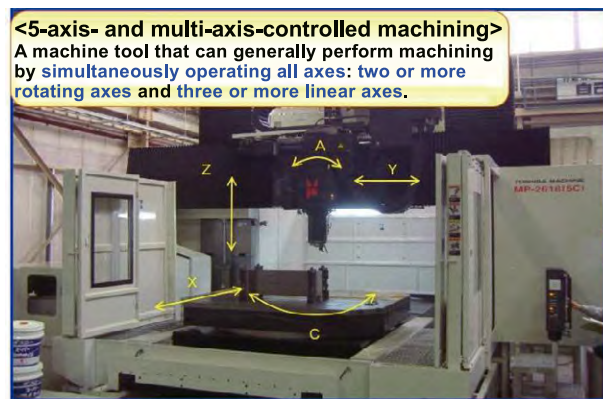


Fig.24. MP-(5C) series of high-speed 5-axis double-column machining center

In 2000, the improvement of efficiency and accuracy of die and mold machining simply by increasing speed was expected to reach the plateau; 5-axis machine tools with 3 linear axes and 2 rotating axes began to be used for die and mold machining. We have also developed the MP-(5C) series of high-speed 5-axis double-column machining centers with a spindle speed of $12,000 \text{ min}^{-1}$, which dealt with increased efficiency of increasingly large-scale and more complex die and mold machining (Fig.24).

5 Making Machines More Multitasking

Machine tools are mother machines used in various industries. Social needs have always been based on efficiency, energy conservation, and high accuracy; therefore, we conceived that 5-axis machines alone could not meet further needs any longer. That is why we came up with the idea of making machines more multitasking. There are various processing methods, such as milling, turning, and gliding. Each machine tool is used for each of these machining methods, and at the machining site, various machine tools are used for producing one workpiece. Believing that realizing such various machining with a single machine would reduce non-machining time and achieve even better efficiency, we presented a new proposal in the category of multitasking processing machines at the 2008 Japan International Machine Tool Fair (JIMTOF). The proposal was about a double-column multitasking machine (Fig.25).

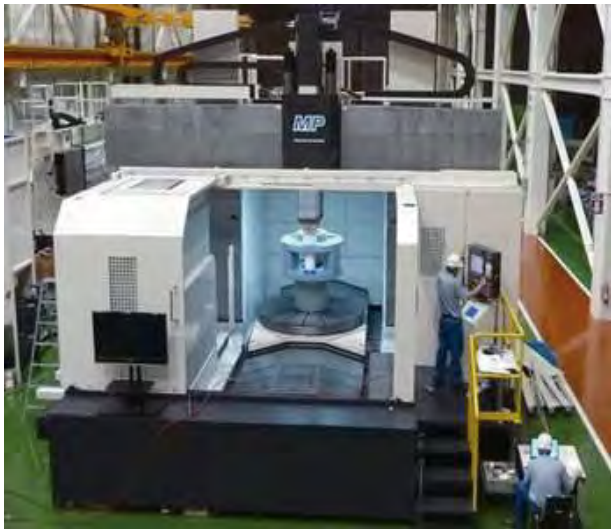


Fig.25. Double-column multitasking machine MP-2620U

The machine is a multitasking machine that can also perform simultaneous 5-axis machining with double-column and vertical lathe elements combined. With a spindle speed of $10,000 \text{ min}^{-1}$, the machine tool can machine workpieces at one step that require 5-axis machining and turning, such as waterwheels, turbine blades, impellers, and wind power generation components, which are complex in shape and require many changeovers, at single setup.

Although I described it as a new proposal, we have long manufactured ultra-large machine tools to meet the demand for heavy and long products. We have considered it inefficient to change setups for each machining process of workpieces weighing several hundred tons, addressing them with multitasking machining. The technology was incorporated into high-speed 5-axis machines. Currently, we are also involved in the integration of machine tools with new joining technologies such as FSW (Friction Stir Welding).

6 Conclusion

I described the very long history of machine tools together with the changes in society, but I would like to apologize for covering only a tiny part thereof. This report describes the introduction of multitasking machines proposed in 2008 and their integration with FSW. However, much remains to be introduced after that, including their relations to aircraft, railways, space, and renewable energy, so I will introduce them at a later time.

Machine tools has continued evolving along with social needs, and society has also changed its demands in response to the evolution of machine tools. As someone who has been involved in machine tools, I believe that the results of these efforts support the delivery of high-quality products to the world and the betterment of our lives.

Today, various industries undergo major changes to

achieve a circular society with sustainability and digitization. One of them is the advancement of electric vehicles and autonomous driving. I hope that our machine tools will follow changes in the world and continue evolving to contribute to a prosperous world.

Patent Introduction

One of our company policies is "Respect for Intellectual Property Rights" and we protect the results of our technological development by intellectual property rights, while we also respect the intellectual property rights of third parties. We focus on technological development to provide products, systems, and services that satisfy our customers. As a result, we hold approximately 1,700 patents in Japan and abroad. Among them, this article focuses on patents related to labor productivity improvement. These patents have been highly rated by the Patent Score from Patent Result Co., Ltd.

(Patent Score: an index for evaluating the degree of attention given to individual patents by scoring them based on information on the examination process)

1 Molding Machine

Patent number: 7,058,794
Inventor: Tetsuya Mita

In the case of typical molding machines, information related to the control unit is displayed on a display screen fixed to the control unit, while information related to the operating unit is displayed on another display screen fixed to the operating unit.

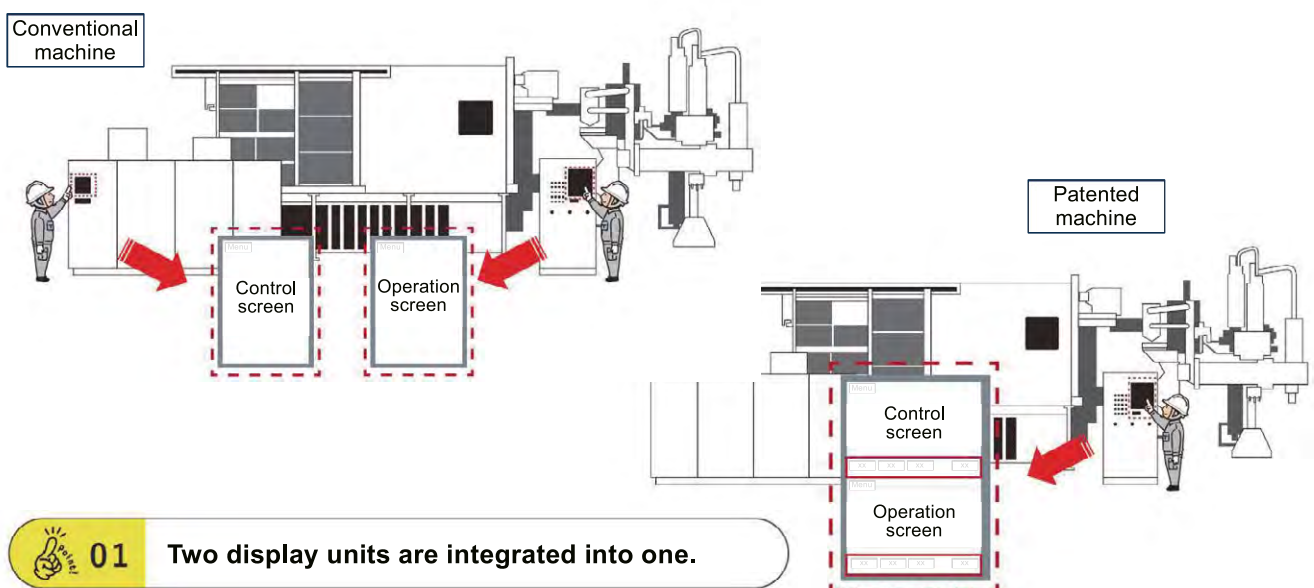
When operating a conventional die casting machine, for example, the operator needs to go back and forth between a display screen fixed to the control unit and another display screen fixed to the operation unit, which causes a problem of reduced operability of the die casting machine.

The patented molding machine display unit can display any two of the following screens on a single display: a setting screen on which parameters used for automatic operation can be displayed and entered; a monitor screen on which the operation status of the clamping unit and injection unit is displayed; and a maintenance screen on which the cause or location of an abnormality in automatic operation, when it occurs, is displayed. Each of the setting screen, monitor

screen, and maintenance screen has a button for switching to the operation screen, which greatly improves the operability of the machine.

In addition, in order to ensure smooth machine operation, the following usability improvements are made.

- ① Automatic switching of the operation screen in conjunction with switching of the machine operation mode.
- ② Combining the display of documents such as instruction manuals (PDF) and the PLC program with the display function for early problem solving.
- ③ Placing indicator lights inside the screen and customizable screen design for each user.
- ④ During production, in which no operation is needed, the operation screen can be closed and another screen can be displayed.



01

Two display units are integrated into one.



02

The operation buttons inside the screen allow for easier operation.

2 Imprinting Machine and Imprinting Method

Patent number: 6,359,167

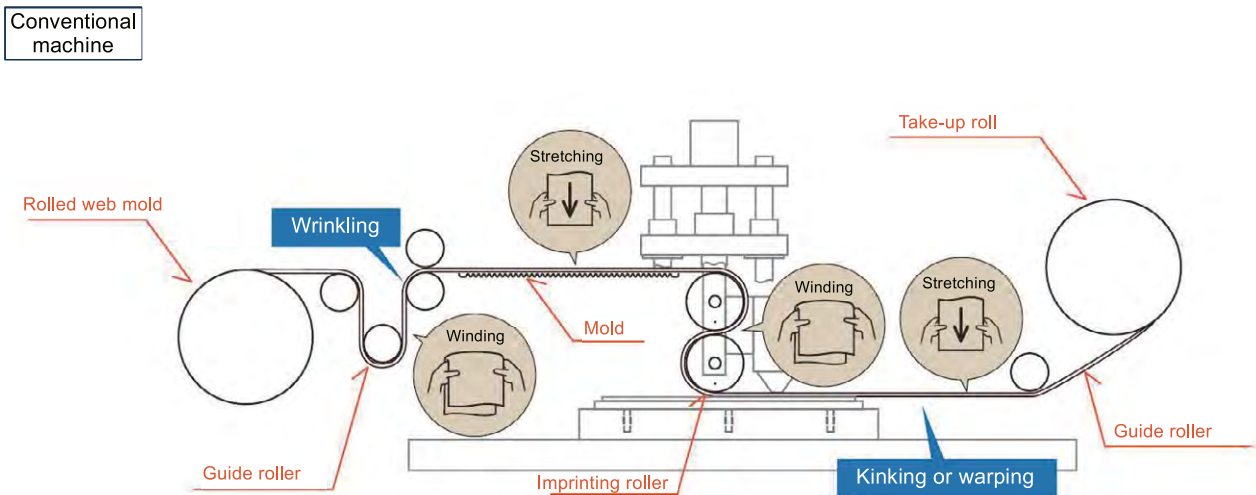
Inventor: Mitsunori Kokubo, Takato Baba, Toshiaki Goto

In an imprinting machine that imprints a fine transfer pattern formed on a mold onto a substrate, the mold used for imprinting is stretched and installed between the rolled web mold and the take-up roll.

In conventional imprinting machines, the mold is manually placed and stretched between the rolled web mold and the take-up roll without using any equipment or tools at all. Therefore, it was very difficult to precisely place the mold between the rolled web mold and the take-up roll, and for example,

wrinkles occurred in the mold when there was a slight kink in the mold being rolled out and stretched from the rolled web mold.

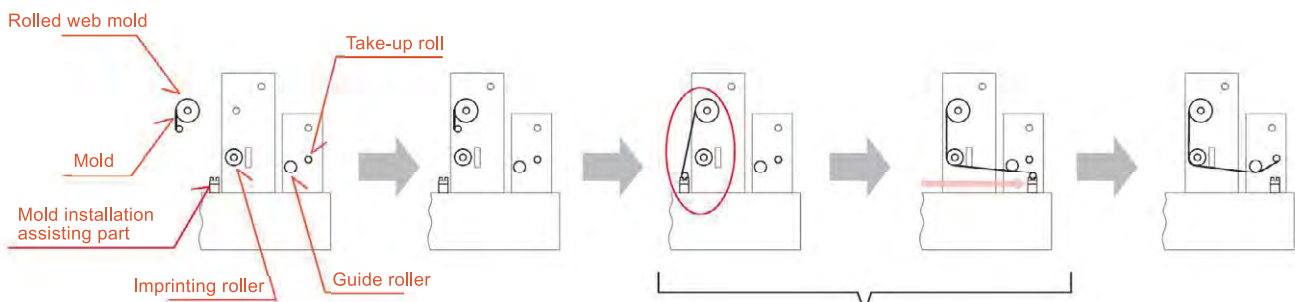
This patented imprinting machine allows a mold, when installed in the rolled web mold installation section, to be wound onto the imprinting roller, wound onto the guide roller, and fed to the take-up roll without manual intervention by the mold installation assisting part that guides the mold to the vicinity of the take-up roll, thereby minimizing wrinkles and facilitating accurate mold installation.



The mold is manually wound and stretched to be installed on the imprinting machine.

The present invention

- ① Mold preparation
- ② Mold placed
- ③ Winding start
- ④ Winding completed
- ⑤ Mold installed



When a mold is placed on the mold installation assisting part, it automatically performs winding.

Molds can be precisely installed without manual intervention thereby minimizing wrinkles.

3 Kneading Method Using Twin-screw Extruder

Patent number: 5,572,776

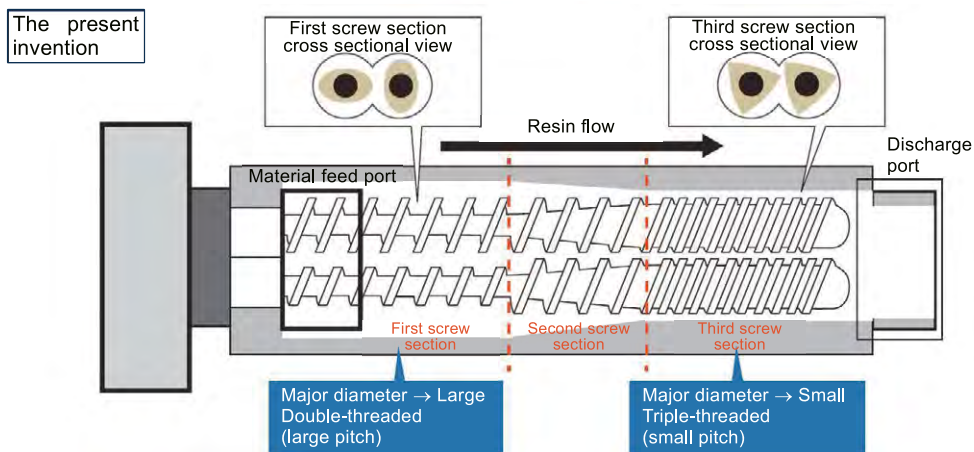
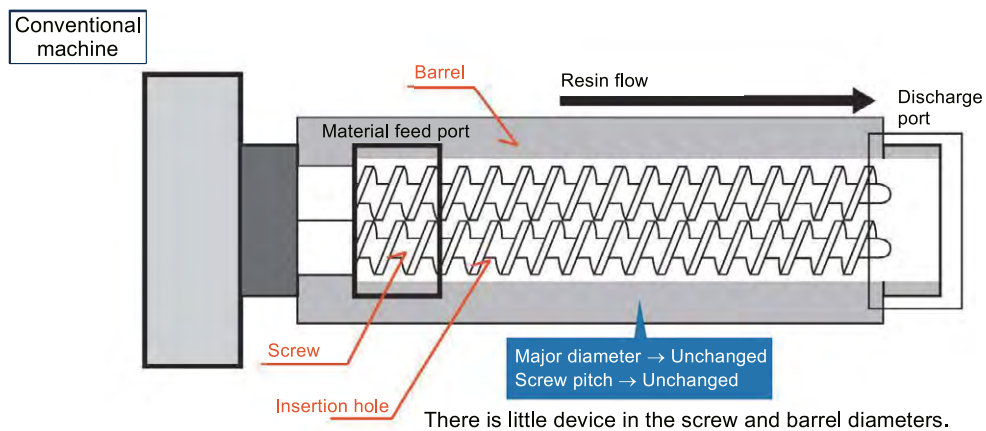
Inventor: Akiyoshi Kobayashi, Toshiki Nakazawa, Masatoshi Ohara, Hiroyuki Saito

The twin-screw extruder, which kneads resin materials in pellet or powder form, has a barrel equipped with a feed port into which materials are input, an insertion hole through which the materials fed from the feed port pass, and a discharge port through which the materials kneaded while passing through the insertion hole are discharged. Two screws are inserted into the insertion hole of this barrel, which are arranged in parallel with a fixed distance between their shafts and rotate in the same direction while engaging each other.

In the past, in order to increase the amount of material processed per unit of time, an improvement was made by employing double-threaded deep-groove screws the minor diameter of which was made smaller in relation to the major diameter to increase the kneading volume, and at the same time by increasing the screw rotational driving force. In order to increase the screw rotational driving force, the screw shaft needs to be stronger. For this reason, shafts with a high-strength spline and other methods

have been used. However, in recent years, the screw minor diameter and the screw shaft outer diameter have reached their design limits.

The patented twin-screw extruder is characterized by its configuration having a first screw section that is double-threaded and has a large major diameter, a third screw section that is triple-threaded and has a small major diameter, and a second screw section that is intermediate between the two screw sections. This characteristic allows the shearing action generated by screw rotation to work properly even when the air mixed in from the supplied resin material and powdered filler material is released and the material volume is reduced, thus keeping the deterioration of the physical properties and the state of dispersion of the kneaded material within acceptable limits. In addition, the appropriate major diameter and distance between the shafts allow for a higher amount of material processed per unit of time. This is a very productive twin-screw extruder.



01 The deterioration of the physical properties and the state of dispersion of the kneaded material can be kept within acceptable limits.

02 The appropriate major diameter and distance between the shafts allow for a higher amount of material processed per unit of time.

4 Handling System, Workpiece Handling Method, and Signal Processing Equipment

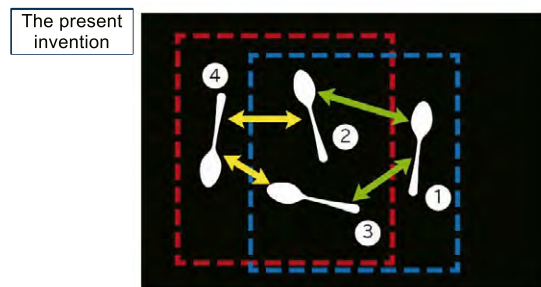
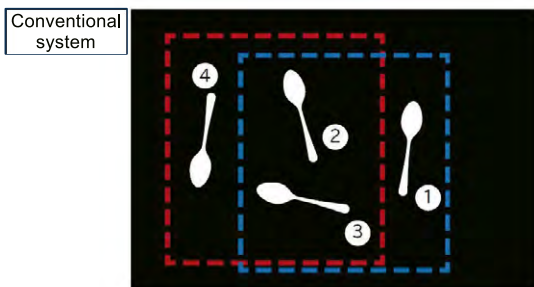
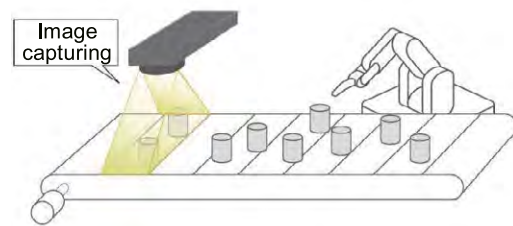
Patent number: 5,198,155
 Inventor: Yasunori Nishihara

There are widely used handling systems that have a visual sensor placed upstream of the conveyor belt to detect objects being conveyed and use the object data generated by the visual sensor to control the robot's actions on the objects.

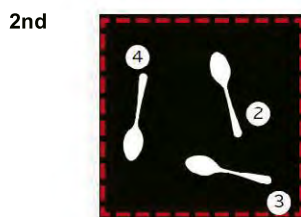
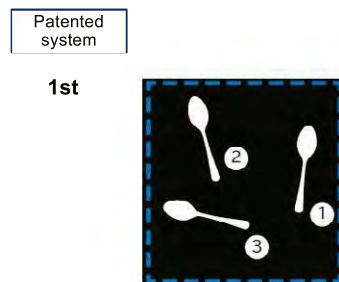
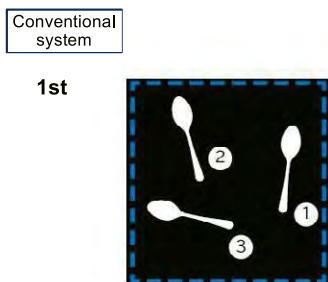
Conventional handling systems sequentially store object data captured by the visual sensors to build a database, and control the robot in accordance with the contents stored in the database. With such a method of handling object data, when the visual sensor takes multiple images in succession, each captured image contains the same object in duplicate, and the duplicated object data are stored in the database, causing an issue of unnecessary robot movements.

The patented handling system extracts objects within the tracking range from the image data, generates object data including the position and movement of the extracted objects, generates tracking data including the number of objects and

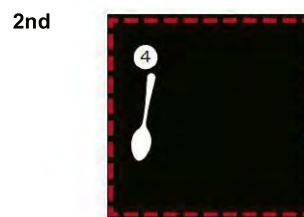
the object data, and determines the relative distance between multiple objects in the tracking area near the robot from the tracking data etc. If the distance is shorter than a certain value, the system judges that there is duplication and instructs the robot to remove one of the duplicated object data, thereby reducing unnecessary robot movements.



Determine duplication based on the relative distance of the objects.



The objects ② and ③ are duplicated in the 1st and 2nd captured images.



The duplicated data of the objects ② and ③ are removed from the 2nd captured image.

 **Unnecessary robot movements can be reduced.**

Volumes 28 and 29 of Engineering Review were issued after the company changed its name from Toshiba Machine to Shibaura Machine, and the commentators for these volumes were Dr. Higuchi and Dr. Yokoi, professors emeritus at The University of Tokyo. To tell the truth, I was bewildered when I was asked to write a comment. However, considering that this would be a good opportunity to convey my thought to Shibaura Machine, I called up my courage to accept the offer, though I am still halfway through my academic career.

My first encounter with Shibaura Machine dates back to the time when I was a fourth grader in the university, and I have been working with the company for a quarter of a century without breaks since then, though the form of collaboration changed from time to time. I was given opportunities to research various themes from process to machining system, and I appreciate Shibaura Machine for its technological cooperation that enabled me to succeed in all these projects. In particular, Mr. Katsutoshi Tanaka has been my mentor since my university days. My focus then was on machine elements and control, and Mr. Tanaka gave me a chance to start working on ultra-precision machining. I was interested in nano-scale machining technologies but I did not have the courage to launch into this area because of a lack of knowledge. Mr. Tanaka kindly said to me, "I will teach you." It was a very powerful encouragement to a young researcher, and I launched into the new area of research without fear. Thus far, Mr. Tanaka has also made various works through research (I want to use the word "works" instead of parts). His works include an aluminum plate that reflects your face if you look in it from 45 degrees (a mirror-surface aluminum plate with fine V-shaped ditches), a polishing apparatus that is too precise for students to assemble (low tolerances for the axis and the hole), and a completely noncontact precision machine with ideal control. Both I and my students can see engineering capabilities embodied in physical items, learn about the depth of manufacturing, and become interested in



Yasuhiro KAKINUMA

Professor,
Integrated Design Engineering,
Graduate School of Science and Technology,
System Design Engineering,
Faculty of Science and Technology,
Keio University

manufacturing. In this respect, industry-academic collaboration has very high educational effects on the students. I am still continuing my research with the cooperation of many engineers from Shibaura Machine, including Mr. Tanaka. The corporate culture of developing young people even in other organizations is a notable strength of Shibaura Machine.

It is a while ago when Industry 4.0 was proposed and the fusion of manufacturing and information technology was advocated. The concepts of cyberphysical systems (CPS) based on the Digital Twin and digital transformation (DX) were discussed, and recent years have seen R&D accelerate on both software and hardware toward implementation. Popular R&D themes in the area of software include data analysis by simulation and machine learning that even cover interactions between the process and the machine tool elements, and those in the area of hardware include machine tool elements that incorporate sensors, and autonomous traveling robots. The final goal of R&D on DX is ultimate automation, and it includes "labor productivity enhancement" covered by this Volume 30 of Engineering Review. Injection molding machine temperature simulation, AI-based evaluation of scraping work, a control structure for autonomous robots, the automaton and labor saving of film manufacturing equipment, logistic robot systems, robot safety systems are initiatives with DX in mind.

If you want to improve labor productivity with existing equipment, DX is a rational approach. In the meantime, the evolution of processes and machines leads to dramatic improvements in labor productivity. From this viewpoint, this volume of Engineering Review covers seed layer forming technology with medium-vacuum PVD equipment, environmental impact reduction technology in die casting, the identification of causes of failures in PMMA forming, and technology for correcting the position of a tool edge. I would say, at the risk of being criticized, that DX with existing technologies will contribute to improvement, safety and a sense of security, whereas the creation of new

processes and machines based on physical phenomena will lead to dramatic innovation. The latter is what Shibaura Machine is good at, and the company has so far developed unique processes and machines, including high precision machines. I expect that using this characteristic as a weapon fused with DX, the company will continue R&D on world-leading innovative technologies and achieve further growth.

Publish : March 21, 2025
Not for sale : All Rights Reserved Reproduction or quotation without permission is prohibited.
Publisher : Mitsunori KOKUBO
Press : SHIBAURA MACHINE CO.,LTD.
Research & Development Center
R&D Department
4-29-1,Hibarigaoka,Zama-shi,
Kanagawa-ken,252-0003,Japan

Shibaura Machine Engineering Review Editonal Commission

Chairman	Mitsunori KOKUBO		
Members	Jun FUJITA	Toshihiro IGARASHI	Hiroyuki MAEHARA
	Kenji MURAKAMI	Masaki YASHIRO	Ryouta OKE
	Hiroyuki KAKISIMA	Kenichi TAKAGI	Yuzuru WATANABE
	Katsumi IZASA	Asao SASAKI	Mitsuaki SERIZAWA
	Yusuke ISHII	Daisuke YAMAGUCHI	
Coordinator	Harumichi TOKUYAMA		
	Hiroaki ARIMATSU	Rintaro SUEKI	Hiroyuki YAMAMOTO

Offices and Manufacturing Sites

Tokyo Headquarters

2-2, Uchisaiwaicho 2-chome, Chiyoda-ku,
Tokyo 100-8503, Japan
TEL: [81]-(0)3-3509-0200
FAX: [81]-(0)3-3509-0333

Numazu Headquarters

2068-3, Ooka, Numazu-shi, Shizuoka-ken
410-8510, Japan
TEL: [81]-(0)55-926-5141
FAX: [81]-(0)55-925-6501

Tohoku Branch

2-11-2, Yaotome, Izumi-ku, Sendai-shi,
Miyagi-ken 981-3112, Japan
TEL: [81]-(0)22-374-6111
FAX: [81]-(0)22-374-6118

Chubu Branch

5-307, Kamiyashiro, Meito-ku, Nagoya-shi,
Aichi-ken 465-0025, Japan
TEL: [81]-(0)52-702-7811
FAX: [81]-(0)52-702-1141

Kansai Branch

3-14-8, Hishie, Higashiosaka-shi, Osaka
578-0984, Japan
TEL: [81]-(0)72-947-0402
FAX: [81]-(0)72-947-0408

Kyusyu Branch

2-3-23, FMT Enokida Build.,
Hakata-ku, Fukuoka-shi,
Fukuoka-ken 812-0004, Japan
TEL: [81]-(0)92-451-2795
FAX: [81]-(0)92-474-1045

Numazu Plant

2068-3, Ooka, Numazu-shi, Shizuoka-ken
410-8510, Japan
TEL: [81]-(0)55-926-5141
FAX: [81]-(0)55-925-6501

Sagami Plant

4-29-1, Hibarigaoka, Zama-shi,
Kanagawa-ken 252-0003, Japan
TEL: [81]-(0)46-258-2801
FAX: [81]-(0)46-258-2900

Gotemba Plant

1-120, Komakado, Gotemba-shi,
Shizuoka-ken 412-0038, Japan
TEL: [81]-(0)550-87-3555
FAX: [81]-(0)550-87-3742

Domestic Group Companies

SHIBAURA MACHINE ENGINEERING CO., LTD.

267-2, Nishi-sawada, Numazu-shi,
Shizuoka-ken 410-0007, Japan
TEL: [81]-(0)55-921-7800
FAX: [81]-(0)55-921-7831
<https://www.shibaura-machine.co.jp/>
smeng

TOEI ELECTRIC CO., LTD.

131, Matsumoto, Mishima-shi,
Shizuoka-ken 411-8510, Japan
TEL: [81]-(0)55-977-4111
FAX: [81]-(0)55-977-4110
[http://www.toei-electric.co.jp/index_](http://www.toei-electric.co.jp/index_.J.htm)
J.htm

TECHNOLINK CO., LTD.

30 Ukita, Kawai-cho, Iwakura-shi, Aichi-ken
482-0015, Japan
TEL: [81]-(0)587-37-3137
FAX: [81]-(0)587-66-7566
<https://www.technolink-sm.co.jp/index.html>

SHIBAURA SEMTEK CO., LTD.

2068-3, Ooka, Numazu-shi, Shizuoka-ken
410-8510, Japan
TEL: [81]-(0)55-924-3450
FAX: [81]-(0)55-925-6556
<http://www.s-semtek.co.jp/>

SHIBAURA SANGYO CO., LTD.

2068-3, Ooka, Numazu-shi, Shizuoka-ken
410-8510, Japan
TEL: [81]-(0)55-922-0816
FAX: [81]-(0)55-924-5816

Major Sites outside Japan

* : HEAD OFFICE

< East Asia >

SHANGHAI SHIBAURA MACHINE CO., LTD.

4788, Jin Du Road, Xinzhuang Industry Zone,
Shanghai, 201108, PEOPLE'S REPUBLIC OF
CHINA
TEL: [86]-(0)21-5442-0606
FAX: [86]-(0)21-5866-2450
SHANGHAI*, BEIJING, TIANJIN, DALIAN,
CHONGQING, NINGBO

SHIBAURA MACHINE (SHANGHAI) CO., LTD.

4788, Jin Du Road, Xinzhuang Industry Zone,
Shanghai, 201108, PEOPLE'S REPUBLIC OF
CHINA
TEL: [86]-(0)21-5442-5455
FAX: [86]-(0)21-5442-5466

SHIBAURA MACHINE (SHENZHEN) CO., LTD.

Room 608, Building 2, Animation Park,
Yuehai Road, Nanhai Street, Nanshan
District, Shenzhen, 518054, PEOPLE'S
REPUBLIC OF CHINA
TEL: [86]-(0)755-8625-0599
FAX: [86]-(0)755-8625-0522
SHENZHEN*, GUANGZHOU

SHIBAURA MACHINE TAIWAN CO., LTD.

7F, No.168, Ruiguang Road, Neihu District,
Taipei City, 11491, TAIWAN
TEL: [886]-(0)2-2659-6558
FAX: [886]-(0)2-2659-6381

< South East Asia >

SHIBAURA MACHINE SINGAPORE PTE. LTD.

123 Pioneer Road, Singapore 639596,
SINGAPORE
TEL: [65]-68611455
FAX: [65]-68612023
SINGAPORE*, KUALA LUMPUR, PENANG

SHIBAURA MACHINE (THAILAND) CO., LTD.

127/28 Panjathanee Tower, 23rd Floor,
Nonthree Road, Khwaeng Chong Nonthree,
Khet Yannawa, Bangkok 10120, THAILAND
TEL: [66]-(0)2-681-0158 ~ 61
FAX: [66]-(0)2-681-0162

PT. SHIBAURA MACHINE INDONESIA

Jalan Ciputat Raya No. 1B Unit 1&2,
Desa/Kelurahan Pondok Pinang, Kec.
Kebayoran Lama, Kota Adm. Jakarta Selatan,
Provinsi DKI Jakarta, 12310, INDONESIA
TEL: [62]-(0)21-22761766, 22761770
FAX: [62]-(0)21-2122761624

SHIBAURA MACHINE VIETNAM COMPANY LIMITED.

2nd Floor, VIT Tower, No. 519, Kim Ma Street,
Ngoc Khanh Ward, Ba Dinh district, Hanoi,
VIETNAM
TEL: [84]-(0)24-2220-8700,1
FAX: [84]-(0)24-2220-8702
HANOI*, HO CHI MINH

SHIBAURA MACHINE INDIA PRIVATE LIMITED

No. 65 (P.O. Box No. 5), Chennai-Bangalore
Highway, Chembarambakkam, Poonamallee
Taluk, Thiruvallur, Chennai, TN 600123,
INDIA
TEL: [91]-(0)44-2681-2000
FAX: [91]-(0)44-2681-0303
CHENNAI*, DELHI, MUMBAI

SHIBAURA MACHINE MANUFACTURING (THAILAND) CO., LTD.

7/499 Moo 6, Tambol Mabyangporn, Amphur
Pluakdaeng, Rayong 21140, THAILAND
TEL: [66]-(0)38-027313
FAX: [66]-(0)38-027317

< The Americas >

SHIBAURA MACHINE COMPANY, AMERICA

755 Greenleaf Avenue, Elk Grove Village, IL
60007, U.S.A.
TEL: [1]-847-593-1616
FAX: [1]-847-593-0897
CHICAGO*, LOS ANGELES, CHARLOTTE,
ATLANTA, ONTARIO/CANADA

SHIBAURA MACHINE MEXICO, S.A. DE C.V.

Circuito Luxma No. 115, Poligono
Industrial, Milenio, C.P. 37290 Leon,
Guanajuato, MEXICO
TEL: [52]-477-101-8600

SHIBAURA MACHINE DO BRASIL COMERCIO DE MAQUINAS LTDA.

Rua Cubatao, 86 Conjunto 1307, Vila
Mariana, Sao Paulo, SP CEP 04013-000,
BRASIL
TEL: [55]-(0)11-3253-3331
FAX: [55]-(0)11-3586-0138

< Europe >

SHIBAURA MACHINE EUROPE S.R.L.

Via Gaudenzio Fantoli 7, Piano 2, 20138,
Milano, ITALIA
TEL: [39]-02-50041667
FAX: [39]-02-50041668

Shibaura Machine

2-2, Uchisaiwaicho 2-chome, Chiyoda-ku, Tokyo 100-8503, Japan
TEL : [81]-(0)3-3509-0200 FAX : [81]-(0)3-3509-0333

2068-3, Ooka, Numazu-shi, Shizuoka-ken 410-8510, Japan
TEL : [81]-(0)55-926-5141 FAX : [81]-(0)55-925-6501

<https://www.shibaura-machine.co.jp/>



This <Shibaura Machine Engineering Review> is made of LIMEX, a new material made mainly from limestone.
It uses less water and trees.

SM25004-800-TP